ISSN 1881-7815 Online ISSN 1881-7823

BST BioScience Trends

Volume 20, Number 2
April 2026

IRCA BSSA

IACMHR

www.biosciencetrends.com

BST
BioScience Trends

ISSN: 1881-7815
Online ISSN: 1881-7823
CODEN: BTIRCZ
Issues/Year: 6
Language: English
Publisher: IACMHR Co., Ltd.

BioScience Trends is one of a series of peer-reviewed journals of the International Research and Cooperation Association for Bio & Socio-Sciences Advancement (IRCA-BSSA) Group. It is published bimonthly by the International Advancement Center for Medicine & Health Research Co., Ltd. (IACMHR Co., Ltd.) and supported by the IRCA-BSSA.

BioScience Trends devotes to publishing the latest and most exciting advances in scientific research. Articles cover fields of life science such as biochemistry, molecular biology, clinical research, public health, medical care system, and social science in order to encourage cooperation and exchange among scientists and clinical researchers.

BioScience Trends publishes Original Articles, Brief Reports, Reviews, Policy Forum articles, Communications, Editorials, News, and Letters on all aspects of the field of life science. All contributions should seek to promote international collaboration.

Editorial Board

Editorial and Head Office

Pearl City Koishikawa 603,
2-4-5 Kasuga, Bunkyo-ku, Tokyo 112-0003, Japan
E-mail: office@biosciencetrends.com

BioScience Trends

Editorial and Head Office

Pearl City Koishikawa 603, 2-4-5 Kasuga, Bunkyo-ku,
Tokyo 112-0003, Japan

E-mail: office@biosciencetrends.com
URL: www.biosciencetrends.com

Editorial Board Members

CONTENTS

Volume 20, Number 2, 2026

Editorial

Review

Original Article

Brief Report

Editorial

DOI: 10.5582/bst.2026.01020

Promoting an international consensus on frailty assessment: An urgent call to address the challenges of perioperative management in an aging population

Ying Xia[1,2], Wei Tang[3,4,*]

[1] Department of Neurosurgery, Integrated Neuroscience Center, Geriatric Hospital of Hainan, Haikou, China;
[2] Department of Neurosurgery, Haikou Affiliated Hospital of Central South University Xiangya School of Medicine , Haikou, China;
[3] International Health Care Center, National Center for Global Health and Medicine, Japan Institute for Health Security, Tokyo, Japan;
[4] Hepato-Biliary-Pancreatic Surgery Division, Department of Surgery, Graduate School of Medicine, University of Tokyo, Tokyo, Japan.

SUMMARY: As populations age at an unprecedented pace globally, frailty has emerged as a critical challenge in perioperative care. While clinicians broadly acknowledge the value of frailty assessment, embedding it systematically in care pathways remains difficult to implement systematically. We compared perioperative frailty guidelines from the United Kingdom, United States, Europe, and the Asia-Pacific, finding significant inconsistencies in tool selection, risk stratification criteria, and pathway design. Strikingly, approximately 99.6% of frailty research remains confined to risk characterization, whereas only 0.4% is directed toward improving care, highlighting a substantial gap between evidence and practice. Digital technologies promise a wider uptake of frailty screening, and yet algorithmic bias threatens to under-detect frailty in underserved groups if left unchecked. We outline five policy priorities: first, an internationally coordinated consensus on core assessment standards needs to be reached; second, end-to-end pathways that span screening, graded assessment, targeted intervention, and outcome tracking need to be devised; third, digital technology needs to be accelerated along with the devising of explicit safeguards for equity; fourth, high-quality evidence needs to be generated through function-centered outcomes and cost-effectiveness analyses to demonstrate the real-world value of frailty-focused care pathways; and fifth, frailty management needs to be integrated into national chronic-disease frameworks. Closing the gap between detection and action will require global collaboration and a reframing of frailty, not as a passive label but as a call to intervene.

Keywords: frailty assessment, perioperative management, international consensus, aging population, chronic disease management, healthcare policy

1. Introduction

Globally, rapid population aging is fundamentally reshaping healthcare systems (*1,2*). The World Health Organization (WHO) projects that adults age 60 and older will nearly double from 1 billion in 2020 to 2.1 billion by 2050 (*3*). Japan, which has the world's first super-aged population with over 29.3% of its population age 65 or older, offers a preview of the challenges other nations will soon face (*4,5*). Against this demographic backdrop, frailty has evolved from a niche research concept into a central target for clinical management (*6*). Defined as a state of diminished physiological reserve across multiple organ systems that compromises homeostasis and heightens vulnerability to stressors, frailty affects an estimated 12–24% of community-dwelling older adults globally (*7*). Crucially, frailty has proven to be an independent predictor of adverse outcomes, hospital admission, postoperative complications, and mortality (*6*).

Yet despite a broad consensus on the clinical value of frailty assessment, its systematic integration in perioperative care pathways remains elusive. Although frailty-related publications have surged worldwide, roughly 99.6% use the construct solely for risk profiling or prognostic validation; only 0.4% translate assessment findings into prospective redesign of care processes (*8*). This gap between evidence generation and clinical implementation underscores the urgent need for an international consensus.

2. Assessment heterogeneity: The case for a unified framework

The most significant barrier to perioperative frailty

assessment is the striking heterogeneity in tool selection and risk thresholds (*9*). An international comparison reveals divergent approaches. The United Kingdom designates the Clinical Frailty Scale (CFS) as the gateway tool and mandates documentation at three key junctures: referral, preoperative assessment, and hospital admission.(*10*). In contrast, the United States does not mandate a specific instrument; instead, frailty assessment is integrated into a broader best-practice framework for the care of geriatric surgical patients (*11*). The European Society of Anaesthesiology and Intensive Care (ESAIC) 2024 guidelines position frailty as one component of multidimensional preoperative risk evaluation rather than as a stand-alone entity (*12*).

The Asia-Pacific region presents a distinctive, public-health-oriented model. Japan employs a government-led strategy in which the Kihon Checklist (KCL) and the Questionnaire for Medical Checkup of Old-Old (QMCOO) are embedded within the system for eligibility for Long-Term Care Insurance (LTCI) (*13,14*). China is progressively adopting a closed-loop paradigm centered on screening, a comprehensive geriatric assessment, and targeted intervention (*15*). South Korea has established a primary-care gatekeeper model for systematic screening (*16*).

Such heterogeneity creates a threefold challenge. First, divergent risk-stratification criteria across instruments impede data comparability between institutions and regions. Second, structural discontinuities disrupt the transfer of frailty information from community screening to acute-care settings. Third, no universally accepted threshold exists for triggering a comprehensive geriatric assessment or multidisciplinary intervention. An internationally coordinated consensus framework is therefore imperative. It should define a core toolkit of validated instruments, harmonize risk-stratification criteria, and specify requirements for data interoperability.

3. Digital transformation: Opportunities and equity considerations

The rapid evolution of digital health technologies presents transformative opportunities for frailty assessment. Japan's "e-Frailty Navi" system, for example, uses AI algorithms to analyze household electricity-consumption patterns, enabling non-invasive detection of frailty risk among older adults living alone (*17*). Wearable devices continuously capture dynamic metrics such as gait speed and physical-activity intensity. The electronic Frailty Index (eFI), derived from electronic medical records (EMR), has been deployed at scale across NHS England; a validation study encompassing roughly 900,000 patient records has demonstrated that the eFI has strong predictive power for mortality, hospitalization, and long-term care admission (*18*).

Digital frailty detection, however, raises equity concerns that cannot be ignored. A landmark study by Obermeyer *et al*. revealed substantial racial bias in certain commercial care-management algorithms: at equivalent risk scores, black patients bore significantly higher actual disease burdens than white patients (*19*). This bias arose because the algorithm used healthcare expenditure as a proxy for health need, and systematic disparities in access to care led to underestimation of need among underserved populations. eFI-type algorithms may embed similar biases. In under-resourced areas or minority communities, EMR documentation tends to be less complete and of lower quality, introducing missingness bias that systematically underestimates the prevalence of frailty precisely among those in whom intervention is most needed (*20*).

Scaling digital frailty detection must therefore be accompanied by equity safeguards: stratified subgroup analyses during algorithm validation, fairness metrics such as equalized odds and calibration across demographic groups, and governance frameworks that incorporate bias audits and community engagement.

4. From detection to intervention: Shared decision-making and care continuity

The ultimate goal of perioperative frailty management extends beyond risk prediction to the initiation of individualized intervention. Best-practice guidelines issued by the American College of Surgeons and the American Geriatrics Society explicitly state that preoperative discussions should prioritize outcomes that matter most to patients, including functional decline, loss of independence, and potential need for skilled nursing care (*21*). For high-risk patients (*e.g.*, a CFS score of $\geq$ 5), clinical pathways should mandate multidisciplinary shared decision-making conferences involving surgery, anesthesiology, geriatrics, and the patient's family.

Current guidelines, however, reveal gaps in the standardization of shared decision-making tools and decision aids (*21*). Future pathways should integrate frailty assessment results with prognostic prediction models to provide quantified risk evidence for shared decision-making, ensuring that care plans genuinely reflect the life goals and value preferences of frail older adults.

Achieving continuity of care likewise depends on an interoperable information infrastructure. Japan's experience is instructive: although a data-linked framework connecting the National Database (NDB) with LTCI records has been established, routine interoperability in clinical practice between community health screening records (such as KCL or QMCOO scores) and hospital EMRs remains limited, with information exchange often relying on traditional or ad hoc channels (*22*). South Korea faces analogous challenges: data linkage between National Health Insurance Service (NHIS) claims data and individual

hospital EMRs is constrained by legal and privacy protection requirements (*23*).

5. Policy recommendations: Towards a systemic framework

The analysis above points to five priorities for advancing perioperative frailty management.

First, an international consensus is needed. The WHO or major geriatric medicine societies should establish a working group charged with defining a core set of validated tools and common risk-stratification thresholds. Because the CFS already anchors several regional guidelines, a CFS score of 5 or higher represents a reasonable threshold to trigger a comprehensive geriatric assessment. In parallel, agreed-upon data standards would allow the results of community screening to accompany patients across acute-care settings.

Second, clinical pathways must be redesigned end to end. Frailty-informed care should not stop at the preoperative visit. Intraoperative protocols and postoperative follow-up should be fully incorporated in the clinical pathway, thereby linking screening, graded assessment, tailored intervention, and outcome tracking. When a patient is identified as frail, the pathway should require a multidisciplinary conference that brings together surgeons, anesthesiologists, geriatricians, and family members. After discharge, dynamic monitoring and clear community hand-off protocols can curb functional decline and preventable readmissions.

Third, digital adoption should be accelerated while safeguarding equity. Electronic frailty indices embedded in primary care records can be used to automate screening at scale. Yet this promise comes with a caveat: algorithms must be stress-tested for fairness. Certification schemes, subgroup-stratified validation, periodic bias audits, and secure interoperability platforms linking community and hospital data are all essential guardrails.

Fourth, high-quality evidence must be generated. The lack of rigorous data remains the chief obstacle to wider implementation of frailty-directed pathways. Multicenter pragmatic trials and stepped-wedge designs should be used to evaluate whether pathway redesign actually improves outcomes and reduces resource use. Outcome sets need to extend beyond 30-day mortality and readmission, as functional trajectories, disability-free survival, and quality of life are more meaningful to older patients, and cost-effectiveness analyses are indispensable for policymakers when evaluating scalability.

Fifth, frailty should be integrated into chronic disease policy. Frailty management should be positioned alongside diabetes and cardiovascular-disease programs within national chronic-care frameworks. Standardized perioperative assessment protocols and quality metrics are needed for older adults living with multimorbidity. Looking ahead, national strategies should embed community-based screening into health system interventions, shifting the focus from treating disease to preserving function.

6. Conclusion

Frailty profoundly shapes perioperative outcomes, yet guideline implementation lags far behind scientific understanding. The imperative now is to complete a paradigm shift by moving from treating frailty as a static risk label to using it as a dynamic trigger for intervention. This demands consensus risk thresholds that activate prehabilitation and monitoring protocols, the integration of automated screening into clinical decision-support systems, and an interoperability infrastructure that enables seamless data transfer across care settings. Only by closing the gap between detection and action can frailty-directed care fulfill its promise of improving surgical outcomes and advancing health equity for older adults.

As aging continues to accelerate globally, forging an international consensus on perioperative frailty assessment is not merely an academic exercise; it is a public health priority affecting the well-being of hundreds of millions of older people. The international community must work together to translate an evidence-based consensus into actionable clinical pathways and policy frameworks, proactively addressing the healthcare challenges of an aging population.

Funding: This work was supported by a grant from the National Natural Science Foundation of China (No. 82460268).

Conflict of Interest: The authors have no conflicts of interest to disclose.

References

1. Deng Y, Zhang K, Zhu J, Hu X, Liao R. Healthy aging, early screening, and interventions for frailty in the elderly. Biosci Trends. 2023; 17:252-261.
2. Hu X, Ma Y, Jiang X, Tang W, Xia Y, Song P. Neurosurgical perioperative management of frail elderly patients. Biosci Trends. 2023; 17:271-282.
3. World Health Organization. Ageing and health. *https://www.who.int/news-room/fact-sheets/detail/ageing-and-health* (accessd January 19, 2026).
4. Deng Y, Sato N. Global frailty screening tools: Review and application of frailty screening tools from 2001 to 2023. Intractable Rare Dis Res. 2024; 13:1-11.
5. Ministry of Health, Labour and Welfare, Japan. State of aging of the population. *https://www8.cao.go.jp/kourei/whitepaper/w-2025/zenbun/pdf/1s1s_01.pdf* (accessed January 19, 2026). (in Japanese)
6. Deng Y, Yamauchi K, Song P, Karako T. Frailty in older adults: A systematic review of risk factors and early intervention pathways. Intractable Rare Dis Res. 2025; 14:93-108.

7. O'Caoimh R, Sezgin D, O'Donovan MR, Molloy DW, Clegg A, Rockwood K, Liew A. Prevalence of frailty in 62 countries across the world: A systematic review and meta-analysis of population-level studies. Age Ageing. 2021; 50:96-104.
8. Hothi H, Paolone AR, Pezeshki M, Griffith LE, Kennedy CC, Leong DP, Marcucci M, Papaioannou A, Lee J. The implementation of frailty assessment tools in the acute care setting: A scoping review. J Am Geriatr Soc. 2025; 73:2571-2578.
9. Ma YN, Karako K, Xia Y, Song PP, Hu XQ. International landscape of guidelines for perioperative frailty assessment and barriers to clinical translation. Biosci Trends. 2026; 20:149-150.
10. Partridge JSL, Ryan J, Dhesi JK, CPOC-BGS perioperative frailty guideline group. New guidelines for the perioperative care of people living with frailty undergoing elective and emergency surgery-A commentary. Age Ageing. 2022; 51:afac237.
11. Chow WB, Rosenthal RA, Merkow RP, Ko CY, Esnaola NF, American College of Surgeons National Surgical Quality Improvement P, American Geriatrics S. Optimal preoperative assessment of the geriatric surgical patient: A best practices guideline from the American College of Surgeons National Surgical Quality Improvement Program and the American Geriatrics Society. J Am Coll Surg. 2012; 215:453-466.
12. Lamperti M, Romero CS, Guarracino F, *et al.* Preoperative assessment of adults undergoing elective noncardiac surgery: Updated guidelines from the European Society of Anaesthesiology and Intensive Care. Eur J Anaesthesiol. 2025; 42:1-35.
13. Satake S, Arai H. Questionnaire for medical checkup of old-old (QMCOO). Geriatr Gerontol Int. 2020; 20:991-992.
14. Deng Y, Karako K, Yamauchi K, Song PP. Implementation and current status of frailty assessment in Japanese hospitals: Processes, epidemiology, and future directions. Biosci Trends. 2026; 20:139-148.
15. Ji M, Liu X. Expert opinions on perioperative management of older frail patients. J Clin Anesthesiol. 2023; 39:991-997. (in Chinese)
16. You HS, Kwon YJ, Kim S, *et al*. Clinical practice guidelines for managing frailty in community-dwelling Korean elderly adults in primary care settings. Korean J Fam Med. 2021; 42:413-424.
17. Chubu Electric Power Company. Launch of "e-Frailty Navi," a frailty detection service for local governments. *https://www.chuden.co.jp/english/corporate/releases/pressreleases/1210613_5163.html* (accessd January 19, 2026).
18. Clegg A, Bates C, Young J, Ryan R, Nichols L, Ann Teale E, Mohammed MA, Parry J, Marshall T. Development and validation of an electronic frailty index using routine primary care electronic health record data. Age Ageing. 2016; 45:353-360.
19. Obermeyer Z, Powers B, Vogeli C, Mullainathan S. Dissecting racial bias in an algorithm used to manage the health of populations. Science. 2019; 366:447-453.
20. Ferryman K, Pitcan M. Fairness in precision medicine. Data & Society Research Institute, New York (NY), 2018. *https://datasociety.net/wp-content/uploads/2018/02/DataSociety_Fairness_In_Precision_Medicine_Feb2018.pdf* (accessed January 19, 2026).
21. Mohanty S, Rosenthal RA, Russell MM, Neuman MD, Ko CY, Esnaola NF. Optimal perioperative management of the geriatric patient: A best practices guideline from the American College of Surgeons NSQIP and the American Geriatrics Society. J Am Coll Surg. 2016; 222:930-947.
22. Ministry of Health Labour, and Welfare, Japan. National database of health insurance claims and specific health checkups of Japan (NDB). *https://www.mhlw.go.jp/stf/seisakunitsuite/bunya/kenkou_iryou/iryouhoken/reseputo/index.html* (accessd January 19, 2026). (in Japanese)
23. Kim HS, Kim J, Bae G. Development of a hospital frailty risk score for community-dwelling older adults using data from electronic hospital records in South Korea. PLoS One. 2023; 18:e0293646.

Received January 18, 2026; Revised January 27, 2026; Accepted January 29, 2026.

**Address correspondence to:*
Wei Tang, International Health Care Center, National Center for Global Health and Medicine, Japan Institute for Health Security, Tokyo 162-8655, Japan.
E-mail: politang-tky@umin.ac.jp

Released online in J-STAGE as advance publication January 31, 2026..

Mini-Review

DOI: 10.5582/bst.2025.01392

Implementation and current status of frailty assessment in Japanese hospitals: Processes, epidemiology, and future directions

Yi Deng[1], Kenji Karako[2,*], Katsuya Yamauchi[3], Peipei Song[4,5,*]

[1] Graduate School of Rehabilitation Medicine, Hamamatsu University School of Medicine, Hamamatsu, Shizuoka, Japan;
[2] Department of Surgery, Graduate School of Medicine, The University of Tokyo, Tokyo, Japan;
[3] Department of Rehabilitation Medicine, Hamamatsu University School of Medicine, Shizuoka, Japan;
[4] National College of Nursing, Japan Institute for Health Security, Tokyo, Japan;
[5] Center for Clinical Sciences, Japan Institute for Health Security, Tokyo, Japan.

SUMMARY: Frailty has become a pressing health concern in Japan as it has entered a super-aged society. Early identification of frailty is essential to preventing disability, hospitalization, and dependency on long-term care, and yet the implementation of standardized screening across clinical settings remains inconsistent. This review synthesizes current evidence on frailty assessment practices in Japan, highlights key challenges in routine implementation, and examines the potential of emerging digital tools. The feasibility of recent digital innovations — including artificial intelligence analysis of home electricity data, wearable-based mobility monitoring, and EMR-integrated frailty indices — has been demonstrated in pilot settings, though evidence of their large-scale clinical effectiveness remains limited. International comparisons have revealed that countries and regions such as the United Kingdom, Canada, Australia, and Singapore are increasingly implementing electronic frailty indices with policy-level support, offering valuable insights for Japan. Overall, although Japan has made significant progress in recognizing the importance of frailty assessment, substantial gaps remain in standardization, system integration, and clinical implementation. Strengthening national policy frameworks, enhancing workforce training, and accelerating a digital transformation may enable the development of a more comprehensive and scalable frailty-screening system to support healthy aging.

Keywords: frailty, frailty screening, hybrid model, community-based comprehensive care system, digital

1. Introduction

Population aging has become one of the most profound demographic shifts of the 21st century, reshaping health-care systems, social structures, and economic sustainability worldwide. According to Ageing and Health from the World Health Organization, the global population age ≥ 60 is projected to rise from 1 billion in 2020 to 1.4 billion by 2050 (*1*). By 2050, the world's population of people age 60 and older will double (2.1 billion). However, no country exemplifies the front line of this transition more starkly than Japan. Driven by unprecedented longevity and historically low fertility, Japan had the world's first "super-aged" population in 2007 (*2*) and now has the highest proportion of adults age ≥ 65 globally, exceeding approximately 29.3% in 2025 (*3*). Japan's demographic shift has been rapid and compressed into a few decades, creating a unique natural laboratory for examining the health consequences of population aging, including frailty, dependence on care, and healthcare system stress. As other countries accelerate toward similar demographic trajectories, Japan's experience provides critical insights into the clinical, organizational, and societal challenges posed by extreme population aging.

The influence of frailty on the health of the elderly has been prominent research focus in recent years. Fried *et al*. (*4*) provided the first standardized definition of the concept of frailty, with decreased internal stability and increased vulnerability due to the diminution of the functional reserves of multiple physiological systems. According to a meta-analysis, the global prevalence of frailty among community-dwelling older adults ranges from 12% to 24%, based on data from 1,755,497 participants across 62 countries and regions (*5*). In epidemiological studies conducted in Japan (*6*), the prevalence of frailty among individuals age 65 and older is 8.7%, while approximately 40.8% are classified as pre-frail. This indicates that nearly half of the older population in Japan faces health risks associated with frailty. As a dynamic and reversible geriatric syndrome, frailty lies between self-reliance and the need for care.

Reasonable preventive interventions can enable the elderly to resume living independently (*7*). A point worth noting is that a number of evidence-based studies have found that frailty could be a predictive factor for adverse outcomes, including prognosis, hospitalization or rehospitalization, postoperative complications, and mortality rates (*8*), which means that screening for frailty is very important in a clinical setting.

Despite the growing recognition of frailty screening in Japan and the rapid emergence of digital health technologies, current approaches remain fragmented and insufficient to meet the complex demands of a super-aged population. Bedside frailty screening tools, while clinically interpretable and well aligned with nursing workflows, are typically cross-sectional and episodic, limiting their ability to capture dynamic functional decline beyond the hospital setting. Conversely, passive digital monitoring approaches offer longitudinal and scalable data streams but often lack clinical context, multidimensional interpretation, and clear linkage to care pathways. In Japan, where frailty assessment is closely tied to nursing practice, discharge planning, and eligibility for long-term care insurance services, neither conventional tools nor digital-only solutions are sufficient in isolation. This gap highlights the need for a hybrid frailty screening model that integrates bedside clinical assessment with passive digital monitoring, enabling continuous risk detection while preserving clinical interpretability and care relevance across hospital, community, and home settings. However, how such a hybrid model should be conceptualized, operationalized, and positioned within Japan's health-care system remains insufficiently discussed.

2. Frailty screening tools and the status of frailty assessment in Japan

2.1. Frailty screening tools in Japan

With the growing burden of disease-related frailty risk (*9*), Japan has, in line with recommendations from the Japanese Geriatrics Society (*10*) and the Ministry of Health, Labour and Welfare (MHLW) (*11*), increasingly recognized the importance of incorporating frailty assessment into routine care. However, the extent of implementation varies substantially across institutions, and efforts to systematically integrate frailty evaluation into standard clinical practice remain incomplete. The most direct and effective tool for evaluating debilitating conditions is a frailty screening tool; despite the wide availability of validated frailty instruments, each tool is designed with a distinct theoretical framework, operational characteristics, and clinical purposes. As a result, no single assessment tool has emerged as a universally accepted gold standard (*12*), and selection typically depends on the clinical setting and the specific outcome of interest. Frailty assessment in Japan has evolved in parallel with the country's rapid demographic aging, and hospitals, community health programs, and long-term care systems increasingly rely on standardized tools to detect early functional decline. Several frailty instruments — some adapted from international standards and others developed domestically — are widely used across clinical and public health settings. Among these, the Japanese Cardiovascular Health Study criteria (J-CHS) (*13,14*), the Kihon Checklist (KCL) (*15,16*), the FRAIL scale (*17,18*), and the Tilburg Frailty Indicator (TFI) (*19,20*) constitute the core group of instruments used in Japanese hospitals and community assessments. Standardized Screening Tools in the Japanese Context: From KCL to Questionnaire for Medical Checkup of Old-Old (QMCOO). Japan has pioneered a policy-driven, tiered approach to frailty screening, uniquely characterized by the integration of self-reported multidimensional instruments into national health programs. Central to this framework is the KCL (*15*), a 25-item validated questionnaire encompassing physical, nutritional, oral, and cognitive domains, as well as social isolation. Unlike purely clinical scales, the KCL serves as a robust "upstream" screening tool with high sensitivity for predicting long-term care insurance (LTCI) certification and all-cause mortality. Its implementation transcends hospital boundaries, functioning as a bridge between community-based primary prevention and clinical risk stratification. Moreover, the introduction of the QMCOO by the MHLW in 2020 represents a strategic shift towards identifying "pre-frailty" in individuals age 75 and older. These instruments, particularly when adapted into digital formats or integrated with electronic health records (EHR), offer a distinctive "Japanese model" of frailty surveillance. This model prioritizes functional reserve and social participation over a mere accumulation of deficits, providing a comprehensive evidentiary base for perioperative optimization and post-discharge rehabilitation planning in a super-aged population.

Despite the widespread availability of validated frailty screening instruments in Japan, a persistent tool–setting mismatch remains a critical challenge in routine clinical practice. Several commonly used tools demonstrate inherent limitations when utilized outside their original target contexts (Table 1). The KCL, while comprehensive and well-suited to community-based screening and long-term care risk stratification, is often impractical in acute-care settings due to its length and reliance on self-reported functional and psychosocial domains, which may be unreliable during acute illness. Conversely, the J-CHS has been widely accepted in epidemiological research and phenotype-based frailty classification, but it provides limited guidance for individualized nursing care planning or multidisciplinary intervention design. In addition, ultra-brief instruments such as the FRAIL scale, despite their feasibility in busy clinical environments, suffer from low information

Table 1. Comparison of scales commonly used in Japan

Tool	Domains covered	Items (*n*)	Frailty classification	Time burden	Rationale for selection	Frequency of use in Japan	Context suitability	Critical appraisal	*Ref.*
J-CHS (Japanese Cardiovascular Health Study Criteria)	Physical frailty phenotype (grip strength, walking speed, exhaustion, physical activity, weight loss)	5	≥ 3 frail; 1–2 pre-frail	Moderate (5–10 min)	Adapted from the original CHS phenotype; standardized definition of physical frailty; widely used in Japanese population-based studies and national surveys	High	Epidemiological studies; community-dwelling older adults; research-oriented frailty phenotyping	Focuses primarily on physical frailty components; limited applicability for nursing care planning, multidisciplinary intervention design, or discharge coordination; insufficient coverage of psychosocial and care-related domains	*13,14*
KCL (Kihon Checklist)	Multidimensional (physical, social, cognitive, mood, nutrition, oral health)	25 5 15	≥ 8 frail; 4–7 pre-frail	Long (10–15 min)	Developed by the Ministry of Health, Labour and Welfare; widely implemented nationwide; covers multidimensional domains including physical, psychological, and social functions; closely linked to assessment of eligibility for long-term care insurance (LTCI)	Very high	Community-based screening; LTCI risk stratification; discharge planning support	Limited feasibility in acute-care settings due to questionnaire length and reliance on self-reported information; responses may be unreliable during acute illness, hospitalization, or cognitive impairment; less suitable for rapid bedside screening	*15,16*
FRAIL Scale	Fatigue, Resistance, Ambulation, Illnesses, Loss of weight		≥ 3 frail; 1–2 pre-frail	Very short (≤ 2 min)	Ultra-brief (5 items); minimal training required; highly feasible in time-constrained settings	Moderate	Rapid screening in busy clinical settings; outpatient clinics; preliminary triage	Low information density; limited sensitivity to multidimensional functional decline; insufficient granularity for rehabilitation planning, care coordination, or individualized intervention strategies	*17,18*
The Tilburg Frailty Indicator (TFI)	Multidimensional (physical, psychological, social)		≥ 5 frail	Moderate (5–10 min)	Explicit multidimensional framework	Low in Japan	Community and outpatient settings; multidimensional frailty assessment	Less commonly integrated into routine hospital workflows; relatively limited uptake in acute-care settings; longer administration time compared to ultra-brief tools	*19,20*

density and may insufficiently capture multidimensional functional deficits relevant to care coordination and discharge planning. These mismatches mean that the challenge with frailty assessment in Japan lies not in the lack of tools, but in the absence of context-appropriate selection frameworks linking screening objectives, clinical settings, and downstream care pathways.

Beyond general screening frameworks, frailty assessment has increasingly been incorporated into disease- and specialty-specific clinical guidance in Japan, and particularly in cardiovascular care. The 2025 Japanese Circulation Society (JCS)/Japanese Heart Failure Society (JHFS) Guideline (*21*) on Diagnosis and Treatment of Heart Failure explicitly incorporates frailty into its recommended evaluation and management pathways, including the revision of methods of assessing frailty in guideline tables to guide risk stratification and treatment planning for older patients with heart failure. Specifically, the revised guideline adds a structured approach to assessing physical and cognitive frailty domains in patients with heart failure, indicating that frailty status should inform peri-interventional decisions and prognostic considerations prior to invasive procedures. This guideline-level endorsement effectively elevates frailty assessment from an optional consideration to a core element of cardiovascular practice in Japan. Together, these developments suggest a gradual shift toward embedding frailty assessment within specialty-specific perioperative and clinical pathways, reinforcing its relevance beyond general population screening, and supporting its routine adoption in surgical and hospital settings.

2.2. Status of frailty assessment in Japan

As physical frailty becomes increasingly prevalent among older adults in Japan, there is growing recognition that frailty status is a critical determinant of hospital outcomes. Although nationwide initiatives have been launched to promote frailty prevention and management, substantial variation remains in how these programs are implemented across the country. Only a limited number of hospitals — particularly those with established geriatric services — have incorporated routine frailty screening into their nursing admission procedures (*22-24*). Frailty assessment is typically included within the first 24–48 hours of admission, integrated into the nursing intake workflow. Screening is usually performed by ward nurses using brief standardized instruments. If the screening indicates a frail status, patients are subsequently referred for a secondary comprehensive geriatric assessment in collaboration with relevant departments — such as geriatrics, rehabilitation, and nutrition. This integrated approach enables the development of a more comprehensive treatment plan tailored to the patient's condition and facilitates timely interdisciplinary communication among healthcare professionals. The assessment results are used to guide early mobilization therapy, nutrition interventions, polypharmacy review, and discharge planning, including linkage to LTCI services and community support programs (*25*), as shown in Figure 1.

Within the Japanese healthcare system, routine screening and management extend beyond physical frailty to include the identification of social vulnerabilities, such as living alone or having limited social support. When such vulnerabilities are recognized during preoperative assessment, perioperative care pathways can initiate early coordination with Community General Support Centers. Established under the Community-based Integrated Care System, these municipally operated centers serve as coordination hubs linking medical facilities with long-term care services, social welfare programs, and community resources. Early engagement allows discharge planning to begin before surgery, enabling advance arrangements for at-home nursing, care management, or transitional facility placement. This approach reflects Japan's administrative–medical integration, whereby hospital-based care is systematically linked to community support mechanisms to facilitate continuity of care perioperatively.

Moreover, coordination between hospitals and community-based care providers still varies, reducing continuity for frail patients after discharge. To address these gaps, Japan is promoting digital solutions such as the use of AI to analyze household electricity consumption patterns, enabling non-invasive detection of frailty risk among older adults living alone (*26*). This approach is particularly noteworthy, as it represents a model that integrates digital technologies with a community-based comprehensive care system. Early pilot programs report improved adherence to screening protocols and enhanced multidisciplinary communication, signaling a national shift towards more systematic frailty management in hospital settings.

3. Digital frailty detection in Japan

Recent advances in digital health technologies have stimulated growing interest in digital frailty detection in Japan, particularly in response to workforce constraints and the need for longitudinal monitoring in a super-aged population. Pilot studies using household electricity–based AI analysis, wearable sensors, and EMR-derived frailty flags have demonstrated technical feasibility and conceptual validity in identifying frailty-related risk signals in both community and hospital settings. These approaches offer important advantages, including passive data collection, a reduced burden of assessment, and potential scalability. However, current evidence remains largely confined to small-scale feasibility studies, retrospective analyses, or regionally limited pilot programs. Robust data demonstrating large-scale clinical effectiveness — such as improvements in patient

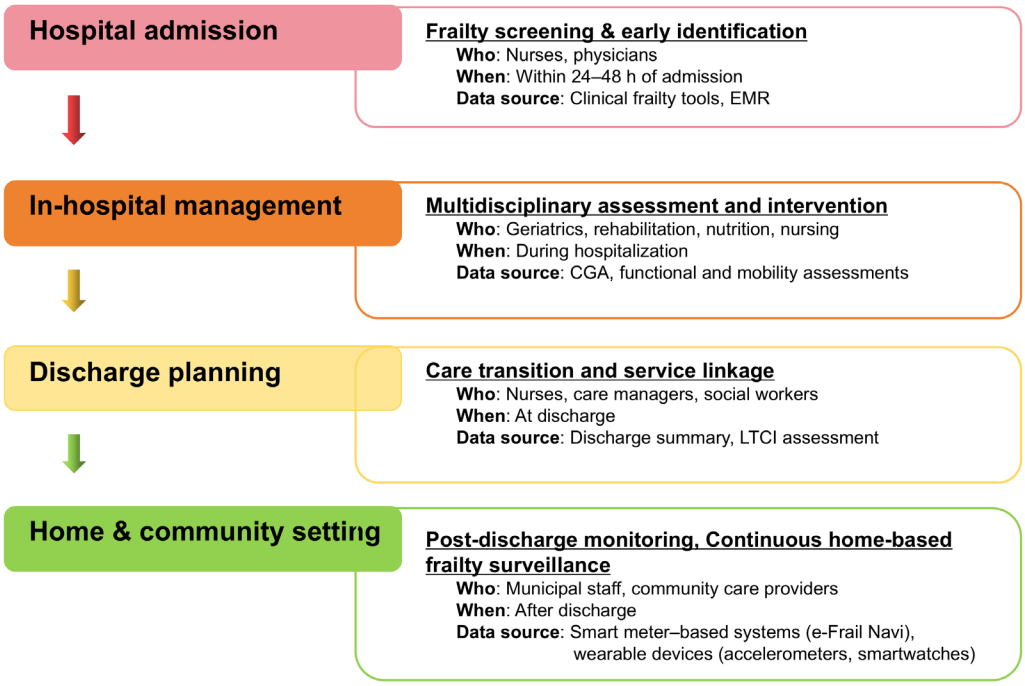

Figure 1. Continuous frailty monitoring across hospital and community settings in Japan.

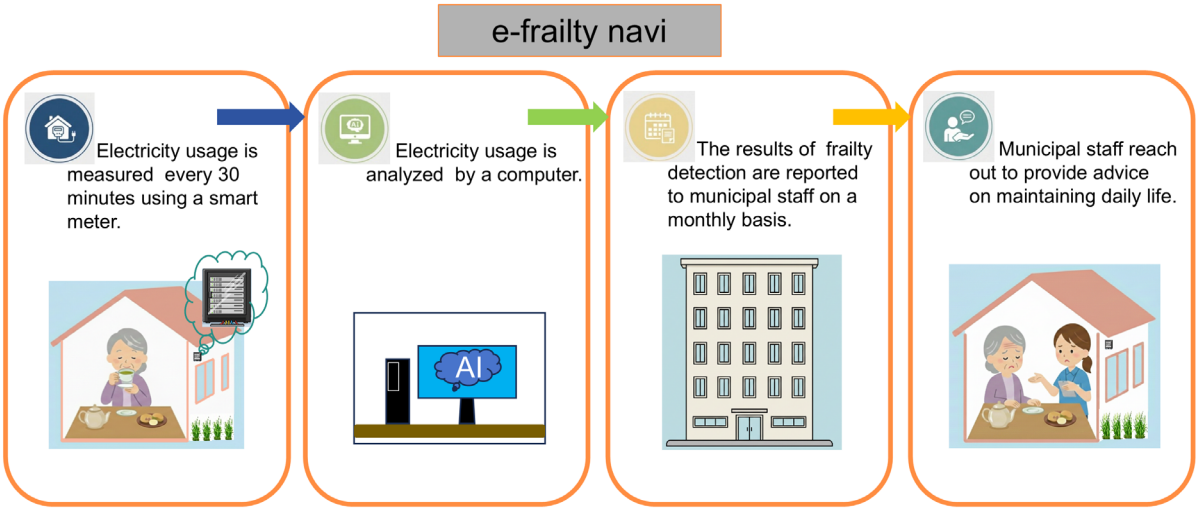

Figure 2. Structure of e-frailty navi (Source: Vol.97: Early Detection of Frailty Risk Using Smart Meter. Data — What Is "eFrailty Navi"?. *https://ene-fro.com/article/ef439_a1/*) (in Japanese)

outcomes, coordination of care, or utilization of long-term care — are still lacking. In addition, heterogeneity in data quality, limited standardization, and unresolved ethical and governance issues further constrain widespread implementation. On the whole, digital frailty detection shows promise in Japan, but its role remains complementary rather than substitutive, underscoring the need for integrated hybrid models supported by prospective, real-world validation studies.

3.1. Household electricity–based AI detection

Japan has taken significant steps toward utilizing technology to address the limitations of conventional methods of assessing frailty. The integration of household electricity usage data with artificial intelligence (AI) algorithms has emerged as a promising approach for early detection and monitoring of frailty (*26,27*). As shown in Figure 2, one of the pioneering efforts in this field is the "e-Frailty Navi" system, developed collaboratively by the Chubu Electric Power Company and the data science firm JDSC. This system collects anonymized data on electricity consumption patterns within individual households, particularly those of elderly residents. By analyzing fluctuations in electricity usage over time — such as changes in appliance use,

cooking times, or heating patterns — the AI algorithm can infer daily routines and detect deviations that may indicate early signs of physical or cognitive decline. For instance, a noticeable delay in morning electricity use could suggest delayed wake-up times, potentially pointing to fatigue or depression. Similarly, decreased evening activity may signal social withdrawal or mobility issues. Reduced usage of kitchen appliances may reflect decreased appetite or difficulty preparing meals — both of which are associated with frailty. Importantly, this approach requires no active participation from the older adult and is thus suitable even for those with cognitive impairment or reluctance to use wearable technology. When behavioral anomalies are detected, alerts are sent to care managers or municipal welfare departments, enabling early intervention. Some local governments in Japan have already incorporated the system into community-based integrated care networks. The technology aligns with national policy goals to promote "aging in place," prevent the progression of frailty, and reduce unnecessary hospital admissions and long-term care facility placements.

This approach offers several unique advantages. First, monitoring is non-intrusive and poses a minimal burden , as older adults do not need to wear sensors or modify their daily routines. Second, passive data collection is particularly suitable for individuals living alone or those reluctant to adopt wearable technologies. Third, Japan's social structure — characterized by the advancement of a super-aged population and a well-developed community-based integrated care system — allows electricity-based monitoring to function as a natural extension of routine "watch-over" activities. Nevertheless, several methodological and ethical challenges remain. Distinguishing behavior-related signals from confounding factors — such as travel, family visits, or changes in household composition — is nontrivial. Long-term governance of data, mechanisms to obtain residents' consent, and frameworks for cross-sector information-sharing also need to be carefully designed. Further evidence from large-scale cohorts is needed to validate generalizability, assess regional variability, and ensure the robust integration of electricity-based monitoring into Japan's long-term care and frailty prevention systems.

3.2. Integration of wearable devices

Wearable devices represent another rapidly expanding modality in Japan's digital frailty surveillance landscape. Wrist-worn accelerometers, and smartwatches are increasingly used to continuously capture real-world physiological and behavioral data, including step count, gait speed, gait stability metrics, and intensity of physical activity (*28-31*). These continuous streams provide dynamic insights into key domains of frailty, and particularly a decline in mobility and reduced physical reserve. A recent Japanese study (*31*) has demonstrated that gait parameters collected from wearable devices over a 7-day period can be used to accurately classify older adults as frail or non-frail and predict adverse outcomes such as hospitalization or mortality.

Despite these advances, several limitations must be addressed. Sustained compliance with device wear remains a major barrier, particularly among very old adults or those with cognitive impairment. Data representativeness is a concern because wearable users tend to be healthier, tech-literate, and more active than the broader high-risk population. Moreover, long-term longitudinal evidence linking sensor-derived metrics to clinically meaningful outcomes — such as a transition to long-term care, fractures, or disability — is still limited. Standardization of sensor modalities, validation across diverse living environments, and cross-device calibration remain necessary for nationwide deployment.

3.3. EMR-based frailty flags

In Japanese medical settings, electronic medical records (EMRs) are increasingly being explored as a tool for automated frailty detection (*32,33*). This approach leverages routinely collected clinical information, including age, comorbidity profiles, polypharmacy status, hospitalization history, laboratory findings, and functional status indicators, to generate algorithm-based frailty "flags" at the point of care. EMR-based detection models offer significant advantages. They require no additional devices and seamlessly integrate into existing clinical workflows, thereby enabling routine screening without added burden. For hospitalized older adults, automated frailty flags can trigger early comprehensive geriatric assessment (CGA), prompt prehabilitation before surgery, assist in discharge planning, and support coordinated interventions from rehabilitation and nutrition teams.

However, several challenges impede widespread implementation. The quality and structure of EMR data vary substantially across hospitals, reducing model generalizability. Functional measures crucial for frailty assessment — such as gait speed, sit-to-stand performance, or detailed Activities of Daily Living/ Instrumental Activities of Daily Living (ADL/IADL) scores — are often absent or inconsistently recorded. Ethical considerations also arise regarding secondary data use without explicit patient consent and the potential impact of frailty labeling on clinical decision-making. Moreover, smaller regional hospitals and clinics may lack the infrastructure or personnel needed to maintain EMR-integrated risk algorithms. At present, Japan has only limited real-world examples of fully deployed EMR-based frailty flagging systems, highlighting the need for further pilot studies, national data standardization efforts, and robust governance frameworks.

Although national digital initiatives such as the My Number Card (Myna Insurance Card) have been

promoted as infrastructure to link community screening data to hospital medical records, their practical impact on frailty-informed care has thus far been limited (*34*). Incomplete adoption, insufficient interoperability with hospital information systems, lack of standardized data formats, and persistent concerns regarding privacy governance continue to hinder effective data integration. As a result, frailty information is often assessed repeatedly yet remains poorly shared across care transitions. Importantly, these challenges are not unique to Japan but reflect a global issue in aging societies, underscoring the need for secure and interoperable frameworks to translate frailty assessment into coordinated clinical action.

4. Global status of electronic frailty screening

As digitalization progresses, electronic frailty screening is increasingly being incorporated into healthcare practices across the globe. Electronic frailty screening has progressed furthest in England, where the National Health Service (NHS) Electronic Frailty Index (eFI) (*35*) has been embedded into primary-care electronic health records and adopted at scale. The NHS eFI is a pragmatic, record-based frailty screening tool that operationalizes 36 health deficits comprising approximately 2,000 Read codes. The score is strongly predictive of adverse outcomes and has been validated in around 900,000 patient records. It presents an output as a score, with higher scores indicating the increasing possibility of a person living with frailty and hence being vulnerable to adverse outcomes. In a large validation study conducted by Clegg *et al*. (*36*), the eFI was found to effectively identify mild, moderate, and severe frailty in older adults and demonstrate strong predictive ability for outcomes such as mortality, hospital admission, and entry into long-term care. The eFI is a technically simple, automatable algorithm combined with policy backing and vendor use that can enable population-level identification of frail individuals while posing a minimal additional clinician burden.

In Canada, electronic frailty screening has gradually emerged through regionally driven initiatives rather than as a nationally standardized program. The earliest implementation can be traced to the CARES program in 2014, where an electronic comprehensive geriatric assessment (eCGA) was incorporated to generate a frailty index (eFI-CGA) for community-dwelling older adults (*37*). Subsequent research efforts adapted the original UK 36-deficit eFI to the Canadian primary care context, leading to the development of a Canadian eFI derived directly from electronic medical record (EMR) data (*38*). Validation studies have demonstrated strong correlations between the Canadian eFI and traditional CGA-based frailty measures, supporting its clinical applicability in primary care settings (*39*). In recent years, several provinces have integrated eFI-based tools into web-based platforms, enabling automated frailty identification during routine clinical encounters (*40*). Despite these advances, Canada still lacks a unified national frailty screening framework, and the degree of implementation varies across jurisdictions. Nonetheless, the progressive incorporation of EMR-based eFI tools highlights a growing commitment to early detection and management of frailty in Canadian healthcare.

In Australia, the implementation of electronic frailty screening has progressed primarily through research-driven initiatives and the increasing availability of electronic health records (EHRs). A retrospective study (*41*) has indicated that eFI derivation began around 2017–2018, when large-scale primary care datasets from more than 700 general practices were used to calculate a 36-deficit eFI for over 79,000 adults age ≥ 70. This study demonstrated the feasibility of deriving frailty status directly from routine clinical records and revealed clear gradients of mild, moderate, and severe frailty among community-dwelling older adults. Subsequent work expanded the use of eFI to residential aged-care settings and acute hospital environments, including ongoing national research initiatives such as the eFI QH Project (*42*), which aims to integrate a validated digital eFI into Queensland's integrated EMR system to support real-time clinical decision-making. Although Australia does not yet have a unified national policy mandating frailty screening, the progressive incorporation of eFI tools across primary care, care for the elderly, and hospital systems highlights a growing commitment to scalable, data-driven frailty identification in an aging population. A 2022 survey of Australian healthcare professionals reported that only approximately 44% had received any training related to frailty, and just 14% had undergone training specifically focused on frailty (*43*). These findings underscore the need to prioritize training and education for healthcare professionals in the future. The Australian Frailty Network (AFN) (*44*) which was established in 2023, aims to generate new knowledge to improve health outcomes, ensure that evidence-based management strategies are effectively translated into clinical practice, and strengthen national capacity in multidisciplinary and translational frailty research. Although frailty screening and frailty-informed care have not yet been fully incorporated into routine clinical practice, the AFN has explicitly identified the promotion of integrating frailty assessment and management into clinical practice guidelines as one of its core missions. Thus, Australia's national policy support and nationwide commitment to addressing frailty are already evident; however, the system is still in the process of institutionalization and standardization.

Singapore's development of frailty screening has progressed through a combination of policy-driven initiatives and clinical implementation. Early frailty screening activities were introduced in hospital and community settings around 2017, primarily using

conventional assessment tools such as the Clinical Frailty Scale *(45)*. A major milestone occurred in 2023, when the Ministry of Health released the National Frailty Strategy, which outlined a nationwide framework to enhance the identification, monitoring, and management of frailty across the health and social care systems (*46*). This strategy emphasized the role of primary care in early detection and called for standardized, evidence-based approaches to support healthy aging. Building on this policy direction, implementation efforts accelerated through programs such as IMPACTFrail (*47*), a translational initiative scheduled for rollout across five polyclinics in 2025 to operationalize frailty and intrinsic capacity screening in routine primary care. While Singapore has not yet established a nationwide electronic frailty index comparable to the United Kingdom's eFI, its current trajectory demonstrates a clear, policy-supported commitment to promoting integrated frailty screening, including digital and system-level approaches, within both clinical and community settings.

International comparisons suggest actionable insights to overcome these barriers. Across these jurisdictions, common factors facilitating successful electronic frailty screening include the following. First, only routinely collected primary-care data are used, therefore requiring no extra data entry or patient burden; once implemented in EHR systems the calculation is automated, enabling effortless population-level identification of frail individuals. Second, the eFI was endorsed and promoted by national bodies and integrated into policy and commissioning levers, so practices had both clinical and organizational incentives to adopt it. Third, major EHR vendors and systems embedded the eFI in clinical software, facilitating a seamless technical rollout across virtually all general practices. Finally, the eFI's large-scale validation provided the empirical confidence needed for national implementation and for linking frailty identification to service reconfiguration.

4. Discussion

The necessity of a hybrid frailty screening model in Japan arises from the unique structural and clinical characteristics of its health-care and long-term care systems. Unlike many Western countries where frailty screening primarily serves as risk stratification, frailty identification in Japan is closely linked to eligibility for services, positioning frailty as a clinical determinant of care access (*48*). Tools such as the Kihon Checklist were explicitly designed to detect future dependence on long-term care and are widely used across community and hospital settings. In hospital and community settings, implementation of frailty screening tools by nursing staff has been associated with the initiation of targeted clinical care plans that include rehabilitation, nutritional optimization, and risk-appropriate discharge planning. Studies show that proactively identifying frail patients using bedside assessment protocols leads to the application of evidence-based interventions and improved clinical outcomes (*49*) and that nurse-led frailty management strategies improve physical function and nutritional status in older adults (*50*). Moreover, Japan's community-based integrated care system emphasizes continuity across hospital, community, and home settings, framing frailty as a longitudinal condition requiring ongoing monitoring and care coordination rather than a static diagnosis. A hybrid model offers a solution that aligns with Japan's care philosophy, workforce structure, and policy framework. Rather than replacing clinical assessment, digital tools should function as complementary extensions that enhance temporal resolution, support early detection, and reinforce continuity across care settings.

Despite growing enthusiasm for digital frailty detection, this review highlights that digital-only solutions are unlikely to fully address Japan's frailty challenges. Standalone digital approaches capture only partial dimensions of frailty and remain vulnerable to selection bias, data incompleteness, and ethical concerns. Importantly, frailty in Japan is not merely a detection problem but a care-navigation problem, requiring interpretation, prioritization, and translation into individualized nursing and multidisciplinary interventions. Digital tools can efficiently identify risk signals, but they cannot replace clinical judgment or patient-centered care planning. These findings support a hybrid model in which brief screening tools, nursing assessment, and digital signals are combined within structured care pathways, ensuring both scalability and clinical relevance.

Future research should prioritize several areas. First, validation studies comparing tool performance across acute, subacute, and community settings are needed to establish context-appropriate selection frameworks. Second, real-world implementation studies should examine how frailty screening influences clinical decision-making, care transitions, and long-term outcomes, rather than focusing solely on predictive accuracy. Third, ethical and governance frameworks must be developed to address consent, data ownership, and the potential unintended consequences of frailty labeling, particularly in digital surveillance models. Finally, interdisciplinary research integrating geriatrics, nursing science, health informatics, and policy analysis will be essential to designing frailty assessment systems that are not only accurate, but also equitable, acceptable, and actionable with regard to Japan's super-aged population.

5. Conclusion

To promote the national implementation of frailty assessment, Japan may need to develop a standardized core frailty dataset and its integration into EMRs.

Aligning frailty assessment with national clinical guidelines and linking screening to policy would also encourage adoption. Overall, the momentum of frailty screening in Japan will depend on coordinated efforts involving clinical guidelines, data standardization, and policy alignment. Lessons from international models such as the NHS eFI indicate that technological capacity alone is insufficient; robust institutional frameworks are essential for nationwide adoption.

Funding: This work was supported by Grants-in-Aid from the Ministry of Education, Culture, Sports, Science and Technology of Japan (24K14216).

Conflict of Interest: The authors have no conflicts of interest to disclose.

References

1. World Health Organization (WHO). Ageing and health, Online Edition. *https://www.who.int/news-room/fact-sheets/detail/ageing-and-health* (accessed December 26, 2025).
2. Ichimura H, Shimizutani S, Hashimoto H. Japanese study of aging and retirement. JSTAR first results; 2009. *https://www.rieti.go.jp/jp/publications/dp/09e047.pdf* (accessed December 26, 2025). (in Japanese)
3. Ministry of Health, Labour and Welfare, Japan. The state of aging of the population. *https://www8.cao.go.jp/kourei/whitepaper/w-2025/zenbun/pdf/1s1s_01.pdf* (accessed December 26, 2025). (in Japanese)
4. Fried LP, Tangen CM, Walston J, Newman AB, Hirsch C, Gottdiener J, Seeman T, Tracy R, Kop WJ, Burke G, McBurnie MA; Cardiovascular Health Study Collaborative Research Group. Frailty in older adults: Evidence for a phenotype. J Gerontol A Biol Sci Med Sci. 2001; 56:M146-56.
5. O'Caoimh R, Sezgin D, O'Donovan MR, Molloy DW, Clegg A, Rockwood K, Liew A. Prevalence of frailty in 62 countries across the world: A systematic review and meta-analysis of population-level studies. Age Ageing. 2021; 50:96-104.
6. Murayama H, Kobayashi E, Okamoto S, Fukaya T, Ishizaki T, Liang J, Shinkai S. National prevalence of frailty in the older Japanese population: Findings from a nationally representative survey. Arch Gerontol Geriatr. 2020; 91:104220.
7. Deng Y, Zhang K, Zhu J, Hu X, Liao R. Healthy aging, early screening, and interventions for frailty in the elderly. Biosci Trends. 2023; 17:252-261.
8. Deng Y, Yamauchi K, Song P, Karako T. Frailty in older adults: A systematic review of risk factors and early intervention pathways. Intractable Rare Dis Res. 2025; 14:93-108.
9. Toyosanae S, Fujimoto Y, Seto N. Characteristics of frailty among older adults with chronic diseases attending outpatient clinics in a medium-sized general hospital. J Jpns Soc Chronic Nursing. 2025; 202519003. (in Japanese)
10. Japanese Geriatrics Society. Statement on Frailty from the Japanese Geriatrics Society. *https://www.jpn-geriat-soc.or.jp/info/topics/pdf/20140513_01_01.pdf* (accessed December 26, 2025). (in Japanese)
11. Ministry of Health, Labour and Welfare, Japan. Health business guidelines based on the characteristics of the elderly. *https://www.mhlw.go.jp/file/05-Shingikai-12401000-Hokenkyoku-Soumuka/0000205009.pdf* (accessed December 26, 2025). (in Japanese)
12. Deng Y, Sato N. Global frailty screening tools: Review and application of frailty screening tools from 2001 to 2023. Intractable Rare Dis Res. 2024; 13:1-11.
13. National Center for Geriatrics and Gerontology. Revised in 2020 Japanese CHS standards (J-CHS standards) *https://www.ncgg.go.jp/ri/lab/cgss/department/frailty/documents/J-CHS2020.pdf* (accessed December 26, 2025). (in Japanese)
14. Satake S, Arai H. The revised Japanese version of the Cardiovascular Health Study criteria (revised J-CHS criteria). Geriatr Gerontol Int. 2020; 20:992-993.
15. Ministry of Health, Labour and Welfare, Japan. Kihon Checklist. *https://www.mhlw.go.jp/topics/2009/05/dl/tp0501-1f_0005.pdf* (accessed December 26, 2025). (in Japanese)
16. Ohashi M, Yoda T, Imai N, Fujii T, Watanabe K, Tashi H, Shibuya Y, Watanabe J, Endo N. Five-year longitudinal study of frailty prevalence and course assessed using the Kihon Checklist among community-dwelling older adults in Japan. Sci Rep. 2021; 11:12399.
17. Morley JE, Malmstrom TK, Miller DK. A simple frailty questionnaire (FRAIL) predicts outcomes in middle aged African Americans. J Nutr Health Aging. 2012; 16:601-8.
18. Egashira R, Sato T, Miyake A, Takeuchi M, Nakano M, Saito H, Moriguchi M, Tonari S, Hagihara K. The Japan Frailty Scale is a promising screening test for frailty and pre-frailty in Japanese elderly people. Gene. 2022; 844:146775.
19. Gobbens RJ, van Assen MA, Luijkx KG, Wijnen-Sponselee MT, Schols JM. The Tilburg Frailty Indicator: Psychometric properties. J Am Med Dir Assoc. 2010; 11:344-55.
20. Katsura T, Abe N, Komata M, Ogura M, Ishikawa N, Hoshino A, Shizawa M, Usui K, Yokoyama E, Hara M. The relationship between the houseboundedness and frailty of community-dwelling elderly persons. J Rural Med. 2018; 13:141-150.
21. Yaku H, Kato T, Kitai T. Proposal for the appropriate frailty assessment in the JCS/JHFS 2025 Guideline on Diagnosis and Treatment of Heart Failure - Reply. Circ J. 2025; 89:1577-1578.
22. Shiwa M, Irahama H, Toorisaka M. A survey on the frailty status of inpatients at our center. J Jpns Red Cross Wakayama Med Center, 2020; 37:77-85. (in Japanese)
23. Yamamoto C, Yokoyama S, Enomoto S, Ouchi Y. Verification of a frailty control program provided in a regional core hospital. Jpns J Geriatrics. 2024; 61:456-462. (in Japanese)
24. Yutaka S, Fujimoto H, Seto N. Characteristics of frailty among older outpatients with chronic diseases at a medium-sized general hospital. J Jpns Society Chronic Care Nursing. 2025; 202519003. (in Japanese)
25. Deng Y, Yamauchi K, Karako K, Song P. Dual community-based care innovations in a super-aged population: The role of Small-scale Multifunctional In-home Care and Nursing Small-scale Multifunctional In-home Care in Japan. Biosci Trends. 2025. 10:5582
26. Chubu Electric Power Company. Launch of "e frailty navi" service to detect frailty for local governments.

https://www.chuden.co.jp/publicity/press/1210554_3273.html (accessed December 26, 2025). (in Japanese)
27. Uenishi M, Song P. Responding to a super-aged society: A community-based model for early frailty detection using AI and smart meter data -Insights from Japan. Glob Health Med. 2025; 7:439-443.
28. Takayanagi N, Sudo M, Yamashiro Y, Chiba I, Lee S, Niki Y, Shimada H. Screening prefrailty in Japanese community-dwelling older adults with daily gait speed and number of steps *via* tri-axial accelerometers. Sci Rep. 202; 11:18673.
29. Watanabe D, Yoshida T, Watanabe Y, Yamada Y, Kimura M, Group KS. Objectively measured daily step counts and prevalence of frailty in 3,616 older adults. J Am Geriatr Soc. 2020; 68:2310-2318.
30. Yuki A, Otsuka R, Tange C, Nishita Y, Tomida M, Ando F, Shimokata H, Arai H. Daily physical activity predicts frailty development among community-dwelling older Japanese adults. J Am Med Dir Assoc. 2019; 20:1032-1036.
31. National Center for Geriatrics and Gerontology. Frailty determined with wearable devices could help predict the risk of hospitalization and death – Based on results of the UK Biobank study-. *https://www.ncgg.go.jp/ri/report/20250902.html* (accessed December 26, 2025). (in Japanese)
32. Yamashita M, Kamiya K, Hotta K, Kubota A, Sato K, Maekawa E, Miyata H, Ako J. Artificial intelligence (AI)-driven frailty prediction using electronic health records in hospitalized patients with cardiovascular disease. Circ Rep. 2024; 6:495-504.
33. Toyoshima K, Araki A, Tamura Y, *et al*. Prognostic value of the electronic Multimorbidity Frailty Index for mortality, change in basic activities of daily living, length of hospital stay and discharge home in older hospitalized patients. Geriatr Gerontol Int. 2025; 25:1185-1193.
34. Japan Wire by Kyodo News. Japan halts issuing health insurance cards, info tied to My Number ID. *https://english.kyodonews.net/articles/-/51659?phrase=Edano&words=* (accessed December 26, 2025).
35. National Health Service, England. Electronic Frailty Index. *https://www.england.nhs.uk/ourwork/clinical-policy/older-people/frailty/efi/* (accessed December 26, 2025).
36. Clegg A, Bates C, Young J, Ryan R, Nichols L, Teale EA, Mohammed MA, Parry J, Marshall T. Development and validation of an electronic frailty index using routine primary care electronic health record data. Age Ageing. 2018; 47:319.
37. Canadian Frailty Network. Development and Implementation of a Web-based eFI-CGA Software Tool for Points of Care Applications. *https://www.cfn-nce.ca/project/cares2020/* (accessed December 26, 2025).
38. Thandi M, Gibb A, Price M, Baumbusch J, Wong ST. Development and testing of an electronic frailty index using Canadian electronic medical record data in primary care. BMC Prim Care. 2025; 26:359.
39. Abbasi M, Khera S, Dabravolskaj J, Vandermeer B, Theou O, Rolfson D, Clegg A. A cross-sectional study examining convergent validity of a frailty index based on electronic medical records in a Canadian primary care program. BMC Geriatr. 2019; 19:109.
40. Web-based eFI-CGA (Clinical). *https://clinical.efi-cga.ca* (accessed December 26, 2025).
41. Lewis ET, Williamson M, Lewis LP, Ní Chróinín D, Dent E, Ticehurst M, Peters R, Macniven R, Cardona M. The feasibility of deriving the electronic frailty index from Australian general practice records. Clin Interv Aging. 2022; 17:1589-1598.
42. eFI QH Project. *https://www.afn.org.au/efi-qh-project/* (accessed December 26, 2025).
43. Hanjani LS, Fox S, Hubbard RE, Gordon E, Reid N, Hilmer SN, Saunders R, Gnjidic D, Young A. Frailty knowledge, training and barriers to frailty management: A national cross-sectional survey of health professionals in Australia. Australas J Ageing. 2024; 43:271-280.
44. Reid N, Young A, Baldassar L, *et al*. The Australian Frailty Network: Development of a consumer-focussed national response to frailty. Australas J Ageing. 2024; 43:852-860.
45. Frailty Screening. *https://www.singhealth.com.sg/community-care/level-up-with-healthup/frailty-screening* (accessed December 26, 2025).
46. Ministry of Health, Singapore. Frailty Strategy Policy Report. *https://www.moh.gov.sg/others/resources-and-statistics/reports-frailty-strategy-policy-report/* (accessed December 26, 2025).
47. Geriatric Education & Research Institute. Intrinsic capacity in Singapore's primary care: IMPACTFrail to be piloted at five polyclinics. https://www.geri.com.sg/about-us/news/intrinsic-capacity-in-singapore-s-primary-care--impactfrail-to-be-piloted-at-five-polyclinics/ (accessed December 26, 2025).
48. Ishikawa N, Katsura T, Hara M. Changes in Kihon Checklist items and new Certification of long-term care needs among Japanese community-dwelling elders. J Rural Med. 2021; 16:270-279.
49. Wilson S, Sutherland E, Razak A, O'Brien M, Ding C, Nguyen T, Rosenkranz P, Sanchez SE. Implementation of a frailty assessment and targeted care interventions and its association with reduced postoperative complications in elderly surgical patients. J Am Coll Surg. 2021; 233:764-775.
50. Kasa AS, Drury P, Traynor V, Lee SC, Chang HR. The effectiveness of nurse-led interventions to manage frailty in community-dwelling older people: A systematic review. Syst Rev. 2023; 12:182.

Received December 22, 2025; Revised January 25, 2026; Accepted January 28, 2026.

**Address correspondence to:*
Kenji Karako, Department of Surgery, Graduate School of Medicine, The University of Tokyo, 7-3-1 Hongo, Bunkyo, Tokyo 113-8655, Japan.
E-mail: tri.leafs@gmail.com

Peipei Song, Center for Clinical Sciences, Japan Institute for Health Security, 1-21-1 Toyama, Shinjuku-ku, Tokyo 162-8655, Japan.
E-mail: psong@jihs.go.jp

Released online in J-STAGE as advance publication January 31, 2026.

Mini-Review

DOI: 10.5582/bst.2025.01389

International landscape of guidelines for perioperative frailty assessment and barriers to clinical translation

Ya-nan Ma[1], Kenji Karako[2], Ying Xia[3], Peipei Song[4,5,*], Xiqi Hu[3,*]

[1] Department of Neurosurgery, Haikou Affiliated Hospital of Central South University Xiangya School of Medicine, Haikou, China;
[2] Department of Surgery, Graduate School of Medicine, The University of Tokyo, Tokyo, Japan;
[3] Department of Neurosurgery, Integrated Neuroscience Center, Geriatric Hospital of Hainan, Haikou, China;
[4] Center for Clinical Sciences, Japan Institute for Health Security, Tokyo, Japan;
[5] National College of Nursing, Japan Institute for Health Security, Tokyo, Japan.

SUMMARY: Frailty significantly influences perioperative outcomes and healthcare resource utilization among older adults. Although the importance of intervention has been recognized, guidelines vary significantly across regions. This review synthesizes geriatric, perioperative, and specialty guidelines from the UK, the US, Europe, and the Asia-Pacific region. We found that, although they widely share core principles such as the use of validated tools and comprehensive geriatric assessment (CGA), guidance specific to the perioperative setting remains limited. Existing recommendations are often restricted to the preoperative phase and lack standardization of risk thresholds. However, high-quality evidence on the clinical and economic impact of frailty-based pathway redesigns is limited. Future research should focus on multicenter pragmatic trials that evaluate integrated care pathways extending from preoperative optimization through postoperative care. In parallel, further development of automated screening using electronic health records and electronic frailty indices is warranted. Such initiatives will require careful evaluation of feasibility and equity to support successful implementation in routine clinical practice. We recommend that clinicians routinely incorporate validated frailty screening into preoperative evaluation for all patients age 65 and older and that healthcare systems prioritize the development of an interoperable data infrastructure to enable the seamless transfer of community-derived frailty information into surgical decision-making workflows.

Keywords: perioperative management, comprehensive geriatric assessment (CGA), Clinical Frailty Scale (CFS), algorithmic fairness, electronic frailty index (eFI), clinical translation

1. Introduction

As the global population ages, frailty has evolved from a theoretical research concept into a central target for healthcare management (*1,2*). Defined as a state of reduced physiological reserve and diminished resistance to stressors, frailty affects approximately 10% of community-dwelling older adults, rising to 25–50% in those age 85 and older (*3,4*). It is a clinically important predictor of adverse outcomes, including falls, hospitalization, and mortality (*5*). Consequently, key organizations dealing with elderly patients, such as the British Geriatrics Society (BGS), and key guidelines for clinical practice, such as the Asia-Pacific Clinical Practice Guidelines, have established a consensus: frailty is a manageable condition rather than an inevitable consequence of aging (*6*). General guidelines universally advocate for a two-step approach involving rapid screening using validated tools followed by a comprehensive geriatric assessment (CGA) to guide multicomponent interventions.

However, translating this consensus into the high-stakes environment of perioperative care remains a significant challenge. Surgery constitutes a substantial physiological stressor, and yet the integration of frailty assessment into surgical pathways is inconsistent. While general guidelines provide a foundational framework, they often lack the specificity required for the complex logistical and clinical demands of the perioperative period.

Recent systematic evaluations highlight substantial gaps in the current guideline landscape. A review by Mehta *et al.* utilizing the AGREE II instrument revealed that while existing guidelines are strong on scope, they frequently exhibit low scores in rigor of development and applicability (*7*). Crucially, recommendations are often fragmented, with only a minority of guidelines providing actionable, consensus-based strategies that can feasibly

be implemented across diverse healthcare systems. This implementation gap is particularly acute in surgery. Engel *et al.* found that among thousands of guidelines, only a small fraction specifically addressed perioperative frailty (*8*). Moreover, these recommendations are predominantly limited to the preoperative period, largely neglecting intraoperative management and postoperative continuity of care.

Despite the overarching agreement on the importance of recognizing frailty, clinicians currently face a fragmented landscape of guidelines with marked heterogeneity in assessment tools, risk thresholds, and pathway designs. This lack of standardization acts as a critical barrier to clinical translation, hindering the widespread provision of frailty-informed perioperative care. Therefore, this review aims to map the international landscape of perioperative frailty guidelines, comparing recommendations across the UK, US, Europe, and Asia-Pacific regions. By examining differences in target populations, timing of assessment, and management pathways, this review highlights key barriers to clinical translation, including issues related to data quality and economic feasibility. Priorities for future research are also proposed to help bridge the gap between evidence and practice.

2. Similarities and differences in perioperative frailty assessment guidance across countries/regions

2.1. The UK model

From the perspective of the overall guideline architecture, the UK frailty-related guidance exhibits a clear functional division of labor and continuity across stages of care. In particular, the BGS Fit for Frailty consensus emphasizes the systematic identification of frailty in community and outpatient settings. In addition, the joint guidance on perioperative care, issued by the Center for Perioperative Care (CPOC) and the BGS, translates frailty identification into stage-specific perioperative care strategies. In this manner, the management of frailty is longitudinally integrated throughout the perioperative pathway.

In terms of target populations and clinical contexts, the Fit for Frailty program is primarily intended for older adults living in the community and receiving outpatient services, including general practice, community hospitals, memory clinics, and specialty outpatient clinics (*9,10*). The program emphasizes that any health professional who encounters older people in these settings should proactively identify frailty (*3*). Conversely, the CPOC-BGS perioperative guideline focuses exclusively on adults with frailty who are undergoing elective or emergency surgery, encompassing the entire perioperative trajectory from referral and preoperative assessment to admission and postoperative recovery (*11*).

With regard to the selection of screening tools, Fit for Frailty proposes a combined approach that prioritizes simplicity and repeatability. Gait speed, defined as a walking time of four meters greater than five seconds or a speed of less than 0.8 meters per second, is regarded as a highly sensitive initial screening indicator. Although it has moderate specificity, it is considered particularly suitable for the early identification of potential frailty in older populations. The timed up-and-go (TUG) test, employing a threshold of > 10 seconds as an indicator of abnormality, is also regarded as a highly sensitive method of functional screening. The PRISMA-7 questionnaire utilizes a set of seven yes-no questions, enabling expeditious risk stratification. A score of ≥ 3 on this scale is typically indicative of a high risk of frailty. Despite the existence of several multidimensional tools (*e.g.*, the Groningen Frailty Indicator), the prevailing consensus places greater emphasis on the combined use of gait speed, the TUG test, and the PRISMA-7 to enhance the feasibility and efficiency of frailty screening in primary care and perioperative contexts.

Conversely, the CPOC-BGS perioperative guideline advocates for the utilization of the Clinical Frailty Scale (CFS) as the instrument for pathway entry (*11*). The guideline suggests that the CFS be documented at three pivotal moments: referral, preoperative evaluation, and admission. This recommendation is applicable to patients age ≥ 65 years undergoing elective or emergency surgery, as well as to younger patients deemed to be at risk of frailty (evidence level B, strong recommendation). The guideline provides an explicit definition of a CFS score ≥ 5 as frailty (living with frailty). Moreover, it strongly advises that all patients with a CFS score ≥ 5 undergo a CGA and preoperative optimization, with assessment domains including multimorbidity, function, nutrition, and medication use. Furthermore, all patients found to have a CFS score ≥ 5 should undergo a preoperative cognitive assessment utilizing validated tools. In addition, hospitals need to establish standards for the prevention and management of delirium.

With regard to the temporal aspect of the UK perioperative frailty framework, a salient feature is early engagement and recurrent assessment at several pivotal points. The Fit for Frailty document, put out by the BGS, advocates for the implementation of opportunistic case-finding methodologies across various healthcare, social care, and related professional contexts. The document recommends the utilization of straightforward, readily implementable tools such as gait speed, TUG, and PRISMA-7 for initial screening purposes. However, it explicitly advises against the incorporation of routine population screening within the general population. The CPOC guidance also recommends repeating CFS assessments at key points in the perioperative pathway, including referral, the preoperative clinic, and ward admission, to ascertain changes in frailty over time. At the community level, when the PRISMA-7 score is ≥ 3,

gait speed is slow, or performance on the TUG is > 10 s, further referral to geriatric teams or relevant specialties for assessment and intervention is recommended. An important point to note is that Fit for Frailty considers the CFS to be more appropriate as a tool to stratify frailty severity on the basis of an adequate clinical assessment. The CFS should not be used as a stand-alone screening measure in the absence of a formal clinical evaluation. At the perioperative level, when the CFS score is ≥ 5, the protocol stipulates a comprehensive management strategy be initiated, encompassing a CGA, cognitive assessment, and delirium prevention measures. This is to be accompanied by continuous follow-up and coordination throughout hospitalization by a perioperative frailty management team.

2.2. The US model

The UK approach is characterized by the utilization of a single, standardized scale (*e.g.*, the CFS) for the assessment of frailty. In contrast, the US has not mandated a specific frailty assessment instrument at the national level. Instead, frailty assessment is systematically embedded within a broader best-practice framework for older surgical patients, gradually forming a multidisciplinary consensus system centered on the American College of Surgeons (ACS)/American Geriatrics Society (AGS) best-practice guidelines and the 2025 American Society of Anesthesiologists (ASA) Practice Advisory.

The ACS and AGS jointly established the *Optimal Preoperative Assessment of the Geriatric Surgical Patient* in 2012 (*12*) and updated it in 2016 to the *Optimal Perioperative Management of the Geriatric Patient* (*13*). These guidelines explicitly incorporate frailty assessment into the standard framework for geriatric surgical care. These guidelines provide a comprehensive framework for evaluation, encompassing nine core domains: cognition and behavior, cardiac function, pulmonary function, functional status and mobility, frailty, nutritional status, perioperative medication management, patient education, and preoperative testing and risk assessment. This structure provides an organized framework to support perioperative risk stratification, individualized decision-making, and multidisciplinary interventions.

Building upon this foundation, the 2025 ASA Practice Advisory for Perioperative Care of Older Adults Scheduled for Inpatient Surgery (*14*) further emphasized the critical role of frailty in risk assessment for elderly patients undergoing inpatient surgery, from the perspective of anesthesia and perioperative medicine. This practice advisory is applicable to all older adults (typically defined as ≥ age 65) scheduled for inpatient surgery. The increasing number of elderly surgical patients means that they will be exposed to increased risks of adverse postoperative outcomes, including delirium, cognitive impairment, and delayed functional recovery. Core risk factors include age-related decline in physiological reserves, increased vulnerability due to frailty, and the presence of multiple comorbid factors.

The ASA 2025 does not stipulate the utilization of a particular frailty scale; however, it advocates for the use of validated assessment tools. Optional methods include gait speed measurement, stand-up-and-walk tests (*e.g.* the TUG test), and relevant components within the CGA. Drawing upon established US clinical practices, the Fried frailty phenotype, the CFS, and the Frailty Index derived from the CGA are tools commonly used to assess frailty. The ACS/AGS guidelines similarly emphasize, within the section on functional/mobility status and frailty, the identification of high-risk elderly patients through objective physical testing (*e.g.* gait speed and strength testing) in combination with questionnaires. The guidelines further posit that frailty should be considered as an interconnected component of a geriatric syndrome spectrum, alongside functional limitations and malnutrition, rather than as an isolated issue.

With regard to the temporal aspect of assessment, the aforementioned ASA advisory emphasizes the completion of an initial systematic assessment at the preoperative clinic and recommends dynamic reassessment of cognition and function during hospitalization in response to changes in clinical course, particularly for patients in the ICU or those with prolonged immobility. The ACS/AGS guidelines conceptualize frailty assessment as spanning the full perioperative period, including preoperative optimization, intraoperative management (*e.g.* adjustments in anesthesia and dosing), and postoperative rounds and follow-up, with the goal of preventing functional decline and postoperative delirium. Once frailty or substantial functional impairment has been identified, both sets of guidance recommend activation of multidisciplinary team interventions (including surgery, anesthesia, geriatrics, rehabilitation, and nursing). Key measures include perioperative optimization of medication, prevention of delirium, encouragement of early mobilization, nutritional support, and individualized anesthesia plans. For patients exhibiting significant frailty, the guidance further recommends an early discussion of goals of care and prognosis, including the consideration of non-operative options and a required reconsideration of advance directives.

2.3. The European model

In Europe, the most recent guidance is provided by the European Society of Anaesthesiology and Intensive Care (ESAIC). In 2024, the ESAIC released an updated guideline on preoperative evaluation for adult patients undergoing elective non-cardiac surgery (*15*). The 2024 update to the 2018 framework issued by the ESAIC (*16*) further emphasizes the importance of frailty assessment as a component of multidimensional preoperative risk

assessment, rather than considering it as a standalone screening or decision-making tool. The guideline notes that frailty is highly correlated with advanced age, comorbidity, functional impairment, and cognitive dysfunction and that it acts as an important risk modifier for predicting perioperative complications, delayed functional recovery, and mortality. Consequently, the guideline advocates a systematic evaluation of functional status and frailty-related characteristics in older patients and those at risk due to functional limitations or multimorbidity. The results of this evaluation are to be incorporated into broader anesthesia and perioperative decision-making processes, rather than relying solely on any single frailty scale.

With regard to the assessment approach, ESAIC 2024 does not stipulate the utilization of a particular frailty screening instrument. Instead, it emphasizes that facilities may adopt an approach tailored to local resources and clinical context, integrating information on functional capacity, gait or exercise tolerance, nutritional status, and cognitive function to reach a comprehensive judgement. The guideline clarifies that the central aim of frailty assessment is to identify high-risk patients and guide personalized perioperative management strategies, including preoperative optimization, choice of anesthesia, level of postoperative monitoring, and rehabilitation planning. Concurrently, ESAIC 2024 acknowledges the paucity of evidence pertaining to the efficacy of perioperative pathways that are modified on the basis of a frailty assessment in enhancing patient outcomes. Consequently, it does not advocate for the utilization of a frailty score in isolation to determine surgical eligibility or decisions on limiting treatment. It recommends that future research concentrate on the prospective validation of frailty-guided interventions and their impact on outcomes that are of significance to patients.

2.4. The Asia-Pacific model

Unlike the UK's centralized pathway involving the National Health Service (NHS) or the US's guideline-embedded approach, the Asia-Pacific region has a public health-first model (Table 1). Frailty assessment is deeply integrated into community health screening and primary care to address rapid population aging. However, specific guidelines on perioperative frailty are still evolving, often appearing as adaptations of a general geriatric consensus or expert opinions rather than mandated national surgical standards.

2.4.1. Regional consensus framework

The Asia-Pacific Clinical Practice Guidelines for the Management of Frailty (*6*) serve as the foundational document for the region. Developed using a modified GRADE methodology, these guidelines explicitly advocate for the identification of frailty using validated measurement tools. While not exclusively designed for surgical populations, the guidelines categorize tools into functional groups:

(i) Rapid screening: The FRAIL scale and PRISMA-7 are recommended for quick identification in outpatient settings.

(ii) Global judgment: The CFS is recognized for its utility in clinical stratification.

(iii) Intervention: The guidelines provide strong recommendations for prescribing individualized physical activity programs (resistance training) and addressing polypharmacy. This framework shifts frailty assessment upstream, identifying patients before clinic presentation and maximizing the lead time for prehabilitation and physiological optimization.

2.4.2. National adaptations and perioperative integration

(1) China: Rapid translation of a consensus into perioperative pathways

In response to a rapidly aging surgical population, China has accelerated the development of expert consensus frameworks. The Chinese Expert Consensus on Frailty Assessment and Intervention underscores the marked heterogeneity in the prevalence of frailty (ranging from 4.0% to > 50% by setting) and it codifies the use of the Fried phenotype, Frailty Index (FI), FRAIL scale, and CFS (*17*). Clinical integration in the perioperative period is advancing based on authoritative guidelines:

(i) CGA-integrated models: Leading facilities, notably Peking Union Medical College Hospital, have embedded frailty screening into routine preoperative workflows, positioning it alongside cognitive and nutritional assessments (*18*).

(ii) Closed-loop management: The 2023 Expert Opinion on Perioperative Management of Older Patients Living with Frailty, spearheaded by the Chinese Society of Anesthesiology, represents the most definitive guidance to date. It advocates a "Screening-CGA-Intervention" closed-loop paradigm, wherein detection of frailty or pre-frailty *via* validated tools (*e.g.*, the Fried phenotype and Edmonton Frailty Scale) triggers an immediate CGA and multidisciplinary optimization, encompassing malnutrition, sarcopenia, and prophylaxis of DVT (*19*).

(2) Japan: Checklist-based screening and specialty integration

Japan's approach is distinguished by the widespread use of government-developed checklists embedded in the national long-term care insurance system.

(i) The Kihon Checklist (KCL): A 25-item self-administered questionnaire covering physical, nutritional, and social domains (*20*). Originally for a community screening, the KCL is increasingly being validated as a predictor of postoperative outcomes.

(ii) Questionnaire for Medical Checkup of Old-

Table 1. Anti-HBV response of TCM and related active compounds in clinical trials

Region/Country/*Ref*	Key authorities	Target population	Preferred tools	Pathway & timing	Primary characteristic
United Kingdom *(11)*	CPOC, BGS	Community-dwelling older adults, surgical patients age ≥65; or <age 65 with multimorbidity	Gait speed, TUG, PRISMA-7, CFS	Longitudinal: Community → Referral → Pre-op → Admission	Comprehensive, multi-stage pathway integration with CFS thresholds
United States *(12)*	ACS, AGS, ASA	≥age 65 surgical patients	Fried phenotype, CFS, FI, Gait speed, TUG	Full-cycle: Pre-op optimization → Intra-op → Post-op follow-up	Multidisciplinary team approach; flexible tool selection
Europe *(15)*	ESAIC	Older adults with multimorbidity or functional decline	multidimensional (gait speed, nutrition, cognition)	Pre-operative risk stratification	Flexible, regionally adaptable framework for frailty integration
Asia-Pacific (General) (*6*)	Asia-Pacific Clinical Practice Guidelines for Frailty	Community & outpatient elderly	FRAIL scale, PRISMA-7, CFS, FI	Upstream identification & prehabilitation	Focus on upstream frailty screening in primary care settings
China *(17, 19)*	CSA & Geriatrics Branch	≥age 70 or weight loss / high-risk patients	Fried Phenotype, CFS, FI, FRAIL scale	Tertiary hospital "Closed-loop": Screening → CGA → Intervention	Integration of frailty within CGA; emphasis on optimizing preoperative care
Japan *(17-20)*	JCS/JHFS, Gov. Policy	Community-dwelling older adults (≥75y for QMCOO) & disease-specific groups	KCL, QMCOO, CFS-J, Fried Phenotype	National health check-ups & disease-specific guidelines	Government-backed tools embedded in long-term care and specialty care
South Korea *(31)*	Korean Academy of Family Medicine	≥age 70 community-dwelling	K-FRAIL, FPQ	Primary care screening → Specialist CGA referral	Systematic screening in primary care to ensure continuity of geriatric data

Abbreviations: CFS, Clinical Frailty Scale; FI, Frailty Index; FPQ, Frailty Phenotype Questionnaire; KCL, Kihon Checklist; K-FRAIL, the Korean version of the FRAIL scale; PRISMA-7, Pictorial Indicators of Frailty and the Risk of Sarcopenia in the Elderly; QMCOO, Questionnaire for Medical Checkup of Old-Old; RAI, Risk Analysis Index; TUG, timed up-and-go test.

Old (QMCOO): A 15-item simplified tool adopted for nationwide health check-ups for adults ≥ age 75 (*21*).

Instead of using a single standalone perioperative guideline, Japan integrates frailty into disease-specific guidelines. For instance, the 2025 JCS/JHFS Guideline on the Diagnosis and Treatment of Heart Failure explicitly categorizes frailty into physical (Fried phenotype), multidimensional (KCL), and social domains, mandating assessment as part of comorbidity management (*22*). In addition, the validation of the Japanese version of the CFS (CFS-J) in inpatient settings suggests a growing convergence with international standards regarding acute care assessment (*23*).

A distinctive infrastructure feature is the national effort to link administrative databases across care settings. In October 2020, the Ministry of Health, Labour and Welfare began accepting applications for third-party provision and linkage analysis of the NDB-Long-Term Care Insurance (LTCI) database under a newly launched data linkage framework (*24-26*). This infrastructure supports the use of the claims-based frailty index (CFI), which was originally developed in the US. The CFI has been validated in a large Japanese cohort of 519,941 older adults. It has shown good predictive ability for LTCI certification and mortality (*27*). Similarly, coding-based algorithms such as the Electronic Frailty Index (eFI) and Hospital Frailty Risk Score (HFRS) have been validated using regional administrative claims databases (*28*).

The policy framework for this integration is the Community-based Integrated Care System, intended for full implementation by 2025. Under this model, care managers coordinate the information flow among primary care physicians, community health nurses, and hospital specialists. Despite the availability of linked claims databases for research purposes, routine clinical interoperability between LTCI screening records (*e.g.*, KCL or QMCOO results) and hospital electronic medical records remains limited. Frailty data collected during municipal health checkups are maintained in separate administrative databases, and information exchanges often still rely on traditional methods such as telephone calls and fax, accompanied by interoperability burdens including redundant forms and duplicate documentation (*29,30*). National initiatives encourage shifting away from paper-based exchanges and enabling multiple stakeholders to view care-related information electronically. However, current care-plan data exchange systems were not designed to routinely connect to medical facilities. This creates ongoing structural barriers to seamless sharing of data between medical and long-term care services in routine perioperative practice.

(3) South Korea: Primary care as the gatekeeper

The Korean Primary Care Guideline (2021) establishes a unique gatekeeper model by mandating frailty screening for all community-dwelling adults age ≥ 70 (*31*). It prioritizes the Frailty Phenotype Questionnaire (FPQ) and the Korean version of the FRAIL scale (K-FRAIL). For perioperative care, this implies that surgical patients referred by primary care facilities increasingly arrive with pre-established frailty data, necessitating improved information continuity between community clinics and surgical centers.

The Korean Frailty Index for Primary Care (KFI-PC) has been validated for comprehensive diagnostic assessment. It is a 54-item tool based on a CGA and covers 10 domains, including cognition, mood, mobility, and nutrition. An optimal cut-off value of 0.23 has been reported (*32*). However, its extensive nature limits practical application in busy clinical environments, underscoring the need for efficient screening instruments in both community and perioperative settings.

South Korea's healthcare system draws on administrative claims data from the National Health Insurance Service (NHIS) database. A Korean Hospital Frailty Risk Score (K-HFRS) has been developed using ICD-10 codes derived from healthcare encounters and linked with NHIS cohort data (*33*), representing an initial step toward claims-based frailty assessment in hospital settings. Digital innovation is advancing through initiatives such as the "SUPERAGING" study, which explores mobile app-based multidomain frailty interventions integrating disease management, cognitive training, and nutrition (*34*). Such digital platforms could theoretically facilitate the seamless transfer of information between community screening and hospital-based perioperative teams.

However, South Korea has, like Japan, not systematically established formal protocols for transferring community-derived frailty assessments to hospital perioperative teams. Linkage between NHIS claims data and individual hospital electronic medical records faces legal and privacy constraints, representing a key barrier to realizing the perioperative potential of South Korea's robust primary care-based screening infrastructure.

In summary, the Asia-Pacific model differs significantly from the Western trajectory. While the UK and Europe emphasize point-of-care assessment using tools like the CFS at the time of surgical admission, the Asia-Pacific region relies heavily on upstream community screening (*e.g.*, the KCL in Japan and K-FRAIL in South Korea). In this setting, the main barrier to translation is not a lack of tools but an interoperability gap. The challenge lies in integrating a host of community-level frailty data into acute perioperative workflows so that those data can meaningfully inform surgical decisions and resource allocation (Figure 1).

3. Translational challenges and future directions

3.1. The evidence-practice gap

A profound discrepancy persists between the proliferation of frailty research and its translation into routine perioperative practice. This translational gap and the overarching framework from evidence to practice are shown in Figure 2. A survey of the literature underscores the rapid growth of this field, with approximately 75% of relevant studies having been published within the past five years. However, the use of this research remains highly skewed. Strikingly, 99.6% of studies have employed frailty measurement exclusively for risk description or prognostic validation, while only 0.4% have utilized assessment results to prospectively modify or redesign care processes (*35*). Consequently, observational data have consistently linked frailty to adverse outcomes, but high-quality causal evidence supporting specific, guideline-recommended intervention pathways remains scarce.

3.2. Heterogeneity in measurement

This translational gap is exacerbated by substantial heterogeneity in assessment tools. Hothi *et al.* reported that while the deficit-accumulation-based Frailty Index (41.0%), the CFS (23.3%), and the Fried phenotype (9.3%) are predominant, over 11.2% of studies employ multiple or non-standard instruments (*35*). Methodological diversity allows for the exploration of the frailty construct, but it severely limits the comparability of findings across trials. More critically, it hinders the establishment of consistent, operational threshold values required to trigger clinical pathways.

3.3. Barriers at the implementation level

Even when validated assessment tools are selected, successful translation from research to practice is frequently impeded by barriers at the human and organizational levels. Successful implementation depends largely on organizational readiness, including adequate funding, infrastructure, and workforce capacity, as well as a strong interdisciplinary culture.

Challenges in workflow integration and cognitive load are particularly prominent. Qualitative evidence from acute care settings in Singapore has revealed a dissonance between tool availability and clinical utility. While participants identified over ten different screening tools, they expressed a lack of familiarity with specific scoring metrics. Consequently, clinicians frequently defaulted to clinical gestalt (or subjective eyeball screening) rather than utilizing standardized instruments to mitigate the perceived administrative burden (*36*).

This lack of standardization is often compounded by ambiguous process ownership. The same study highlighted a critical phenomenon of diffusion of responsibility: while frailty was universally recognized as a significant clinical priority, the ambiguity surrounding specific roles led to a scenario where everyone agreed that it mattered, but no one assumed responsibility for it. Without a clear delineation of who performs the screening and who acts on the results, the pathway collapses.

Moreover, structural resource constraints present a formidable barrier to sustainability. Implementation

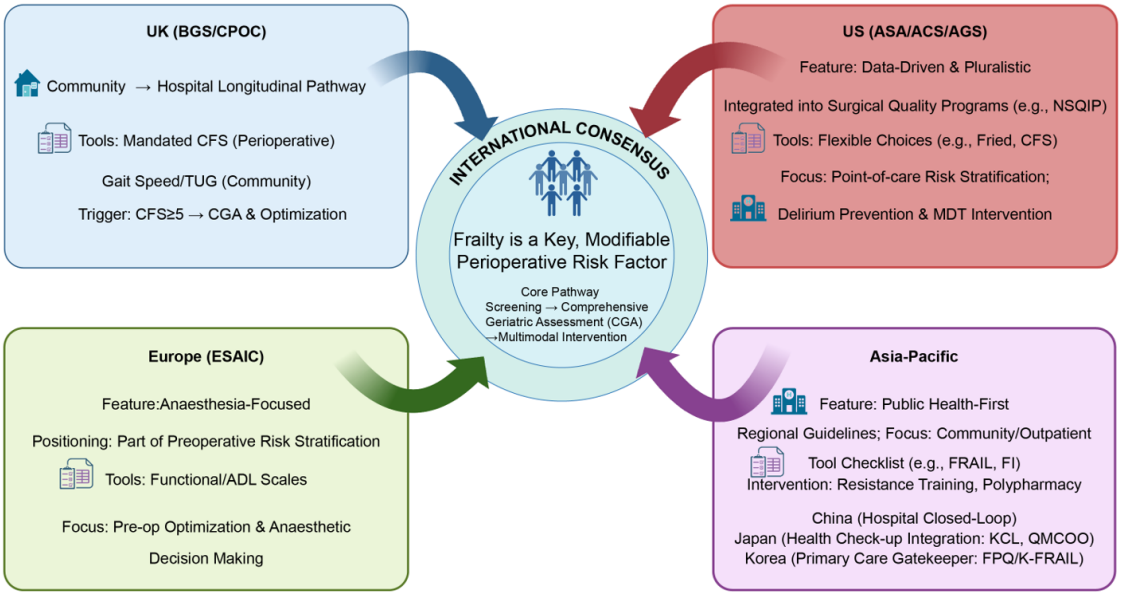

Figure 1. Global landscape & translational pathway of perioperative frailty assessment. *Abbreviations*: ADL, Activities of Daily Living scales; CFS, Clinical Frailty Scale; CGA, comprehensive geriatric assessment; FI, Frailty Index; FPQ, Frailty Phenotype Questionnaire; KCL, Kihon Checklist; K-FRAIL, the Korean version of the FRAIL scale; MDT, multidisciplinary team; NSQIP, National Surgical Quality Improvement Program; QMCOO, Questionnaire for Medical Checkup of Old-Old; RAI, Risk Analysis Index; TUG, timed up-and-go test.

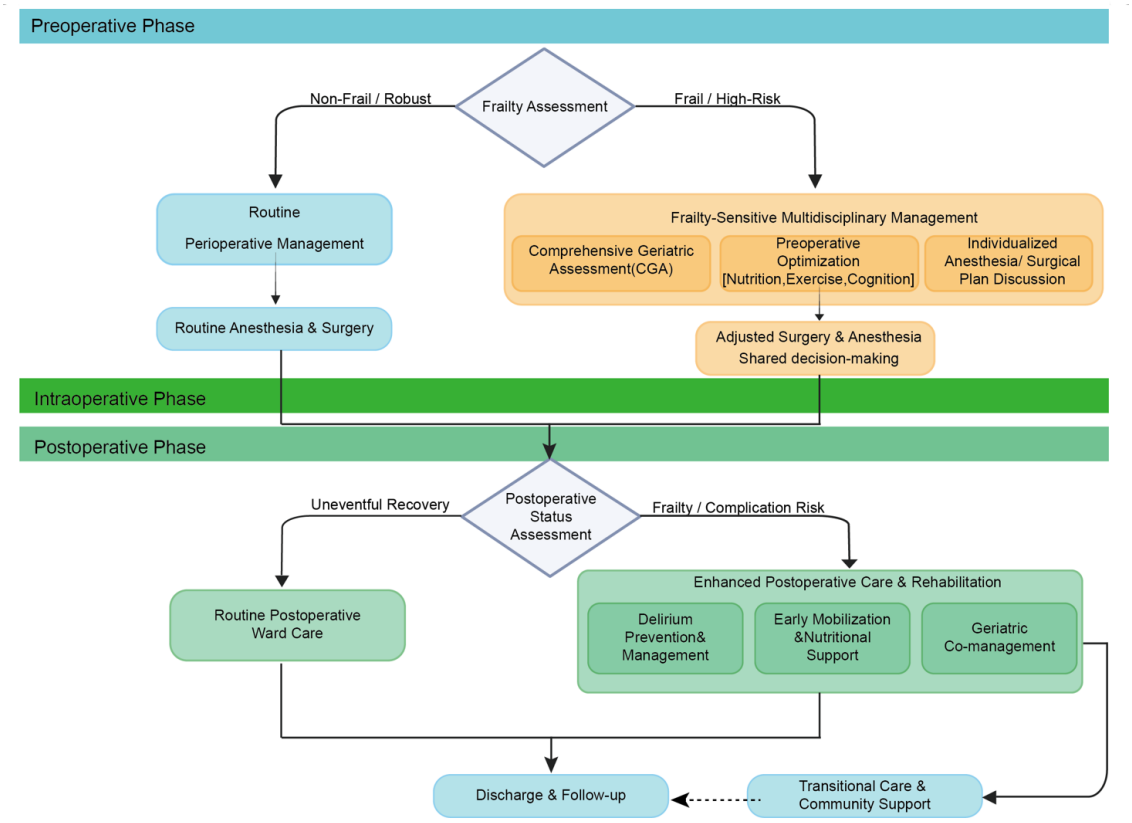

Figure 2. Schematic diagram of perioperative management pathways based on frailty assessment.

research from Germany examining multimodal prehabilitation has indicated that workforce capacity and the complexity of redesigning workflows (*e.g.*, integrating assessments in existing anesthesia clinics) are primary concerns for healthcare providers. The findings suggest that the absence of designated coordination teams and mechanisms of secured financing often stall the critical transition from assessment to actionable intervention (*37*).

Beyond resource and workflow barriers, a critical gap exists in translating frailty identification into patient-centered care: the systematic incorporation of shared decision-making (SDM). In perioperative frailty management, assessment should serve not merely as a risk-prediction exercise but as a trigger for goal-oriented discussions. In line with the ACS/AGS Best Practices, surgical teams should prioritize preoperative discussions on personal goals, explicitly addressing outcomes that matter most to older patients: functional decline, loss of independence, and the potential need for skilled care (*13*).

For patients identified as high-risk (*e.g.*, a CFS score ≥ 5 per UK guidelines), clinical pathways should mandate multidisciplinary SDM conferences involving surgeons, anesthesiologists, geriatricians, and patients' families. For frail patients, who face profound risks of complications and disability, the clinical question must evolve from technical feasibility ("Can we operate?") to goal alignment ("Should we operate?"). This requires prioritizing the patient's values, independence, and risk tolerance over surgical intervention alone (*38*).

However, current guidelines, while acknowledging the importance of goal-oriented discussions, lack standardized SDM tools and decision aids tailored to the perioperative context (*39*). Future pathway design should integrate frailty assessment results with prognostic prediction models to provide quantified risk evidence for SDM, ensuring that care plans authentically reflect the life goals and preferences of frail older adults. Such integration may help reduce both overtreatment and undertreatment, ultimately improving patient welfare and resource allocation.

3.4. Digital opportunities and data challenges

To mitigate the frontline workload, digital approaches such as the eFI, derived from routine electronic health records (EHR), offer a promising solution for automated screening (*40,41*). In the perioperative context, leveraging preoperative diagnostic codes, laboratory results, and medication records could facilitate the pre-screening of high-risk patients without adding to the clinical burden. However, the scalability of eFI-based pathways faces its own challenges, primarily concerning the completeness of data, algorithmic bias, and equity across different healthcare settings. The promise of algorithmic frailty assessment must be tempered by a

critical examination of equity implications. Obermeyer *et al.*'s landmark study revealed substantial racial bias in a widely used commercial algorithm for care management. Crucially, the study found that at equivalent risk scores, black patients were significantly sicker than their white counterparts.(*42*). This bias arose because the algorithm used healthcare costs as a proxy for health needs; however, due to systemic barriers to care access, less money was historically spent on black patients compared to white patients with an equivalent illness burden. A similar concern applies to frailty algorithms. An eFI trained mainly on data from well-resourced tertiary care centers may embed comparable biases. For example, lower healthcare use among underserved populations may be misread as better health rather than reflecting barriers to accessing care.

Three specific equity challenges warrant attention in the perioperative context:

(i) Bias in the representativeness of data. The predictive performance of eFI-type algorithms is highly dependent on the completeness and uniformity of underlying clinical documentation. In resource-constrained settings or regions with higher proportions of minority populations, EHR documentation may be less structured or complete, leading to "missingness bias" that systematically underestimates frailty prevalence in precisely those populations who may benefit the most from perioperative optimization (*43*).

(ii) Amplification of structural inequities. If training datasets are drawn disproportionately from well-resourced academic medical centers, the resulting algorithms may embed socioeconomic assumptions that are not generalizable. Cultural or linguistic barriers that result in incomplete assessment documentation may be misinterpreted as "low risk", potentially leading to inequitable allocation of perioperative resources such as prehabilitation programs or enhanced recovery pathways.

(iii) Equity-conscious validation standards. Future work on automated frailty screening should consider fairness alongside performance. This includes using measures such as equalized odds, calibration across demographic groups, and stratified positive predictive values, in addition to standard discrimination metrics like the C-statistic. Before deploying eFI-triggered perioperative pathways, implementation studies should evaluate whether algorithmic performance is consistent across levels of education, levels of income, and racial/ethnic groups through stratified subgroup analyses.

In conclusion, digital frailty assessment should not be viewed merely as a tool for greater technical efficiency but as a sociotechnical system requiring ongoing audits to ensure that automation does not inadvertently exacerbate existing health inequities. Governance frameworks that mandate transparency, periodic audits for bias, and community engagement will be essential to the ethical scaling of these technologies in perioperative care.

3.5. Priorities for future research

In view of these challenges, the research agenda must pivot decisively from prognostic association studies towards pragmatic implementation studies. First, there is an urgent need for well-designed multicenter cluster-randomized controlled trials or stepped-wedge studies to generate high-quality causal evidence. Unlike traditional individual randomization, these designs are better suited to evaluating complex, system-level interventions. They allow comparison between routine care and integrated frailty pathways that include systematic screening, a CGA, individualized preoperative optimization, and continuity of care after surgery.

Second, the evaluation framework must evolve. Outcome measures should extend beyond traditional surgical metrics (*e.g.*, 30-day mortality or readmission) to prioritize outcomes that are important to patients, such as functional recovery trajectories, disability-free survival, and quality of life. Concurrently, health economic analyses (cost-effectiveness and cost-utility) must be embedded within these trials to evaluate the feasibility and scalability of frailty-guided pathways in resource-constrained real-world settings.

Finally, as digital tools gain prominence, future studies must rigorously validate automated screening approaches. Research utilizing quasi-experimental designs needs to assess the predictive performance and real-world impact of eFI-triggered pathways. Crucially, this validation must explicitly address algorithmic fairness, ensuring that data-driven approaches do not exacerbate health inequities across diverse patient populations.

4. Conclusion

Frailty profoundly influences perioperative outcomes, and yet guideline formulation has not kept pace with scientific understanding. This review highlights marked regional differences. The UK tends to emphasize standardized pathways, the US favors more pluralistic approaches, and the Asia-Pacific region faces challenges in linking community screening to acute care workflows. Across all settings, however, a common issue remains: frailty is increasingly detected but not consistently acted upon.

Moving forward, care must transition from viewing frailty as a static risk label to considering it as a dynamic signal for intervention. This requires consensus risk thresholds that trigger the activation of prehabilitation and surveillance protocols, the integration of automated screening into clinical decision-making support systems, and interoperable infrastructure enabling seamless data transfer across care settings. Only by bridging detection and intervention can frailty-guided care achieve its potential to improve surgical outcomes and healthcare equity for older adults.

Funding: This work was supported by a grant from the Hainan Province Postdoctoral Research Project, from the National Natural Science Foundation of China (No. 82460268), and Grants-in-Aid from the Ministry of Education, Culture, Sports, Science and Technology of Japan (24K14216).

Conflict of Interest: The authors have no conflicts of interest to disclose.

References

1. Deng Y, Zhang K, Zhu J, Hu X, Liao R. Healthy aging, early screening, and interventions for frailty in the elderly. Biosci Trends. 2023; 17:252-261.
2. Hu X, Ma Y, Jiang X, Tang W, Xia Y, Song P. Neurosurgical perioperative management of frail elderly patients. Biosci Trends. 2023; 17:271-282.
3. Turner G, Clegg A, British Geriatrics S, Age UK, Royal College of General P. Best practice guidelines for the management of frailty: A British Geriatrics Society, Age UK and Royal College of General Practitioners report. Age Ageing. 2014; 43:744-747.
4. Deng Y, Sato N. Global frailty screening tools: Review and application of frailty screening tools from 2001 to 2023. Intractable Rare Dis Res. 2024; 13:1-11.
5. Deng Y, Yamauchi K, Song P, Karako T. Frailty in older adults: A systematic review of risk factors and early intervention pathways. Intractable Rare Dis Res. 2025; 14:93-108.
6. Dent E, Lien C, Lim WS, *et al.* The Asia-Pacific clinical practice guidelines for the management of frailty. J Am Med Dir Assoc. 2017; 18:564-575.
7. Mehta P, Lemon G, Hight L, Allan A, Li C, Pandher SK, Brennan J, Arumugam A, Walker X, Waters DL. A systematic review of clinical practice guidelines for identification and management of frailty. J Nutr Health Aging. 2021; 25:382-391.
8. Engel JS, Tran J, Khalil N, Hladkowicz E, Lalu MM, Huang A, Wong CL, Hutton B, Dhesi JK, McIsaac DI. A systematic review of perioperative clinical practice guidelines for care of older adults living with frailty. Br J Anaesth. 2023; 130:262-271.
9. British Geriatrics Society. Fit for Frailty Part 2: Developing, commissioning and managing services for people living with frailty in community settings. London, UK, 2015. *https://www.bgs.org.uk/sites/default/files/content/resources/files/2018-05-23/fff2_full.pdf* (accessed December 6, 2025).
10. British Geriatrics Society . Fit for Frailty Part 1: Consensus best practice guidance for the care of older people living in community and outpatient settings. London, UK, 2014. *https://www.activesurrey.com/Portals/0/adam/ResourceSort/VPbfAk1FaEe4mkNE-iSwjw/Link/fff_full.pdf* (accessed December 6, 2025).
11. Partridge JSL, Ryan J, Dhesi JK, group C-Bpfg. New guidelines for the perioperative care of people living with frailty undergoing elective and emergency surgery-A commentary. Age Ageing. 2022; 51:afac237.
12. Chow WB, Rosenthal RA, Merkow RP, Ko CY, Esnaola NF, American College of Surgeons National Surgical Quality Improvement P, American Geriatrics S. Optimal preoperative assessment of the geriatric surgical patient: A best practices guideline from the American College of Surgeons National Surgical Quality Improvement Program and the American Geriatrics Society. J Am Coll Surg. 2012; 215:453-466.
13. Mohanty S, Rosenthal RA, Russell MM, Neuman MD, Ko CY, Esnaola NF. Optimal perioperative management of the geriatric patient: A best practices guideline from the American College of Surgeons NSQIP and the American Geriatrics Society. J Am Coll Surg. 2016; 222:930-947.
14. Sieber F, McIsaac DI, Deiner S, *et al.* 2025 American Society of Anesthesiologists practice advisory for perioperative care of older adults scheduled for inpatient surgery. Anesthesiology. 2025; 142:22-51.
15. Lamperti M, Romero CS, Guarracino F, *et al.* Preoperative assessment of adults undergoing elective noncardiac surgery: Updated guidelines from the European Society of Anaesthesiology and Intensive Care. Eur J Anaesthesiol. 2025; 42:1-35.
16. De Hert S, Staender S, Fritsch G, *et al.* Pre-operative evaluation of adults undergoing elective noncardiac surgery: Updated guideline from the European Society of Anaesthesiology. Eur J Anaesthesiol. 2018; 35:407-465.
17. Chinese Society of Geriatrics, Chinese Medical Association. Chinese expert consensus on frailty assessment and intervention in geriatrics. Chin J Geriatrics. 2017; 36:251-256. (in Chinese)
18. Zhu ML, Huang YG, Liu XH, Zhang BZ, Liu Y, Liu DW, Yu JC, Chen W, He XD, Zhu L, Kang L, Tang S, Qin MW, Li ZJ, Yao HY. Expert consensus on perioperative management of older surgical patients at Peking Union Medical College Hospital. Med J Peking Union Med Coll Hosp. 2018; 9:36-41. (in Chinese)
19. XS JML. Expert opinion on perioperative management of frail elderly patients. Journal of Clinical Anesthesiology. 2023; 39:991-997.
20. Ishikawa N, Katsura T, Hara M. Changes in Kihon Checklist items and new Certification of long-term care needs among Japanese community-dwelling elders. J Rural Med. 2021; 16:270-279.
21. Satake S, Arai H. Questionnaire for medical checkup of old-old (QMCOO). Geriatr Gerontol Int. 2020; 20:991-992.
22. Kitai T, Kohsaka S, Kato T, *et al.* JCS/JHFS 2025 guideline on diagnosis and treatment of heart failure. Circ J. 2025; 89:1278-1444.
23. Egashira R, Sato T, Miyake A, Takeuchi M, Nakano M, Saito H, Moriguchi M, Tonari S, Hagihara K. The Japan Frailty Scale is a promising screening test for frailty and pre-frailty in Japanese elderly people. Gene. 2022; 844:146775.
24. Jin X, Tamiya N. The use of Japanese long-term care insurance claims in health services research: Current status and perspectives. Glob Health Med. 2021; 3:142-148.
25. Ministry of Health, Labour and Welfare. Explanatory materials on the provision of long-term care DB data (1): Data edition. Ministry of Health, Labour and Welfare, 2025. *https://www.mhlw.go.jp/content/12301000/001545569.pdf* (accessed December 6, 2025). (in Japanese)
26. Ministry of Health, Labour and Welfare. National database of health insurance claims and specific health checkups of Japan (NDB). *https://www.mhlw.go.jp/stf/seisakunitsuite/bunya/kenkou_iryou/iryouhoken/reseputo/index.html* (in Japanese) (accessed December 6, 2025).
27. Nakatsuka K, Ono R, Murata S, Akisue T, Fukuda H.

Claims-based frailty index in Japanese older adults: A cohort study using LIFE study data. J Epidemiol. 2024; 34:112-118.
28. Nishimura S, Kumamaru H, Shoji S, Nakatani E, Yamamoto H, Ichihara N, Miyachi Y, Sandhu AT, Heidenreich PA, Yamauchi K, Watanabe M, Miyata H, Kohsaka S. Assessment of coding-based frailty algorithms for long-term outcome prediction among older people in community settings: A cohort study from the Shizuoka Kokuho Database. Age Ageing. 2022; 51:afac009.
29. Kinjo K, Sairenji T, Koga H, Osugi Y, Yoshida S, Ichinose H, Nagai Y, Imura H, South-Paul JE, Meyer M, Honda Y. Cost of physician-led home visit care (Zaitaku care) compared with hospital care at the end of life in Japan. BMC Health Serv Res. 2017; 17:40.
30. Yoshimoto T, Nawa N, Uemura M, Sakano T, Fujiwara T. The impact of interprofessional communication through ICT on health outcomes of older adults receiving home care in Japan - A retrospective cohort study. J Gen Fam Med. 2022; 23:233-240.
31. You HS, Kwon YJ, Kim S, *et al*. Clinical practice guidelines for managing frailty in community-dwelling Korean elderly adults in primary care settings. Korean J Fam Med. 2021; 42:413-424.
32. Won CW, Lee Y, Lee S, Kim M. Development of Korean Frailty Index for Primary Care (KFI-PC) and its criterion validity. Ann Geriatr Med Res. 2020; 24:125-138.
33. Kim HS, Kim J, Bae G. Development of a hospital frailty risk score for community-dwelling older adults using data from electronic hospital records in South Korea. PLoS One. 2023; 18:e0293646.
34. Jung S, Kang HJ, Moon SY, Choi M, Jung J, Kim HR, Jung S, Jeong JH, Choi SH, Park YK. South Korean study to prevent the progression of frailty and aging-related diseases using a digital multidomain intervention (SUPERAGING): Protocol of a feasibility pilot study. Digit Health. 2026; 12:20552076251410995.
35. Hothi H, Paolone AR, Pezeshki M, Griffith LE, Kennedy CC, Leong DP, Marcucci M, Papaioannou A, Lee J. The implementation of frailty assessment tools in the acute care setting: A scoping review. J Am Geriatr Soc. 2025; 73:2571-2578.
36. Liu X, Le MK, Lim AYC, Koh EJ, Nguyen TN, Malik NA, Lien CTC, Lee JE, Au LSY, Low J, Wee SL. Perspectives on frailty screening, management and its implementation among acute care providers in Singapore: A qualitative study. BMC Geriatr. 2022; 22:58.
37. Fuchs TI, Pfab C, Kiselev J, Schaller SJ, Spies C, Rombey T. Barriers and facilitators to the implementation of prehabilitation for elderly frail patients prior to elective surgery: A qualitative study with healthcare professionals. BMC Health Serv Res. 2024; 24:536.
38. Fowler AJ, Stephens TJ, Partridge J, Dhesi J. Surgery in older patients: Learning from shared decision-making in intensive care. Br J Anaesth. 2022; 129:652-655.
39. Weiss Y, Zarour S, Neuman MD, Politi MC, Tang VL, Gisselbaek M, Berger-Estilita J, Saxena S. Shared decision-making for older adults in the peri-operative setting: A narrative review. Eur J Anaesthesiol. 2025; 42:767-773.
40. Best K, Shuweihdi F, Alvarez JCB, Relton S, Avgerinou C, Nimmons D, Petersen I, Pujades-Rodriguez M, Conroy SP, Walters K, West RM, Clegg A. Development and external validation of the electronic frailty index 2 using routine primary care electronic health record data. Age Ageing. 2025; 54:afaf077.
41. Clegg A, Bates C, Young J, Ryan R, Nichols L, Ann Teale E, Mohammed MA, Parry J, Marshall T. Development and validation of an electronic frailty index using routine primary care electronic health record data. Age Ageing. 2016; 45:353-360.
42. Obermeyer Z, Powers B, Vogeli C, Mullainathan S. Dissecting racial bias in an algorithm used to manage the health of populations. Science. 2019; 366:447-453.
43. Pridham G, Rockwood K, Rutenberg A. Strategies for handling missing data that improve Frailty Index estimation and predictive power: Lessons from the NHANES dataset. Geroscience. 2022; 44:897-923.

Received December 24, 2025; Revised January 26, 2026; Accepted January 28, 2026.

**Address correspondence to:*
Peipei Song, Center for Clinical Sciences, Japan Institute for Health Security, 1-21-1 Toyama, Shinjuku-ku, Tokyo 162-8655, Japan.
E-mail: psong@jihs.go.jp

Xiqi Hu, Department of Neurosurgery, Integrated Neuroscience Center, Geriatric Hospital of Hainan, Haikou 570300, China.
E-mail: 218302048@csu.edu.cn

Released online in J-STAGE as advance publication January 31, 2026.

Review

DOI: 10.5582/bst.2026.01032

Characteristics and management of constitutional indocyanine green excretory defect

Jiaao Wang, Ziqi Hou, Jun Ji, Ding Hu, Changlong Wei, Zhihong Zhang, Yuanzhi Zhou, Haichuan Wang*, Jiwei Huang*

Division of Liver Surgery, Department of General Surgery, West China Hospital, Sichuan University, Chengdu, China.

SUMMARY: Indocyanine green (ICG) test is a popular and widely implied assessment of hepatic functional reserve (HFR) due to its safety and efficiency. However, as the application of ICG expanded, an exceedingly rare disorder, the constitutional ICG excretory defect (CIED), gradually emerged. CIED is considered as a harmless dye excretory defect, which features remarkable ICG plasma retention (plasma ICG 15-min retention rate is higher than 50%) without any severe liver impairments. Previous investigations revealed that it has no particular symptoms and it is not a contraindication of surgical treatments. The deficiency of the organic anion transporting polypeptide 1B3 is affirmed to be the underlying cause of CIED. It is of great significance to identify this disorder from other reasons elevating ICG-R15 and provide such patients with effective and safe treatments. The utility of ^{99m}Tc-GSA liver scintigraphy, Child-Pugh and ALBI scores, and liver biopsy in identification and supplementary HFR assessment in CIED has been affirmed. Moreover, other methods based on radioactive tracers, serum biomarkers and imaging examinations have potential. Based on existing evidence, we proposed a clinical strategy that prioritizes ALBI and Child-Pugh scores, as well as imaging examinations, such as computerized tomography and ultrasound examinations, for the initial identification of CIED. Thereafter, ^{99m}Tc-GSA liver scintigraphy or biopsy is used to verify CIED and assess HFR. In conclusion, we comprehensively reviewed the characteristics, mechanisms and coping strategies of CIED, aiming to provide updated insights of this disorder.

Keywords: indocyanine green, organic anion transport, liver function test, liver surgery, liver disease

1. Introduction

Hepatic functional reserve (HFR) represents the liver's residual functional capacity to maintain physiological demands following injury or surgical resection, primarily determined by the quantity of viable hepatocytes and the integrity of hepatic microstructure (*1*). As a critical preoperative assessment in hepatic surgery, accurate HFR evaluation serves dual purposes: it identifies surgical candidates while guiding optimal surgical strategies to achieve complete lesion resection while minimizing postoperative complications, particularly post hepatectomy liver failure (PHLF) (*2*). This balance between radical tumor removal and preservation of sufficient functional liver tissue underscores the essential role of HFR assessment in modern hepatobiliary surgery.

So far, plenty of methods have been developed to assess HFR accurately, including laboratory tests, score systems, liver specific biomarkers, radioactive tracers, *etc*. (*1,3-7*). Among these, indocyanine green (ICG) is one of the most common methods due to its safety and accuracy in preoperative HFR evaluation (*5,8*). ICG was firstly introduced as a supplantation of bromosulphophthalein (BSP) because BSP occasionally causes severe complications. BSP is also taken up by the liver and undergoes enterohepatic circulation, leading to less accurate test results compared with ICG (*9,10*). The most used parameter is the retention rate of ICG at 15 minutes (ICG-R15), which was first introduced by Makuuchi *et al*. (*11*). However, in the past few decades an intriguing category of cases was encountered, which features extremely high blood retention rates of ICG (ICG-R15 usually higher than 50%) with other liver function being normal or only mildly abnormal. Such cases were defined as constitutional ICG excretory defect (CIED) (Figure 1) (*12-14*).

Following intravenous administration, ICG directly binds to plasma proteins and is transported to hepatic sinusoids by blood flow (*10,15*). Then the ICG, existing as an organic anion, is absorbed by organic anion transporters over the basolateral membrane, passes through the hepatic cell without metabolic changes

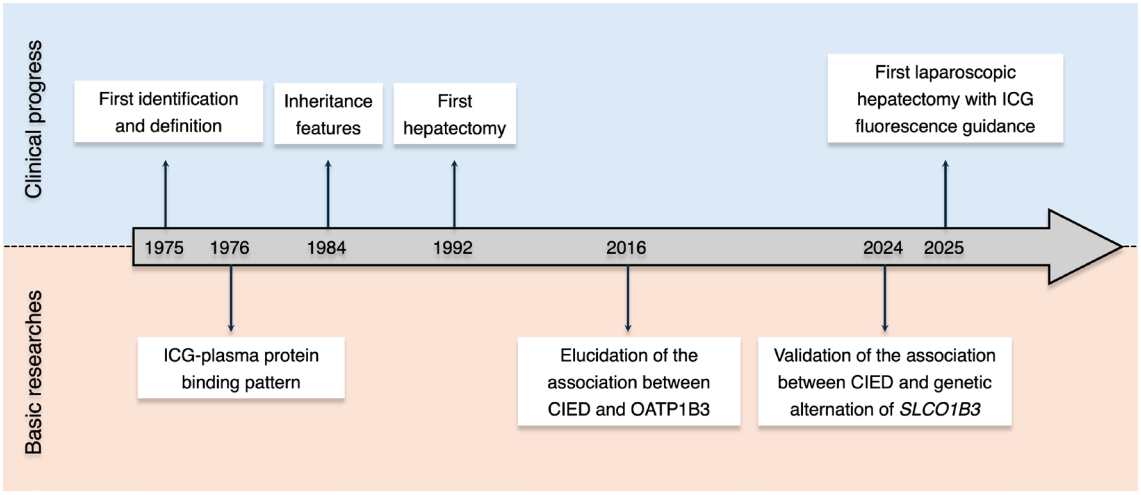

Figure 1. Milestones of CIED research in clinical and basic aspects.

and is excreted with bile acid through canaliculi membranes (*15,16*). This efficient hepatic clearance can be disrupted by multiple pathophysiological factors, such as architectural distortion in fibrosis/cirrhosis, impairing sinusoidal perfusion and hepatocyte function, hemodynamic alterations, competitive inhibition from hyperbilirubinemia and genetic or acquired variations in transporter expression (*15-20*). These mechanisms collectively contribute to the spectrum of observed ICG retention abnormalities in clinical practice.

Despite its rarity, accurate identification of CIED carries significant clinical implications, necessitating both reliable diagnostic criteria and validated alternative HFR assessment strategies for affected patients. Our systematic literature review (search terms: "indocyanine green" and "excretory defect" or "plasma retention" in PubMed and Google Scholar), initially identified 30 relevant publications. After excluding publications without specific cases and unavailable ones, 22 of the most relevant publications were reviewed. In this paper, we first reviewed the typical cases and studies of CIED and then concluded the features. Thereafter, studies related to the pathogenicity of CIED were thoroughly discussed. The last part focused on the examinations with differentiation significance and potential substitute HFR assessments for such patients. The findings aim to guide clinical decision-making while highlighting knowledge gaps requiring further investigation.

2. Epidemiology and clinical manifestations

Due to the rarity of CIED, there is lack of epidemiology investigations on large populations. Till now, all of CIED-related publications were reported in Japan (*12,13,21-39*) and China (*40*). Few reports of CIED in other countries were published. This might be attributed to the application of ICG mainly at these specific areas (*2*). Additionally, there has been no exact evidence to demonstrate that CIED is significantly affected by age, sex or race.

Namihisa *et al.* first reported 4 typical CIED cases. Relevant basic information is listed in Table 1. The laboratory tests and physical examinations revealed no abnormal findings. The only abnormal results were extremely high ICG-R15, which were all higher than 69%. The plasma ICG disappearance curve of 4 cases revealed there was a significant delay in the initial stage, and a step-form transitional delay in 15-25 minutes after injection. The ICG plasma disappearance rate also remarkably decreased, ranging from 0.017 to 0.025, significantly lower than normal limit of 0.15 (*41*). The following analysis revealed the transfer rate of ICG from plasma to liver was markedly decreased, with the normal transfer rate of ICG from liver to bile and liver back to plasma. Neither structural change nor heterogeneous cell infiltration were observed in liver biopsies of 4 cases. Additionally, the electron-microscopy found that there were increases of "lipofuscin-like" lysosomes in the hepatocyte and reticulum fiber in Disse's space, paracrystalline-like arrangement of mitochondria, and fragmentation of rough-surfaced endoplasmic reticulum (*12*). This study generally concluded the clinical characters and ICG kinetics features of CIED. The 2 stages delay in the plasma disappearance curve and significantly decreased ICG clearance rate (KICG) based on normal liver laboratory and histology tests were suggested as features of CIED (*12*). A further study by Adachi *et al.* supported previous findings. Also, the analysis of ICG plasma protein binding pattern revealed that there was no difference between cases and normal people, providing more evidence suggesting that the plasma retention of ICG was caused by limited uptake function of hepatocytes (*21*). Subsequently, other similar studies were conducted, with consistent conclusions (*22,23,25*).

Moreover, Taketazu *et al.* reported a case of CIED with malaria and hereditary elliptocytosis, which is another rare congenital disorder featuring elliptical-

Table 1. A summary of case reports of CIED

Author	Time	Report ccontent	Case number	Age & Gender	ICG-R15%	Disease	*Ref.*
Namihisa, *et al.*	1975	High retention of ICG test and normal retention of BSP test	4	52F 32M 28F 60M	70.5 78.4 70.2 69.4	cholecystitis duodenal ulcer healthy colon carcinoma	(*12*)
Adachi, *et al.*	1976	Serum protein binding pattern in high ICG retention patients	5	28M 24M 65M 37M 19M	75.7 74.1 82.8 88.3 84.9	Gilbert's Syndrome Gilbert's Syndrome diabetes mellitus and liver cirrhosis chronic persistent hepatitis with fatty infiltration Lung tuberculosis	(*21*)
Okuda, *et al.*	1976	High retention of ICG test and normal results of BSP test	5	22M 34M 25M 35F 70M	67.3 68.4 88.2 76.0 64.0	Gilbert's Syndrome Gilbert's Syndrome chronic cervical lymphadenitis acute HBsAg-negative hepatitis prostate carcinoma	(*13*)
Taketazu, *et al.*	1984	CIED patients with hereditary elliptocytosis	1	28F	94.0	malaise and elliptocytosis	(*23*)
Gotoh, *et al.*	1992	Hepatectomy in biliary cystadenocarcinoma with CIED	1	45F	99.8	biliary cystadenocarcinoma and Hepatitis B	(*24*)
Ikejima, *et al.*	1993	Chronic persistent hepatitis with high retention of ICG and BSP without hyperbilirubinemia	1	51M	70.0	HBV carrier	(*25*)
Hanazaki, *et al.*	2000	Hepatectomy in cavernous hemangioma patient with CIED	1	47F	59.8	cavernous hemangioma	(*27*)
Yamanaka, *et al.*	2001	Hepatectomy in HCC patient with chronic HBV, HCV and CIED	1	61M	72.0	HCC with chronic HBV, HCV	(*28*)
Kadono, *et al.*	2006	Effectiveness of ^{99m}Tc-GSA in preoperative evaluating patient with CIED and choledocholithiasis, receiving hepatectomy	1	78F	79.3	biliary cystadenocarcinoma	(*29*)
Maeda, *et al.*	2007	Hepatectomy in HCC patient with CIED	1	69F	83.5	HCC	(*30*)
Aoki, *et al.*	2013	Hepatectomy in HCC patient with Dubin–Johnson syndrome and CIED	1	77M	77.1	HCC with Dubin-Johnson syndrome	(*31*)
Imada, *et al.*	2016	Association between CIED and the expression of OATPs and NTCPs	1	81M	79.1	HCC	(*32*)
Nakatake, *et al.*	2018	Hepatectomy in a case of HCC with CIED	1	83M	76.2	HCC	(*34*)
Masuoka, *et al.*	2020	Effectiveness of gadoxetic acid-enhanced MRI in CIED	3	58M 70M 69M	83.0 68.0 73.0	HCC with HBV CRLM after right hemicolectomy hilar cholangiocarcinoma	(*37*)
Liu, *et al.*	2021	Hepatectomy in HCC patient with constitutional ICG excretory defect	1	68M	82.9	HCC	(*40*)
Morikawa, *et al.*	2025	Laparoscopic hepatectomy using ICG fluorescence staining in HCC patient with CIED	1	64M	70.0	HCC	(*39*)

Abbreviation: M, male; F, female; ICG-R15, ICG plasma retention in 15 minutes; HCC, hepatocellular carcinoma; CRLM, colorectal carcinoma liver metastasis.

shaped red blood cells (*23,42*). With the exception of observation of basic features, this study focused on the hereditary characteristics of CIED. The pedigree investigation showed that the patient was born to parents with consanguineous marriage. Including the reported case, 9 of 12 living family members received ICG testing, of which 6 showed markedly elevated ICG-R15 (> 78%), and 1 had a moderately elevated value (31.5%). The familial clustering is consistent with CIED being a congenital disorder and supports an autosomal recessive mode of inheritance. Notably, no direct evidence was observed to suggest that CIED corelates with hereditary elliptocytosis (*23*). Additionally, extremely high ICG retention rate was also observed in patients with congenital hyperbilirubinemia disorders, including Rotor's syndrome (RS) (*43*), Dubin-Johnson's syndrome (D-JS) (*31*) and Gilbert's syndrome (GS) (*13,21*). However, the genetic interaction among these disorders needs further investigation.

As a brief conclusion, existing evidence suggests that the main feature of CIED is remarkably increased ICG-R15, which is higher than 50% and mostly over 70%. The value of KICG significantly decreases. The ICG plasma disappearance curve demonstrates two distinctive delayed stages: the initial delay and transitional delay in 15-25 minutes after intravenous injection. The binding pattern of ICG to plasma proteins is normal. The laboratory tests of liver functions are within normal ranges or only mildly abnormal, including routine blood and liver biochemistry tests. Additionally, there is no evidence of significant liver impairment consistent with elevated ICG-R15 in histological dimension.

3. Treatment and prognosis for CIED patients with other liver diseases

Most studies noted that this disorder would not be detected unless the patient receives an ICG test. No particular symptoms or pathophysiological changes are observed before and CIED was considered a harmless excretory disorder. Therefore, except for the treatment of primary diseases, previous reports did not provide CIED patients with particular interventions (*12,13,21,25,26*).

In the early years, CIED patients were identified because they occasionally received ICG tests. After the Makuuchi's criteria were established and widely adopted, ICG test was widely applied as a credible preoperative HFR assessment (*11,44*). More CIED cases emerged in the liver surgery area. To date, as detailed in Table 1, 9 CIED cases receiving hepatectomy were reported, in which 6 were HCC patients, 2 were biliary cystadenocarcinoma, and 1 was cavernous hemangioma. The first CIED case receiving hepatectomy was reported by Gotoh *et al*. (*24*). The preoperative examinations of ultrasonography (US), computerized tomography (CT) and percutaneous cystography revealed a cystic lesion located at the left lobe and a connection between gallbladder and liver. Other laboratory tests were unremarkable. But ICG testing showed a significant retention, in which ICG-R15 was 99.8%. The findings supported the diagnosis of biliary cystadenocarcinoma and CIED. The left lobectomy was subsequently conducted successfully. The histology examination showed cystadenocarcinoma cells and normal liver background, consistent with preoperative diagnosis. This research first pointed out that CIED is not a contraindication to hepatectomy (*24*). However, this operation was empirically performed, without other preoperative assessments of HFR, which is dangerous for patients with unexplained high ICG retention.

The other 8 cases reported similar findings (Table 1). Except for one case with D-JS and conjugated hyperbilirubinemia (*31*), other potential causes of high ICG plasma retention, such as severe cirrhosis, intrahepatic vascular shunts, or hyperbilirubinemia were excluded in the remaining cases that underwent surgical treatment (*24,27,28,30,32,34,39,40*). The available levels of tumor markers including alpha-fetoprotein, protein induced by vitamin K absence or antagonist-II, carcinoembryonic antigen, and carbohydrate antigen 19-9 were within normal ranges or moderately increased. Repeated preoperative ICG tests all demonstrated similar significant delay. Various alternative preoperative assessments were implied. Seven of these cases employed ^{99m}Tc-galactosyl human serum albumin liver scintigraphy (^{99m}Tc-GSA) as a supplementary assessment for HFR (*27-29,31,32,34,39*). One of them implied enhanced CT and magnetic resonance imaging (MRI) as supplementary assessments (*30*) and one case implied liver biopsy preoperatively (*28*). None of the methods detected signs of severe liver impairment correlating with the markedly elevated ICG-R15 values. Among these methods, ^{99m}Tc-GSA liver scintigraphy was recognized as the most valuable for assessing unexplained high ICG-R15 (*27-29,31,32, 34,35,39*). The radioactive concentration distribution and quantitative parameters could provide viable evaluations of HFR (*35*).

It is worth noting that only one recent case by Morikawa *et al.* was performed using laparoscopy. The preoperative situation was similar to previous cases, indicating CIED. With normal liver function and ^{99m}Tc-GSA liver scintigraphy results, the patient successfully underwent laparoscopic anatomical liver resection. This study suggested intraoperative ICG fluorescence guidance remains feasible in CIED and proposed that negative staining with 2.5 mg intravenous ICG injection during the operation provides optimal surgical guidance (*39*).

Notably, gadolinium ethoxybenzyl diethylenetriaminepentaacetic acid is a common paramagnetic magnetic resonance contrast agent, which is specifically absorbed by hepatocytes and excreted through biliary and partially urinary systems (*45*). The gadoxetic acid-enhanced MRI (EOB-MRI) is a

widely applied examination of hepatobiliary lesions with excellent sensitivity (*46,47*). However, a study by Masuoka *et al.* observed that EOB-MRI presented decreased parenchymal signal intensity and impaired lesion detectability in CIED patients (*37*). It was believed the underlying cause was that gadoxetic acid shares the same hepatic uptake pathway with ICG. The low expression of related transporters in CIED decreases the liver uptake of gadoxetic acid (*16,37,38*).

All hepatic resections were completed successfully, with patients experiencing uncomplicated recoveries (*24,27,28,30-32,34,39,40*). However, postoperative ICG tests indicated that ICG excretion remained markedly delayed (*27,29,31,39*). The long-term observation showed that it would take at least 1 month to completely eliminate ICG in CIED patients (*39*). Additionally, no evidence suggested that CIED either accelerates or moderates the progression of liver tumor or other diseases.

4. The pathogenesis of CIED

Following intravenous injection, ICG generally circulates as follows: (*i*) binding to plasma proteins, mainly albumin and lipoproteins, (*ii*) hepatic delivery *via* blood flow, (*iii*) uptake by hepatocytes as organic anions, (*iv*) direct biliary excretion without metabolism or enterohepatic circulation. Previous studies have affirmed in CIED, that the ICG binding pattern with plasma protein and excretion to biliary tract is the same as in normal people (*12,13*). Therefore, the reason of CIED is possibly localized to the dysfunction of hepatic uptake.

In the past decades, the exploration of hepatocytes' transportation systems has been broadly conducted and gained plenty of advancements (Figure 2) (*48-51*). The channels for organic anion transport in hepatocytes have been identified as Na^+-independent organic anion transporters and Na^+-taurocholate cotransporting polypeptides (NTCPs). The Na^+-independent organic anion transporters can be further classified into organic anion transporters (OATs) and organic anion transporting polypeptides (OATPs) (*15,52-54*). Among these, OATP1B1, OATP1B3 and OATP2B1 isoforms are specifically expressed on the basolateral membrane of human hepatocytes. These OATPs have been demonstrated to mediate the transport of various organic anions, including bilirubin, bile acids and drugs (*55*). Moreover, the observed inhibitory effect of ICG on the transport of the aforementioned substrates suggests that ICG might utilize the same transportation pathways

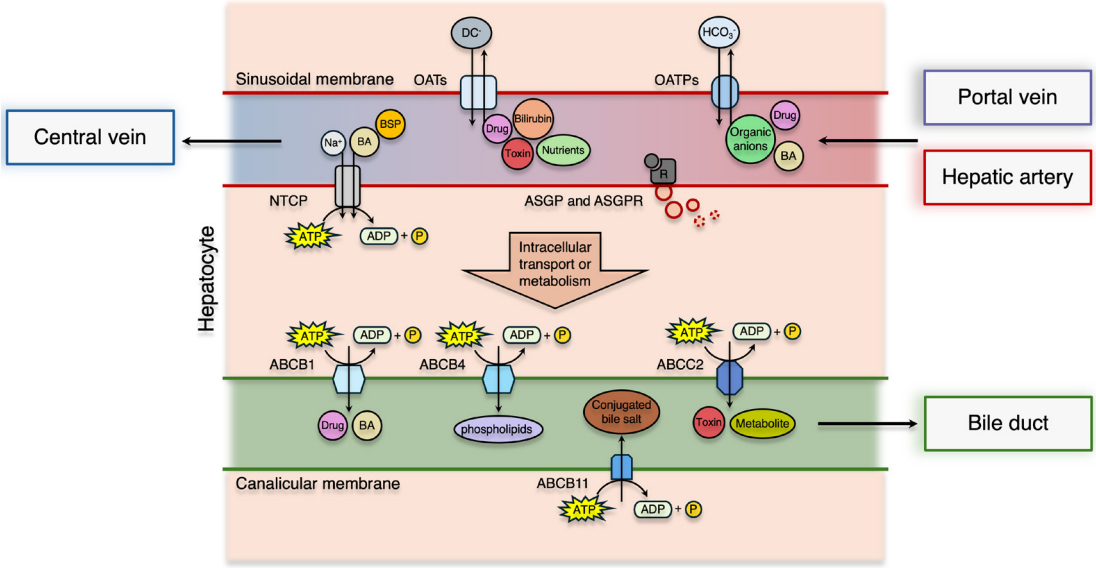

Figure 2. A scheme for the human hepatocyte transport systems. Regarding the transporters located on the sinusoidal membrane, sodium taurocholate co-transporting polypeptide (NTCP) is a unidirectional, ATP and sodium ion dependent transporter, which uptakes conjugated bile acids (BAs), partially unconjugated BAs, bromosulphophthalein (BSP), and thyroid hormones (*50*). Organic anion transporters (OATs) are bidirectional, ATP-independent transporters, including OAT2, OAT3, OAT5, and OAT7. OATs mediate the uptake of common drugs (such as nonsteroidal anti-inflammatory drugs, antibiotics, diuretics), toxins (such as mercury, aristolochic acid), nutrients (such as vitamins, flavonoids), and bilirubin. OATs are driven by the exchange of dicarboxylates (DC^-). Organic anion transporting polypeptides (OATPs) are also bidirectional, ATP-independent transporters, including OATP1B1, OATP1B3, and OATP2B1, which mediate the uptake of drugs, endogenous and exogenous organic anions, and partial BAs. OATPs are driven by the export of bicarbonate (HCO_3^-) (*51*). Asialoglycoprotein (ASGP) specifically binds with the asialoglycoprotein receptor (ASGPR) and forms complex, mediating the subsequent endocytosis. As for the transporters located on the bile canalicular membrane of hepatocytes, most belong to ATP-binding cassette (ABC) family, which are ATP-dependent unidirectional export transporters. ABCB1, formally called multi-drug resistance protein 1 (MDR1) or permeabilization glycoprotein, mediates the export of hydrophobic drugs, anticancer agents, and some bile acids. ABCB4, formally called multi-drug resistance protein 2 (MDR2), mediates the export of phospholipids, particularly phosphatidylcholine, into bile for bile formation, which helps the secretion of bile salts and lipids into the bile canaliculus. ABCB11, formally called bile salt export pump (BSEP), mediates the export of conjugated bile salts. ABCC2, formally called multidrug resistance-associated protein 2 (MRP2), mediates the export of metabolite and toxin (*49*).

(*19*). Subsequently, de Graaf *et al*. affirmed by cellular experiments that OATP1B3 and NTCP are the main transporter of ICG (*16*). Another study by Vaz *et al.* pointed out that defective NTCP expression is typically accompanied by conjugated hypercholanemia, which features extremely high concentrations of conjugated bile salts with relatively mild symptoms (*56*).

With these essential conclusions, further investigation about the expression of OATP1B3 and NTCP in CIED patients was conducted by Kagawa *et al.* In their study, no NTCP-associated hypercholanemia was observed, ruling out the deficiency of NTCP expression as the underlying cause. Therefore, they suggested the absence of OATP1B3 expression was the ultimate reason of CIED. As a result, the hepatic uptake of ICG is accomplished by passive diffusion, significantly limiting the transport efficiency. At the genetic level, the study revealed the deficiency was caused by a homozygous mutation of L1 retrotransposon insertion in *Solute Carrier Organic Anion Transporter Family Member 1B3* (*SLCO1B3)*, which encodes OATP1B3 (*33*). Another follow-up study by Anzai *et al.* observed that heterozygous *SLCO1B3* null mutations did not affect OATP1B3 expression levels, remaining comparable to those in wild-type individuals. Additionally, they confirmed that heterozygous *SLCO1B3* alteration does not result in CIED (*36*), supporting an autosomal recessive inheritance pattern for this condition.

Recently, a retrospective study by Tanimoto *et al.* validated the conclusions with a larger cohort. Among 49 patients who underwent hepatectomy and preoperative ICG tests, absence of OATP1B3 expression was observed in 6 patients, all of whom exhibited characteristic CIED features. Genetic analysis of available frozen tissue blocks confirmed homozygous *SLCO1B3* alterations in all 6 cases. Furthermore, in a separate cohort of 59 colorectal liver metastasis (CRLM) patients, heterozygous alterations of *SLCO1B3* were detected in 5 patients. It's worth noting that these heterozygous carriers showed no significant differences in ICG test results compared to wild-type *SLCO1B3* patients, which is consistent with previous findings (*38*).

Previous studies mentioned that extremely high ICG retention rate was also observed in patients with congenital hyperbilirubinemia disorders, including RS (*43*), D-JS (*31*) and GS (*13,21*). A study by van de Steeg *et al.* affirmed that in RS patients, complete OATP1B1 and 1B3 deficiency leads to the Rotor-type hyperbilirubinemia and ICG excretory defect (*57*). Nambu and Namihisa reported that the average values of ICG-R15 and KICG of 21 D-JS patients were 10.4% and 0.167 respectively, compared to the average values of 73% and 0.020 in 20 CIED patients. Thereby, they indicated that the ICG values are within normal ranges in D-JS (*26*), with reported cases of concurrent CIED and D-JS representing coincidental occurrences (*31*). Many studies have confirmed that hyperbilirubinemia in GS is caused by decreased activity of bilirubin-UDP glucuronosyl transferase (*58*). However, a previous study pointed out that a defect of hepatic organic anion transport could not be attributed to such deficiencies (*59*).

Figure 3 illustrates the difference in ICG circulation

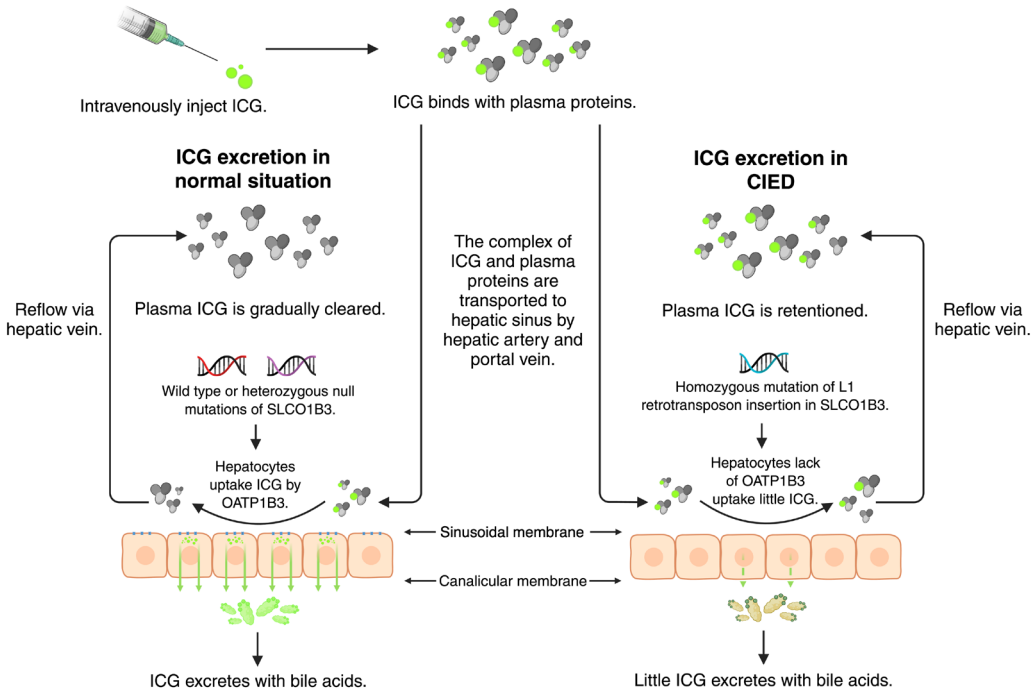

Figure 3. A comparison of ICG excretion patterns in normal circumstances versus in CIED cases. ICG: indocyanine green, OATP1B3: organic anion transporting polypeptide 1B3.

Table 2. Specific subtracts of OATP1B3

Category	Examples	*Ref.*
Exogenous compounds		
Drugs		
Lipid-lowering drugs	rosuvastatin, pitavastatin	(*65*)
Antihypertensive drugs	valsartan, telmisartan, olmesartan, enalapril	
Antidiabetic drugs	repaglinide	
Antibiotics	rifampin	
Chemotherapy agents	hydroxyurea, methotrexate, carboplatin, cisplatin, oxaliplatin, docetaxel, paclitaxel, imatinib	
Imaging Agents		
Organic dyes	bromosulphophthalein, indocyanine green	(*51*)
Radioactive scintigraphy agents	^{99m}Tc-mebrofenin, ^{99m}Tc-diethylenetriaminepentaacetic acid–chenodeoxycholic acid conjugate (^{99m}Tc-DTPA-CDCA)	
MRI contrast agents	gadolinium-ethoxybenzyl-diethylenetriaminepentaacetic acid (Gd-EOB-DTPA)	
Toxins	okadaic acid, ochratoxin A	(*64, 66*)
Endogenous compounds		
Bile acids	taurodeoxycholate, cholate, taurocholate, taurochenodeoxycholate	(*62*)
Bilirubin and conjugates	bilirubin, bilirubinmonoglucuronide	
Steroid and steroid metabolites	dehydroepiandrostenone sulfate, estradiol-17β-glucuronide, estrone-3-sulfate	
Gastrointestinal hormones and leukotrienes	cholecystokinin octapeptide 8, leukotriene C4, prostaglandine E2	
Hormones	triiodothyronine, thyroxine	
Toxins	kynurenic acid, indoxyl sulfate,	(*63*)

between normal situations and CIED. Although existing studies have confirmed that OATP1B3 deficiency impairs hepatocellular ICG uptake and sporadic reports have linked CIED to *SLCO1B3* gene mutations, several critical knowledge gaps remain. First, robust evidence from large-scale population studies and *in vivo* experiments is still lacking to definitively establish pathogenicity. Second, the mechanisms underlying elevated ICG plasma retention in certain congenital hyperbilirubinemia disorders remain poorly understood. Importantly, given OATPs' essential role in hepatic drug or metabolite uptake, its deficiency may predispose patients to dose-induced toxicity, though this requires further clinical validation (*33,51,60,61*). Patients suspected of having CIED should exercise extreme caution when exposed to known OATP1B3-specific substrates and structurally similar potential substrates (Table 2) (*62-66*). Monitoring of circulating concentrations and early prevention of dose-related adverse reactions are necessary. Additionally, while early observations of familial clustering suggested CIED may be a congenital disorder (*23*), subsequent studies have failed to systematically investigate its inheritance pattern at the molecular genetic level. These unresolved issues, including population-level prevalence, precise molecular mechanisms, pharmacological implications, and genetic determinants, represent crucial areas for future research to advance our understanding and clinical management of CIED.

5. Reliable identification and alternative HFR assessment in CIED patients

Many factors have been shown to cause the high ICG plasma retention in patients without CIED. The most common reasons are severe fibrosis and cirrhosis, leading to changes of liver hemodynamics and biliary excretion (*15,17,67*). Vascular abnormalities like intrahepatic vascular shunts and portal/hepatic vein thrombosis similarly compromise liver perfusion and contribute to ICG retention (*18*). Additionally, in severe functional insufficiency and hepatitis, liver ICG uptake capacity decreases remarkably (*5,16,20*). Under such circumstances, elevated ICG values typically contraindicate surgical treatment due to the associated hepatic functional impairment. Importantly, unlike these pathological conditions, CIED does not affect the effectiveness and safety of patients undergoing liver operation. This distinction underscores the critical need for accurate preoperative differentiation between CIED-mediated and pathology-driven ICG retention. Current diagnostic challenges highlight two key requirements: (*i*) reliable methods to distinguish CIED from other causes of ICG retention, and (*ii*) validated alternative approaches for HFR assessment when ICG testing is confounded. Although liver biopsy is regarded as a golden criterion in the diagnosis of liver impairments, its invasive nature and occasional technical limitations necessitate alternative diagnostic strategies (*28*). Here we systematically evaluate several clinical examinations for distinguishing CIED from the other causes and providing accurate supplementary HFR assessments.

5.1. Radioactive tracing technology

As previously presented, the application of radioactive tracers in HFR assessment in patients with normal or defective ICG excretion has been widely recognized and sophisticated (*28,29,31,32,34,39,68*). ^{99m}Tc-GSA liver scintigraphy is one of the most prominent

methods. The liver elimination of glycoprotein is based on the combination of asialoglycoprotein (ASGP) and asialoglycoprotein receptor (ASGPR) on the cell membrane of hepatocytes (*69*). ^{99m}Tc-GSA is a radiolabeled molecular probe synthesized from GSA, an ASGP analogue, and the radioactive isotope technetium-99m. After intravenous injection, the probes would specifically bind to ASGPRs, which only occurs in hepatocytes. Both the disappearance in blood and the uptake in liver can be measured clearly and continuously (*70*). When hepatocytes are impaired or lesions appear, the number of functional hepatocytes decrease, manifesting as reduced uptake and concentration of ^{99m}Tc-GSA. The general and regional liver function could be demonstrated visually and noninvasively by single photon emission computed tomography (SPECT). The quantitative indexes could also be calculated, of which the mostly used are LHL15 (receptor index), HH15 (blood clearance index) and GSA-Rmax (regional maximal removal rate) (*18,71-74*). A recent study revealed HH15 and LHL15 have good capacity in predicting ICG-R15 ≥ 20%, with AUC of 0.844 (95%CI: 0.747–0.915) and 0.878 (95%CI: 0.759–0.944) respectively (*75*). Thereafter, the development of dynamic SPECT/CT fusion imaging technology sparked new ideas for preoperative liver function assessment. Using the new method, Mao *et al.* proposed a prediction system of the uptake index (UI) and three-dimensional (3D) reconfigurations including overall and future liver remnant (FLR) functions. The UI value was calculated from the dynamic radioactive intensity caused by hepatic uptake and degradation processes of ^{99m}Tc-GSA, quantifying the risk of developing PHLF. Concomitantly, the 3D reconfigurations provide visualized and intuitive information for surgeons to evaluate surgical plans and risks (*76*).

Additionally, Okabayashi *et al.* proposed a prediction index for postoperative remnant liver function, the remKGSA, which is calculated from LHL15 and volumetric rate of the FLR using ^{99m}Tc-GSA SPECT/CT fusion imaging. The index was very useful in predicting safe and accurate liver resection. The researchers pointed out that the remKGSA provides detailed and accurate information to decide whether patients would benefit from surgery (*70*). Furthermore, another study by Sumiyoshi *et al.* affirmed the efficiency of remKGSA in 13 patients with abnormally deteriorated ICG values. It presented that only 3 patients receive hepatectomy along with the Makuuchi's criteria. While the other 10 patients received operations exceeding the criteria and no postoperative mortality occurred in all patients. The study supported the conclusion that the technology would provide accurate assessments of liver function in patients with severely deteriorated ICG levels (*35*). Generally, SPECT/CT fusion technology not only overcomes CT's deficit of estimating liver volume without assessing liver function but also eliminates SPECT's disadvantage of low spatial resolution. Evidence to date suggests it is a reliable assessment technique for liver surgery, including surgery for CIED patients. However, the widespread adoption of this technology is limited by its high costs and technical complexities to some extent, demanding further improvement.

Notably, in addition to ^{99m}Tc-GSA, ^{99m}Tc-mebrofenin hepatobiliary scintigraphy (HBS) is another common radioactive tracing technology for HFR assessments (*77*). However, studies have indicated that the ^{99m}Tc-mebrofenin shares a similar pharmacokinetic pathway with ICG; both undergo hepatic uptake mediated by OATP1B1 and OATP1B3 (*16,78*). Given this mechanistic overlap, the applicability of ^{99m}Tc-mebrofenin HBS in CIED patients remains uncertain, as no studies have yet investigated its performance in this specific population. Therefore, although the ^{99m}Tc-mebrofenin HBS has demonstrated excellent capacity and reliability in liver surgery, it demands more relevant research to explore its application in CIED (*77,79,80*).

5.2. Serum examination and clinical score systems

Plasma bilirubin levels provide basic information about the metabolism and excretion function of the liver. Increasing bilirubin levels act as specific markers for the impairment and loss of function of the liver (*6*). Besides, albumin and proteins related to hemostasis and fibrinolysis are used as indirect indicators of liver synthesis functions (*5*). Based on such biochemistry parameters and common symptoms of insufficient liver function, clinical grading systems like the Child-Pugh score were developed and gained broad application on a global scale (*4*). According to present experience, Child-Pugh scores could provide valuable information in selection of patients with liver diseases for resection or transplantation (*2,3*). Previous case reports also mentioned the application of Child-Pugh scores in CIED patients, which affirmed its effectiveness in assessing surgical tolerance (*39,40*). However, relatively strong subjectivity and poor differentiation capacity weaken the accuracy of the Child-Pugh score. Thorough discussions of its limitations have been conducted (*2,3*). In addition, another common clinical score system, the model for end-stage liver disease (MELD), faces similar troubles, which is narrow for patients undergoing a hepatectomy (*5*).

Based on Child-Pugh scores, Johnson *et al*. proposed an objective score system, albumin-bilirubin score (ALBI), literally calculated by the 2 laboratory values. This international multicenter clinical research provides solid evidence that it has better distinctiveness than conventional Child-Pugh scores in HCC patients' HFR assessment and prognosis prediction. In particular, a significant discrepancy in median survival was observed among patients classified as Child-Pugh A, and subdivided into ALBI grade 1 and 2, which is

over 10 months in different country cohorts. ALBI, thereby, provides further information for surgeons to decide treatment plans (*81*). So far, the ALBI score has gained worldwide recognition and has become a crucial component of the preoperative assessment for hepatic surgery (*82-84*).

Subsequently, considerable efforts were dedicated to enhancing the discriminatory and predictive capabilities of the ALBI score. A. Hiraoka *et al*. advised that in addition to the liver function state, the disease burden would also affect the treatment strategies and prognosis of patients, which could be measured by Tumor Node Metastasis (TNM) staging system. As detailed in Table 3, researchers developed the ALBI-Tumor score (ALBI-T) by combining the ALBI and TNM staging system from the Liver Cancer Study Group of Japan (5th edition) (*85*). The results revealed that it is a comprehensive clinical score for strategic decisions and predicting survival of HCC patients (*82,86*). The research team also made efforts to promote the differentiation ability of ALBI scores. The new cut-off value was derived from the ALBI value with the ICG-R15 < 30%, which is believed to be the limit of the minimal anatomical resection in Makuuchi's criteria (*11,87*). As for the results, a good correlation between ALBI and ICG-R15 was observed (r = 0.563; 95%CI: 0.550–0.570; p < 0.0001). The new cut-off value of the modified-ALBI score (mALBI) was -2.27, with an AUC of 0.828 (95%CI: 0.823–0.833). The subsequent studies were conducted in different centers around the world, further affirming its value in clinical practice (*88,89*). Besides, the utility of mALBI in CIED patients was validated, thereby indicating the mALBI as a reliable and effective method for the detection and evaluation of such patients (*38*).

Other studies attempted to reduce the calculation complexity of ALBI scores. Kariyama *et al*. proposed a simplified calculation, the EZ-ALBI, avoiding the logarithmic change of serum total bilirubin. The validation of the effectiveness of EZ-ALBI and EZ-ALBI-T showed that they performed excellently like the previous scores, with a correlation coefficient of 0.981 (95%CI: 0.980-0.982). The researchers highlighted that the simplicity of EZ-ALBI allows clinical workers to mentally perform the calculation and grasp HFR intuitively (*90*).

Moreover, a variety of dimensions of HFR assessment were integrated into the ALBI to enhance its comprehensiveness. Some researchers advised that the platelet counts should be integrated into the ALBI scores, as it is an effective surrogate metric for evaluating portal hypertension (PHT). Liu *et al*. incorporated blood platelet counts into ALBI, thereby forming the PALBI (Table 3). The following studies further corroborated the utility of PALBI in HFR assessment and PHLF prediction, demonstrating its equivalence to other ALBI scores (*91-94*). However, the complexity of its calculation limits the application of PALBI to some extent. More efforts were needed to promote its practicability. The ALBI score can also be combined with imaging examinations. Preoperative 3D-CT reconstruction is used as an effective approach to measure FLR volume (*95*). Zou *et al*. proposed that ALBI could compensate for the weaknesses of FLR measurements, which has difficulty in simultaneously assessing the functional state of preserved livers. The results suggested the combination of ALBI and standardized FLR was effective and precise in predicting PHLF (*96*). Similarly to previously mentioned dynamic SPECT/CT fusion imaging, the application of ALBI and FLR in CIED patients is quite promising. To provide adequate evidence, however, more in-depth studies are demanded.

Besides the methods based on ALBI scores, there were other laboratory indexes that could assist in the evaluation of liver function status and HFR. Aspartate transaminase-Platelet-ratio-index (APRI), first proposed by Wai *et al.* , was originally designed for the noninvasive examination of liver fibrosis and cirrhosis (Table 3) (*97*). Further studies highlighted the fact that APRI has an excellent capacity to predict PHLF and postoperative mortality, due to the reason that such risks are highly related to liver fibrosis or cirrhosis (*98,99*). Recent studies focused on the combination of the ALBI scores and APRI. The results indicated that simultaneous consideration of HFR and severity of liver cirrhosis promotes the accuracy of preoperative assessment and safety of surgery (*100,101*). The four-factor fibrosis index (FIB-4) is another non-invasive tool for the examination of liver cirrhosis (Table 3) (*102*). Recent studies also highlighted the capacity of FIB-4 as an independent predictor of prognosis and post-operative outcomes (*103,104*). H. Toyoda and P. J. Johnson comprehensively discussed the fluctuation trends of the above scores at different stages of liver disease progression. The ALBI scores increase before cirrhosis develops, providing sensitive detection of early liver function deterioration. They are also closely associated with cirrhosis indicators, FIB-4 and APRI, in the progression of liver disease. In the late stages of liver disease, ALBI scores have a comparable ability to MELD and Child-Pugh scores to predict mortality (*84*).

5.3. Imaging examination

Common preoperative imaging examination includes CT, US and MRI. These imaging diagnostic technologies provide comprehensive diagnostic information, offering both direct visualization of liver anatomy and pathological lesions (including location, size and characteristics) and functional estimation of HFR (*105*). First, it is widely accepted that preoperative CT is one of the indispensable preparations for the evaluation of FLR, liver anatomy, cirrhosis and PHT, which are all essential references for treatment decisions (*95,106-108*). Previous case reports pointed out that in CIED

Table 3. A summary of assessments based on serum biomarkers

Author	Time	Name	Formula	Cut-off value	Advantages	*Ref.*
Johnson, *et al.*	2015	ALBI	$ALBI=[ALB\times(-0.085)]+(log_{10}STB\times 0.66)$ *ALB*(*g/L*), *STB*(*μmol/L*)	ALBI-1:(-∞,-2.66] ALBI-2:(-2.66,-1.39] ALBI-3:(-1.39,+∞)	Objective, accurate score for FLR assessment	(*81*)
Liu, *et al.*	2017	PALBI	$PALBI=(2.02\times log_{10}STB)+[-0.37\times(log_{10}STB)^2]+(-0.04\times ALB)+(-3.48\times \log_{10}PLT)+[1.01\times(log_{10}PLT)^2]$ *ALB*(*g/L*), *STB*(*μmol/L*), *PLT*(10^3/*μL*)	PALBI-1:(-∞,-2.53] PALBI-2:(-2.53,-2.09] PALBI-3:(-2.09,+∞)	Objective, accurate score for FLR assessment including portal hypertension	(*91*)
Hiraoka, *et al.*	2016	ALBI-T	$ALBI\text{-}T=ALBI\ Grade+TNM\text{-}2$ *ALB*(*g/L*), *STB*(*μmol/L*),*TNM*(*LCSGJ 5th edtion*)	Grade 0~5	Objective, accurate, and comprehensive score including FLR and disease burden	(*86*)
Hiraoka, *et al.*	2017	mALBI	$ALBI=[ALB\times(-0.085)]+(log_{10}STB\times 0.66)$ *ALB*(*g/L*), *STB*(*μmol/L*)	mALBI-1:(-∞,-2.66] mALBI-2a:(-2.66,-2.27] mALBI-2b:(-2.27,-1.39] mALBI-3:(-1.39,+∞)	More delicate stratifications	(*87*)
Kariyama, *et al.*	2020	EZ-ALBI	$EZ\text{-}ALBI=STB\text{-}9ALB$ conversion with ALBI: [*ALBI*]=0.099[*EZ-ALBI*]+0.81; [*EZ-ALBI*]=9.75[*ALBI*]-9.1 *STB*(*mg/dL*), *ALB*(*g/dL*)	EZ-ALBI-1:(-∞,-34.4] EZ-ALBI-2:(-34.4,-22.2] EZ-ALBI-3:(-22.2,+∞)	Simplified calculation, with the same objectivity and accuracy	(*90*)
Wai	2003	APRI	$APRI=\frac{AST\times 100}{PLT}$ *AST*(*/UNL*), *PLT*(10^9/*L*)	A: (0,0.5] B: (1.5, +∞) q1C: (0,1.0] D: (2.0, +∞)	Simple, noninvasive examination of liver fibrosis and liver cirrhosis	(*97*)
Vallet-Pichard	2007	FIB-4	$FIB-4=\frac{Age\times AST}{PLT\times\sqrt{ALT}}$ *Age*(*years*),*AST,ALT*(*U/L*), *PLT*(10^9/*L*)	FIB-4A: (0,1.45] FIB-4B: [1.45,3.25] FIB-4C: (3.25,+∞)	Simple, noninvasive examination of liver fibrosis and liver cirrhosis	(*102*)

Abbreviation: ALB, albumin; STB, serum total bilirubin; PLT, platelet; AST, aspartate transaminase; ALT, alanine transaminase.

patients, enhanced CT remains an effective method for evaluating liver volume and structure (*28,30-32,34,39*). Beyond anatomical assessment, CT-based parameters are also promising as alternative HFR assessments. The combination of CT with other HFR assessments, such as ALBI scores, could promote its utility (*96*). In addition, Tu *et al*. proposed a novel CT-based approach to assess HFR, which incorporates both quantitative and qualitative parameters of FLR. It included an index and a grading system, the percentage of remnant liver volume (PRLV) and CT grade, for the assessment of HFR (Table 4). The results revealed that the two parameters correlate with postoperative survival. The combination of them formed a brief prediction line for the evaluation of HFR. The line showed that for patients with better liver status (lower CT grade), a larger resection range (lower PRLV) would be acceptable (*109*). Other studies focused on the effectiveness of dividing spleen or liver volume by body surface area (BSA), including SV_{BSA} and LV_{BSA}, both of which are useful in the assessment of cirrhosis, PHT and HFR (*75,110-112*).

Enhanced multiphase CT provides richer information. Iodine-uptake parameters, such as extracellular volume fraction (ECV) and iodine washout rate (IWR), have been proposed as potential indicators of cirrhosis and HFR (Table 4). Initiated by the deposition of collagen and matrix proteins, the enlargement of ECV is another feature of cirrhosis, which could be precisely measured by enhanced CT (*113-115*). IWR reflects the change of intrahepatic hemodynamics. In livers with severe cirrhosis, the parenchymal demonstrates prolonged iodine retention and reduced IWR. The integration of CT images with IWR could visualize the heterogeneous fibrosis deposition spatially, including the tumor area, which is valuable for surgery (*116*). Furthermore, the previously mentioned study by Nagayama *et al*. compared several common methods in HFR assessment, including IWR, ICG-R15, SV_{BSA} and LV_{BSA}, ^{99m}Tc-GSA liver scintigraphy. The results revealed that all the CT measured indicators correlate with ICG-R15. Among them, IWR, SV_{BSA} and LV_{BSA} are independent predictors of severe liver function insufficiency of ICG-R15 ≥ 20%. The IWR performs the best discriminative capacity with an AUC of 0.845 (95%CI: 0.698–0.931). They also pointed that the combined CT model of IWR and volumetric indicators could provide more accurate evaluation, with an AUC of 0.924 (95%CI: 0.860–0.965), compared to SV_{BSA} and LV_{BSA} with AUCs of 0.653 (95%CI: 0.501–0.790) and 0.694 (95%CI: 0.553–0.820) respectively (*75*).

In summary, current evidence supports the use of CT-derived parameters as objective, accurate, and clinically accessible tools for HFR assessment. These imaging indicators provide reproducible quantitative data that can enhance preoperative risk stratification and surgical planning. However, further large-scale validation studies are warranted to strengthen the reliability of these findings and explore their broader applications in HFR

Table 4. CT-based assessments for hepatic functional reserve

Author	Time	Name	Formula	Cut-off value	Ref.
Tu, *et al.*	2007	PRLV	$\boldsymbol{PRLV=pRLV/pTLV\times100\%}$ $\boldsymbol{pTLV}$=121.75+16.49×*body mass* $\boldsymbol{pRLV}$=*pTLV-(tumor volume+peritumor volume)* *volume(ml),body mass(kg)*	CT Grade-1: SI<300, with no sign of PVH CT Grade-2: 300<SI<600, with 2~3 signs of PVH CT Grade-3: SI>600 with 3~4 PVH signs, moderate ascites(≤2cm) CT Grade-4: SI>600 with 3~4 PVH signs, severe ascites(>2cm)	(*109*)
		CT Grade	***spleen index=diameter of thickness×diameter fore and aft×diameter up and down diameter*** *(cm)*		
Nagayama, *et al.*	2025	IWR	$\boldsymbol{IWR=(1-HE_{DP}/HE_{PVP})\times100}$	ICG≥20%: ≤35.9%	(*75*)
		ECV	$\boldsymbol{ECV=(HE_{DP}\times(100-Hct))/AE_{DP}}$	ICG≥20%: ≥30.2%	
		SV_{BSA} LV_{BSA}	$\boldsymbol{SV_{BSA}=SV/BSA}$ $\boldsymbol{LV_{BSA}=LV/BSA}$ *volume(ml),body surface area(m^2)*	ICG≥20%: ≤705.8 mL/m^2 ICG≥20%: >156.8mL/m^2	

Abbreviation: PRLV, percentage of remnant liver volume; pRLV, predicted remnant liver volume; pTLV, predicted total liver volume; SI, spleen index; PHT, portal hypertension; ECV, extracellular volume; HE, hepatic enhancement; AE, aortic enhancement; Hct, hematocrit level; PVP, portal vein phase; DP, 3minutes delayed phase; SV, spleen volume; LV, liver volume; BSA, body surface area.

evaluation. Additionally, the development of integrated automated algorithms incorporating multiparametric CT data with machine learning techniques could significantly improve standardization, reduce interobserver variability, and optimize clinical workflow, thereby facilitating wider adoption in routine practice.

The applications of non-invasive US examination in liver fibrosis and cirrhosis are well developed (*117*). Common US evaluating dimensions include hepatic and splenic morphology, stiffness changes, and hemodynamic alterations (*118*). Transient elastography and shear wave elastography represent two main technologies in organ stiffness measurement, with substantial evidence supporting their accuracy and efficiency in the early diagnosis and evaluation of liver fibrosis (*119-121*). These elastographic methods also demonstrate clinical utility in assessing splenomegaly, a hallmark complication of PHT, thereby providing valuable diagnostic information to evaluate PHT and cirrhosis (*122,123*). Moreover, recent studies revealed that the US-measured stiffness and volume of liver and spleen could provide predictive information of PHLF (*124,125*). Hemodynamic alteration is another key manifestation of PHT and cirrhosis, which demonstrates increased hepatic venous pressure gradient, decreased portal vein velocity, and portal and total hepatic perfusion. Some studies reported that the doppler US was a potential tool to preliminarily evaluate the portal vein velocity to provide the degree of PHT (*126,127*).

Conventional MRI provides superior soft-tissue contrast for morphological information (*118*), while advanced MR techniques provide functional assessment capabilities. The ECV measured by MR T1 mapping technology could also be useful in the identification and assessment of cirrhosis (*128*). MR elastography has emerged as a particularly promising assessment for liver fibrosis, demonstrating superior sensitivity and specificity in identification of hepatic cirrhosis compared to other non-invasive methods (*129,130*). However, EOB-MRI, while providing excellent hepatobiliary lesion characterization in normal liver function (*46*), appears to have limited diagnostic performance in patients with CIED due to impaired hepatic contrast agent uptake (*37,46*) This limitation significantly reduces its clinical utility in such populations despite its otherwise excellent imaging capabilities.

6. Conclusion

CIED represents a rare dye metabolism disorder characterized solely by markedly elevated plasma ICG retention without other distinctive clinical or laboratory findings. While current research has elucidated the fundamental mechanisms underlying CIED, significant knowledge gaps remain regarding its precise pathogenesis in certain congenital hyperbilirubinemia disorders and its inheritance patterns. The published literature on CIED epidemiology, clinical characteristics, management strategies, and prognostic outcomes is limited not only by small sample sizes but also by the inherently low amount of evidence. Given the extreme rarity of CIED, most available data are derived from isolated case reports and small retrospective case series, which are susceptible to selection bias, reporting bias, and incomplete follow-up. To date, there is an absence of large-scale population-based epidemiological investigations and robust prospective cohort studies that could more accurately define incidence, risk factors, and long-term outcomes. Additionally, no convincing *in vivo* experimental models have been established to validate the underlying biological processes, limiting mechanistic interpretation and causal inference. Moreover, another important limitation concerns geographic concentration. Nearly all reported cases originate from Japan and China. The lack of data from other ethnic and geographic populations substantially restricts the assessment of global generalizability. Potential ethnic, genetic, environmental, or practice-related differences cannot currently be evaluated. Future efforts should focus on multinational collaborative investigations and mechanistic studies to clarify epidemiology, validate pathophysiology, and improve risk stratification. Basic research should prioritize the development of reproducible *in vivo* models incorporating susceptibility backgrounds, coupled with intervention and biodistribution studies, to validate causality and define actionable mechanistic targets.

Our review identifies several key modalities for differentiating CIED and supplementing HFR assessment. First, the application and utility of ^{99m}Tc-GSA liver scintigraphy has gained relatively considerable validation. Next, the serum biomarkers and relevant clinical scores like the ALBI scores are quite useful. Finally, most imaging examinations, including CT, US and MR, generally focus on the differentiation and evaluation of cirrhosis and PHT, and provide detailed anatomy information of liver and lesions. Several of them provide assessment of HFR. CT is widely applied due to its affordability and rich information, making it an indispensable examination in CIED. Notably, due to the impaired lesion detectability observed in CIED patients, it is lamentable that the utility of EOB-MRI is rather limited. Based on existing findings, we proposed a strategy to cope with unexplained high ICG retention patients (Figure 4). In our perspective, this strategy would be simple to apply in clinical practice and helpful for such patients. However, it demands further validation. Nowadays, with recent advancement of next-generation screening (NGS), molecular testing technology is playing an increasingly vital role in precise surgery. Genetic testing, whether based on blood or pathological samples, not only provides a detailed molecular diagnosis but also guides perioperative targeted therapy and immunotherapy in different types of malignancy (*131-133*). Although the molecular diagnosis and therapy of HCC remains

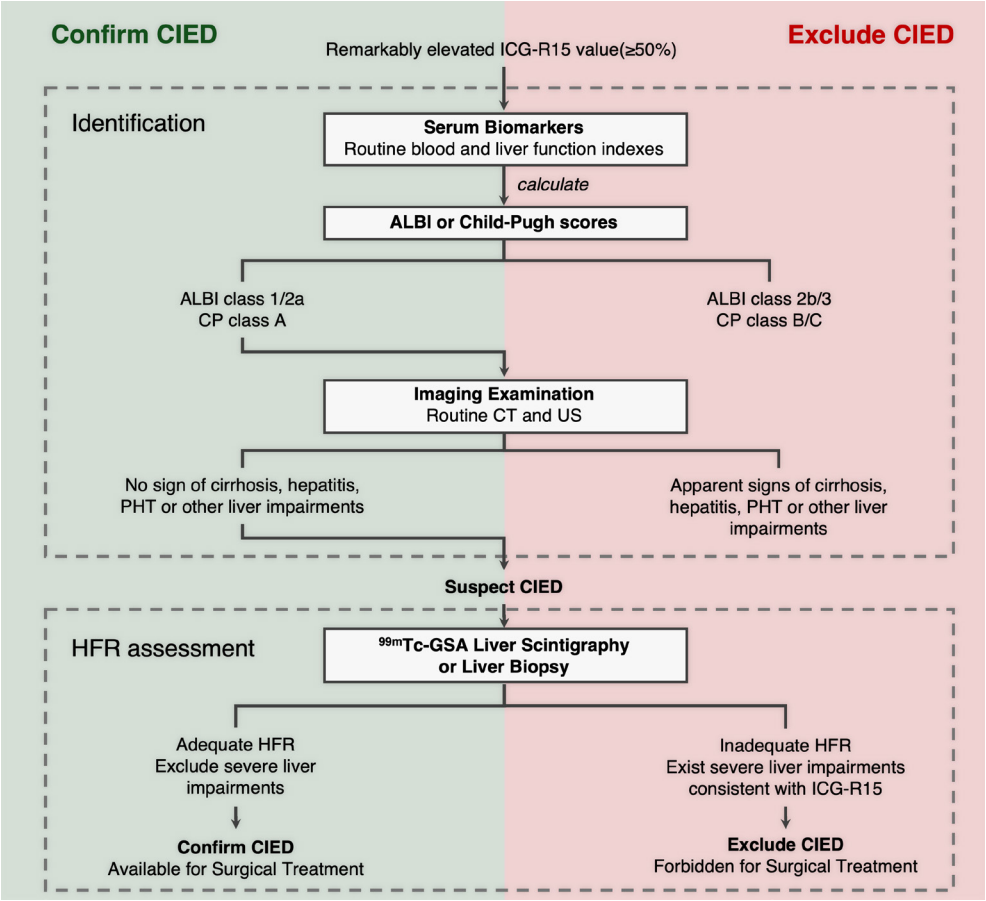

Figure 4. A strategy to cope with unexplained high ICG retention patients. CIED: constitutional indocyanine green excretory defect, ICG-R15: plasma indocyanine green retention rate at 15 minutes, ALBI: albumin-bilirubin scores, CT: computer tomography, US: ultrasonography, PHT: portal hypertension, HFR: hepatic functional reserve, ^{99m}Tc-GSA liver scintigraphy: ^{99m}Tc-Galactosyl human Serum Albumin liver scintigraphy.

divergent, hopefully such high-throughput sequencing technologies could improve *SLCO1B3* mutation screening, thus reducing the cost of CIED diagnosis and assisting with clinical decision-making (*134*).

The expanding use of ICG tests in hepatic surgery will likely increase CIED detection rates, underscoring the importance of reliable diagnostic and assessment protocols. However, the rarity of CIED has constrained study sizes, necessitating external validation of current findings in larger populations. Future research should prioritize multicenter studies to validate existing diagnostic algorithms, develop of standardized assessment protocols, and investigate novel functional imaging parameters. The proposed diagnostic strategy balances clinical practicality with comprehensive evaluation, though its implementation requires further validation. As hepatic surgery advances, establishing evidence-based approaches for CIED management will become increasingly crucial for optimal patient care and surgical outcomes.

Acknowledgements

We would like to appreciate all the staff in our team for their valuable support.

Funding: This work was supported by a grant from the National Key Research and Development Program of China (No. 2023YFB3810004 for Huang J).

Conflict of Interest: The authors have no conflicts of interest to disclose.

References

1. Dong J, Zheng S, Chen X, Dou K, Fan J, Bie P, Geng X, Lv W. Consensus on evaluation of hepatic functional reserve before hepatectomy (2011 edition). Chin J Dig Surg. 2011; 10:20-25.
2. Fan ST. Liver functional reserve estimation: state of the art and relevance for local treatments: the Eastern perspective. J Hepatobiliary Pancreat Sci. 2010; 17:380-384.
3. Durand F, Valla D. Assessment of prognosis of cirrhosis. Semin Liver Dis. 2008; 28:110-122.
4. Garcea G, Ong SL, Maddern GJ. Predicting liver failure following major hepatectomy. Dig Liver Dis. 2009; 41:798-806.
5. Hoekstra LT, de Graaf W, Nibourg GA, Heger M, Bennink RJ, Stieger B, van Gulik TM. Physiological and biochemical basis of clinical liver function tests: a review.

Ann Surg. 2013; 257:27-36.
6. Woreta TA, Alqahtani SA. Evaluation of abnormal liver tests. Med Clin North Am. 2014; 98:1-16.
7. Kaibori M, Matsui K, Shimada M, Kubo S, Hasegawa K. Update on perioperative management of patients undergoing surgery for liver cancer. Ann Gastroenterol Surg. 2022; 6:344-354.
8. Lau H, Man K, Fan ST, Yu WC, Lo CM, Wong J. Evaluation of preoperative hepatic function in patients with hepatocellular carcinoma undergoing hepatectomy. Br J Surg. 1997; 84:1255-1259.
9. Cherrick GR, Stein SW, Leevy CM, Davidson CS. Indocyanine green: observations on its physical properties, plasma decay, and hepatic extraction. J Clin Invest. 1960; 39:592-600.
10. Caesar J, Shaldon S, Chiandussi L, Guevara L, Sherlock S. The use of indocyanine green in the measurement of hepatic blood flow and as a test of hepatic function. Clin Sci. 1961; 21:43-57.
11. Miyagawa S, Makuuchi M, Kawasaki S, Kakazu T. Criteria for safe hepatic resection. Am J Surg. 1995; 169:589-594.
12. Namihisa T, Nambu M, Kobayashi N, Kuroda H. The constitutional indocyanine green excretory defect--report of four cases. Gastroenterol Jpn. 1975; 10:70-76.
13. Okuda K, Ohkubo H, Musha H, Kotoda K, Abe H, Tanikawa K. Marked delay in indocyanine green plasma clearance with a near-normal bromosulphophthalein retention test: a constitutional abnormality? Gut. 1976; 17:588-594.
14. Namihisa T, Nambu M, Kobayashi N, Kuroda H. Nine cases with marked retention of indocyanine green test and normal sulfobromophthalein test without abnormal liver histology: constitutional indocyanine green excretory defect. Hepatogastroenterology. 1981; 28:6-12.
15. Ott P. Hepatic elimination of indocyanine green with special reference to distribution kinetics and the influence of plasma protein binding. Pharmacol Toxicol. 1998; 83 Suppl 2:1-48.
16. de Graaf W, Häusler S, Heger M, van Ginhoven TM, van Cappellen G, Bennink RJ, Kullak-Ublick GA, Hesselmann R, van Gulik TM, Stieger B. Transporters involved in the hepatic uptake of (99m)Tc-mebrofenin and indocyanine green. J Hepatol. 2011; 54:738-745.
17. Huet PM, Du Reau A, Marleau D. Arterial and portal blood supply in cirrhosis: a functional evaluation. Gut. 1979; 20:792-796.
18. Kwon AH, Ha-Kawa SK, Uetsuji S, Inoue T, Matsui Y, Kamiyama Y. Preoperative determination of the surgical procedure for hepatectomy using technetium-99m-galactosyl human serum albumin (99mTc-GSA) liver scintigraphy. Hepatology. 1997; 25:426-429.
19. Cui Y, König J, Leier I, Buchholz U, Keppler D. Hepatic uptake of bilirubin and its conjugates by the human organic anion transporter SLC21A6. J Biol Chem. 2001; 276:9626-9630.
20. Geier A, Wagner M, Dietrich CG, Trauner M. Principles of hepatic organic anion transporter regulation during cholestasis, inflammation and liver regeneration. Biochim Biophys Acta. 2007; 1773:283-308.
21. Adachi Y, Yamamoto T, Onishi S, Tanaka S, Wakisaka G. The discrepancy between plasma clearance tests of indocyanine green (ICG) and sulfobromophthalein (BSP): --report of cases and a study of ICG-binding pattern of serum proteins. Gastroenterol Jpn. 1976; 11:75-87.
22. Takase S, Takada A, Matsuda Y. Studies on the pathogenesis of the constitutional excretory defect of indocyanine green. Gastroenterol Jpn. 1982; 17:301-309.
23. Taketazu F, Sanada I, Ngamatsu N, Mukai R, Suetomo Y, Toyoda N, Takada M, Hida K, Kubota K, Maezawa M. A case of hereditary elliptocytosis associated with constitutional indocyanine green excretory defect. Jpn J Med. 1984; 23:139-143.
24. Gotoh K, Konaga E, Takeuchi H, Mano S, Kohno H. A case of biliary cystadenocarcinoma arising in the liver with a congenital retention of indocyanine green. Acta Med Okayama. 1992; 46:389-393.
25. Ikejima K, Ichikawa S, Kitamura T, Watanabe S, Hirose M, Yokoi Y, Uchida S, Oide H, Suzuki H, Kitami N. Marked retention of indocyanine green and sulfobromophthalein with chronic persistent hepatitis. J Gastroenterol Hepatol. 1993; 8:489-494.
26. Nambu M, Namihisa T. Hepatic transport of serum bilirubin, bromsulfophthalein, and indocyanine green in patients with congenital non-hemolytic hyperbilirubinemia and patients with constitutional indocyanine green excretory defect. J Gastroenterol. 1996; 31:228-236.
27. Hanazaki K, Wakabayashi M, Makiuchi A, Igarashi J, Sodeyama H, Wada S, Amano J. Hepatectomy of cavernous hemangioma with constitutional indocyanine green excretory defect. Hepatogastroenterology. 2000; 47:1719-1721.
28. Yamanaka N, Shimizu S, Chijiiwa K, Nishiyama K, Noshiro H, Yamaguchi K, Tanaka M. Hepatectomy and marked retention of indocyanine green and bromosulfophtalein. Hepatogastroenterology. 2001; 48:1450-1452.
29. Kadono J, Kumemura H, Nishida S, Nakamura N, Gejima K, Nakajo M, Tsuchimochi S, Matsumoto J, Hamada N, Sakata R. 99mTc-DTPA-galactosyl-human-serum-albumin liver scintigraphy for evaluating hepatic functional reserve before hepatectomy in a patient with indocyanine green excretory defect: report of a case. Surg Today. 2006; 36:481-484.
30. Maeda H, Okabayashi T, Kobayashi M, Sugimoto T, Namikawa T, Okamoto K, Araki K. Hepatectomy for hepatocellular carcinoma with indocyanine green excretory defect: a case report. Hepatogastroenterology. 2007; 54:1810-1812.
31. Aoki H, Morihiro T, Arata T, Kanaya N, Takeda S, Ninomiya T, Seita M, Katsuda K, Tanakaya K, Takeuchi H. Hepatectomy in a hepatocellular carcinoma case with Dubin-Johnson syndrome and indocyanine green excretory defect. Clin J Gastroenterol. 2013; 6:69-74.
32. Imada S, Kobayashi T, Kitao A, Matsui O, Hashimoto M, Ide K, Ishiyama K, Arihiro K, Tashiro H, Ohdan H. Central bisectionectomy for hepatocellular carcinoma in a patient with indocyanine green excretory defect associated with reduced expression of the liver transporter. Surg Case Rep. 2016; 2:89.
33. Kagawa T, Adachi Y, Hashimoto N, Mitsui H, Ohashi T, Yoneda M, Hasegawa I, Hirose S, Tsuruya K, Anzai K, Mine T. Loss of organic anion transporting polypeptide 1B3 function causes marked delay in indocyanine green clearance without any clinical symptoms. Hepatology. 2017; 65:1065-1068.
34. Nakatake R, Ishizaki M, Miyasaka C, Matsui K, Kaibori M. Hepatectomy in a case of hepatocellular carcinoma with constitutional indocyanine green excretory defect. Int J Surg Case Rep. 2018; 53:231-234.

35. Sumiyoshi T, Okabayashi T, Negoro Y, Hata Y, Noda Y, Sui K, Iwata J, Matsumoto M. (99m)Tc-GSA SPECT/CT fusion imaging for hepatectomy candidates with extremely deteriorated ICG value. Jpn J Radiol. 2018; 36:537-543.
36. Anzai K, Tsuruya K, Morimachi M, Arase Y, Hirose S, Hirabayashi K, Adachi Y, Kagawa T. The Impact of a Heterozygous SLCO1B3 Null Variant on the Indocyanine Green Retention Test. J Pharm Sci. 2020; 109:3206-3209.
37. Masuoka S, Nasu K, Takahashi H, Kitao A, Sakai M, Ishiguro T, Saida T, Minami M. Impaired lesion detectability on gadoxetic acid-enhanced MR imaging in indocyanine green excretory defect: case series of three patients. Jpn J Radiol. 2020; 38:997-1003.
38. Tanimoto M, Nishioka Y, Inagaki Y, Kokudo T, Ishizawa T, Arita J, Akamatsu N, Kaneko J, Hasegawa K. Genetic alteration of SLCO1B3 defines constitutional indocyanine green excretory defect in patients who underwent hepatectomy. Hepatol Res. 2024.
39. Morikawa T, Wakui Y, Hasegawa Y, Sugisawa N, Kimura S, Hirashima T, Kinouchi M, Iwasashi H. Laparoscopic Anatomical Liver Resection for the Patients With Constitutional Indocyanine Green Excretory Defect: A Case Report. Asian J Endosc Surg. 2025; 18:e13415.
40. Liu W, Chen LJ, Jiang Y, Xu LJ, Qiu X. Hepatocellular carcinoma with indocyanine green excretory defect: a case report and review of the literature. J Int Med Res. 2021; 49:3000605211004025.
41. Ishigami Y, Masuzawa M, Miyoshi E, Kato M, Tamura K, Kanda M, Awazu K, Taniguchi K, Kurita M, Hayashi N. Clinical applications of ICG Finger Monitor in patients with liver disease. J Hepatol. 1993; 19:232-240.
42. Soderquist C, Bagg A. Hereditary elliptocytosis. Blood. 2013; 121:3066.
43. Kawasaki H, Kimura N, Irisa T, Hirayama C. Dye clearance studies in Rotor's syndrome. Am J Gastroenterol. 1979; 71:380-388.
44. Makuuchi M, Kosuge T, Takayama T, Yamazaki S, Kakazu T, Miyagawa S, Kawasaki S. Surgery for small liver cancers. Semin Surg Oncol. 1993; 9:298-304.
45. Tanimoto A, Lee JM, Murakami T, Huppertz A, Kudo M, Grazioli L. Consensus report of the 2nd International Forum for Liver MRI. Eur Radiol. 2009; 19 Suppl 5:S975-989.
46. Huppertz A, Balzer T, Blakeborough A, Breuer J, Giovagnoni A, Heinz-Peer G, Laniado M, Manfredi RM, Mathieu DG, Mueller D, Reimer P, Robinson PJ, Strotzer M, Taupitz M, Vogl TJ. Improved detection of focal liver lesions at MR imaging: multicenter comparison of gadoxetic acid-enhanced MR images with intraoperative findings. Radiology. 2004; 230:266-275.
47. Tsurusaki M, Sofue K, Murakami T. Current evidence for the diagnostic value of gadoxetic acid-enhanced magnetic resonance imaging for liver metastasis. Hepatol Res. 2016; 46:853-861.
48. Nigam SK, Bush KT, Martovetsky G, Ahn SY, Liu HC, Richard E, Bhatnagar V, Wu W. The organic anion transporter (OAT) family: A systems biology perspective. Physiol Rev. 2015; 95:83-123.
49. Kroll T, Prescher M, Smits SHJ, Schmitt L. Structure and Function of Hepatobiliary ATP Binding Cassette Transporters. Chem Rev. 2021; 121:5240-5288.
50. Tan X, Xiang Y, Shi J, Chen L, Yu D. Targeting NTCP for liver disease treatment: A promising strategy. J Pharm Anal. 2024; 14:100979.
51. Hagenbuch B, Stieger B, Locher KP. Organic anion transporting polypeptides: Pharmacology, toxicology, structure, and transport mechanisms. Pharmacol Rev. 2025; 77:100023.
52. Sekine T, Cha SH, Endou H. The multispecific organic anion transporter (OAT) family. Pflugers Arch. 2000; 440:337-350.
53. Hagenbuch B, Meier PJ. Organic anion transporting polypeptides of the OATP/ SLC21 family: phylogenetic classification as OATP/ SLCO superfamily, new nomenclature and molecular/functional properties. Pflugers Arch. 2004; 447:653-665.
54. König J, Seithel A, Gradhand U, Fromm MF. Pharmacogenomics of human OATP transporters. Naunyn Schmiedebergs Arch Pharmacol. 2006; 372:432-443.
55. Ho RH, Tirona RG, Leake BF, Glaeser H, Lee W, Lemke CJ, Wang Y, Kim RB. Drug and bile acid transporters in rosuvastatin hepatic uptake: function, expression, and pharmacogenetics. Gastroenterology. 2006; 130:1793-1806.
56. Vaz FM, Paulusma CC, Huidekoper H, de Ru M, Lim C, Koster J, Ho-Mok K, Bootsma AH, Groen AK, Schaap FG, Oude Elferink RP, Waterham HR, Wanders RJ. Sodium taurocholate cotransporting polypeptide (SLC10A1) deficiency: conjugated hypercholanemia without a clear clinical phenotype. Hepatology. 2015; 61:260-267.
57. van de Steeg E, Stránecký V, Hartmannová H, *et al*. Complete OATP1B1 and OATP1B3 deficiency causes human Rotor syndrome by interrupting conjugated bilirubin reuptake into the liver. J Clin Invest. 2012; 122:519-528.
58. Vítek L, Tiribelli C. Gilbert's syndrome revisited. J Hepatol. 2023; 79:1049-1055.
59. Martin JF, Vierling JM, Wolkoff AW, Scharschmidt BF, Vergalla J, Waggoner JG, Berk PD. Abnormal hepatic transport of indocyanine green in Gilbert's syndrome. Gastroenterology. 1976; 70:385-391.
60. Fahrmayr C, Fromm MF, König J. Hepatic OATP and OCT uptake transporters: their role for drug-drug interactions and pharmacogenetic aspects. Drug Metab Rev. 2010; 42:380-401.
61. Alam K, Crowe A, Wang X, Zhang P, Ding K, Li L, Yue W. Regulation of Organic Anion Transporting Polypeptides (OATP) 1B1- and OATP1B3-Mediated Transport: An Updated Review in the Context of OATP-Mediated Drug-Drug Interactions. Int J Mol Sci. 2018; 19:855.
62. Hagenbuch B, Stieger B. The SLCO (former SLC21) superfamily of transporters. Mol Aspects Med. 2013; 34:396-412.
63. Sato T, Yamaguchi H, Kogawa T, Abe T, Mano N. Organic anion transporting polypeptides 1B1 and 1B3 play an important role in uremic toxin handling and drug-uremic toxin interactions in the liver. J Pharm Pharm Sci. 2014; 17:475-484.
64. Ikema S, Takumi S, Maeda Y, Kurimoto T, Bohda S, Chigwechokha PK, Sugiyama Y, Shiozaki K, Furukawa T, Komatsu M. Okadaic acid is taken-up into the cells mediated by human hepatocytes transporter OATP1B3. Food Chem Toxicol. 2015; 83:229-236.
65. Schulte RR, Ho RH. Organic Anion Transporting Polypeptides: Emerging Roles in Cancer Pharmacology. Mol Pharmacol. 2019; 95:490-506.
66. Wang J, Gan C, Qi X, Lebre MC, Schinkel AH. Human organic anion transporting polypeptide (OATP) 1B3 and mouse OATP1A/1B affect liver accumulation of

Ochratoxin A in mice. Toxicol Appl Pharmacol. 2020; 401:115072.
67. Wissler EH. Identifying a long standing error in single-bolus determination of the hepatic extraction ratio for indocyanine green. Eur J Appl Physiol. 2011; 111:641-646.
68. Kaibori M, Ha-Kawa SK, Maehara M, Ishizaki M, Matsui K, Sawada S, Kwon AH. Usefulness of Tc-99m-GSA scintigraphy for liver surgery. Ann Nucl Med. 2011; 25:593-602.
69. Stockert RJ, Morell AG. Hepatic binding protein: the galactose-specific receptor of mammalian hepatocytes. Hepatology. 1983; 3:750-757.
70. Okabayashi T, Shima Y, Morita S, Shimada Y, Sumiyoshi T, Sui K, Iwata J, Iiyama T. Liver Function Assessment Using Technetium 99m-Galactosyl Single-Photon Emission Computed Tomography/CT Fusion Imaging: A Prospective Trial. J Am Coll Surg. 2017; 225:789-797.
71. Sawamura T, Nakada H, Hazama H, Shiozaki Y, Sameshima Y, Tashiro Y. Hyperasialoglycoproteinemia in patients with chronic liver diseases and/or liver cell carcinoma. Asialoglycoprotein receptor in cirrhosis and liver cell carcinoma. Gastroenterology. 1984; 87:1217-1221.
72. Kondo M. Usefulness of 99mTc-GSA scintigraphy for estimation of residual hepatic functions and postoperative changes of HH15 and LHL15. Kaku Igaku. 2001; 38:191-200.
73. Iimuro Y, Kashiwagi T, Yamanaka J, Hirano T, Saito S, Sugimoto T, Watanabe S, Kuroda N, Okada T, Asano Y, Uyama N, Fujimoto J. Preoperative estimation of asialoglycoprotein receptor expression in the remnant liver from CT/99mTc-GSA SPECT fusion images correlates well with postoperative liver function parameters. J Hepatobiliary Pancreat Sci. 2010; 17:673-681.
74. Kudo M, Todo A, Ikekubo K, Yamamoto K, Vera DR, Stadalnik RC. Quantitative assessment of hepatocellular function through *in vivo* radioreceptor imaging with technetium 99m galactosyl human serum albumin. Hepatology. 1993; 17:814-819.
75. Nagayama Y, Hokamura M, Taguchi N, Yokota Y, Osaki T, Ogasawara K, Shiraishi S, Yoshida R, Harai R, Kidoh M, Oda S, Nakaura T, Hirai T. Liver function estimation using multiphase hepatic CT: diagnostic performance of iodine-uptake and volumetric parameters. Eur Radiol. 2025; 35:5781–5791.
76. Mao Y, Du S, Ba J, *et al*. Using Dynamic 99mTc-GSA SPECT/CT fusion images for hepatectomy planning and postoperative liver failure prediction. Ann Surg Oncol. 2015; 22:1301-1307.
77. Bennink RJ, Dinant S, Erdogan D, Heijnen BH, Straatsburg IH, van Vliet AK, van Gulik TM. Preoperative assessment of postoperative remnant liver function using hepatobiliary scintigraphy. J Nucl Med. 2004; 45:965-971.
78. Trauner M, Meier PJ, Boyer JL. Molecular pathogenesis of cholestasis. N Engl J Med. 1998; 339:1217-1227.
79. Erdogan D, Heijnen BH, Bennink RJ, Kok M, Dinant S, Straatsburg IH, Gouma DJ, van Gulik TM. Preoperative assessment of liver function: A comparison of 99mTc-Mebrofenin scintigraphy with indocyanine green clearance test. Liver Int. 2004; 24:117-123.
80. Bakos A, Libor L, Urbán S, Géczi T, Bukva M, Hőhn J, Lázár G, Nagy A, Farkas I, Sipka G, Pávics L, Besenyi Z. Dynamic [(99m)Tc]Tc-mebrofenin SPECT/CT in preoperative planning of liver resection: a prospective study. Sci Rep. 2024; 14:30305.
81. Johnson PJ, Berhane S, Kagebayashi C, *et al*. Assessment of liver function in patients with hepatocellular carcinoma: a new evidence-based approach-the ALBI grade. J Clin Oncol. 2015; 33:550-558.
82. Hiraoka A, Kumada T, Michitaka K, Kudo M. Newly Proposed ALBI Grade and ALBI-T Score as Tools for Assessment of Hepatic Function and Prognosis in Hepatocellular Carcinoma Patients. Liver Cancer. 2019; 8:312-325.
83. Reig M, Forner A, Rimola J, *et al*. BCLC strategy for prognosis prediction and treatment recommendation: The 2022 update. J Hepatol. 2022; 76:681-693.
84. Toyoda H, Johnson PJ. The ALBI score: From liver function in patients with HCC to a general measure of liver function. JHEP Rep. 2022; 4:100557.
85. Japan Lcsgo. The general rules for the clinical and pathological study of primary liver cancer. The 5th edition. 2009; 24.
86. Hiraoka A, Kumada T, Michitaka K, *et al*. Usefulness of albumin-bilirubin grade for evaluation of prognosis of 2584 Japanese patients with hepatocellular carcinoma. J Gastroenterol Hepatol. 2016; 31:1031-1036.
87. Hiraoka A, Michitaka K, Kumada T, Izumi N, Kadoya M, Kokudo N, Kubo S, Matsuyama Y, Nakashima O, Sakamoto M, Takayama T, Kokudo T, Kashiwabara K, Kudo M. Validation and Potential of Albumin-Bilirubin Grade and Prognostication in a Nationwide Survey of 46,681 Hepatocellular Carcinoma Patients in Japan: The Need for a More Detailed Evaluation of Hepatic Function. Liver Cancer. 2017; 6:325-336.
88. Zhong CR, Qiu JL, Yuan YC, Qiu ZY, Li K, Wang CW, Shi YX, Li KR, Lin Z, Huang ZK, He W, Li BK, Yuan YF. A detailed assessment of liver function in patients with hepatocellular carcinoma *via* the modified albumin-bilirubin (mALBI) grade. Am J Cancer Res. 2022; 12:2711-2720.
89. Hiraoka A, Kumada T, Tsuji K, *et al*. Validation of Modified ALBI Grade for More Detailed Assessment of Hepatic Function in Hepatocellular Carcinoma Patients: A Multicenter Analysis. Liver Cancer. 2019; 8:121-129.
90. Kariyama K, Nouso K, Hiraoka A, *et al*. EZ-ALBI Score for Predicting Hepatocellular Carcinoma Prognosis. Liver Cancer. 2020; 9:734-743.
91. Liu PH, Hsu CY, Hsia CY, Lee YH, Chiou YY, Huang YH, Lee FY, Lin HC, Hou MC, Huo TI. ALBI and PALBI grade predict survival for HCC across treatment modalities and BCLC stages in the MELD Era. J Gastroenterol Hepatol. 2017; 32:879-886.
92. Lu LH, Zhang YF, Mu-Yan C, Kan A, Zhong XP, Mei J, Ling YH, Li SH, Shi M, Wei W, Guo RP. Platelet-albumin-bilirubin grade: Risk stratification of liver failure, prognosis after resection for hepatocellular carcinoma. Dig Liver Dis. 2019; 51:1430-1437.
93. Wang Q, Qiao W, Zhang H, Liu B, Li J, Zang C, Mei T, Zheng J, Zhang Y. Nomogram established on account of Lasso-Cox regression for predicting recurrence in patients with early-stage hepatocellular carcinoma. Front Immunol. 2022; 13:1019638.
94. Wang Q, Sheng S, Xiong Y, Han M, Jin R, Hu C. Machine learning-based model for predicting tumor recurrence after interventional therapy in HBV-related hepatocellular carcinoma patients with low preoperative platelet-albumin-bilirubin score. Front Immunol. 2024; 15:1409443.
95. Simpson AL, Geller DA, Hemming AW, Jarnagin WR,

Clements LW, D'Angelica MI, Dumpuri P, Gönen M, Zendejas I, Miga MI, Stefansic JD. Liver planning software accurately predicts postoperative liver volume and measures early regeneration. J Am Coll Surg. 2014; 219:199-207.
96. Zou H, Wen Y, Yuan K, Miao XY, Xiong L, Liu KJ. Combining albumin-bilirubin score with future liver remnant predicts post-hepatectomy liver failure in HBV-associated HCC patients. Liver Int. 2018; 38:494-502.
97. Wai CT, Greenson JK, Fontana RJ, Kalbfleisch JD, Marrero JA, Conjeevaram HS, Lok AS. A simple noninvasive index can predict both significant fibrosis and cirrhosis in patients with chronic hepatitis C. Hepatology. 2003; 38:518-526.
98. Hung HH, Su CW, Lai CR, Chau GY, Chan CC, Huang YH, Huo TI, Lee PC, Kao WY, Lee SD, Wu JC. Fibrosis and AST to platelet ratio index predict post-operative prognosis for solitary small hepatitis B-related hepatocellular carcinoma. Hepatol Int. 2010; 4:691-699.
99. Shen SL, Fu SJ, Chen B, Kuang M, Li SQ, Hua YP, Liang LJ, Guo P, Hao Y, Peng BG. Preoperative aspartate aminotransferase to platelet ratio is an independent prognostic factor for hepatitis B-induced hepatocellular carcinoma after hepatic resection. Ann Surg Oncol. 2014; 21:3802-3809.
100. Luo H, Li C, Chen L. Preoperative albumin-bilirubin grade combined with aspartate aminotransferase-to-platelet count ratio index predict outcomes of patients with hepatocellular carcinoma within Milan criteria after liver resection. Biosci Trends. 2019; 13:176-181.
101. Starlinger P, Ubl DS, Hackl H, Starlinger J, Nagorney DM, Smoot RL, Habermann EB, Cleary SP. Combined APRI/ALBI score to predict mortality after hepatic resection. BJS Open. 2021; 5:zraa043.
102. Vallet-Pichard A, Mallet V, Nalpas B, Verkarre V, Nalpas A, Dhalluin-Venier V, Fontaine H, Pol S. FIB-4: an inexpensive and accurate marker of fibrosis in HCV infection. Comparison with liver biopsy and fibrotest. Hepatology. 2007; 46:32-36.
103. Toyoda H, Kumada T, Tada T, Kaneoka Y, Maeda A. A laboratory marker, FIB-4 index, as a predictor for long-term outcomes of hepatocellular carcinoma patients after curative hepatic resection. Surgery. 2015; 157:699-707.
104. Zhou P, Chen B, Miao XY, Zhou JJ, Xiong L, Wen Y, Zou H. Comparison of FIB-4 Index and Child-Pugh Score in Predicting the Outcome of Hepatic Resection for Hepatocellular Carcinoma. J Gastrointest Surg. 2020; 24:823-831.
105. Sahani D, Mehta A, Blake M, Prasad S, Harris G, Saini S. Preoperative hepatic vascular evaluation with CT and MR angiography: implications for surgery. Radiographics. 2004; 24:1367-1380.
106. Kubota K, Makuuchi M, Kusaka K, Kobayashi T, Miki K, Hasegawa K, Harihara Y, Takayama T. Measurement of liver volume and hepatic functional reserve as a guide to decision-making in resectional surgery for hepatic tumors. Hepatology. 1997; 26:1176-1181.
107. Shukla A, Giri S. Portal Vein Thrombosis in Cirrhosis. J Clin Exp Hepatol. 2022; 12:965-979.
108. Heo S, Lee SS, Choi SH, Kim DW, Park HJ, Kim SY, Lee SJ, Kim KM, Shin YM. CT Rule-in and Rule-out Criteria for Clinically Significant Portal Hypertension in Chronic Liver Disease. Radiology. 2023; 309:e231208.
109. Tu R, Xia LP, Yu AL, Wu L. Assessment of hepatic functional reserve by cirrhosis grading and liver volume measurement using CT. World J Gastroenterol. 2007; 13:3956-3961.
110. Son JH, Lee SS, Lee Y, Kang BK, Sung YS, Jo S, Yu E. Assessment of liver fibrosis severity using computed tomography-based liver and spleen volumetric indices in patients with chronic liver disease. Eur Radiol. 2020; 30:3486-3496.
111. Yan C, Han X, Liang X, Jia J, Xu Y, Zhao L. Non-invasive evaluation of esophageal varices in patients with liver cirrhosis using low-dose splenic perfusion CT. Eur J Radiol. 2022; 152:110326.
112. Romero-Cristóbal M, Clemente-Sánchez A, Ramón E, *et al*. CT-derived liver and spleen volume accurately diagnose clinically significant portal hypertension in patients with hepatocellular carcinoma. JHEP Rep. 2023; 5:100645.
113. Bak S, Kim JE, Bae K, Cho JM, Choi HC, Park MJ, Choi HY, Shin HS, Lee SM, Kim HO. Quantification of liver extracellular volume using dual-energy CT: utility for prediction of liver-related events in cirrhosis. Eur Radiol. 2020; 30:5317-5326.
114. Morita K, Nishie A, Ushijima Y, Takayama Y, Fujita N, Kubo Y, Ishimatsu K, Yoshizumi T, Maehara J, Ishigami K. Noninvasive assessment of liver fibrosis by dual-layer spectral detector CT. Eur J Radiol. 2021; 136:109575.
115. Varenika V, Fu Y, Maher JJ, Gao D, Kakar S, Cabarrus MC, Yeh BM. Hepatic fibrosis: evaluation with semiquantitative contrast-enhanced CT. Radiology. 2013; 266:151-158.
116. Nagayama Y, Kato Y, Inoue T, Nakaura T, Oda S, Kidoh M, Ikeda O, Hirai T. Liver fibrosis assessment with multiphasic dual-energy CT: diagnostic performance of iodine uptake parameters. Eur Radiol. 2021; 31:5779-5790.
117. Barr RG, Wilson SR, Rubens D, Garcia-Tsao G, Ferraioli G. Update to the Society of Radiologists in Ultrasound Liver Elastography Consensus Statement. Radiology. 2020; 296:263-274.
118. Duan T, Jiang HY, Ling WW, Song B. Noninvasive imaging of hepatic dysfunction: A state-of-the-art review. World J Gastroenterol. 2022; 28:1625-1640.
119. Sande JA, Verjee S, Vinayak S, Amersi F, Ghesani M. Ultrasound shear wave elastography and liver fibrosis: A Prospective Multicenter Study. World J Hepatol. 2017; 9:38-47.
120. Nguyen-Khac E, Thiele M, Voican C, *et al*. Non-invasive diagnosis of liver fibrosis in patients with alcohol-related liver disease by transient elastography: an individual patient data meta-analysis. Lancet Gastroenterol Hepatol. 2018; 3:614-625.
121. Selvaraj EA, Mózes FE, Jayaswal ANA, *et al*. Diagnostic accuracy of elastography and magnetic resonance imaging in patients with NAFLD: A systematic review and meta-analysis. J Hepatol. 2021; 75:770-785.
122. Berzigotti A, Seijo S, Arena U, Abraldes JG, Vizzutti F, García-Pagán JC, Pinzani M, Bosch J. Elastography, spleen size, and platelet count identify portal hypertension in patients with compensated cirrhosis. Gastroenterology. 2013; 144:102-111.e101.
123. Berzigotti A. Non-invasive evaluation of portal hypertension using ultrasound elastography. J Hepatol. 2017; 67:399-411.
124. Long H, Zhong X, Su L, Huang T, Duan Y, Ke W, Xie X, Lin M. Liver Stiffness Measured by Two-Dimensional Shear Wave Elastography for Predicting

Symptomatic Post-hepatectomy Liver Failure in Patients with Hepatocellular Carcinoma. Ann Surg Oncol. 2022; 29:327-336.
125. Cheng GW, Fang Y, Xue LY, Zhang Y, Xie XY, Qiao XH, Li XQ, Guo J, Ding H. Nomogram based on liver stiffness and spleen area with ultrasound for posthepatectomy liver failure: A multicenter study. World J Gastroenterol. 2024; 30:3314-3325.
126. Shastri M, Kulkarni S, Patell R, Jasdanwala S. Portal vein Doppler: a tool for non-invasive prediction of esophageal varices in cirrhosis. J Clin Diagn Res. 2014; 8:MC12-15.
127. Elkenawy YN, Elarabawy RA, Ahmed LM, Elsawy AA. Portal vein flow velocity as a possible fast noninvasive screening tool for esophageal varices in cirrhotic patients. JGH Open. 2020; 4:589-594.
128. Evrimler S, Swensson JK, Are VS, Tirkes T, Vuppalanchi R, Akisik F. Quantitative assessment of disease severity of primary sclerosing cholangitis with T1 mapping and extracellular volume imaging. Abdom Radiol (NY). 2021; 46:2433-2443.
129. Jhaveri KS, Hosseini-Nik H, Sadoughi N, Janssen H, Feld JJ, Fischer S, Menezes R, Cheung AC. The development and validation of magnetic resonance elastography for fibrosis staging in primary sclerosing cholangitis. Eur Radiol. 2019; 29:1039-1047.
130. Tafur M, Cheung A, Menezes RJ, Feld J, Janssen H, Hirschfield GM, Jhaveri KS. Risk stratification in primary sclerosing cholangitis: comparison of biliary stricture severity on MRCP versus liver stiffness by MR elastography and vibration-controlled transient elastography. Eur Radiol. 2020; 30:3735-3747.
131. Aleksakhina SN, Imyanitov EN. Cancer Therapy Guided by Mutation Tests: Current Status and Perspectives. Int J Mol Sci. 2021; 22:10931.
132. Tan AC, Tan DSW. Targeted Therapies for Lung Cancer Patients With Oncogenic Driver Molecular Alterations. J Clin Oncol. 2022; 40:611-625.
133. Casolino R, Beer PA, Chakravarty D, Davis MB, Malapelle U, Mazzarella L, Normanno N, Pauli C, Subbiah V, Turnbull C, Westphalen CB, Biankin AV. Interpreting and integrating genomic tests results in clinical cancer care: Overview and practical guidance. CA Cancer J Clin. 2024; 74:264-285.
134. Tsilimigras DI, Kurzrock R, Pawlik TM. Molecular Testing and Targeted Therapies in Hepatobiliary Cancers: A Review. JAMA Surg. 2025; 160:576-585.

Received February 2, 2026; Revised March 13, 2026; Accepted March 20, 2026.

*Address correspondence to:
Jiwei Huang and Haichuan Wang, Division of Liver Surgery, Department of General Surgery, West China Hospital, Sichuan University, #37 Guoxue Alley, Wuhou District, Chengdu 610041, Sichuan, China.
E-mail: huangjiwei@wchscu.cn (JW); haichuan.wang@wchscu.edu.cn (HW)

Released online in J-STAGE as advance publication March 25, 2026.

Review

DOI: 10.5582/bst.2026.01042

The orchestrated network of skin photoaging: From intercellular crosstalk to molecular signaling

Bingmin Li[1,2,§], Cong Ren[3,§], Lixia Zhang[4,*], Weijie Gu[2,*]

[1] Department of Dermatology, Fourth Medical Center of the Chinese PLA General Hospital, Beijing, China;
[2] Department of Dermatology, Air Force Medical Center, Fourth Military Medical University, Beijing, China;
[3] The Second Clinical Medical College, Chongqing Medical University, Chongqing, China;
[4] Department of Burns and Plastic Surgery, Fourth Medical Center of the Chinese PLA General Hospital, Beijing, China.

SUMMARY: Photoaging is a distinct form of pathological skin aging driven primarily by chronic ultraviolet (UV) radiation, which clinically manifests as wrinkles, dyspigmentation, and loss of elasticity. Although core molecular events induced by UV—such as oxidative stress and DNA damage—are relatively well-understood, there is still a lack of a systematic and integrated understanding of how diverse cell types in the skin collectively drive photoaging through complex interactive networks. This review systematically elaborates the cellular and molecular mechanisms underlying skin photoaging. The key pathways involved are examined, including oxidative stress, apoptosis, dysregulated autophagy, activation of inflammatory cascades, and degradation of the extracellular matrix (ECM). This review further details the pivotal roles of and reciprocal crosstalk among fibroblasts, keratinocytes, melanocytes, and various immune cells. By providing an integrated perspective on these interactions, this review outlines the cellular and molecular mechanism of UV-associated senescence, which uniquely integrates the roles of the immune microenvironment and cellular crosstalk, providing a roadmap for next-generation anti-photoaging strategies.

Keywords: skin photoaging, senescence-associated secretory phenotype (SASP), inflammaging, extracellular matrix remodeling, therapeutic targets

1. Introduction

Photoaging results from chronic and repeated exposure to ultraviolet (UV) radiation—primarily UVA and UVB—along with other environmental factors such as infrared and visible light. Clinically, it is characterized by wrinkles, skin laxity, roughness, dyspigmentation, and telangiectasia. This condition represents a distinct, exogenous form of pathological skin aging. In contrast to intrinsic aging, photoaging is largely confined to areas exposed to the sun including the face, neck, the dorsum of the hands, and the extensors of the forearms. Oxidative stress constitutes the central molecular mechanism underlying its progression.

Chronic sun exposure is a major etiological factor in skin aging, with studies attributing up to 80% of facial skin aging to UV exposure (*1*). Solar UV radiation (UVR) consists of three wavelength ranges: UVA (320–400 nm), UVB (280–320 nm), and UVC (100–280 nm). Although UVC carries the highest energy, it is predominantly absorbed by the Earth's ozone layer and thus poses minimal risk to human health. The biologically relevant UVR that reaches the Earth's surface consists mainly of UVB and UVA. UVB, characterized by its short wavelength and high energy, penetrates the skin to a depth of approximately 160–180 μm and is largely absorbed by the epidermis. It induces DNA damage *via* oxidative stress, leading to sunburn, erythema, and skin carcinogenesis. In contrast, UVA constitutes 90–95% of solar UVR and is considered the primary driver of photoaging (*2*). Despite its lower energy, UVA's longer wavelength enables deeper penetration, penetrating as deep as 1,000 μm into the dermis. Rather than causing direct DNA damage, UVA promotes reactive oxygen species (ROS)-mediated skin aging and pigmentation (*3,4*).

This review discusses the cellular and molecular mechanisms underlying skin photoaging. Special emphasis is placed on the orchestrating roles of cells—fibroblasts, keratinocytes, melanocytes, and immune cells—as they interact with each other and jointly drive the development of the disease. This work contributes to the systematic understanding of the mechanisms underlying photoaging.

2. The pathogenesis of skin photoaging

2.1. Oxidative stress injury

Oxygen can be enzymatically or non-enzymatically converted into reactive intermediates, collectively termed ROS. Major ROS include the superoxide anion (O_2^-), the hydroxyl radical (·OH), and hydrogen peroxide (H_2O_2). The link between ROS and aging is well established and is historically rooted in two influential theories: the free radical theory of aging and the mitochondrial theory of aging (*5*). Chronic exposure to UV radiation promotes ROS accumulation in skin cells, resulting in oxidative damage, cellular dysfunction, and ultimately, skin photoaging (*6-8*). Multiple studies have demonstrated that UVR induces ROS and oxygen-derived free radicals in a dose-dependent manner (*9-12*). In skin keratinocytes and fibroblasts, UV exposure elevates lipid peroxidation, protein carbonylation, and DNA damage (*13-15*).

A primary defense against this oxidative stress is the Nrf2-Keap1 pathway, which plays a critical role in protecting skin cells from UV-induced damage during photoaging (Figure 1). Under basal conditions, Nrf2 is sequestered in the cytoplasm by its inhibitor Keap1. Oxidative stress triggers the dissociation of Nrf2 from Keap1, allowing Nrf2 to translocate to the nucleus, where it forms a heterodimer with a Maf protein (*16*). This Nrf2-Maf complex binds to antioxidant response elements (AREs) in the promoter regions of genes encoding antioxidant and detoxifying enzymes (*17*), thereby activating their transcription. The subsequent synthesis of these enzymes helps neutralize ROS and mitigate oxidative damage (*7,18*). In concurrence, molecular analyses have confirmed that UVA irradiation markedly upregulates oxidative stress-responsive genes such as heme oxygenase-1 (HO-1), NAD(P)H:quinone oxidoreductase 1 (NQO1), and the glutamate-cysteine ligase catalytic subunit (GCLC) (*19*). Beyond the Nrf2 system, peroxisomes also play an essential role in regulating cellular ROS levels, particularly under homeostatic conditions (*20*).

2.2. Apoptosis

Apoptosis is a genetically programmed, energy-dependent process of controlled cellular self-destruction and represents a key mechanism implicated in skin photoaging (*21*). UV-induced apoptosis proceeds through two temporally distinct pathways. In the early phase following exposure, UVA1 generates singlet oxygen, which depolarizes mitochondrial membranes and triggers immediate apoptosis. After 24 hours, ROS produced by both UVA and UVB subsequently induce oxidative DNA damage, leading to delayed apoptosis (*22,23*). The accumulation of DNA lesions activates the p53 pathway, which promotes the transcription of

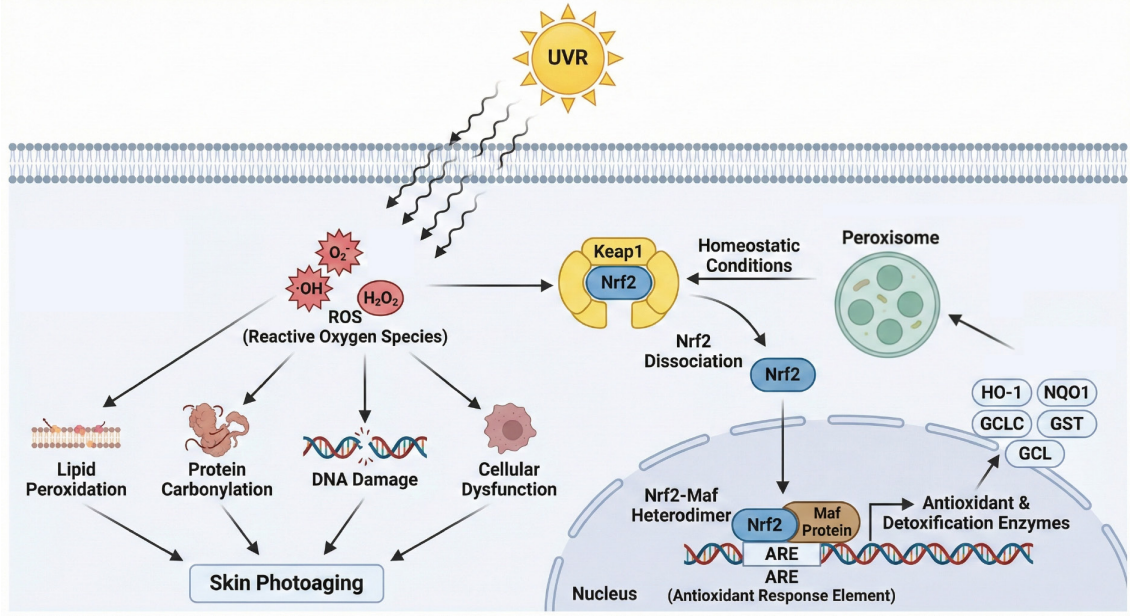

Figure 1. The mechanism of oxidative stress injury. Under ultraviolet (UV) radiation, oxygen is converted into reactive oxygen species (ROS), such as the superoxide anion (O_2^-), the hydroxyl radical (·OH), and hydrogen peroxide (H_2O_2). These ROS induce lipid peroxidation, protein carbonylation, DNA damage, and cellular dysfunction. The Nrf2-Keap1 pathway plays a critical role in protecting skin cells from UV-induced damage during photoaging. Under basal conditions, Nrf2 is sequestered in the cytoplasm by Keap1. Upon oxidative stress, Nrf2 dissociates from Keap1 and translocates into the nucleus, where it forms a heterodimer with a Maf protein. This complex binds to antioxidant response elements (AREs) in the promoters of genes encoding antioxidant and detoxifying enzymes, activating their transcription. The resulting enzymes help neutralize ROS and alleviate oxidative damage. Consistent with this mechanism, molecular analyses confirm that UVA irradiation markedly upregulates oxidative stress-responsive genes, including heme oxygenase-1 (HO-1), NAD(P)H:quinone oxidoreductase 1 (NQO1), and the glutamate-cysteine ligase catalytic subunit (GCLC).

autophagy-related genes such as AMP-activated protein kinase (AMPK), Sestrin 2 (SESN2), and Unc-51-like autophagy-activating kinase 1 (ULK1). Activated ULK1, in turn, phosphorylates Beclin-1 to initiate phagophore nucleation (*24*). The intrinsic (mitochondrial) apoptotic pathway is finely regulated by the balance between anti-apoptotic (*e.g.*, Bcl-2 and Bcl-xL) and pro-apoptotic (*e.g.*, Bax, Bak, and Bid) members of the Bcl-2 protein family, which ultimately determines cellular fate.

2.3. Autophagy

Autophagy is a highly regulated degradation process essential for maintaining cellular homeostasis through the clearance of damaged organelles, misfolded proteins, and other macromolecular debris (Figure 2). It is broadly categorized into macroautophagy, microautophagy, and selective autophagy (*25*). Based on the specific cellular components targeted for degradation, selective autophagy can be further classified into mitophagy (degrading damaged mitochondria), aggrephagy (degrading protein aggregates), and pexophagy (degrading peroxisomes) (*26,27*). In skin cells, mitochondria are a primary source of ROS. Sustained UVR induces mitochondrial DNA mutations and excessive ROS production. Mitophagy acts as a protective mechanism by removing dysfunctional mitochondria, thereby attenuating oxidative stress and genomic damage (*28*). Similarly, aggrephagy eliminates cytotoxic protein aggregates formed upon UV exposure, while pexophagy degrades impaired peroxisomes that would otherwise exacerbate oxidative stress and accelerate skin aging (*29,30*).

The autophagic process is orchestrated by a network of signaling pathways and effector molecules. In senescent human dermal fibroblasts, mitochondrial dysfunction is often associated with dysregulation of the PI3K/AKT/mTOR cascade (*31*). Conversely, AMPK signaling serves as a key positive regulator of autophagy (*32,33*). Both the inhibition of mTOR and activation of AMPK have protective roles in skin photoaging by promoting the clearance of damaged cellular components and reducing oxidative and DNA damage induced by UVR (*34-36*).

Central to autophagy are autophagy-related (ATG) proteins. ULK1, a key initiator kinase regulated upstream by mTOR and AMPK, phosphorylates downstream

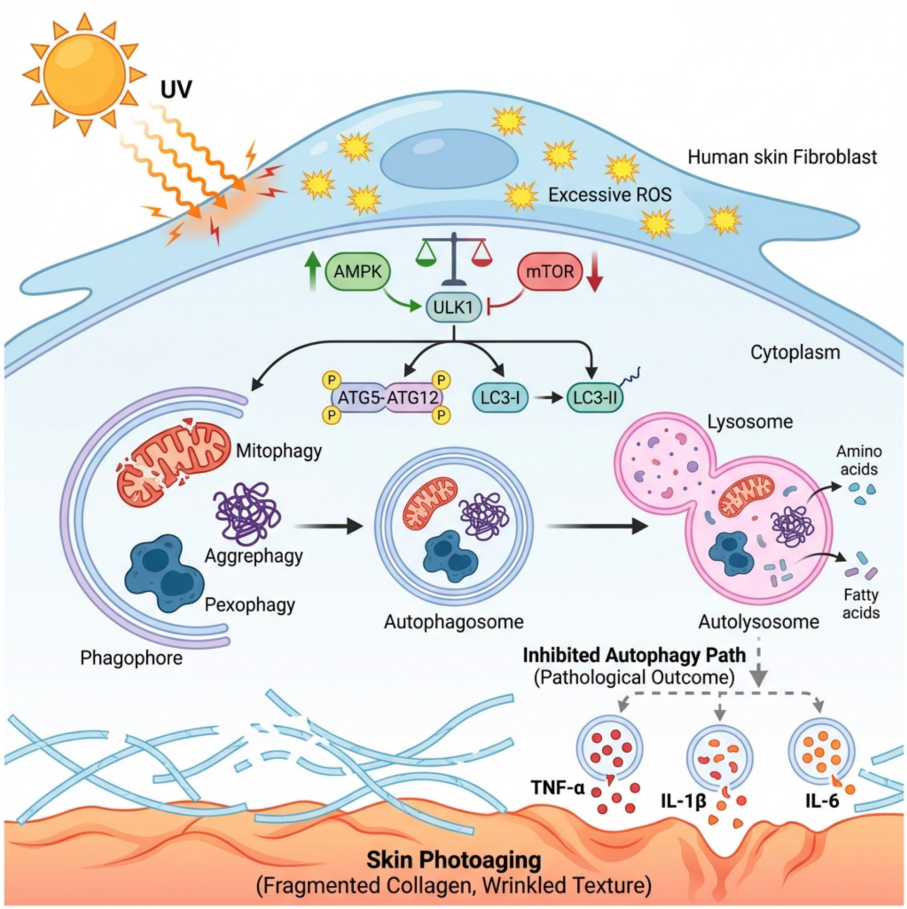

Figure 2. The mechanism of autophagy. Selective autophagy can be classified into mitophagy, aggrephagy, and pexophagy. In senescent human dermal fibroblasts, mitochondrial dysfunction is often accompanied by mTOR inhibition and AMPK activation, which subsequently activates the autophagy-related protein ULK1. ULK1 phosphorylates downstream ATG proteins, such as ATG5, ATG12, and LC3, thereby driving autophagosome formation. This process further promotes the expression of pro-inflammatory mediators, including TNF-α, IL-1β, and IL-6, collectively exacerbating skin photoaging.

ATG proteins such as ATG5, ATG12, and LC3 to drive autophagosome formation. Importantly, excessive UVR suppresses autophagic flux, leading to the subsequent activation of pro inflammatory mediators such as tumor necrosis factor-α (TNF α), interleukin 1β (IL-1β), and interleukin 6 (IL-6), which collectively exacerbate skin photoaging (*37*).

2.4. Inflammation-related pathways

The p38 MAPK and NF-κB signaling pathways are pivotal mediators of the inflammatory response triggered by UVR (*38*). UV exposure activates multiple members of the MAPK family, including extracellular signal-regulated kinase (ERK), c-Jun N-terminal kinase (JNK), and p38 MAPK. While ERK primarily regulates cell proliferation and survival, its sustained activation upregulates the senescence-associated secretory phenotype (SASP), thereby driving cellular senescence (*39,40*). Concurrently, NF-κB is activated under UV stress and promotes the transcription of pro-inflammatory cytokines such as TNF-α, interleukin 1α (IL-1α), and IL-1β. These cytokines recruit immune cells—including monocytes, macrophages, and natural killer (NK) cells—to the site of damage (*41,42*). Subsequently, these infiltrating immune cells release additional inflammatory chemokines, such as CCL3, CXCL1, CXCL3, and CXCL5 (*43*). Moreover, MAPK signaling enhances cyclooxygenase-2 (COX-2) production, which exacerbates inflammation and tissue injury during photoaging (*44*). After the early vasodilatory phase, skin is infiltrated by neutrophils, monocytes, and T cells. These cells not only secrete pro-inflammatory mediators but also induce the release of anti-inflammatory cytokines, including IL-4, IL-10, and transforming growth factor β (TGF-β) (*45,46*). These regulatory cytokines facilitate the transition from acute inflammation to a prolonged, resolution-phase immunosuppression, a shift that accompanies tissue repair processes at the inflamed site.

2.5. Extracellular matrix (ECM) degradation-related pathways

The degradation of the ECM represents a central hallmark of skin photoaging. As previously outlined, excessive UVR elicits a robust inflammatory response. This process involves the upregulation of pro-inflammatory cytokines such as IL-1α and IL-1β, which in turn stimulate the expression of several matrix metalloproteinases (MMPs)—including MMP-1 (collagenase), MMP-3 (stromelysin), and MMP-9 (gelatinase). These enzymes collectively degrade collagen and other critical ECM components (*47,48*). Concurrently, UV-induced ERK activation promotes the expression of c-Fos, which forms the transcription factor AP-1 with c-Jun. AP-1 binds to promoter regions of MMP genes, further enhancing their transcription. The resultant overexpression of MMPs leads to extensive collagen breakdown and disruption of the three-dimensional elastin network, ultimately manifesting as skin wrinkling and loss of elasticity (*49,50*).

3. Roles of cells in skin photoaging

3.1. Fibroblasts

The pathogenesis of dermal fibroblast photoaging is predominantly initiated by chronic UVR, which induces a cascade of intracellular damage (*51*). Core mechanisms involve the excessive generation of ROS, accumulation of DNA damage, and mitochondrial dysfunction (*52,53*). Critically, prolonged UV exposure drives cellular senescence, marked by irreversible cell-cycle arrest and the acquisition of an SASP (*54*). Consequently, photoaged fibroblasts exhibit a profound decline in collagen and elastin production along with elevated expression of matrix-degrading enzymes such as MMPs, collectively leading to ECM disintegration (Table 1) (*55*).

3.2. Keratinocytes

As the outermost layer of the skin, the epidermis is directly and chronically exposed to solar UVR, rendering it highly susceptible to photoaging (*55*). In keratinocytes, UVR triggers photoaging through interconnected mechanisms, including oxidative stress with ROS generation, mitochondrial dysfunction, DNA damage, and activation of inflammatory pathways such

Table 1. Key regulators in skin photoaging

Cell type	Upregulated factors	Downregulated factors
Fibroblasts	ROS, SASP, MMPs	Collagen production, elastin production
Keratinocytes	ROS, SASP, MMP-1, MMP-9, IL-1β, IL-6	Antioxidant defenses
Melanocytes	Melanogenesis, β-catenin signaling	SDF1
Macrophages	MMP-1, MMP-3, MMP-9, Pro-inflammatory factors, M1/M2 ratio	Anti-inflammatory cytokines
Th17/Treg Cells	IL-17A, IL-8, IL-17F, IL-21, IL-22, IL-26, TNF-α, IL-10, TGF-β, SASPs	Immune surveillance
Mast Cells	Serine proteases (tryptase, chymase), Histamine, MMP-9	Not specified

Abbreviation: ROS, reactive oxygen species; SASP, senescence-associated secretory phenotype; MMPs, matrix metalloproteinases; SDF1, stromal cell-derived factor 1.

as NF-κB and MAPK signaling (*5657*). These negative factors collectively promote an SASP, characterized by elevated expression of MMPs (*e.g.*, MMP-1 and MMP-9), increased secretion of pro-inflammatory cytokines (*e.g.,* IL-1β, and IL-6), and a concomitant decline in antioxidant defenses (*58,59*).

3.3. Melanocytes

Melanocytes, situated primarily within the basal epidermal layer, are responsible for melanin production and proliferate at a low rate. Upon exposure to UVR, keratinocytes release paracrine factors including interleukin 17 (IL-17), endothelin 1 (ET 1), and stem cell factor (SCF) (*60*). These ligands bind to their respective receptors—MC1R, the endothelin B receptor (ETB), and c Kit—on melanocytes (Figure 3). ET 1 and SCF binding, in particular, activates the ERK1/2 MAPK pathway, thereby promoting melanogenesis (*61*). Newly synthesized melanin is subsequently transferred to adjacent keratinocytes, where it functions as a natural photoprotectant by absorbing UVR and mitigating DNA damage (*62*).

Beyond keratinocytes, senescent dermal fibroblasts also contribute significantly to skin hyperpigmentation (*63*). Senescent fibroblasts upregulate the secretion of pro-melanogenic growth factors such as hepatocyte growth factor (HGF), keratinocyte growth factor (KGF), and SCF, which directly stimulate melanocytic activity (*64-66*). Additionally, factors such as secreted frizzled related protein 2 (sFRP2) and growth differentiation factor 15 (GDF15) further enhance melanin synthesis by activating the β-catenin signaling pathway (*67*). Epigenetic alterations also play a regulatory role, including the downregulation of stromal cell-derived factor 1 (SDF1) and the upregulation of Wnt inhibitory factor 1 (WIF-1), collectively shaping the pigmentary response to chronic UV exposure (*68*).

3.4. Macrophages

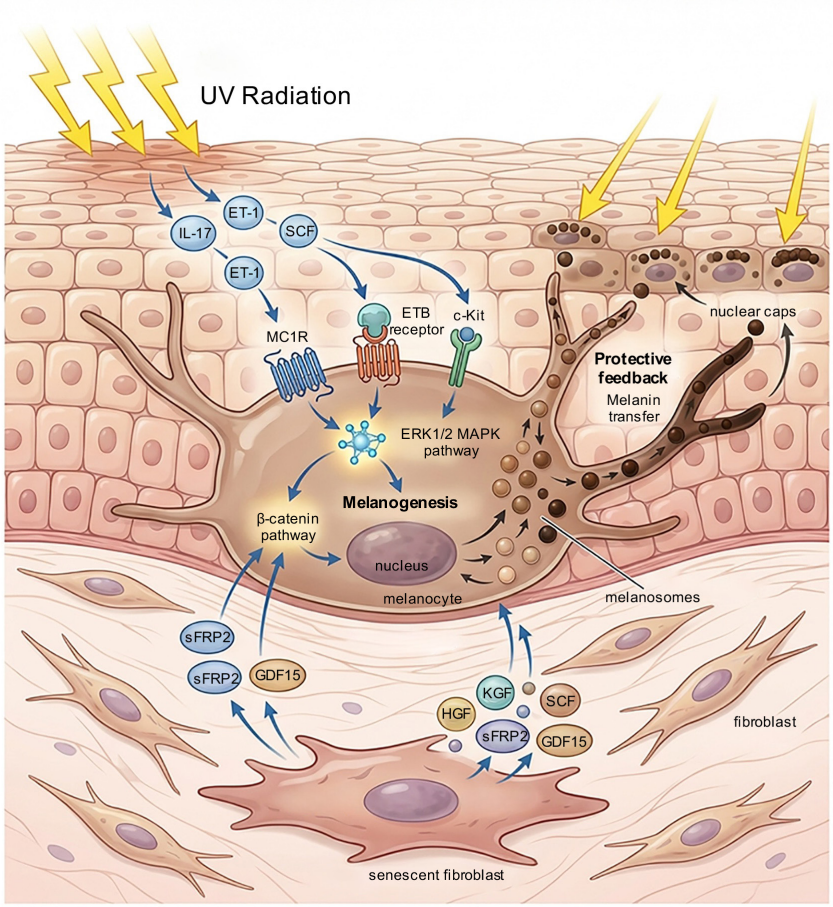

Figure 3. The alteration of melanocytes under UV exposure. Upon UVR, keratinocytes release paracrine factors such as interleukin-17 (IL-17), endothelin-1 (ET-1), and stem cell factor (SCF). These ligands bind to their respective receptors—MC1R, endothelin B receptor (ETB), and c-Kit—on melanocytes. The binding of ET-1 and SCF activates the ERK1/2 MAPK pathway, thereby promoting melanogenesis. In fibroblasts, UV-induced epigenetic alterations downregulate stromal cell-derived factor-1 (SDF1) and upregulate Wnt inhibitory factor-1 (WIF-1), which collectively enhance the secretion of pro-melanogenic factors including hepatocyte growth factor (HGF), keratinocyte growth factor (KGF), SCF, secreted frizzled-related protein 2 (sFRP2), and growth differentiation factor-15 (GDF15). These factors further stimulate melanin synthesis by activating the β-catenin signaling pathway. Newly synthesized melanin is transferred to adjacent keratinocytes, where it acts as a natural photoprotectant by absorbing UVR and reducing DNA damage.

As key components of the innate immune system, macrophages play an important role in maintaining skin homeostasis. In response to various stimuli, macrophages can polarize into two primary subsets: the pro-inflammatory M1 phenotype and the anti-inflammatory M2 phenotype. In response to UVR, M1 macrophages are recruited *via* activation of the p38 MAPK and NF-κB signaling pathways. They recognize damage-associated molecular patterns (DAMPs) and pathogen-associated molecular patterns (PAMPs) in photodamaged skin through Toll-like receptors (TLRs) and inflammasome signaling, thereby amplifying local inflammation (*69*). Moreover, they secrete MMPs, including MMP-1, MMP-3, and MMP-9, which are central to the degradation of type I collagen during photoaging (*70*). In contrast, M2 macrophages, which are polarized by cytokines such as IL-4 and IL-13 *via* the STAT6 pathway (M2a), or by immune complexes and IL-1 receptor antagonists (M2b), or *via* the JAK1/STAT3 pathway in response to IL-10 and TGF-β (M2c), are crucial to tissue repair and remodeling (*71*). M2 macrophages promote the activation of fibroblasts and ECM deposition by releasing growth factors (*e.g.*, PDGF, VEGF, TGF-β1, and IGF-1), while downregulating inflammatory markers and MMPs. In photoaged skin, the macrophage balance shifts toward an M1-dominant state, resulting in an elevated M1/M2 ratio (*72*). This imbalance is significantly correlated with reduced levels of type I, V, and VI collagen in the dermis (*73*). The sustained inflammatory environment may accelerate fibroblast senescence, which in turn exacerbates collagen dysregulation through the secretion of deleterious factors (*74*). Notably, the disruption particularly affects type V and VI collagen, which serve as critical bridging molecules that stabilize type I collagen fibrils. Consequently, the altered M1/M2 equilibrium contributes to chronic inflammation, impaired collagen homeostasis, and ultimately to the structural breakdown of the dermal matrix, manifesting as skin laxity and wrinkling (*75*).

3.5. Th17/Treg cells

T helper 17 (Th17) cells and regulatory T (Treg) cells, as key effector subsets derived from the differentiation of $CD4^+$ T cells, play functionally antagonistic roles in immune responses. Th17 cells are characterized by the production of interleukin (IL)-17A and also secrete pro-inflammatory cytokines such as IL-8, IL-17F, IL-21, IL-22, IL-26, and TNF-α, aggravating inflammation-induced skin photoaging (*76*). In contrast, Tregs, defined by the expression of the transcription factor FoxP3 and surface markers CD25 and CTLA-4, are central to maintaining immune tolerance and homeostasis, largely through the secretion of anti-inflammatory cytokines such as IL-10, IL-35, and TGF-β1. Beyond accelerating aging, UVR has also been implicated in skin immunosuppression, this phenomenon is predominantly governed by Tregs (*77*). Their activation in UV-exposed skin is initiated through two major pathways. Primarily, UVR triggers the migration of Langerhans cells (LC) to regional lymph nodes, where they present antigen and imprint Tregs with skin-homing specificity (*78,79*). Additionally, UVB acts as a direct photochemical trigger, converting tryptophan into the aryl hydrocarbon receptor (AhR) ligand 6-formylindolo[3,2-b] carbazole (FICZ) and activating the kynurenine pathway, the metabolites of which also serve as AhR agonists (*80,81*). UVR further stimulates the production of cis-urocanic acid, which results in an inflammatory environment and which promotes the synthesis of prostaglandin E2, collectively establishing a signaling cascade that expands and recruits Tregs to the skin (*82,83*).

Once localized, Tregs drive photoaging through two synergistic mechanisms that fuel a self-perpetuating cycle of damage. First, through the secretion of IL-10 and TGF-β, Tregs dampen the effector functions of $CD4^+$/$CD8^+$ T cells, NK cells, and dendritic cells (*84-86*). This suppression of immunosurveillance compromises the clearance of senescent cells, leading to their accumulation. The senescent cells release SASPs such as ROS, cytokines, and MMPs, exacerbating local inflammation and reinforcing the immunosuppressive microenvironment that sustains Treg activity (*87,88*). Second, Tregs directly promote tissue degradation. Treg-derived TGF-β inhibits keratinocyte proliferation, upregulates collagen-degrading MMPs, and can induce senescence in resident skin cells (*89-91*). While IL-10 typically has anti-inflammatory effects, under chronic photo-inflammatory conditions it disrupts proteostasis by suppressing autophagy and antigen presentation. Moreover, ROS released by recruited immune cells activate latent TGF-β, amplifying its tissue-destructive effects (*92,93*).

3.6. Mast cells

Mast cells are common innate immune cells, recognized as key effector cells in immunoglobulin E (IgE)-mediated allergic inflammation, and play important roles in various physiological and pathological processes (*94,95*). Mast cells contain a variety of bioactive substances. UV stimulation can promote their activation and degranulation, leading to the release of serine proteases and other mediators, such as tryptase, chymase, histamine, and TNF, which are involved in changes observed in photoaged skin, including solar elastosis, degradation of the ECM, disruption of the basement membrane, and hyperpigmentation (*96,97*). Tryptase is the most abundant serine protease in mast cells and also functions as a gelatinase. This enzyme is associated with degradation of the basement membrane and the formation of perivascular alterations induced by UVR. Tryptase participates in the degradation of the

dermal ECM by processing MMP precursors into active forms or directly damaging ECM proteins. Repeated UV exposure can also promote the production of mast cell tryptase (*98*). Mast cell tryptase activates MMP-9 and degrades type IV collagen, thereby promoting wrinkle formation. In summary, tryptase can contribute to ECM damage, disruption of the basement membrane, and solar elastosis in photoaged skin, thereby influencing the progression of photoaging (*99-101*). Thus, tryptase may serve as a promising therapeutic target for preventing skin photoaging (*102*).

Histamine is the only recognized amine stored in human mast cells. It can induce MMP-9 production in human primary keratinocytes, promote immune cell migration in the basal layer of the skin, and degrade type IV collagen. Malaviya *et al*. (*103*) found that under UVR, upregulated histamine release from dermal mast cells in human skin may enhance collagen degradation and promote wrinkle formation. Kim *et al*. (*104*) treated mice chronically exposed to UV with the antihistamine ketotifen, and they found that ketotifen significantly reduced UV-induced wrinkles and effectively inhibited and delayed skin aging. Besides promoting wrinkle formation in photoaged skin, histamine is also associated with the development of hyperpigmentation. Yoshida *et al*. (*105*) found that treating human melanocytes with histamine induced morphological changes and increased tyrosinase activity, and they confirmed that histamine activates protein kinase A *via* the H_2 receptor, stimulating melanogenesis in cultured human melanocytes. Topical application of famotidine (an H_2 antagonist) to UVB-irradiated mouse skin significantly reduced skin pigmentation and the increase in Dopa-positive melanocytes (*105*).

4. SASP-mediated intercellular crosstalk

In the pathophysiology of skin photoaging, the SASP serves as a central mechanistic hub orchestrating complex intercellular crosstalk among fibroblasts, keratinocytes, melanocytes, and infiltrating immune cells (Figure 4). Chronic UVR initially leads to fibroblast and keratinocyte senescence and SASP accumulation, including MMPs, pro-inflammatory cytokines (*e.g.*, IL-1β, and IL-6), and growth factors, that not only degrade the ECM but that also have paracrine effects on neighboring cells. Specifically, senescent fibroblast-derived SASP factors such as IGF-1 induce keratinocyte senescence *via* p53/p21 activation, while HGF, KGF, and SCF promote melanogenesis and contribute to hyperpigmentation (Figure 4) (*54,106,107*). This secretome further recruits and polarizes macrophages toward a pro-inflammatory M1 phenotype, elevating the M1/M2 ratio and perpetuating MMP-mediated collagenolysis. Concurrently, UV-induced Tregs suppress immune surveillance *via* IL-10 and TGF-β, impairing senescent cell clearance and fostering a self-sustaining niche of SASP-producing cells. Mast cells, activated by

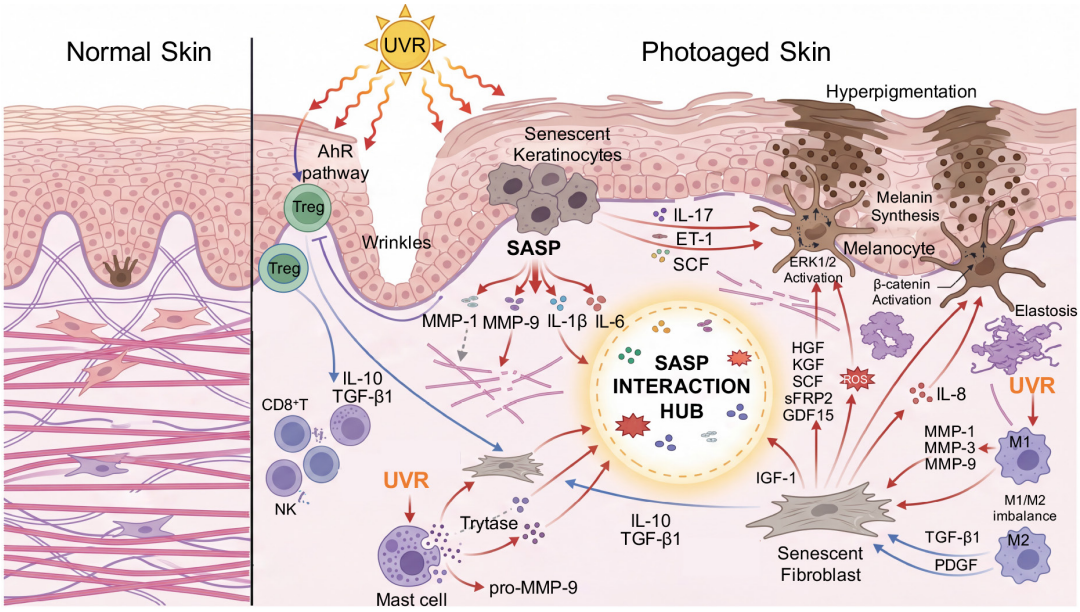

Figure 4. The multicellular SASP network driving skin photoaging. In skin photoaging, the senescence-associated secretory phenotype (SASP) acts as a central hub for intercellular communication. Chronic UV exposure induces senescence in fibroblasts and keratinocytes, leading them to secrete SASP factors (*e.g.*, MMPs, IL-1β, and IL-6). This secretome degrades the extracellular matrix (ECM) and drives paracrine effects: SASP from fibroblasts promotes senescence in keratinocytes (via IGF-1), stimulates melanogenesis (via HGF/KGF/SCF), and recruits pro-inflammatory M1 macrophages, which amplify MMP-driven collagen breakdown. Concurrently, UV-induced regulatory T cells (Tregs) suppress immune clearance of senescent cells *via* IL-10/TGF-β, while mast cells release proteases that further degrade the ECM. These interactions form a vicious cycle—immune and epidermal signals exacerbate fibroblast senescence, the SASP of which in turn reinforces inflammation and matrix destruction—leading to the hallmark deterioration of photoaged skin.

UV, release tryptase and histamine, which amplify MMP activity and ECM degradation. The resultant chronic inflammatory microenvironment establishes reciprocal feedback loops—wherein inflammatory signals from immune and epidermal cells exacerbate fibroblast senescence, while SASP from fibroblasts reinforces immune dysregulation and matrix disintegration—collectively driving the progressive structural and functional deterioration characteristic of photoaged skin (*51,63*).

5. Emerging therapeutic strategies

Current therapeutic strategies targeting skin photoaging focus on antioxidants, ECM metabolism modulators, and senescence-directed interventions (Table 2). In keratinocytes, several natural compounds such as hesperetin and chrysanthemum attenuate senescence by suppressing the MAPK/AP-1 and NF-κB signaling axes, thereby reducing MMP expression (*108,109*). Nicotinamide (NAM) promotes DNA repair and enhances cellular energy metabolism to delay senescence (*110*), while mesenchymal stem cell-derived extracellular vesicles (MSC-EVs) deliver tissue inhibitor of metalloproteinase 1 (TIMP1) to inhibit Notch1 signaling, concurrently alleviating inflammation and cellular aging (*111*). Additional keratinocyte-targeted strategies include pharmacological inhibition of protease-activated receptor 2 (PAR2), enhancement of δ-catenin-mediated DNA repair, and activation of CISD2—a mitochondrial protein that reduces ROS production, suppresses MMP-1 expression, and restores mitochondrial function (*112*). In parallel, fibroblast-oriented interventions are categorized into antioxidants, ECM metabolism modulators, and senescence-directed therapies. Numerous phytochemicals, such as resveratrol, salvianolic acid B, galangin, and urolithin A, have antioxidant effects *via* activation of stress-responsive NRF2 and SIRT1 pathways, leading to upregulated antioxidant enzymes (HO-1 and SOD), ROS scavenging, and mitophagy-mediated mitochondrial rejuvenation (*113-116*). Other agents, including protocatechuic aldehyde, gallic acid, and Scutellaria barbata extracts, primarily remodel ECM homeostasis by inhibiting MMP expression through an AP-1/NF-κB blockade and concurrently enhancing collagen synthesis *via* TGF-β/IGF-1 pathway activation (*117,118*). As senescence-targeting approaches, chlorogenic acid attenuates fibroblast senescence by inhibiting the glycolytic enzyme ENO1 and suppressing the SASP (*119*), whereas metformin modulates the PI3K/AKT/mTOR axis and alleviates excessive mitophagy (*31*). Physical and cell-based approaches, such as low-dose aminolevulinic acid photodynamic therapy (*120*), microneedling (*121*), and MSC-based therapies (*122,123*), represent complementary avenues for restoring dermal homeostasis. Beyond these preclinical and translational efforts, several intervention paradigms have advanced to clinical-stage investigation. For example, 0.5% retinol serums and topical rapamycin provide significant clinical benefits against photoaging, including improved uniformity of skin color, enhanced overall skin tone, increased elasticity, and optimized moisture retention (*124,125*). Moreover, topical and systemic modulation of the cutaneous microbiome has emerged as a novel strategy to reinforce epidermal barrier function and mitigate low-grade inflammatory drift associated with photoaging (*126,127*). These evolving

Table 2. Therapeutic strategies for skin photoaging

Therapeutic mechanism	Target/Pathway	Candidate drug/Intervention	*Ref.*
Antioxidant/Anti-inflammatory	MAPK/AP-1, NF-κB signaling	Hesperetin, chrysanthemum	(*108,109*)
Antioxidant/Mitochondrial rejuvenation	NRF2, SIRT1 pathways	Resveratrol, salvianolic acid B, galangin, urolithin A	(*113-116*)
DNA repair	DNA repair	Nicotinamide	(*110*)
ECM metabolism modulation	AP-1/NF-κB, TGF-β/IGF-1, TIMP1/Notch1	Protocatechuic aldehyde, gallic acid, Scutellaria barbata extracts	(*117,118*)
Anti-SASP	ENO1, PAR2, PI3K/AKT/mTOR	Chlorogenic acid, metformin	(*31,119*)
Physical therapy	Photodynamic effect, mechanical stimulation	Aminolevulinic acid photodynamic therapy, microneedling	(*120,121*)
MSC-based therapy	Skin regeneration	Adipose-derived MSC, MSC-EVs	(*122,123*)
Clinical stage	Retinoic acid receptor	0.5% retinol serums	(*124,125*)
Clinical stage	mTOR inhibition	Topical rapamycin	(*124,125*)
Clinical stage	Cutaneous microbiome modulation	Topical and systemic modulation	(*126,127*)

therapeutic strategies collectively define a precision-oriented landscape for the clinical management of skin photoaging.

6. Perspective

In the investigation of pathogenesis, single-cell sequencing technologies have provided a revolutionary perspective for understanding the complex mechanisms underlying photoaging. Compared to bulk analysis, this technology has enabled the construction of a high-resolution transcriptomic atlas of human skin aging, revealing distinct changes in cellular composition that differentiate photoaging from chronological aging (*128,129*). Moreover, single-cell analysis has precisely identified key regulators in photoaging, such as HES1 and KLF6 (*130*). Furthermore, by integrating analyses of intercellular communication networks, this approach has elucidated the underlying mechanism (*129*). Epigenetics is another approach that has further revealed the pathogenesis of photoaging. DNA methylation and histone alterations alter the three-dimensional conformation of DNA and subsequent gene expression without altering the underlying genetic sequence, thereby mediating cutaneous photoaging. Given the enduring and heritable nature of these epigenetic modifications, their cumulative effects are considered a key mechanism driving chronic photodamage and the aging process (*131*).

Over the past few years, rapid progress has been made in artificial intelligence-assisted diagnosis of dermatological conditions. Studies have shown that AI-assisted analysis of reflectance confocal microscopy (RCM) images, which evaluates the morphology (degree of flattening) of the dermal-epidermal junction (DEJ) and classifies dermal collagen fiber types, can intelligently identify photoaging (*132*).

Therapeutically, exosomes afford a promising strategy to treat photoaging. Derived from stem cells and plants, exosomes have been proven to have regenerative effects on photo-damaged skin. Moreover, as natural extracellular vesicles, exosomes show considerable potential as drug delivery vehicles. Future research could focus on the bioengineering of exosomes—including modification with targeting peptides, cargo optimization (*e.g.*, with specific circRNAs or miRNAs), and the development of novel delivery systems—to achieve efficient and precise delivery (*133*). Concurrently, investigations into the skin microbiome have revealed that certain probiotic derivatives, such as the supernatant from Pediococcus acidophilus LS, have photoprotective and anti-melanogenic effects by inhibiting both the PKA/CREB and MAPK signaling pathways. This offers early evidence for a "microbe-skin axis" in photoaging regulation, although the mechanisms underlying the interaction between microbial metabolites and the host epigenome remain largely unexplored (*134*).

7. Conclusion

Photoaging is a distinct form of skin aging primarily caused by chronic exposure to UVR (UVA and UVB), clinically manifesting as wrinkles, pigmentation disorders, and loss of elasticity. Its core molecular mechanisms involve oxidative stress, apoptosis, dysregulated autophagy, activation of inflammatory pathways, and degradation of the ECM. Multiple types of skin cells—including fibroblasts, keratinocytes, melanocytes, and immune cells—interact through complex signaling networks to collectively drive disease progression. Recent advances in photoaging research, encompassing the elucidation of pathogenic mechanisms, AI-assisted diagnosis, and therapeutic development, have not only increased our understanding of this process but also expanded the potential for clinical translation. These breakthroughs have laid a robust theoretical foundation for the further development of targeted interventions and precision treatment strategies, holding promise for developing anti-photoaging therapies for more personalized and precision-based approaches.

Funding: This study was supported by the Beijing National Nature Science Foundation (L254701), the National Nature Science Foundation of China (82373460), and Funding Support from the Air Force Medical Center (2025RCZZ29).

Conflict of Interest: The authors have no conflicts of interest to disclose.

References

1. Guan LL, Lim HW, Mohammad TF. Sunscreens and photoaging: A review of current literature. Am J Clin Dermatol. 2021; 22:819-828.
2. Ronsch H, Bauer A. The preventive value of sun protection. Curr Probl Dermatol. 2021; 55:316-328.
3. Gromkowska-Kepka KJ, Puscion-Jakubik A, Markiewicz-Zukowska R, Socha K. The impact of ultraviolet radiation on skin photoaging - Review of *in vitro* studies. J Cosmet Dermatol. 2021; 20:3427-3431.
4. Pourang A, Tisack A, Ezekwe N, Torres AE, Kohli I, Hamzavi IH, Lim HW. Effects of visible light on mechanisms of skin photoaging. Photodermatol Photoimmunol Photomed. 2022; 38:191-196.
5. Schneider JL, Rowe JH, Garcia-de-Alba C, Kim CF, Sharpe AH, Haigis MC. The aging lung: Physiology, disease, and immunity. Cell. 2021; 184:1990-2019.
6. Tada T, Sakamoto R, Wajima T. Effects of metformin on high glucose- and UVA-induced oxidative stress and cellular senescence in Rat Keratinocytes. Biol Pharm Bull. 2025; 48:1732-1740.
7. Hajialiasgary Najafabadi A, Soheilifar MH, Masoudi-Khoram N. Exosomes in skin photoaging: Biological functions and therapeutic opportunity. Cell Commun Signal. 2024; 22:32.
8. Wang L, Lee W, Oh JY, Cui YR, Ryu B, Jeon YJ. Protective effect of sulfated polysaccharides from

celluclast-assisted extract of Hizikia fusiforme against ultraviolet B-induced skin damage by regulating NF-κB, AP-1, and MAPKs signaling pathways *in vitro* in human dermal fibroblasts. Mar Drugs. 2018; 16:239.
9. Jang J, Ye BR, Heo SJ, Oh C, Kang DH, Kim JH, Affan A, Yoon KT, Choi YU, Park SC, Han S, Qian ZJ, Jung WK, Choi IW. Photo-oxidative stress by ultraviolet-B radiation and antioxidative defense of eckstolonol in human keratinocytes. Environ Toxicol Pharmacol. 2012; 34:926-934.
10. Budluang P, Kim JE, Park ES, *et al*. N-benzyl-N-methyldecane-1-amine derived from garlic ameliorates UVB-induced photoaging in HaCaT cells and SKH-1 hairless mice. Sci Rep. 2025; 15:6979.
11. Jo WS, Yang KM, Park HS, Kim GY, Nam BH, Jeong MH, Choi YJ. Effect of microalgal extracts of Tetraselmis suecica against UVB-induced photoaging in human skin fibroblasts. Toxicol Res. 2012; 28:241-248.
12. Ung TPL, Lim S, Solinas X, Mahou P, Chessel A, Marionnet C, Bornschlogl T, Beaurepaire E, Bernerd F, Pena AM, Stringari C. Simultaneous NAD(P)H and FAD fluorescence lifetime microscopy of long UVA-induced metabolic stress in reconstructed human skin. Sci Rep. 2021; 11:22171.
13. Duan X, Wu T, Liu T, Yang H, Ding X, Chen Y, Mu Y. Vicenin-2 ameliorates oxidative damage and photoaging *via* modulation of MAPKs and MMPs signaling in UVB radiation exposed human skin cells. J Photochem Photobiol B. 2019; 190:76-85.
14. Rodrigues RB, de Oliveira MM, Garcia FP, Ueda-Nakamura T, de Oliveira Silva S, Nakamura CV. Dithiothreitol reduces oxidative stress and necrosis caused by ultraviolet A radiation in L929 fibroblasts. Photochem Photobiol Sci. 2024; 23:271-284.
15. Wang L, Jayawardena TU, Hyun J, Wang K, Fu X, Xu J, Gao X, Park Y, Jeon YJ. Antioxidant and anti-photoaging effects of a fucoidan isolated from Turbinaria ornata. Int J Biol Macromol. 2023; 225:1021-1027.
16. Niture SK, Khatri R, Jaiswal AK. Regulation of Nrf2-An update. Free Radic Biol Med. 2014; 66:36-44.
17. Bellezza I, Giambanco I, Minelli A, Donato R. Nrf2-Keap1 signaling in oxidative and reductive stress. Biochim Biophys Acta Mol Cell Res. 2018; 1865:721-733.
18. Lee JJ, Ng SC, Hsu JY, Liu H, Chen CJ, Huang CY, Kuo WW. Galangin reverses H_2O_2-induced dermal fibroblast senescence *via* SIRT1-PGC-1alpha/Nrf2 signaling. Int J Mol Sci. 2022; 23:1387.
19. Vikram A, Patel SK, Pathania D, Srivastava N, Rai AK, Ratnasekhar CH, Singh S, Ray RS, Dwivedi A. Ferulic acid photoconversion maintains Nrf2-mediated antioxidant defense against UVA damage. Phytomedicine. 2026; 150:157616.
20. Bellezza I, Mierla AL, Minelli A. Nrf2 and NF-kappaB and their concerted modulation in cancer pathogenesis and progression. Cancers (Basel). 2010; 2:483-497.
21. Bernerd F, Passeron T, Castiel I, Marionnet C. The damaging effects of long UVA (UVA1) rays: A major challenge to preserve skin health and integrity. Int J Mol Sci. 2022; 23:8243.
22. Breuckmann F, von Kobyletzki G, Avermaete A, Radenhausen M, Hoxtermann S, Pieck C, Schoneborn P, Gambichler T, Freitag M, Hoffmann K, Altmeyer P. Mechanisms of apoptosis: UVA1-induced immediate and UVB-induced delayed apoptosis in human T cells *in vitro*. J Eur Acad Dermatol Venereol. 2003; 17:418-429.
23. Godar DE. UVA1 radiation triggers two different final apoptotic pathways. J Invest Dermatol. 1999; 112:3-12.
24. Sample A, He YY. Autophagy in UV damage response. Photochem Photobiol. 2017; 93:943-955.
25. Zhang Z, Tan R, Xiong Z, Feng Y, Chen L. Dysregulation of autophagy during photoaging reduce oxidative stress and inflammatory damage caused by UV. Front Pharmacol. 2025; 16:1562845.
26. Bajdzienko J, Bremm A. Mammalian pexophagy at a glance. J Cell Sci. 2024; 137:jcs259775.
27. Rubio-Tomas T, Sotiriou A, Tavernarakis N. The interplay between selective types of (macro)autophagy: Mitophagy and xenophagy. Int Rev Cell Mol Biol. 2023; 374:129-157.
28. Picca A, Faitg J, Auwerx J, Ferrucci L, D'Amico D. Mitophagy in human health, ageing and disease. Nat Metab. 2023; 5:2047-2061.
29. Gallagher ER, Holzbaur ELF. SQSTM1/P62 promotes lysophagy *via* formation of liquid-like condensates maintained by HSP27. Autophagy. 2023; 19:3029-3030.
30. Li L, Hongying C, Heng G. Autophagy-related LncRNA PRDM10-DT responds to UVB radiation in keratinocytes. Biochem Biophys Res Commun. 2023; 677:105-112.
31. Chen Q, Zhang H, Yang Y, Zhang S, Wang J, Zhang D, Yu H. Metformin attenuates UVA-induced skin photoaging by suppressing mitophagy and the PI3K/AKT/mTOR pathway. Int J Mol Sci. 2022; 23:6960.
32. Chu J, Xiang Y, Lin X, He M, Wang Y, Ma Q, Duan J, Sun S. Handelin protects human skin keratinocytes against ultraviolet B-induced photodamage *via* autophagy activation by regulating the AMPK-mTOR signaling pathway. Arch Biochem Biophys. 2023; 743:109646.
33. Lin X, Chu J, Xiang Y, He M, Ma Q, Duan J, Wang Y, Sun S. Kangfuxin liquid reduces the ultraviolet B-induced photodamage of HaCaT cells by regulating autophagy. Biosci Biotechnol Biochem. 2023; 87:1485-1494.
34. Vikram A, Patel SK, Singh A, Pathania D, Ray RS, Upadhyay AK, Dwivedi A. Natural autophagy activators: A promising strategy for combating photoaging. Phytomedicine. 2024; 132:155508.
35. Tang QQ, Wang ZD, An XH, Zhou XY, Zhang RZ, Zhan X, Zhang W, Zhou J. Apigenin ameliorates H_2O_2-induced oxidative damage in melanocytes through nuclear factor-E2-related factor 2 (Nrf2) and phosphatidylinositol 3-kinase (PI3K)/protein kinase B (Akt)/mammalian target of rapamycin (mTOR) pathways and reducing the generation of reactive oxygen species (ROS) in zebrafish. Pharmaceuticals (Basel). 2024; 17:1302.
36. Gu Y, Han J, Jiang C, Zhang Y. Biomarkers, oxidative stress and autophagy in skin aging. Ageing Res Rev. 2020; 59:101036.
37. Rubinsztein DC, Marino G, Kroemer G. Autophagy and aging. Cell. 2011; 146:682-695.
38. Ciazynska M, Olejniczak-Staruch I, Sobolewska-Sztychny D, Narbutt J, Skibinska M, Lesiak A. Ultraviolet radiation and chronic inflammation-molecules and mechanisms involved in skin carcinogenesis: A narrative review. Life (Basel). 2021; 11:326.
39. Bhui K, Prasad S, George J, Shukla Y. Bromelain inhibits COX-2 expression by blocking the activation of MAPK regulated NF-kappa B against skin tumor-initiation triggering mitochondrial death pathway. Cancer Lett. 2009; 282:167-176.
40. Kim KM, Im AR, Park SK, Shin HS, Chae SW. Protective effects of timosaponin AIII against UVB-radiation induced

inflammation and DNA injury in human epidermal keratinocytes. Biol Pharm Bull. 2019; 42:1524-1531.
41. Hasegawa T, Nakashima M, Suzuki Y. Nuclear DNA damage-triggered NLRP3 inflammasome activation promotes UVB-induced inflammatory responses in human keratinocytes. Biochem Biophys Res Commun. 2016; 477:329-335.
42. Korhonen E, Bisevac J, Hyttinen JMT, Piippo N, Hytti M, Kaarniranta K, Petrovski G, Kauppinen A. UV-B-induced inflammasome activation can be prevented by cis-urocanic acid in human corneal epithelial cells. Invest Ophthalmol Vis Sci. 2020; 61:7.
43. Dawes JM, Antunes-Martins A, Perkins JR, Paterson KJ, Sisignano M, Schmid R, Rust W, Hildebrandt T, Geisslinger G, Orengo C, Bennett DL, McMahon SB. Genome-wide transcriptional profiling of skin and dorsal root ganglia after ultraviolet-B-induced inflammation. PLoS One. 2014; 9:e93338.
44. Surowiak P, Gansukh T, Donizy P, Halon A, Rybak Z. Increase in cyclooxygenase-2 (COX-2) expression in keratinocytes and dermal fibroblasts in photoaged skin. J Cosmet Dermatol. 2014; 13:195-201.
45. Salminen A, Kaarniranta K, Kauppinen A. Photoaging: UV radiation-induced inflammation and immunosuppression accelerate the aging process in the skin. Inflamm Res. 2022; 71:817-831.
46. Enk CD, Sredni D, Blauvelt A, Katz SI. Induction of IL-10 gene expression in human keratinocytes by UVB exposure *in vivo* and *in vitro*. J Immunol. 1995; 154:4851-4856.
47. Lee TH, Chen JL, Tsai MM, Wu YH, Tseng HC, Cheng LC, Shanmugam V, Hsieh HL. Protective effects of sophoraflavanone G by inhibiting TNF-alpha-iduced MMP-9-mediated events in brain microvascular endothelial cells. Int J Mol Sci. 2023; 25:283.
48. Feng C, Chen X, Yin X, Jiang Y, Zhao C. Matrix metalloproteinases on skin photoaging. J Cosmet Dermatol. 2024; 23:3847-3862.
49. Imokawa G, Ishida K. Biological mechanisms underlying the ultraviolet radiation-induced formation of skin wrinkling and sagging I: Reduced skin elasticity, highly associated with enhanced dermal elastase activity, triggers wrinkling and sagging. Int J Mol Sci. 2015; 16:7753-7775.
50. Nakajima H, Ezaki Y, Nagai T, Yoshioka R, Imokawa G. Epithelial-mesenchymal interaction during UVB-induced up-regulation of neutral endopeptidase. Biochem J. 2012; 443:297-305.
51. Shin JW, Kwon SH, Choi JY, Na JI, Huh CH, Choi HR, Park KC. Molecular mechanisms of dermal aging and antiaging approaches. Int J Mol Sci. 2019; 20:2126.
52. Haser WG, Saito H, Koyama T, Tonegawa S. Cloning and sequencing of murine T3 gamma cDNA from a subtractive cDNA library. J Exp Med. 1987; 166:1186-1191.
53. Hooda R, Madke B, Choudhary A. Photoaging: Reversal of the oxidative stress through dietary changes and plant-based products. Cureus. 2023; 15:e37321.
54. Zheng Y, Lei J, Zhang A, Cao C, Xu A, Zhou M, Lin F. Regulatory mechanisms of transforming growth factor-beta in senescence of fibroblast associated with refractory skin diseases. Exp Gerontol. 2025; 211:112900.
55. Ke Y, Wang XJ. TGFbeta signaling in photoaging and UV-induced skin cancer. J Invest Dermatol. 2021; 141:1104-1110.
56. Ge Y, Li M, Bai S, Chen C, Zhang S, Cheng J, Wang X. Doxercalciferol alleviates UVB-induced HaCaT cell senescence and skin photoaging. Int Immunopharmacol. 2024; 127:111357.
57. Belzer A, Parker ER. Climate change, skin health, and dermatologic disease: A guide for the dermatologist. Am J Clin Dermatol. 2023; 24:577-593.
58. Pal S, Bandyopadhyay S. Thermal unfolding of barstar and the properties of interfacial water around the unfolded forms. J Chem Phys. 2013; 139:235101.
59. Bang E, Kim DH, Chung HY. Protease-activated receptor 2 induces ROS-mediated inflammation through Akt-mediated NF-kappaB and FoxO6 modulation during skin photoaging. Redox Biol. 2021; 44:102022.
60. Swope VB, Abdel-Malek ZA. Significance of the melanocortin 1 and endothelin B receptors in melanocyte homeostasis and prevention of sun-induced genotoxicity. Front Genet. 2016; 7:146.
61. Yang G, Li Y, Nishimura EK, Xin H, Zhou A, Guo Y, Dong L, Denning MF, Nickoloff BJ, Cui R. Inhibition of PAX3 by TGF-beta modulates melanocyte viability. Mol Cell. 2008; 32:554-563.
62. Lin P, Hwang E, Ngo HTT, Seo SA, Yi TH. Sambucus nigra L. ameliorates UVB-induced photoaging and inflammatory response in human skin keratinocytes. Cytotechnology. 2019; 71:1003-1017.
63. Kim JC, Park TJ, Kang HY. Skin-aging pigmentation: Who is the real enemy? Cells. 2022; 11:2541.
64. Kovacs D, Cardinali G, Aspite N, Cota C, Luzi F, Bellei B, Briganti S, Amantea A, Torrisi MR, Picardo M. Role of fibroblast-derived growth factors in regulating hyperpigmentation of solar lentigo. Br J Dermatol. 2010; 163:1020-1027.
65. Hasegawa K, Fujiwara R, Sato K, Shin J, Kim SJ, Kim M, Kang HY. Possible involvement of keratinocyte growth factor in the persistence of hyperpigmentation in both human facial solar lentigines and melasma. Ann Dermatol. 2015; 27:626-629.
66. Kim M, Kim SM, Kwon S, Park TJ, Kang HY. Senescent fibroblasts in melasma pathophysiology. Exp Dermatol. 2019; 28:719-722.
67. Kim Y, Kang B, Kim JC, Park TJ, Kang HY. Senescent fibroblast-derived GDF15 induces skin pigmentation. J Invest Dermatol. 2020; 140:2478-2486.e4.
68. Yoon JE, Kim Y, Kwon S, Kim M, Kim YH, Kim JH, Park TJ, Kang HY. Senescent fibroblasts drive ageing pigmentation: A potential therapeutic target for senile lentigo. Theranostics. 2018; 8:4620-4632.
69. Battie C, Jitsukawa S, Bernerd F, Del Bino S, Marionnet C, Verschoore M. New insights in photoaging, UVA induced damage and skin types. Exp Dermatol. 2014; 23 Suppl 1:7-12.
70. Fligiel SE, Varani J, Datta SC, Kang S, Fisher GJ, Voorhees JJ. Collagen degradation in aged/photodamaged skin *in vivo* and after exposure to matrix metalloproteinase-1 *in vitro*. J Invest Dermatol. 2003; 120:842-848.
71. Wynn TA, Vannella KM. Macrophages in tissue repair, regeneration, and fibrosis. Immunity. 2016; 44:450-462.
72. Horiba S, Kami R, Tsutsui T, Hosoi J. IL-34 Downregulation–associated M1/M2 macrophage imbalance is related to inflammaging in sun-exposed human skin. JID Innov. 2022; 2:100112.
73. Horiba S, Kawamoto M, Tobita R, Kami R, Ogura Y, Hosoi J. M1/M2 macrophage skewing is related to reduction in types I, V, and VI collagens with aging in sun-exposed human skin. JID Innov. 2023; 3:100222.

74. Kim H, Jang J, Song MJ, Park CH, Lee DH, Lee SH, Chung JH. Inhibition of matrix metalloproteinase expression by selective clearing of senescent dermal fibroblasts attenuates ultraviolet-induced photoaging. Biomed Pharmacother. 2022; 150:113034.
75. Fisher GJ, Sachs DL, Voorhees JJ. Ageing: Collagenase-mediated collagen fragmentation as a rejuvenation target. Br J Dermatol. 2014; 171:446-449.
76. Kroemer G, Maier AB, Cuervo AM, Gladyshev VN, Ferrucci L, Gorbunova V, Kennedy BK, Rando TA, Seluanov A, Sierra F, Verdin E, Lopez-Otin C. From geroscience to precision geromedicine: Understanding and managing aging. Cell. 2025; 188:2043-2062.
77. Schwarz T. 25 years of UV-induced immunosuppression mediated by T cells-From disregarded T suppressor cells to highly respected regulatory T cells. Photochem Photobiol. 2008; 84:10-18.
78. Schwarz A, Maeda A, Schwarz T. Alteration of the migratory behavior of UV-induced regulatory T cells by tissue-specific dendritic cells. J Immunol. 2007; 178:877-886.
79. Yamazaki S, Odanaka M, Nishioka A, Kasuya S, Shime H, Hemmi H, Imai M, Riethmacher D, Kaisho T, Ohkura N, Sakaguchi S, Morita A. Ultraviolet B-induced maturation of CD11b-type langerin(-) dendritic cells controls the expansion of Foxp3(+) regulatory T cells in the skin. J Immunol. 2018; 200:119-129.
80. Rannug A, Rannug U. The tryptophan derivative 6-formylindolo[3,2-b]carbazole, FICZ, a dynamic mediator of endogenous aryl hydrocarbon receptor signaling, balances cell growth and differentiation. Crit Rev Toxicol. 2018; 48:555-574.
81. Vogeley C, Esser C, Tuting T, Krutmann J, Haarmann-Stemmann T. Role of the aryl hydrocarbon receptor in environmentally induced skin aging and skin carcinogenesis. Int J Mol Sci. 2019; 20:6005.
82. Walterscheid JP, Nghiem DX, Kazimi N, Nutt LK, McConkey DJ, Norval M, Ullrich SE. Cis-urocanic acid, a sunlight-induced immunosuppressive factor, activates immune suppression *via* the 5-HT2A receptor. Proc Natl Acad Sci U S A. 2006; 103:17420-17425.
83. Newson J, Motwani MP, Kendall AC, Nicolaou A, Muccioli GG, Alhouayek M, Bennett M, Van De Merwe R, James S, De Maeyer RPH, Gilroy DW. Inflammatory resolution triggers a prolonged phase of immune suppression through COX-1/mPGES-1-derived prostaglandin E2. Cell Rep. 2017; 20:3162-3175.
84. Ghiringhelli F, Menard C, Terme M, *et al*. CD4+CD25+ regulatory T cells inhibit natural killer cell functions in a transforming growth factor-beta-dependent manner. J Exp Med. 2005; 202:1075-1085.
85. Salminen A. Activation of immunosuppressive network in the aging process. Ageing Res Rev. 2020; 57:100998.
86. Nasti TH, Yusuf N, Sherwani MA, Athar M, Timares L, Elmets CA. Regulatory T cells play an important role in the prevention of murine melanocytic nevi and melanomas. Cancer Prev Res (Phila). 2021; 14:165-174.
87. Xie Y, Yang A, Li N, Zheng H, Zhong Y, Jin Y, Li J, Ye R, Du L, Hu F. Lapagyl mitigates UV-induced inflammation and immunosuppression *via* Foxp3+ Tregs and CCL pathway: A single-cell transcriptomics study. Phytomedicine. 2024; 129:155679.
88. Nelson G, Wordsworth J, Wang C, Jurk D, Lawless C, Martin-Ruiz C, von Zglinicki T. A senescent cell bystander effect: Senescence-induced senescence. Aging Cell. 2012; 11:345-349.
89. Toyama S, Moniaga CS, Nakae S, Kurosawa M, Ogawa H, Tominaga M, Takamori K. Regulatory T cells exhibit interleukin-33-dependent migratory behavior during skin barrier disruption. Int J Mol Sci. 2021; 22:7443.
90. Gao W, Yuan LM, Zhang Y, Huang FZ, Gao F, Li J, Xu F, Wang H, Wang YS. miR-1246-overexpressing exosomes suppress UVB-induced photoaging *via* regulation of TGF-beta/Smad and attenuation of MAPK/AP-1 pathway. Photochem Photobiol Sci. 2023; 22:135-146.
91. Liu Z, Li Y, Song H, He J, Li G, Zheng Y, Li B. Collagen peptides promote photoaging skin cell repair by activating the TGF-beta/Smad pathway and depressing collagen degradation. Food Funct. 2019; 10:6121-6134.
92. Harris J. Autophagy and cytokines. Cytokine. 2011; 56:140-144.
93. Wu TT, Li WM, Yao YM. Interactions between autophagy and inhibitory cytokines. Int J Biol Sci. 2016; 12:884-897.
94. Iddamalgoda A, Le QT, Ito K, Tanaka K, Kojima H, Kido H. Mast cell tryptase and photoaging: possible involvement in the degradation of extra cellular matrix and basement membrane proteins. Arch Dermatol Res. 2008; 300 Suppl 1:S69-S76.
95. Korhonen J, Siiskonen H, Haimakainen S, Harvima RJ, Harvima IT. Expression of mast cell tryptase and immunoglobulin E is increased in cutaneous photodamage: Implications for carcinogenesis. J Dermatolog Treat. 2024; 35:2307488.
96. Hernandez-Barrera R, Torres-Alvarez B, Castanedo-Cazares JP, Oros-Ovalle C, Moncada B. Solar elastosis and presence of mast cells as key features in the pathogenesis of melasma. Clin Exp Dermatol. 2008; 33:305-308.
97. Lestarevic S, Savic S, Dejanovic M, Mijovic M, Mandic P, Marjanovic D, Filipovic M, Rancic IB, Jorgacevic T. The effect of aging on mast cell density in human skin: A comparative analysis of photoexposed and photoprotected regions. Folia Morphol (Warsz). 2024. doi: 10.5603/fm.102163.
98. Fajardo I, Pejler G. Human mast cell beta-tryptase is a gelatinase. J Immunol. 2003; 171:1493-1499.
99. Bosset S, Bonnet-Duquennoy M, Barre P, Chalon A, Kurfurst R, Bonte F, Schnebert S, Le Varlet B, Nicolas JF. Photoageing shows histological features of chronic skin inflammation without clinical and molecular abnormalities. Br J Dermatol. 2003; 149:826-835.
100. Lee H, Hong Y, Kim M. Structural and functional changes and possible molecular mechanisms in aged skin. Int J Mol Sci. 2021; 22:12489.
101. Helfrich YR, Maier LE, Cui Y, Fisher GJ, Chubb H, Fligiel S, Sachs D, Varani J, Voorhees J. Clinical, histologic, and molecular analysis of differences between erythematotelangiectatic rosacea and telangiectatic photoaging. JAMA Dermatol. 2015; 151:825-836.
102. Ishitsuka Y, Maniwa F, Koide C, Kato Y, Nakamura Y, Osawa T, Tanioka M, Miyachi Y. Increased halogenated tyrosine levels are useful markers of human skin ageing, reflecting proteins denatured by past skin inflammation. Clin Exp Dermatol. 2012; 37:252-258.
103. Malaviya R, Morrison AR, Pentland AP. Histamine in human epidermal cells is induced by ultraviolet light injury. J Invest Dermatol. 1996; 106:785-789.
104. Kim MS, Lee DH, Lee CW, Kim YK, Lee MJ, Shin CY, Cho KH, Chung JH. Mast cell stabilizer, ketotifen, prevents UV-induced wrinkle formation. J Invest

Dermatol. 2013; 133:1104-1107.
105. Yoshida M, Hirotsu S, Nakahara M, Uchiwa H, Tomita Y. Histamine is involved in ultraviolet B-induced pigmentation of guinea pig skin. J Invest Dermatol. 2002; 118:255-260.
106. Bohm M, Stegemann A, Paus R, Kleszczynski K, Maity P, Wlaschek M, Scharffetter-Kochanek K. Endocrine controls of skin aging. Endocr Rev. 2025; 46:349-375.
107. Wlaschek M, Maity P, Makrantonaki E, Scharffetter-Kochanek K. Connective tissue and fibroblast senescence in skin aging. J Invest Dermatol. 2021; 141:985-992.
108. Shen ZQ, Chang CY, Yeh CH, Lu CK, Hung HC, Wang TW, Wu KS, Tung CY, Tsai TF. Hesperetin activates CISD2 to attenuate senescence in human keratinocytes from an older person and rejuvenates naturally aged skin in mice. J Biomed Sci. 2024; 31:15.
109. Xu S, Sun X, Zhu Z, Xin Y, Chen C, Luo J. The extract of buds of Chrysanthemum morifolium ramat alleviated UVB-induced skin photoaging by regulating MAPK and Nrf2/ARE pathways. J Ethnopharmacol. 2024; 332:118352.
110. Tan CYR, Tan CL, Chin T, Morenc M, Ho CY, Rovito HA, Quek LS, Soon AL, Lim JSY, Dreesen O, Oblong JE, Bellanger S. Nicotinamide prevents UVB- and oxidative stress–induced photoaging in human primary keratinocytes. J Invest Dermatol. 2022; 142:1670-1681 e1612.
111. Zhang H, Xiao X, Wang L, Shi X, Fu N, Wang S, Zhao RC. Human adipose and umbilical cord mesenchymal stem cell-derived extracellular vesicles mitigate photoaging *via* TIMP1/Notch1. Signal Transduct Target Ther. 2024; 9:294.
112. Shen Y, Kim K, Zhu Z, Zhang S, Jiang M, Liu Z, Zheng Y, Li X, Jin L, Cong W. delta-catenin requirement in keratinocyte proliferation and DNA repair identifies a therapeutic target for photoaging. J Invest Dermatol. 2023; 143:26-36 e28.
113. Liu W, Yan F, Xu Z, Chen Q, Ren J, Wang Q, Chen L, Ying J, Liu Z, Zhao J, Qiu J, Zhang C, Jiang M, Xiang L. Urolithin A protects human dermal fibroblasts from UVA-induced photoaging through NRF2 activation and mitophagy. J Photochem Photobiol B. 2022; 232:112462.
114. Xia Y, Zhang H, Wu X, Xu Y, Tan Q. Resveratrol activates autophagy and protects from UVA-induced photoaging in human skin fibroblasts and the skin of male mice by regulating the AMPK pathway. Biogerontology. 2024; 25:649-664.
115. Sun JM, Liu YX, Liu YD, Ho CK, Tsai YT, Wen DS, Huang L, Zheng DN, Gao Y, Zhang YF, Yu L. Salvianolic acid B protects against UVB-induced skin aging *via* activation of NRF2. Phytomedicine. 2024; 130:155676.
116. Wen SY, Ng SC, Chiu YT, Tai PY, Chen TJ, Chen CJ, Huang CY, Kuo WW. Enhanced SIRT1 activity by galangin mitigates UVB-induced senescence in dermal fibroblasts *via* p53 acetylation regulation and activation. J Agric Food Chem. 2024; 72:23286-23294.
117. Hwang E, Park SY, Lee HJ, Lee TY, Sun ZW, Yi TH. Gallic acid regulates skin photoaging in UVB-exposed fibroblast and hairless mice. Phytother Res. 2014; 28:1778-1788.
118. Jung JM, Choi JK, Kwon OY, Lee SH. Anti-photoaging activity of Scutellaria barbata D. Don (Family Lamiaceae) on ultraviolet B-irradiated NIH-3T3 skin fibroblast and SKH-1 hairless mouse. Molecules. 2022; 27:3803.
119. He X, Wang C, Zhang Q, Yang T, Guo Q, Wang Y, Guo J, Wang P, Zhang J, Tang H, Zhu Y, Wang J. Identifying ENO1 as a protein target of chlorogenic acid to inhibit cellular senescence and prevent skin photoaging in mice. Aging Cell. 2025; 24:e14433.
120. Chen J, Luo J, Tan Y, Wang M, Liu Z, Yang T, Lei X. Effects of low-dose ALA-PDT on fibroblast photoaging induced by UVA irradiation and the underlying mechanisms. Photodiagnosis Photodyn Ther. 2019; 27:79-84.
121. Tang Z, Liu Z, Zhang Y, Luo S, Xu Y, Ren L. Functional hyaluronic acid microneedles for skin photoaging based on collagen induction and oxidative stress regulation strategies. Int J Biol Macromol. 2024; 277:134080.
122. Gentile P, Garcovich S. Adipose-derived mesenchymal stem cells (AD-MSCs) against ultraviolet (UV) radiation effects and the skin photoaging. Biomedicines. 2021; 9:532.
123. Yan T, Huang L, Yan Y, Zhong Y, Xie H, Wang X. Bone marrow mesenchymal stem cell-derived exosome miR-29b-3p alleviates UV irradiation-induced photoaging in skin fibroblast. Photodermatol Photoimmunol Photomed. 2023; 39:235-245.
124. Zasada M, Budzisz E, Erkiert-Polguj A. A clinical anti-ageing comparative study of 0.3 and 0.5% retinol serums: A clinically controlled trial. Skin Pharmacol Physiol. 2020; 33:102-116.
125. Chung CL, Lawrence I, Hoffman M, Elgindi D, Nadhan K, Potnis M, Jin A, Sershon C, Binnebose R, Lorenzini A, Sell C. Topical rapamycin reduces markers of senescence and aging in human skin: An exploratory, prospective, randomized trial. Geroscience. 2019; 41:861-869.
126. Seo E, Song HH, Kim H, Kim BY, Park S, Suh HJ, Ahn Y. Oral administration of mixed probiotics improves photoaging by modulating the cecal microbiome and MAPK pathway in UVB-irradiated hairless mice. Mol Nutr Food Res. 2023; 67:e2200841.
127. Qu L, Ma X, Wang F. The roles of gut microbiome and metabolites associated with skin photoaging in mice by intestinal flora sequencing and metabolomics. Life Sci. 2024; 341:122487.
128. Yu GT, Ganier C, Allison DB, Tchkonia T, Khosla S, Kirkland JL, Lynch MD, Wyles SP. Mapping epidermal and dermal cellular senescence in human skin aging. Aging Cell. 2025; 24:e14358.
129. Hu X, Du S, Chen M, Yang H, He J, Zhang L, Tan B, Wu T, Duan X. Single-cell sequencing combined with transcriptome sequencing to explore the molecular mechanisms related to skin photoaging. J Inflamm Res. 2024; 17:11137-11160.
130. Zou Z, Long X, Zhao Q, *et al*. A single-cell transcriptomic atlas of human skin aging. Dev Cell. 2021; 56:383-397 e388.
131. Barnes BM, Shyne A, Gunn DA, Griffiths CEM, Watson REB. Epigenetics and ultraviolet radiation: Implications for skin ageing and carcinogenesis. Skin Health Dis. 2024; 4:e410.
132. Mehrabi JN, Baugh EG, Fast A, Lentsch G, Balu M, Lee BA, Kelly KM. A clinical perspective on the automated analysis of reflectance confocal microscopy in dermatology. Lasers Surg Med. 2021; 53:1011-1019.
133. Tang H, Wang F, Yang R, Zhao Z, Zhang Y, Yang L, Li B. Baricitinib-loaded EVs promote alopecia areata mouse hair regrowth by reducing JAK-STAT-mediated inflammation and promoting hair follicle regeneration. Drug Discov Ther. 2025; 18:368-374.

134. Sinha S, Lin G, Ferenczi K. The skin microbiome and the gut-skin axis. Clin Dermatol. 2021; 39:829-839.

Received February 7, 2026; Revised March 12, 2026; Accepted March 19, 2026.

[§]These authors contributed equally to this work.

*Address correspondence to:
Weijie Gu, Department of Dermatology, Air Force Medical Center, Fourth Military Medical University, Beijing 100142, China.
E-mail: guweijie113@163.com

Lixia Zhang, Department of Burns and Plastic Surgery, Fourth Medical Center of the Chinese PLA General Hospital, Beijing 100048, China.
E-mail: vivian-0506@163.com

Released online in J-STAGE as advance publication March 21, 2026.

Original Article

DOI: 10.5582/bst.2026.01026

The ATF5-GPER1 axis drives female protection in hepatocellular carcinoma through dual tumor-suppressive and immune-modulatory mechanisms

Zhiquan Xu[1,§], Hao Wang[1,§], Qiang He[1,§], Hongshuai Cui[2], Zhongjun Wu[1,*], Rui Liao[1,*]

[1] Department of Hepatobiliary Surgery, the First Affiliated Hospital of Chongqing Medical University, Chongqing, China;
[2] Department of Gastrointestinal Surgery, Qingdao Central Hospital, University of Health and Rehabilitation Sciences, Qingdao, China.

SUMMARY: Hepatocellular carcinoma (HCC) exhibits marked sexual dimorphism, with females demonstrating superior survival, yet the underlying molecular mechanisms remain unclear. We integrated bulk transcriptomics (GSE39791, TCGA-LIHC, GSE14520) and single-cell RNA sequencing (five datasets, n = 58 patients, 238,982 cells) with machine learning (LASSO, SVM, random forest) to identify female-protective genes driving HCC disparities. Activating transcription factor 5 (ATF5) emerged as a female-protective gene with higher expression in females versus males across cohorts. Single-cell analyses revealed ATF5 defines a female-enriched, low-grade malignant subcluster with elevated apoptotic programs and reduced proliferative signaling, and pseudotime analysis showed coordinated ATF5-GPER1 downregulation during malignant progression (Spearman $\rho = -0.52$ and -0.48; both $p < 0.001$). In the immune compartment, ATF5 marked a female-enriched IFN-γ^+ macrophage state with enhanced immunostimulatory programs and preferential CXCL9/10–CXCR3-mediated communication with CD8/NK cells. Mechanistically, ATF5 transcriptionally activates G protein-coupled estrogen receptor 1 (GPER1), forming an estrogen-responsive regulatory module that functionally suppresses proliferation, induces apoptosis (HepG2: 26.45% *vs*. 11.88%, $p < 0.0001$), and inhibits migration in a GPER1-dependent manner as demonstrated by rescue experiments. Tissue microarray validation (n = 167) confirmed high ATF5 expression predicts improved recurrence-free survival specifically in female patients (HR = 0.34, $p = 0.040$) but not males ($p = 0.080$). The ATF5-GPER1 axis represents a female-protective circuit operating through tumor-intrinsic suppression and immune remodeling, offering mechanistic insight into HCC sexual dimorphism and identifying ATF5 as a sex-specific prognostic biomarker with potential therapeutic implications.

Keywords: sex differences, transcription factor, estrogen signaling, tumor-associated macrophages, single-cell RNA sequencing

1. Introduction

Hepatocellular carcinoma (HCC) ranks as the sixth most common tumor globally and is the third leading cause of cancer-related mortality, accounting for 865,269 new cases and 757,948 deaths annually (*1*). A defining feature of HCC is its striking sexual dimorphism: men exhibit 2–3-fold higher incidence and consistently poorer survival compared to women (*2,3*). This robust pattern persists after adjusting for viral hepatitis, alcohol consumption, and metabolic factors, implicating intrinsic sex-based biological mechanisms (*4*).

Classical estrogen receptor pathways, particularly ERα, inhibit hepatocyte proliferation and suppress pro-inflammatory networks (*5,6*). However, clinical trials with estrogen-based interventions have failed (*7*), and accumulating evidence suggests canonical ER signaling alone cannot fully explain the sex disparity in HCC. This highlights a critical gap: unidentified sex-specific molecular circuits operating independently of classical estrogen-ER pathways.

Sex also profoundly influences the tumor immune microenvironment. Female HCC patients exhibit higher proportions of cytotoxic lymphocytes and M1-polarized macrophages, while male tumors are enriched for immunosuppressive myeloid populations (*8,9*). Female patients show more durable benefit from immune checkpoint inhibitors despite lower initial response rates (*10*), suggesting sex-specific immune architectures reshape therapeutic vulnerability. Yet the molecular determinants linking sex-biased gene expression to immune remodeling remain unexplored.

Single-cell RNA sequencing (scRNA-seq) has revolutionized understanding of tumor heterogeneity

(*11,12*), identifying sex-specific malignant cell states and immune vulnerabilities in lung cancer, melanoma, and bladder cancer (*13-15*). However, integrative single-cell analyses systematically interrogating sex differences in HCC at cellular resolution remain scarce.

Activating transcription factor 5 (ATF5), a member of the ATF/CREB transcription factor family, has been implicated in stress responses, differentiation, and survival (*16*). While exhibiting oncogenic functions in glioblastoma and breast cancer (*17*), its role in liver cancer and involvement in sex-biased HCC biology remain undefined. G protein-coupled estrogen receptor 1 (GPER1), a membrane-bound estrogen receptor mediating rapid non-genomic signaling (*18*), has emerged as a candidate mediator of estrogen's protective effects, yet its transcriptional regulation and contribution to HCC sexual dimorphism are unknown.

We employed an integrative approach combining bulk transcriptomics, single-cell RNA sequencing (five datasets, n = 58 patients, 238,982 cells), machine learning, and functional validation to identify molecular drivers of sexual dimorphism in HCC. We identified ATF5 as a female-biased tumor suppressor preferentially expressed in malignant hepatocytes and tumor-associated macrophages. ATF5 directly transactivates GPER1, establishing an estrogen-responsive circuit suppressing proliferation, inducing apoptosis, and inhibiting migration. Single-cell analyses revealed ATF5 delineates a female-enriched, low-grade malignant subcluster and an immunostimulatory IFN-γ^+ macrophage state with enhanced chemokine-mediated lymphocyte recruitment. Clinical validation (n = 167) confirmed high ATF5 predicts improved recurrence-free survival specifically in females. Our findings identify the ATF5-GPER1 axis as a novel female-protective circuit operating through dual tumor-intrinsic and immune-modulatory mechanisms.

2. Materials and Methods

2.1. Data acquisition and pprocessing

A retrospective HCC tissue microarray (TMA) was constructed from 167 patients who underwent curative hepatectomy at the First Affiliated Hospital of Chongqing Medical University (January 2020–January 2025). The study was approved by the institutional ethics committee (Approval No. 2024-607-01). Public bulk transcriptomic datasets were obtained from GEO (GSE39791, GSE14520) and TCGA-LIHC (GDC; 374 tumors and 59 adjacent tissues). Five GEO scRNA-seq datasets (GSE242898, GSE146115, GSE156625, GSE151530, GSE149614) were integrated, comprising 58 patients (14 females, 44 males) and 238,982 cells after quality control. Samples were categorized as female/male tumor (FC/MC) or adjacent tissue (FP/MP).

A retrospective HCC tissue microarray (TMA) was constructed from 167 patients who underwent curative hepatectomy at the First Affiliated Hospital of Chongqing Medical University (January 2020–January 2025). Of these, 140 patients (83.8%) were HBsAg-positive, reflecting the HBV-predominant etiology of HCC in this Chinese cohort. The study was approved by the institutional ethics committee (Approval No. 2024-607-01). Public bulk transcriptomic datasets were obtained from GEO (GSE39791, GSE14520) and TCGA-LIHC (GDC; 374 tumors and 59 adjacent tissues). Five GEO scRNA-seq datasets (GSE242898, GSE146115, GSE156625, GSE151530, GSE149614) were integrated, comprising 58 patients (14 females, 44 males) and 238,982 cells after quality control. Samples were categorized as female/male tumor (FC/MC) or adjacent tissue (FP/MP).

2.2. Transcriptomic and machine learning analyses

Differential expression analysis was conducted using limma (FDR < 0.05, $|\log_2 FC| > 0.58$). Feature selection was performed using LASSO, SVM, and random forest with 10-fold cross-validation, and pathway enrichment was evaluated by GSEA. Prognostic analyses used Kaplan–Meier (log-rank) and Cox regression. Diagnostic performance was assessed by ROC analysis (AUC with DeLong confidence intervals).

2.3. Single-cell RNA-seq data processing

scRNA-seq data were processed in Seurat with standard quality control, normalization, integration, clustering, and UMAP visualization, followed by cell-type annotation using canonical markers. Malignant cells were inferred by inferCNV using immune/stromal cells as references and a conservative CNV-score threshold (0.0321), yielding 38,844 malignant cells. Macrophages (23,093 cells) were re-clustered and annotated into functional subtypes, including IFN-γ^+ macrophages defined by interferon-stimulated gene expression. Pseudotime trajectories were reconstructed using Monocle3 (Cluster 3 as the root), cell–cell communication was analyzed using CellChat, and bulk immune infiltration in TCGA-LIHC was estimated by ssGSEA with Bindea immune signatures.

2.4. Multiplex immunofluorescence and quantification

FFPE TMA sections (4 μm) were subjected to antigen retrieval (Tris–EDTA, pH 9.0) and sequential multiplex immunofluorescence using primary antibodies against ATF5 (Cell Signaling Technology #94850), CD68 (Abcam ab125212), and GPER1 (Abcam ab39742), followed by microwave-based stripping between cycles and DAPI counterstaining. Slides were scanned on a Vectra Polaris system and quantified with QuPath. Mean fluorescence intensity per core was background-corrected and normalized; survival analyses used median cutoffs and Cox regression.

2.5. Transcription factor binding site prediction

ATF5 motif analysis was performed using JASPAR (MA0833.1). The GPER1 promoter region (−2 kb from TSS; hg38) was retrieved from UCSC, and binding sites were predicted using FIMO ($p < 1\times10^{-4}$). To explore the mechanistic basis of female-biased ATF5 expression, the ATF5 promoter region (chr19:49,926,906–49,928,906, GRCh38) was scanned for estrogen response elements (EREs) using FIMO with JASPAR position weight matrices for ESR1 (MA0112.3, $p < 1\times10^{-4}$) and ESR2 (MA0258.1, $p < 0.001$). DNA methylation at ATF5 promoter CpG probes (HM450 array) was retrieved from TCGA-LIHC and compared between sexes using Wilcoxon tests; Spearman correlation was used to assess the relationship between promoter methylation (mean β value) and ATF5 mRNA expression.

2.6. Cell culture and hhormone treatments

HepG2 (CL-0103) and Huh7 (CL-0120) cells (Procell, Wuhan, China) were maintained in DMEM with 10% FBS and antibiotics at 37°C with 5% CO_2 and authenticated by STR profiling. For hormone stimulation, cells were conditioned in phenol red–free medium with charcoal-stripped FBS and treated with E2 (10 nM), G-1 (100 nM), and/or G36 (10 μM) for 24 h, with G36 added 1 h before E2 where indicated.

2.7. Gene manipulation

ATF5 knockdown was achieved using lentiviral shRNA with puromycin selection. ATF5 overexpression used pcDNA3.1-based transfection, and GPER1 knockdown used siRNA transfection. Perturbation efficiency was validated by qRT-PCR and Western blotting.

2.8. Molecular assays

qRT-PCR was performed using standard TRIzol-based RNA extraction, reverse transcription, and SYBR-based quantification with β-actin normalization ($2^{-\Delta\Delta Ct}$). Western blotting was performed using RIPA lysates, SDS-PAGE, PVDF transfer, immunodetection, and ImageJ quantification. Dual-luciferase assays were conducted using WT/MUT GPER1 promoter reporters co-transfected with ATF5 and Renilla control, and measured at 48 h.

2.9. Functional assays

Cell proliferation was assessed by CCK-8. Apoptosis was quantified by Annexin V/7-AAD flow cytometry. Migration was evaluated by wound-healing assays with image-based quantification.

2.10. Macrophage–T ccell co-culture assay

PMA-differentiated THP-1 macrophages were transduced with lentiviral shATF5 or shNC constructs and selected with puromycin. Conditioned medium was collected after 24 h serum-free culture and filtered (0.22 μm). Peripheral blood-derived $CD8^+$ T cells were stimulated with anti-CD3/CD28 beads and cultured in conditioned medium (1:1 ratio) for 48 h. CXCL9 and CXCL10 concentrations in conditioned medium were quantified by ELISA (R&D Systems). $CD8^+$ T cell activation was assessed by flow cytometry using anti-CD8 and anti-CD69 antibodies, with $CD8^+CD69^+$ frequency reported as the activation index.

2.11. Statistical analysis

Analyses were performed in R or GraphPad Prism. Two-group comparisons used Welch's *t*-test or Wilcoxon tests; multi-group comparisons used ANOVA or Kruskal–Wallis tests with appropriate post hoc corrections. Correlations used Spearman tests. Survival analyses used Kaplan–Meier and Cox regression. A multivariable nomogram for predicting 1- and 3-year recurrence-free survival was constructed using the rms package in R, incorporating ATF5 expression, sex, BCLC stage, age, and AFP as covariates based on a Cox proportional hazards model; model discrimination was assessed by Harrell's C-index and time-dependent AUC using the timeROC package, with calibration evaluated by bootstrap resampling (B = 200). Incremental predictive value of ATF5 was assessed by comparing the full model versus a base clinical model (BCLC stage, age, AFP, and sex) using time-dependent AUC at 1- and 3-year timepoints. Two-sided $p < 0.05$ was considered significant, and all cell-based experiments included ≥ 3 independent biological replicates.

3. Results

3.1. Integrative transcriptomic and machine learning analyses identify ATF5 as a female-protective ggene

To systematically identify molecular drivers of sexual dimorphism in HCC, we performed differential expression analysis on GSE39791 (72 samples: 58 males, 14 females). Comparing tumor versus adjacent tissues identified 4,235 differentially expressed genes (DEGs), while female versus male tumors revealed 196 sex-associated DEGs, with 100 genes overlapping both comparisons (Figure 1A-B). Directionally consistent filtering yielded 29 candidates: 4 female-protective (P>C and FC>MC) and 25 male-risk (C>P and MC>FC) genes, enriched for antigen processing pathways (adjusted $p < 0.05$; Figure 1C-D).

Three machine learning algorithms (LASSO, SVM, random forest) with 10-fold cross-validation identified nine consensus genes for tumor discrimination and six for sex stratification. Only ATF5 and WDR72 were

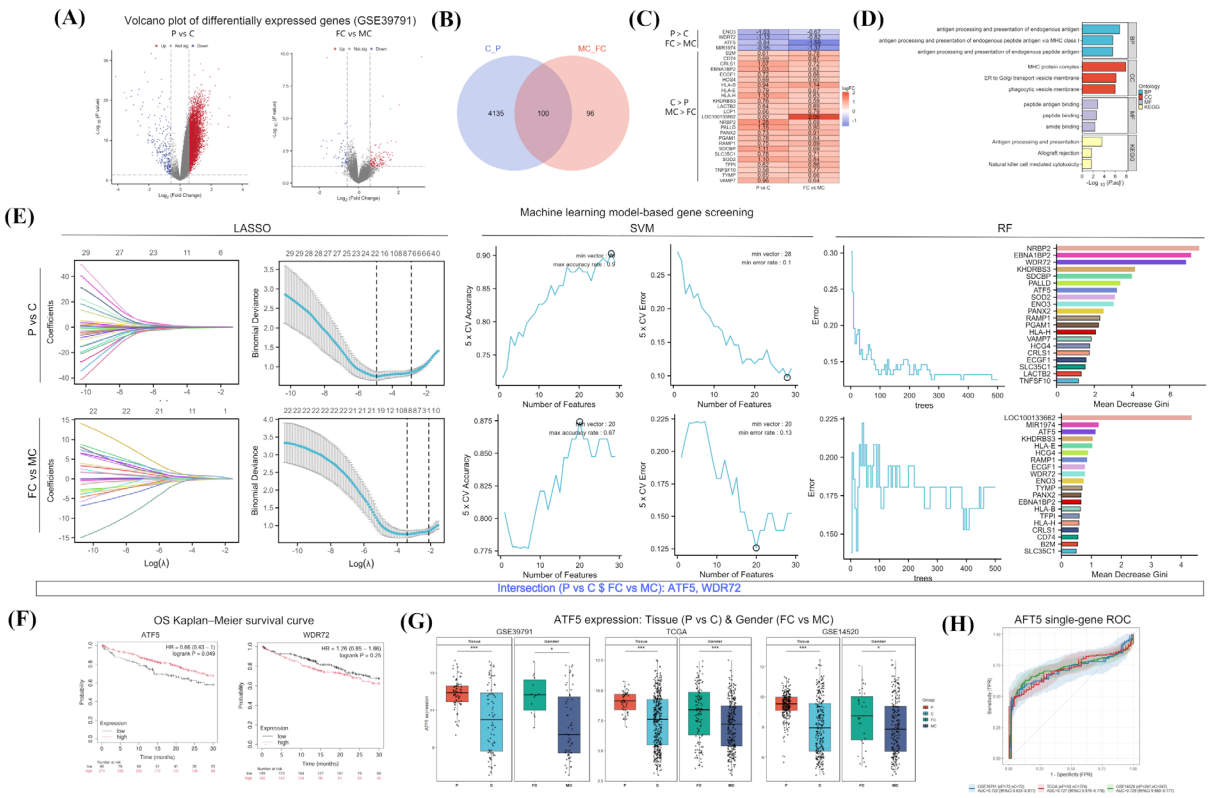

Figure 1. Integrated bulk transcriptomics and machine learning identify ATF5 as a female-protective candidate in hepatocellular carcinoma (HCC). (A) Volcano plots of differentially expressed genes (DEGs) in GSE39791 for tumor versus adjacent non-tumor tissues (C *vs*. P) and female versus male tumors (FC *vs*. MC). Significant DEGs are highlighted ($|\log_2 FC| > 0.58$, false discovery rate [FDR] < 0.05). **(B)** Venn diagram showing overlap between tumor-associated DEGs (C *vs*. P) and sex-associated DEGs (FC *vs*. MC). **(C)** Directionally consistent filtering of shared genes to define female-protective (P > C and FC > MC) and male-risk (C > P and MC > FC) patterns; heatmap shows $\log_2$ fold changes. **(D)** Gene Ontology (GO) and Kyoto Encyclopedia of Genes and Genomes (KEGG) enrichment analysis of candidate genes. **(E)** Feature selection using least absolute shrinkage and selection operator (LASSO), support vector machine (SVM), and random forest (RF) with 10-fold cross-validation for C *vs*. P and FC *vs*. MC tasks; shared features are indicated. **(F)** Kaplan–Meier overall survival in The Cancer Genome Atlas Liver Hepatocellular Carcinoma cohort (TCGA-LIHC) stratified by median gene expression (ATF5 and comparator gene shown). **(G)** ATF5 expression validation across independent datasets (GSE39791, TCGA-LIHC, GSE14520) by tissue status and sex. **(H)** Receiver operating characteristic (ROC) curves and area under the curve (AUC) for ATF5 discriminating tumor versus adjacent tissue across datasets (AUC with 95% confidence interval shown). Statistical significance is denoted as: ns, not significant; *$p < 0.05$; **$p < 0.01$; ***$p < 0.001$; ****$p < 0.0001$.

shared across both tasks (Figure 1E). Kaplan-Meier analysis in TCGA-LIHC showed ATF5 associated with improved overall survival (median: high 65.2 *vs*. low 42.8 months; log-rank $p = 0.048$), whereas WDR72 lacked prognostic value ($p = 0.25$; Figure 1F).

ATF5 consistently showed higher expression in adjacent versus tumor tissues and in female versus male tumors across three independent datasets (GSE39791, TCGA-LIHC, GSE14520; all $p < 0.01$; Figure 1G). ROC analysis demonstrated reproducible diagnostic performance (AUC: GSE39791 0.89 [95% CI: 0.82–0.96], TCGA-LIHC 0.76 [0.71–0.81], GSE14520 0.71 [0.64–0.78]; Figure 1H).

3.2. Single-cell transcriptomic atlas confirms female-biased ATF5 expression in malignant hepatocytes

Integration of five scRNA-seq datasets (GSE242898, GSE146115, GSE156625, GSE151530, GSE149614; 58 patients, 238,982 cells) with Harmony batch correction yielded 23 clusters annotated into epithelial/hepatocyte-lineage, immune, and stromal populations (Supplementary Figure S1A, *https://www.biosciencetrends.com/action/getSupplementalData.php?ID=290*, Figure 2A-B). inferCNV analysis using epithelial-lineage cells (n = 59,071) as observation and immune/stromal cells (n = 49,154) as reference classified 38,844 malignant cells based on CNV score threshold (95th percentile = 0.0321), comprising 65.2% hepatocyte-like and 31.1% epithelial-like cells (Figure 2C-D).

ATF5 expression concentrated in epithelial/hepatocyte-lineage cells and macrophages (Figure 2E). Within malignant cells, ATF5 showed female bias: mean expression FC 0.26 versus MC 0.21 (Wilcoxon $p < 0.01$); ATF5-positive fraction FC 17.5% versus MC 12.4% (chi-square $p < 0.001$; Figure 2F).

Multiplex immunofluorescence on independent tissue microarray (n = 167: FC 27, MC 140, FP 26, MP 133) confirmed female-biased ATF5 protein expression (Figure 2G). Quantification showed significantly

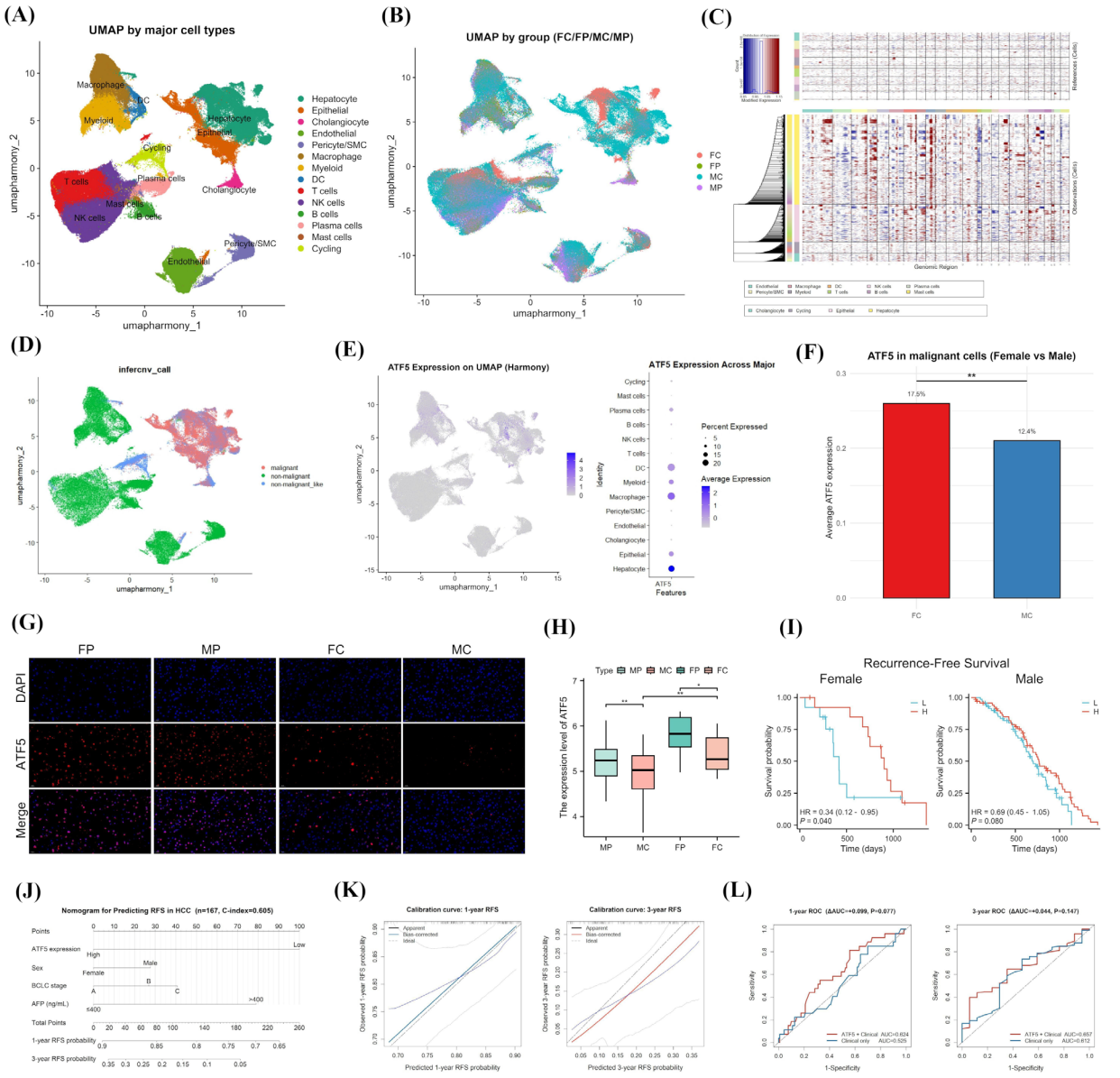

Figure 2. Single-cell and tissue-level validation confirms female-biased ATF5 expression in malignant cells and association with recurrence-free survival. (A) Uniform manifold approximation and projection (UMAP) of the integrated single-cell RNA-seq (scRNA-seq) atlas from five GEO datasets, colored by annotated major cell types. **(B)** UMAP colored by clinical group (FC/FP/MC/MP), illustrating Harmony-based integration. **(C)** inferCNV heatmap showing copy-number variation (CNV) profiles in reference (immune/stromal) and observation (epithelial-lineage) cells. **(D)** UMAP showing inferCNV-based malignancy classification using a reference-derived CNV-score threshold (malignant *vs*. non-malignant-like). **(E)** ATF5 expression in the atlas (feature plot) and across major cell types (dot plot). **(F)** Sex-stratified ATF5 expression and ATF5-positive cell fraction in malignant cells (tests indicated in the panel). **(G)** Representative multiplex immunofluorescence (mIF) images of ATF5 with 4′,6-diamidino-2-phenylindole (DAPI) across FP/MP/FC/MC groups (scale bar shown). **(H)** Quantification of ATF5 fluorescence intensity across groups (global and pairwise comparisons indicated in the panel). **(I)** Sex-stratified Kaplan–Meier recurrence-free survival (RFS) in the tissue microarray (TMA) cohort using median ATF5 as cutoff; hazard ratio (HR) and log-rank P are shown. **(J)** Nomogram integrating ATF5 expression, sex, BCLC stage, and AFP (ng/mL) for predicting 1- and 3-year RFS probability in the TMA cohort (n = 167, C-index = 0.605). **(K)** Calibration curves for the nomogram-predicted 1-year (left) and 3-year (right) RFS probabilities; the black line indicates apparent performance, the colored line indicates bias-corrected performance (bootstrap, B = 200), and the dashed line represents ideal calibration. **(L)** Time-dependent ROC curves comparing the full model (ATF5 + clinical variables) versus the base clinical model at 1-year (left) and 3-year (right) timepoints; AUC values and ΔAUC are shown.

higher ATF5 in FC versus MC (Dunn's p = 0.001) and FP versus MP (p = 0.020; Figure 2H). Sex-stratified survival analysis revealed high ATF5 predicted improved recurrence-free survival in females (median 48.2 *vs*. 28.6 months; HR = 0.34, 95% CI 0.12–0.95, p = 0.040) but not males (36.4 *vs*. 28.9 months; HR = 0.69, p = 0.080; Figure 2I).

To further evaluate the clinical utility of ATF5, we constructed a nomogram integrating ATF5 expression, sex, BCLC stage, and AFP to predict RFS in the TMA cohort (Figure 2J). The nomogram achieved a C-index of 0.605, and calibration curves demonstrated

good agreement between predicted and observed RFS probabilities at both 1- and 3-year timepoints (Figure 2K). Time-dependent ROC analysis showed that incorporating ATF5 into the clinical model improved the AUC at 1-year (0.624 *vs*. 0.525, ΔAUC = +0.099) and 3-year (0.657 *vs*. 0.612, ΔAUC = +0.044) timepoints compared to the base model. Although statistical significance was not reached, likely due to the limited sample size of this single-center cohort (n = 167), the consistent AUC improvement across both timepoints supports the incremental prognostic contribution of ATF5 beyond conventional clinical staging (Figure 2L).

3.3. ATF5 ddelineates an IFN-γ$^+$ macrophage subset with enhanced immunostimulatory programs

Macrophage reclustering (n = 23,093, resolution 0.6) identified 16 subclusters including IFN-γ$^+$ macrophages characterized by interferon-stimulated genes (ISG15, IFIT1, IFIT2, MX1, OAS1, STAT1), which showed highest ATF5 expression (Figure 3A-B, Supplementary Figure S2A-B, *https://www.biosciencetrends.com/action/getSupplementalData.php?ID=290*). Among 53 patients with sufficient macrophages (12 females, 41 males), females showed significantly higher ATF5-high cell proportions within IFN-γ$^+$ macrophages (median 28.4% *vs*. 18.7%; Wilcoxon $p < 0.05$; Figure 3C).

Differential expression analysis identified 319 upregulated and 149 downregulated genes in ATF5-high versus ATF5-low IFN-γ$^+$ macrophages ($|\log FC| \geq 0.25$, FDR < 0.05; Figure 3D). AUCell scoring revealed ATF5-high cells exhibited higher activity in antigen presentation (median AUC 0.52 *vs*. 0.38; $p < 0.001$), IFN response (0.61 *vs*. 0.42; $p < 0.001$), inflammatory response (0.58 *vs*. 0.44; $p < 0.001$), phagocytosis (0.48 *vs*. 0.39; $p < 0.01$), and cytotoxicity (0.44 *vs*. 0.32; $p < 0.01$), but lower immunosuppression (0.28 *vs*. 0.41; $p < 0.001$) and lipid metabolism (0.31 *vs*. 0.46; $p < 0.001$) scores (Figure 3E).

CellChat analysis revealed ATF5-high IFN-γ$^+$ macrophages preferentially engaged CD8/NK cells *via* CXCL9/10–CXCR3 (interaction strength 0.42 *vs*. 0.08; $p < 0.01$) and CCL5–CCR5 (0.36 *vs*. 0.12; $p < 0.01$), whereas ATF5-low cells showed stronger TGFB–TGFBR (0.38 *vs*. 0.15; $p < 0.01$) and SPP1–CD44 (0.41 *vs*. 0.18; $p < 0.01$) interactions (Figure 3F, Supplementary Figure S2C, *https://www.biosciencetrends.com/action/getSupplementalData.php?ID=290*).

In TCGA-LIHC (n = 374), ATF5-high tumors showed elevated macrophage scores (median 0.58 *vs*. 0.42; $p < 0.01$; Figure 3G). An IFN-γ$^+$ macrophage signature score constructed from top 30 marker genes was higher in ATF5-high females (0.52 *vs*. 0.36; $p < 0.01$) but not males (0.42 *vs*. 0.38; $p = 0.12$; Figure 3H). Tissue microarray validation confirmed higher ATF5$^+$CD68$^+$ proportions in FC versus MC tumors (2.8% *vs*. 1.6%; Wilcoxon $p < 0.05$; Figure 3I-J).

To functionally validate these findings, we knocked down ATF5 in PMA-differentiated THP-1 macrophages (Figure 3K). ELISA showed that ATF5 knockdown significantly reduced CXCL9 (118.4 ± 14.5 *vs*. 309.2 ± 44.9 pg/mL; $p < 0.01$) and CXCL10 (164.9 ± 18.3 *vs*. 401.4 ± 45.9 pg/mL; $p < 0.01$) secretion (Figure 3L). Conditioned medium from shATF5 macrophages markedly attenuated CD8$^+$ T cell activation (CD8$^+$CD69$^+$: 6.74 ± 0.77% *vs*. 25.47 ± 1.65%; $p < 0.001$; Figure 3M), confirming a causal role of ATF5 in macrophage-mediated CD8$^+$ T cell recruitment *via* the CXCL9/10–CXCR3 axis.

3.4. ATF5 directly transactivates GPER1 through an estrogen-responsive circuit

Gene Set Enrichment Analysis on ATF5-stratified GSE39791 tumors revealed significant enrichment of estrogen-related pathways in ATF5-high tumors (all NES > 1.5, FDR < 0.05), including Reactome Estrogen Dependent Gene Expression (NES = 1.652), WikiPathway Estrogen Metabolism (NES = 1.909), WikiPathway Estrogen Receptor Pathway (NES = 1.929), and WikiPathway Estrogen Signaling Pathway (NES = 1.654; Figure 4A).

Spearman correlation analysis identified GPER1 as most strongly associated with ATF5 ($\rho = 0.356$, $p < 0.001$) compared to ESR1 ($\rho = 0.209$, $p = 0.012$) and ESR2 ($\rho = 0.289$, $p < 0.001$; Figure 4B), reproducible across TCGA-LIHC (ρ=0.078, $p < 0.001$) and GSE14520 ($\rho = 0.339$, $p < 0.001$; Figure 4C). Single-cell patient-level pseudobulk analysis confirmed ATF5-GPER1 correlation ($\rho = 0.345$, $p = 0.040$; Figure 4D). ATF5-high malignant cells showed markedly elevated GPER1 (median 0.045 *vs*. 0.021; Wilcoxon $p = 2.24 \times 10^{-29}$), more pronounced in females (Figure 4E).

JASPAR motif analysis identified ATF5 binding sites in GPER1 promoter (−2kb to +200bp; FIMO $p < 1\times10^{-4}$; Figure 4F, Supplementary Figure S3A, *https://www.biosciencetrends.com/action/getSupplementalData.php?ID=290*). Lentiviral shRNA-mediated ATF5 knockdown reduced GPER1 protein concomitantly with ATF5 depletion (HepG2: ATF5 to 32% of control, $p = 0.003$; GPER1 to 38%, $p = 0.001$; Huh7: ATF5 to 28%, $p = 0.004$; GPER1 to 35%, $p = 0.001$; n = 3; Figure 4G). Dual-luciferase assays showed ATF5 increased wild-type GPER1 promoter activity 3.14-fold ($p = 5.35 \times 10^{-5}$) but not mutant promoter ($p = 0.277$; Figure 4H).

Hormone treatments (E2 10nM, G-1 100nM) upregulated ATF5 (E2: 1.82-fold, $p < 0.01$; G-1: 1.64-fold, $p < 0.05$) and GPER1 mRNA (E2: 2.15-fold, $p < 0.01$; G-1: 1.88-fold, $p < 0.05$), while GPER1 antagonist G36 (10μM) blocked E2-induced upregulation (both $p < 0.05$; Figure 4I, Supplementary Figure S3B, *https://www.biosciencetrends.com/action/getSupplementalData.php?ID=290*). Western blot confirmed protein-level regulation (E2: ATF5 1.76-fold, $p < 0.05$; GPER1 2.08-

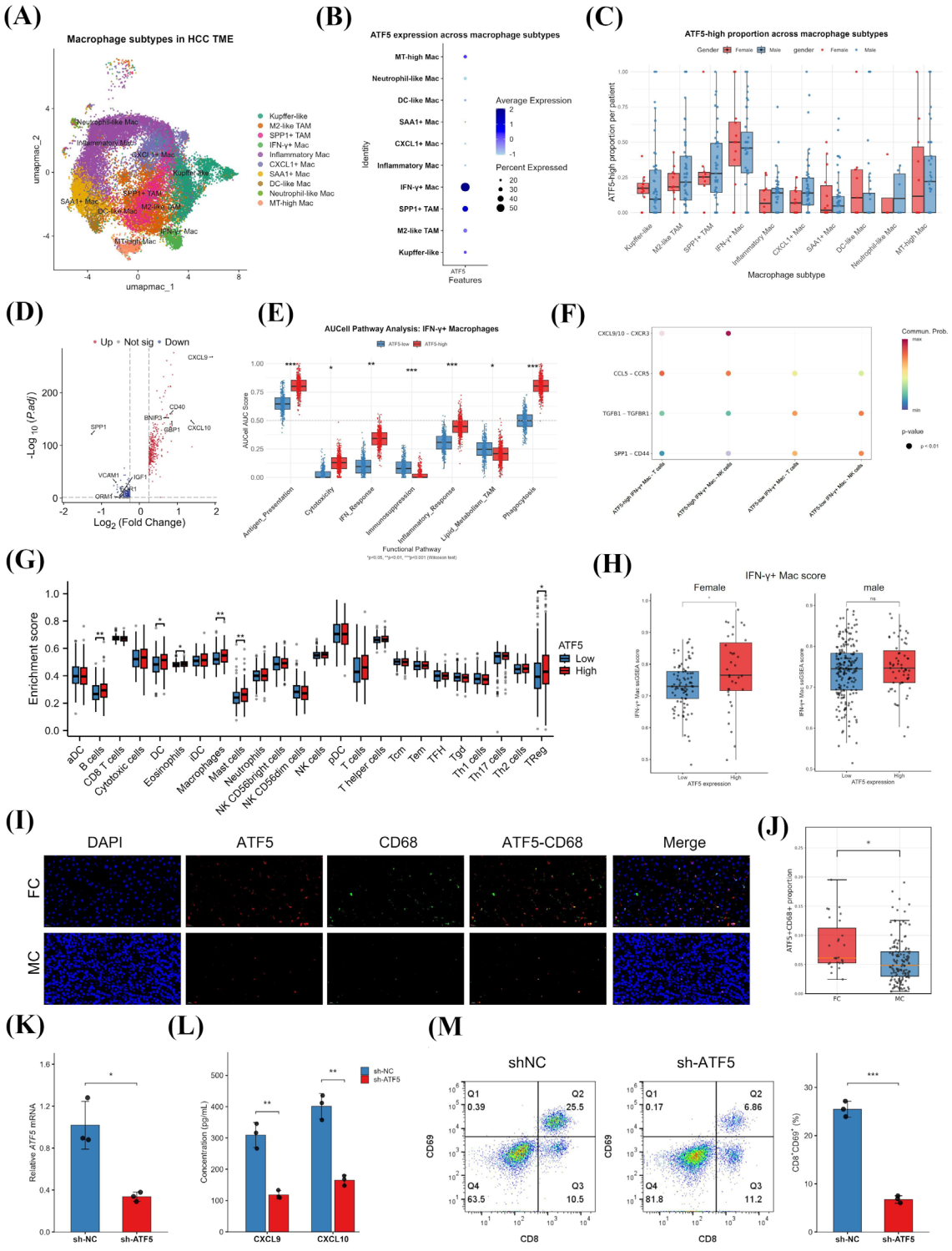

Figure 3. ATF5 delineates a female-enriched tumor-associated macrophage (TAM) state with enhanced immunostimulatory programs and CD8/NK communication. (A) UMAP of macrophage subclusters and subtype annotation; interferon-γ (IFN-γ)$^+$ macrophages are defined by interferon-stimulated gene expression. **(B)** ATF5 expression across macrophage subtypes (dot plot). **(C)** Sex-stratified proportion of ATF5-high macrophages within subtypes (definition indicated in the panel). **(D)** Differential expression between ATF5-high and ATF5-low IFN-γ$^+$ macrophages (volcano plot; thresholds indicated in the panel). **(E)** AUCell module scores comparing ATF5-high versus ATF5-low IFN-γ$^+$ macrophages (modules and significance indicated in the panel). **(F)** CellChat ligand–receptor communication from IFN-γ$^+$ macrophages to CD8 T and natural killer (NK) cells; representative interactions are highlighted. **(G)** TCGA-LIHC bulk immune infiltration estimated by single-sample gene set enrichment analysis (ssGSEA) stratified by ATF5 expression. **(H)** IFN-γ$^+$ macrophage signature score (ssGSEA) stratified by ATF5 and sex. **(I)** Representative mIF images of ATF5 and CD68 in FC *vs*. MC tumors (scale bar shown). **(J)** Quantification of ATF5$^+$CD68$^+$ cells (summary statistic and test indicated in the panel). **(K)** qPCR validation of ATF5 knockdown efficiency in PMA-differentiated THP-1 macrophages. **(L)** ELISA quantification of CXCL9 and CXCL10 in conditioned medium from sh-NC and shATF5 macrophages. **(M)** Representative flow cytometry dot plots (left) and quantification (right) of CD8$^+$CD69$^+$ T cells after co-culture with conditioned medium from sh-NC or shATF5 macrophages.

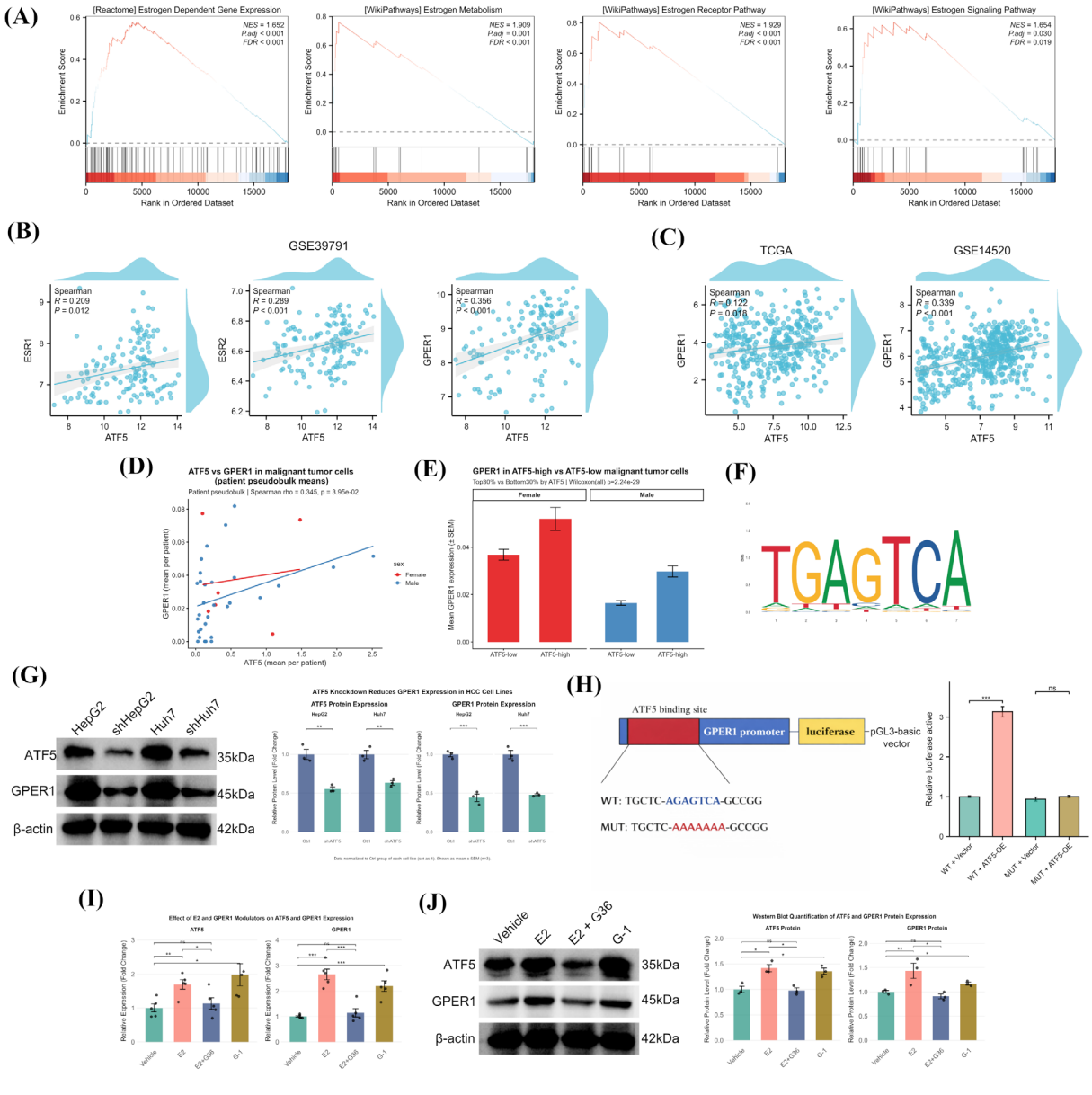

Figure 4. ATF5 transcriptionally activates GPER1 and responds to estrogen signaling. (A) Gene set enrichment analysis (GSEA) showing enrichment of estrogen-related pathways in ATF5-high versus ATF5-low tumors (GSE39791). **(B)** Correlation of ATF5 with estrogen receptor genes (ESR1/ESR2) and G protein–coupled estrogen receptor 1 (GPER1) in GSE39791 (Spearman ρ and *p* shown). **(C)** Validation of ATF5–GPER1 correlation in independent bulk cohorts (TCGA-LIHC and GSE14520). **(D)** Patient-level pseudobulk correlation of ATF5 and GPER1 in malignant cells from the scRNA-seq atlas. **(E)** GPER1 expression in malignant cells stratified by ATF5 (ATF5-high vs ATF5-low), with sex stratification. **(F)** ATF5 motif logo from the JASPAR database. **(G)** Western blot showing short hairpin RNA (shRNA)-mediated ATF5 knockdown reduces GPER1 in HepG2 and Huh7 (quantification shown). **(H)** Dual-luciferase assay using wild-type and motif-mutant (WT/MUT) GPER1 promoter reporters demonstrating ATF5-dependent transactivation. **(I)** Quantitative real-time PCR (qRT-PCR) of ATF5 and GPER1 following hormone/GPER1-modulator treatments (Vehicle, 17β-estradiol [E2], G-1, and E2+G36). **(J)** Western blot validation under the same treatment conditions.

fold, $p < 0.01$; Figure 4J).

To explore the mechanistic basis of female-biased ATF5 expression, we examined whether the ATF5 promoter contains EREs or exhibits sex-differential DNA methylation. FIMO analysis identified no classical ESR1-binding EREs (JASPAR MA0112.3, $p < 1\times10^{-4}$), but revealed three putative ERβ binding sites (JASPAR MA0258.1, $p < 0.001$), with ESR2 Site 1 located only 24 bp from CpG probe cg00423055 (Supplementary Figure S4A, *https://www.biosciencetrends.com/action/getSupplementalData.php?ID=290*). DNA methylation at all four ATF5 promoter CpG probes showed no significant sex difference in either tumor or normal tissue (all $p > 0.05$; Supplementary Figure S4B, S4C, *https://www.biosciencetrends.com/action/getSupplementalData.php?ID=290*), and promoter methylation did not correlate significantly with ATF5 expression in tumor tissue (Spearman r = −0.097, $p = 0.061$; Supplementary

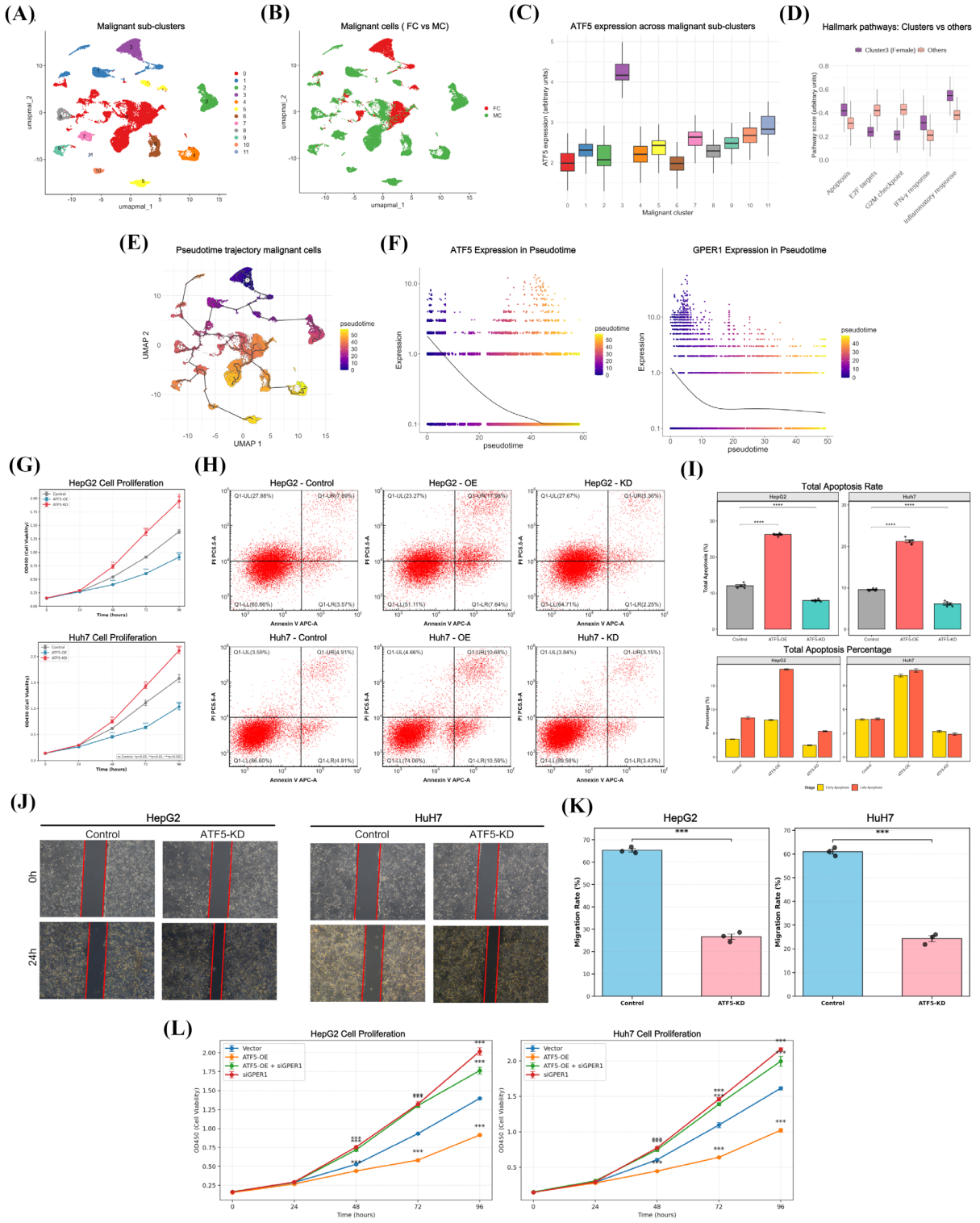

Figure 5. ATF5 defines a female-enriched malignant subcluster and suppresses HCC progression *via* GPER1-dependent mechanisms. (A) UMAP of inferCNV-defined malignant cells re-clustered into malignant subclusters. **(B)** UMAP colored by sex, highlighting a female-enriched malignant subcluster. **(C)** ATF5 expression across malignant subclusters (box plots; comparison indicated in the panel). **(D)** Hallmark pathway activity (AUCell) comparing the female-enriched subcluster versus other malignant cells. **(E)** Monocle3 pseudotime trajectory of malignant cells (root indicated in the panel). **(F)** ATF5 and GPER1 expression dynamics along pseudotime. **(G)** Cell Counting Kit-8 (CCK-8) proliferation assays following ATF5 overexpression (OE) or knockdown (KD) in HepG2 and Huh7. **(H)** Representative flow cytometry plots for apoptosis measured by Annexin V/7-AAD staining. **(I)** Quantification of apoptosis across conditions (tests indicated in the panel). **(J)** Representative wound-healing images at 0 h and 24 h. **(K)** Quantification of migration/wound closure (tests indicated in the panel). **(L)** GPER1 rescue experiment showing reversal of ATF5-mediated growth suppression by small interfering RNA (siRNA)-mediated GPER1 knockdown.

Figure S4D, *https://www.biosciencetrends.com/action/getSupplementalData.php?ID=290*). These results indicate that promoter hypomethylation does not drive female-biased ATF5 expression, and suggest that estrogen regulates ATF5 preferentially through non-classical ERβ/GPER signaling, consistent with the ATF5 upregulation observed following G-1 treatment.

3.5. ATF5 defines a low-grade malignant subcluster and suppresses tumor progression *via* GPER1-dependent mechanisms

Malignant cell reclustering (n = 38,844, resolution 0.8) identified 12 subclusters, with Cluster 3 being female-enriched and exhibiting highest ATF5 expression (median 0.476 *vs*. others 0.15–0.35; Wilcoxon $p < 0.001$; Figure 5A-C). Hallmark pathway enrichment revealed Cluster 3 elevated in Apoptosis (median AUC 0.448 *vs*. 0.321; FDR = 0.008), Inflammatory response (0.572 *vs*. 0.381; FDR < 0.001), and IFN-γ response (0.351 *vs*. 0.224; FDR = 0.042), but reduced in E2F targets (0.253 *vs*. 0.428; FDR < 0.001) and G2M checkpoint (0.218 *vs*. 0.451; FDR < 0.001; Figure 5D).

Pseudotime trajectory analysis using Monocle3 positioned Cluster 3 at the origin (pseudotime 0), with coordinated downregulation of ATF5 (mean expression: pseudotime 0 = 0.51 to pseudotime 60 = 0.09; Spearman $\rho = -0.52$, $p < 0.001$) and GPER1 ($\rho = -0.48$, $p < 0.001$) during malignant progression (Figure 5E-F).

Functional validation showed ATF5 overexpression (ATF5-OE) suppressed proliferation at 96 hours (HepG2: OD_{450} 0.911 ± 0.107 *vs*. Control 1.383 ± 0.086, $p < 0.001$; Huh7: 1.036 ± 0.136 *vs*. 1.581 ± 0.168, $p < 0.001$), while ATF5 knockdown (ATF5-KD) enhanced growth (HepG2: 1.949 ± 0.277; Huh7: 2.017 ± 0.126; both $p < 0.001$; Figure 5G). Flow cytometric analysis using Annexin V-APC/7-AAD demonstrated ATF5-OE markedly increased total apoptosis (HepG2: 26.45 ± 0.35% *vs*. Control 11.88 ± 0.87%, $p < 0.0001$; Huh7: 21.20 ± 0.75% *vs*. 9.49 ± 0.27%, $p < 0.0001$), including both early and late apoptotic populations, whereas ATF5-KD reduced apoptosis (HepG2: 7.95 ± 0.61%; Huh7: 6.14 ± 0.57%; both $p < 0.001$; Figure 5H-I). Wound-healing assays demonstrated ATF5-KD enhanced migration at 24 hours (HepG2: 26.61% remaining wound area *vs*. Control 65.31%, $p < 0.001$; Huh7: 24.29% *vs*. 60.99%, $p < 0.001$; Figure 5J-K).

GPER1 rescue experiments demonstrated that siRNA-mediated GPER1 knockdown (siGPER1) reversed ATF5-OE-mediated growth suppression at 96 hours (HepG2: ATF5-OE 0.914 ± 0.016 *vs*. Vector 1.397 ± 0.027, $p < 0.001$; ATF5-OE + siGPER1 1.764 ± 0.100, $p < 0.001$ *vs*. ATF5-OE alone; Huh7: ATF5-OE 1.023 ± 0.060 *vs*. Vector 1.614 ± 0.056, $p < 0.001$; ATF5-OE + siGPER1 1.996 ± 0.155, $p < 0.001$ *vs*. ATF5-OE alone; Figure 5L), establishing GPER1 as functionally required for ATF5-mediated tumor suppression.

4. Discussion

This study identifies the ATF5-GPER1 axis as a female-protective molecular circuit in hepatocellular carcinoma operating through integrated tumor-suppressive and immune-modulatory mechanisms. Our tissue-specific demonstration of ATF5's tumor-suppressive function in liver cancer contrasts with its oncogenic roles in other malignancies (*17*), —most notably in glioblastoma, where ATF5 sustains tumor cell survival through BCL-2 and MCL-1 upregulation and is actively pursued as a therapeutic target *via* dominant-negative peptides (*19,20*); in breast cancer, where ATF5 loss of function selectively induces apoptosis in malignant but not normal mammary cells (*19*); and in lung adenocarcinoma, where ATF5 promotes radioresistance and malignant regrowth through cell cycle acceleration (*21*). This striking context-dependency—oncogenic in neural, mammary, and pulmonary tumors yet tumor-suppressive in hepatocytes—likely reflecting differential cofactor availability and chromatin landscapes across tissues—a phenomenon observed with other transcription factors such as PPARγ (*22*). In hepatocytes specifically, the abundant availability of ATF/CREB family co-activators and the liver-enriched chromatin architecture may redirect ATF5 transcriptional output toward pro-apoptotic and stress-response gene programs rather than the survival circuits it activates in glioma. This interpretation is consistent with the tissue-restricted expression patterns of ATF5's known co-repressors and with our observation that ATF5 overexpression in hepatocellular lines drives apoptosis and growth arrest rather than the resistance phenotypes described in neural tumor models (*19,20*). Understanding this switch in transcriptional polarity will be essential before any therapeutic strategy targeting ATF5 can be considered across cancer types. Critically, ATF5's protective effects are mediated through direct GPER1 transactivation, establishing a non-canonical estrogen signaling pathway that reconciles the long-standing paradox of why classical ERα-targeted therapies have failed clinically despite strong epidemiologic evidence for female survival advantage (*23,24*). This finding suggests that therapeutic strategies should pivot toward GPER1-selective agonists or interventions enhancing ATF5 expression rather than continuing to target classical nuclear estrogen receptors.

A central innovation of our study lies in applying single-cell transcriptomics to systematically dissect sex differences in HCC at cellular resolution—an approach that has revealed sex-biased tumor cell states in lung cancer and melanoma but remained underutilized in HCC (*14,25*). Through inferCNV-based malignant cell identification and pseudotime analysis, we discovered that ATF5 marks a female-enriched, transcriptionally distinct malignant subcluster positioned at the origin of tumor progression trajectories. The coordinated downregulation of ATF5 and GPER1 during malignant

evolution (Spearman ρ = −0.52 and −0.48) suggests that loss of this axis may represent a critical evolutionary bottleneck in HCC development, particularly relevant for female patients who initially benefit from higher ATF5 expression. This extends beyond previous sex-dimorphism studies that focused predominantly on hormone receptors or chromosomal factors by identifying a transcription factor whose sex-biased expression arises from complex hormonal and microenvironmental regulation (*26*).

Our macrophage-focused analyses revealed an unexpected role for ATF5 in shaping tumor immunity. The identification of a female-enriched IFN-γ$^+$ macrophage subset marked by high ATF5 expression provides mechanistic insight into how sex-specific gene expression translates to differential immune infiltration patterns—a phenomenon widely observed but poorly understood mechanistically (*9,27*). The preferential engagement of CD8$^+$ T cells and NK cells through CXCL9/10–CXCR3 and CCL5 signaling by ATF5-high macrophages, contrasted with immunosuppressive TGFB and SPP1 interactions in ATF5-low cells, suggests that ATF5 status may predict immunotherapy responsiveness. This hypothesis aligns with emerging evidence that female cancer patients show more durable benefit from immune checkpoint inhibitors despite lower initial response rates and warrants prospective validation in clinical trials stratifying patients by ATF5 expression (*10,28*).

The mechanistic demonstration that ATF5 directly transactivates GPER1 through consensus motif binding, coupled with functional rescue experiments showing GPER1 dependence, establishes a regulatory hierarchy absent from prior literature. GPER1 has emerged as a mediator of rapid non-genomic estrogen signaling distinct from classical nuclear ER pathways (*29,30*), with protective effects demonstrated in cardiovascular and nervous systems (*31*). However, its role in HCC has remained controversial (*32*), likely due to overlooking the requirement for ATF5-mediated transcriptional activation. Our hormone modulation experiments showing coordinated upregulation of both ATF5 and GPER1 by estradiol and G-1, with G36 antagonist abrogating these effects, establish a positive feedback loop that amplifies estrogen-responsive protection specifically in females with elevated endogenous ATF5. This context-dependency explains previous inconsistencies and underscores the importance of considering transcriptional regulation and hormonal milieu when evaluating GPER1's function.

From a precision oncology perspective, several translational opportunities emerge. First, ATF5 expression could stratify patients for immunotherapy trials, as ATF5-high tumors exhibit immunostimulatory macrophage enrichment and enhanced chemokine-mediated lymphocyte recruitment—features associated with checkpoint inhibitor responsiveness (*33,34*). Second, the sex-specific prognostic value of ATF5 (HR = 0.34 in females, p = 0.040 *vs*. HR = 0.69 in males, P=0.080) supports developing sex-stratified risk calculators incorporating ATF5 status alongside established clinical variables, moving beyond one-size-fits-all prognostic models. Third, female patients with low ATF5 expression represent a high-risk subgroup lacking protective benefit who may warrant more aggressive surveillance or adjuvant therapy, whereas ATF5-high females with early-

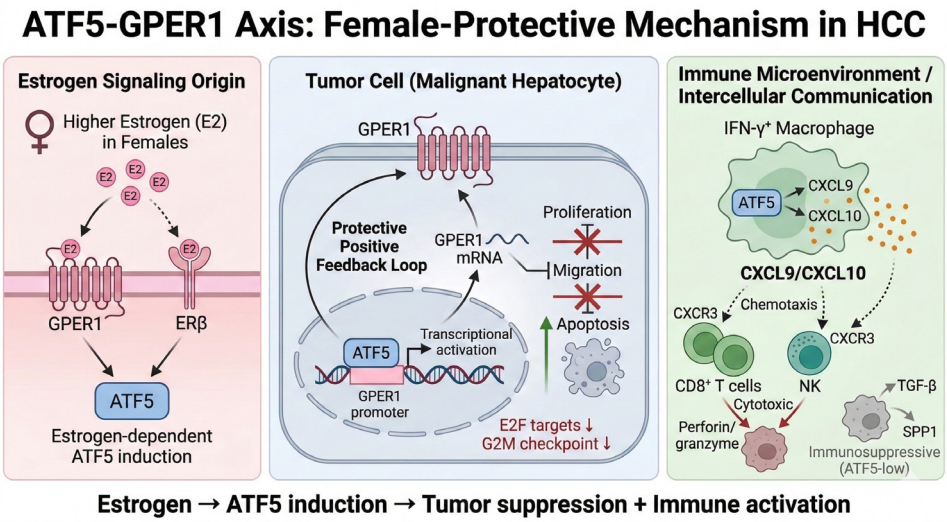

Figure 6. Schematic model of the ATF5–GPER1 axis as a female-protective mechanism in hepatocellular carcinoma. In females, higher circulating estrogen (E2) activates ATF5 through GPER1 (solid arrow) and ERβ (dashed arrow) signaling. Within malignant hepatocytes, ATF5 transcriptionally activates the GPER1 promoter, forming a protective positive feedback loop that suppresses proliferation and migration while promoting apoptosis, with concurrent downregulation of E2F targets and G2M checkpoint pathways. In IFN-γ$^+$ macrophages, ATF5 drives secretion of CXCL9 and CXCL10, which recruit cytotoxic CD8$^+$ T cells and NK cells to the tumor microenvironment *via* the CXCR3 axis. In contrast, ATF5-low macrophages exhibit immunosuppressive phenotypes characterized by TGF-β and SPP1 signaling.

stage disease could benefit from less intensive follow-up.

Several limitations warrant consideration. Our immune findings are primarily correlative from single-cell data; definitive causality requires macrophage-specific ATF5 manipulation in appropriate preclinical models. The modest TMA cohort size (n = 167) and single-center derivation limit generalizability, necessitating multi-center validation across diverse etiologies (HBV, HCV, NASH, alcohol-related) and geographic populations. The incomplete characterization of ATF5's complete transcriptional program beyond GPER1, and undefined mechanisms underlying ATF5's sex-biased expression (epigenetic regulation, microRNA control), represent areas for future investigation. Additionally, whether therapeutic modulation of the ATF5-GPER1 axis through GPER1 agonists or ATF5-enhancing interventions can recapitulate naturally occurring protection requires extensive preclinical optimization and safety evaluation.

In conclusion, our study establishes ATF5-GPER1 as a female-protective axis in hepatocellular carcinoma, linking tumor suppression with an immunostimulatory macrophage program (Figure 6). By demonstrating direct ATF5-dependent GPER1 transactivation, we define a non-canonical estrogen pathway that reconciles the clinical failure of ERα-directed approaches with consistent female survival advantage. Targeting this axis—through GPER1-selective agonists or interventions boosting ATF5—may offer a rational sex-informed therapeutic strategy.

Funding: This study was funded by the National Natural Science Foundation of China (No. 82170666 and 82572988), and Chongqing science and health joint project (2024GGXM005).

Conflict of Interest: The authors have no conflicts of interest to disclose.

Ethical statement: This study was reviewed and approved by the Ethics Committee of the First Affiliated Hospital of Chongqing Medical University (Approval No. 2024-607-01) and received institutional scientific review approval (Approval No. KX2024-KYC0273-01).

Availability of data and materials: All original data can be available from the corresponding authors based on the reasonable request.

References

1. Bray F, Laversanne M, Sung H, Ferlay J, Siegel RL, Soerjomataram I, Jemal A. Global cancer statistics 2022: GLOBOCAN estimates of incidence and mortality worldwide for 36 cancers in 185 countries. CA Cancer J Clin. 2024; 74:229-263.
2. Burra P, Bizzaro D, Gonta A, Shalaby S, Gambato M, Morelli MC, Trapani S, Floreani A, Marra F, Brunetto MR, Taliani G, Villa E. Clinical impact of sexual dimorphism in non-alcoholic fatty liver disease (NAFLD) and non-alcoholic steatohepatitis (NASH). Liver Int. 2021; 41:1713-1733.
3. Xu ZQ, Luo SQ, Wu ZJ, Liao R. Current status and perspectives of molecular mechanisms of gender difference in hepatocellular carcinoma: The tip of the iceberg? Biosci Trends. 2025; 19:266-280.
4. Haupt S, Caramia F, Klein SL, Rubin JB, Haupt Y. Sex disparities matter in cancer development and therapy. Nat Rev Cancer. 2021; 21:393-407.
5. Ruggieri A, Gagliardi MC, Anticoli S. Sex-Dependent Outcome of Hepatitis B and C Viruses Infections: Synergy of Sex Hormones and Immune Responses? Front Immunol. 2018; 9:2302.
6. Shi L, Feng Y, Lin H, Ma R, Cai X. Role of estrogen in hepatocellular carcinoma: is inflammation the key? J Transl Med. 2014; 12:93.
7. Llovet JM, Montal R, Sia D, Finn RS. Molecular therapies and precision medicine for hepatocellular carcinoma. Nat Rev Clin Oncol. 2018; 15:599-616.
8. Pfister D, Núñez NG, Pinyol R, *et al*. NASH limits anti-tumour surveillance in immunotherapy-treated HCC. Nature. 2021; 592:450-456.
9. Shen KY, Zhu Y, Xie SZ, Qin LX. Immunosuppressive tumor microenvironment and immunotherapy of hepatocellular carcinoma: current status and prospectives. J Hematol Oncol. 2024; 17:25.
10. Wallis CJD, Butaney M, Satkunasivam R, Freedland SJ, Patel SP, Hamid O, Pal SK, Klaassen Z. Association of Patient Sex With Efficacy of Immune Checkpoint Inhibitors and Overall Survival in Advanced Cancers: A Systematic Review and Meta-analysis. JAMA Oncol. 2019; 5:529-536.
11. Qian J, Olbrecht S, Boeckx B, *et al*. A pan-cancer blueprint of the heterogeneous tumor microenvironment revealed by single-cell profiling. Cell Res 2020; 30:745-762.
12. Yu Y, You Y, Duan Y, *et al*. Multi-omics approaches for identifying the PANoptosis signature and prognostic model *via* a multimachine-learning computational framework for intrahepatic cholangiocarcinoma. Hepatology. 2026; 83:466-483.
13. Laughney AM, Hu J, Campbell NR, *et al*. Regenerative lineages and immune-mediated pruning in lung cancer metastasis. Nat Med. 2020; 26:259-269.
14. Jerby-Arnon L, Shah P, Cuoco MS, *et al*. A Cancer Cell Program Promotes T Cell Exclusion and Resistance to Checkpoint Blockade. Cell. 2018; 175:984-997.e924.
15. Chen Z, Zhou L, Liu L, Hou Y, Xiong M, Yang Y, Hu J, Chen K. Single-cell RNA sequencing highlights the role of inflammatory cancer-associated fibroblasts in bladder urothelial carcinoma. Nat Commun. 2020; 11:5077.
16. Ishihara S, Enomoto A, Sakai A, Iida T, Tange S, Kioka N, Nukuda A, Nagasato AI, Yasuda M, Tokino T, Haga H. Stiff extracellular matrix activates the transcription factor ATF5 to promote the proliferation of cancer cells. iScience. 2025; 28:112057.
17. Sheng Z, Li L, Zhu LJ, Smith TW, Demers A, Ross AH, Moser RP, Green MR. A genome-wide RNA interference screen reveals an essential CREB3L2-ATF5-MCL1 survival pathway in malignant glioma with therapeutic implications. Nat Med. 2010; 16:671-677.
18. Barton M, Filardo EJ, Lolait SJ, Thomas P, Maggiolini M, Prossnitz ER. Twenty years of the G protein-coupled

estrogen receptor GPER: Historical and personal perspectives. J Steroid Biochem Mol Biol. 2018; 176:4-15.
19. Dluzen D, Li G, Tacelosky D, Moreau M, Liu DX. BCL-2 is a downstream target of ATF5 that mediates the prosurvival function of ATF5 in a cell type-dependent manner. J Biol Chem. 2011; 286:7705-7713.
20. Cates CC, Arias AD, Nakayama Wong LS, Lamé MW, Sidorov M, Cayanan G, Rowland DJ, Fung J, Karpel-Massler G, Siegelin MD, Greene LA, Angelastro JM. Regression/eradication of gliomas in mice by a systemically-deliverable ATF5 dominant-negative peptide. Oncotarget. 2016; 7:12718-12730.
21. Ishihara S, Yasuda M, Ishizu A, Ishikawa M, Shirato H, Haga H. Activating transcription factor 5 enhances radioresistance and malignancy in cancer cells. Oncotarget. 2015; 6:4602-4614.
22. Yoshimura R, Matsuyama M, Segawa Y, Hase T, Mitsuhashi M, Tsuchida K, Wada S, Kawahito Y, Sano H, Nakatani T. Expression of peroxisome proliferator-activated receptors (PPARs) in human urinary bladder carcinoma and growth inhibition by its agonists.Int J Cancer. 2003; 104:597-602.
23. Naing C, Ni H, Aung HH. Tamoxifen for adults with hepatocellular carcinoma. Cochrane Database Syst Rev. 2024; 8:Cd014869.
24. Zhang L, Wu J, Wu Q, Zhang X, Lin S, Ran W, Zhu L, Tang C, Wang X. Sex steroid axes in determining male predominance in hepatocellular carcinoma. Cancer Lett. 2023; 555:216037.
25. Kim N, Kim HK, Lee K, *et al*. Single-cell RNA sequencing demonstrates the molecular and cellular reprogramming of metastatic lung adenocarcinoma. Nat Commun. 2020; 11:2285.
26. Kur P, Kolasa-Wołosiuk A, Misiakiewicz-Has K, Wiszniewska B. Sex Hormone-Dependent Physiology and Diseases of Liver. Int J Environ Res Public Health. 2020; 17.
27. Jacobsen H, Klein SL. Sex Differences in Immunity to Viral Infections. Front Immunol. 2021; 12:720952.
28. Vacher L, Bernadach M, Molnar I, Passildas-Jahanmohan J, Dubray-Longeras P. The efficacy of immune checkpoint inhibitors following discontinuation for long-term response or toxicity in advanced or metastatic non-small-cell lung cancers: A retrospective study. Health Sci Rep. 2024; 7:e1825.
29. Tang X, Liao Q, Li Q, Jiang L, Li W, Xu J, Xiong A, Wang R, Zhao J, Wang Z, Ding L, Yang L. Lusianthridin ameliorates high fat diet-induced metabolic dysfunction-associated fatty liver disease *via* activation of FXR signaling pathway. Eur J Pharmacol. 2024; 965:176196.
30. Xu S, Yu S, Dong D, Lee LTO. G Protein-Coupled Estrogen Receptor: A Potential Therapeutic Target in Cancer. Front Endocrinol (Lausanne). 2019; 10:725.
31. Dinh QN, Vinh A, Arumugam TV, Drummond GR, Sobey CG. G protein-coupled estrogen receptor 1: a novel target to treat cardiovascular disease in a sex-specific manner? Br J Pharmacol. 2021; 178:3849-3863.
32. Chaturantabut S, Shwartz A, Evason KJ, *et al.* Estrogen Activation of G-Protein-Coupled Estrogen Receptor 1 Regulates Phosphoinositide 3-Kinase and mTOR Signaling to Promote Liver Growth in Zebrafish and Proliferation of Human Hepatocytes. Gastroenterology. 2019; 156:1788-1804.e1713.
33. Llovet JM, Pinyol R, Kelley RK, El-Khoueiry A, Reeves HL, Wang XW, Gores GJ, Villanueva A. Molecular pathogenesis and systemic therapies for hepatocellular carcinoma. Nat Cancer. 2022; 3:386-401.
34. Wu K. Research highlights of clinical oncology early 2022. Holist Integr Oncol. 2022; 1:6.

Received January 28, 2026; Revised March 6, 2026; Accepted March 14, 2026.

[§]These authors contributed equally to this work.

**Address correspondence to:*
Zhongjun Wu and Rui Liao, Department of Hepatobiliary Surgery, the First Affiliated Hospital of Chongqing Medical University, 1 Youyi Road, Yuzhong District, Chongqing 400016, China.
E-mail: wzjtcy@126.com (ZW); liaorui99@163.com (RL)

Released online in J-STAGE as advance publication March 19, 2026.

Original Article

DOI: 10.5582/bst.2025.01335

Comparative safety and efficacy of BIC/FTC/TAF versus DTG+3TC in antiretroviral treatment-naive patients with HIV as first-line regimens: A real-world cohort study

Liqin Sun[1,§], Yuxin Jiang[2,§], Stephane Isnard[3,§], Jingyi Chen[4,§], Yanjun Li[5], Hui Wang[1], Fang Zhao[1], Man Rao[1], Xinyun Jia[1], Jinping Huang[5], Jinwei Wu[5], Yinsong Luo[2], Dian Zhao[2], Chenye Liu[2], Xiaorui Li[2], Jean-Pierre Routy[3,*], Jiaye Liu[2,*], Yun He[1,*], Ping Cen[5,*], Hongzhou Lu[1,*]

[1] Department of Infectious Diseases, National Clinical Research Center for Infectious Diseases, Shenzhen Third People's Hospital, Shenzhen, Guangdong, China;
[2] School of Public Health, Shenzhen University Medical School, Shenzhen, Guangdong, China;
[3] Division of Hematology, Chronic Viral Illness Service, and Research Institute of the McGill University Health Centre, Montreal, QC, Canada;
[4] School of Medicine, Southern University of Science and Technology, Shenzhen, Guangdong, China;
[5] Laboratory of Infectious Diseases, HIV/AIDS Clinical Treatment Center of Guangxi (Nanning), The Fourth People's Hospital of Nanning, Nanning, Guangxi, China.

SUMMARY: While bictegravir/emtricitabine/tenofovir alafenamide (BIC/FTC/TAF) and dolutegravir plus lamivudine (DTG+3TC) are first-line regimens for treatment-naive people with HIV (PWH), long-term real-world head-to-head comparisons of their metabolic and renal outcomes remain limited. We conducted a retrospective cohort study of ART-naive PWH initiating these regimens in China, utilizing 1:2 propensity score matching (PSM) to balance baseline covariates for 1,445 participants (901 BIC/FTC/TAF; 544 DTG+3TC). Over a 24-month follow-up, the study demonstrated comparable virologic suppression (99.7% *vs*. 100.0%; $p = 0.623$), weight changes, and cumulative incidence of metabolic abnormalities between the two groups. Conversely, although the crude 24-month incidence of eGFR decline was higher with DTG+3TC (54.8% *vs*. 40.7%; $p = 0.039$), adjusted Cox models revealed that the regimen was not independently associated with this decline (HR 1.20; 95% CI 0.97–1.48; $p = 0.18$).These findings indicate that both regimens offer comparable long-term virologic efficacy and metabolic safety profiles, supporting their routine clinical utility while highlighting the need for cautious interpretation of renal markers during integrase inhibitor-based therapy.

Keywords: antiretroviral therapy, BIC/FTC/TAF, DTG+3TC, weight change, metabolic complications, cohort study

1. Introduction

Combination antiretroviral therapy (ART) has transformed HIV infection into a manageable chronic condition. Long-term goals of ART are sustained viral suppression, preservation of immunological functions, and minimization of drug-related toxicities to enable lifelong treatment (*1,2*). Over the past decade, integrase strand transfer inhibitors (INSTIs) have emerged as the cornerstone of first-line ART due to potent antiviral activity, high genetic barrier to resistance, favorable tolerability, and fewer drug–drug interactions (*3,4*).

Current international guidelines, including those from the World Health Organization (WHO), the U.S. Department of Health and Human Services (DHHS), and the European AIDS Clinical Society (EACS), uniformly recommend INSTI-based regimens as preferred first-line options for treatment-naive people with HIV (PWH). Among these, the single-tablet regimen bictegravir/emtricitabine/tenofovir alafenamide (BIC/FTC/TAF) and the two-drug regimen dolutegravir plus lamivudine (DTG+3TC) are widely used, evidence-supported first-line options (*3-6*).

BIC/FTC/TAF is a once-daily fixed-dose regimen with a high genetic barrier to resistance and efficacy against hepatitis B virus (HBV). However, TAF has been associated with weight gain and alterations in lipid metabolism in both clinical trials and real-world studies (*7,8*). Although TAF generally demonstrates improved renal and bone safety compared with tenofovir disoproxil

fumarate (TDF), comparative evidence regarding renal and metabolic outcomes across contemporary INSTI-based regimens remains limited, particularly for non–tenofovir-based options and longer follow-up (*9*). DTG+3TC reduces overall antiretroviral exposure and has shown non-inferior virologic efficacy versus triple-drug regimens in randomized trials (*6-9*). However, DTG-based regimens have also been linked to weight gain and metabolic complications, raising concerns about long-term safety in routine clinical practice (*10-12*).

Thus, metabolic and renal safety are pivotal considerations when selecting INSTI-based ART (*7,10,11*). Pivotal randomized controlled trials (*e.g.* GEMINI, GS-US-380) established virologic non-inferiority for DTG+3TC and BIC/FTC/TAF, but their selected populations and trial settings may limit generalizability to clinical care (*6,7*). Real-world studies on metabolic and renal outcomes remain limited by short follow-up, modest sample sizes, or lack of direct head-to-head comparisons. Comparative evidence from China and Asia is particularly scarce, where participant characteristics, viral subtypes, comorbidity patterns, and healthcare delivery may differ from those in Western cohorts, potentially affecting the external validity of existing data.

Accordingly, we conducted a retrospective, propensity score–matched cohort study in two centers in Shenzhen and Nanning, China, to directly compare virologic and immunologic responses, as well as metabolic, hepatic, and renal outcomes between BIC/FTC/TAF and DTG+3TC among over 1400 treatment-naive PWH.

2. Methods

2.1. Study design and participants

This retrospective cohort study was conducted at the Third People's Hospital of Shenzhen and the Fourth People's Hospital of Nanning, China, the designated centers for HIV treatment and management in each city. Adults with HIV-1 who initiated ART between March 1, 2020, and May 1, 2023, were eligible if they were: (1) ART-naïve at baseline; (2) age ≥ 18 years; and (3) initiated either BIC/FTC/TAF or DTG+3TC as their first-line ART regimen. Exclusion criteria included: (1) absence of baseline HIV RNA viral load or lipid profile data; (2) history of malignancy, decompensated liver disease, or autoimmune disease at baseline; (3) active opportunistic infections at baseline; (4) pregnancy or lactation during the follow-up period; and (5) use of lipid-lowering agents at baseline.

A total of 1,697 eligible ART-naive participants were enrolled in the cohort, among whom 1,046 (61.6%) initiated BIC/FTC/TAF and 651 (38.4%) initiated DTG+3TC.

2.2. Data collection

Baseline and follow-up data were extracted from hospital electronic systems, including sociodemographic and HIV-related clinical data, ART regimen, and laboratory measurements. Under routine care, follow-up visits occurred approximately every 3 months for up to 24 months; baseline values were obtained at or immediately prior to ART initiation.

Covariates included age, sex, body mass index (BMI), time from HIV diagnosis to ART initiation, transmission route, HIV-1 RNA, $CD4^+$ and $CD8^+$ T-cell counts, weight, fasting plasma glucose, total cholesterol (TC), triglycerides (TG), low-density lipoprotein cholesterol (LDL-C), high-density lipoprotein cholesterol (HDL-C), estimated glomerular filtration rate (eGFR), alanine aminotransferase (ALT), and aspartate aminotransferase (AST).

2.3. Treatment regimens

Participants initiated BIC/FTC/TAF (bictegravir 50 mg, emtricitabine 200 mg, tenofovir alafenamide 25 mg; once daily) or DTG+3TC (dolutegravir 50 mg, lamivudine 300 mg; once daily) per national guidelines and clinician judgment (*13*).

2.4. Follow-up and outcomes

Participants were followed from ART initiation (baseline) for up to 24 months, with scheduled visits at approximately three-month intervals, until the end of follow-up on May 1, 2025. For time-to-event analyses, follow-up commenced 3 months after ART initiation to ensure adequate exposure time and minimize misclassification of early events. Participants were censored at the earliest occurrence of death, loss to follow-up, regimen change to a non-study ART regimen, or the end of the follow-up period. Loss to follow-up was defined as absence from scheduled visits for more than 9 consecutive months, consistent with standard clinical practice.

The primary outcomes were virologic suppression rates and longitudinal immunologic responses during follow-up. Virologic suppression was defined as an HIV-1 RNA level < 50 copies/mL (below the lower limit of detection) after ART initiation, in accordance with the 2024 Chinese Guidelines for the Diagnosis and Treatment of HIV/AIDS (*13*).

Secondary outcomes included changes in body weight and between-group differences in the cumulative incidence of metabolic and organ function-related abnormalities over the 24-month follow-up period, encompassing dyslipidemia, elevated liver enzymes, hyperglycemia, and renal dysfunction. Dyslipidemia was defined according to the 2023 Chinese Guideline for the Management of Dyslipidemia as any of the following: total cholesterol (TC) ≥ 5.2 mmol/L, triglycerides (TG)

≥ 1.7 mmol/L, LDL-C ≥ 3.4 mmol/L, or HDL-C < 1.0 mmol/L (*14*). Elevated liver enzymes were defined as ALT > 40 U/L or AST > 40 U/L, consistent with criteria established by the American Association for the Study of Liver Diseases (*15*). Hyperglycemia was defined as fasting plasma glucose ≥ 7.0 mmol/L in accordance with the 2024 Chinese Guidelines for the Prevention and Treatment of Diabetes (*16*). Renal dysfunction was defined as an eGFR < 90 mL/min/1.73 m^2 based on the National Kidney Foundation criteria (*17*).

2.5. Statistical analysis

Analyses were performed in R (v4.4.2). Propensity scores were estimated by logistic regression including age, sex, BMI, time from diagnosis to ART, transmission route, HIV RNA, $CD4^+$/$CD8^+$ counts, fasting glucose, TC, TG, LDL-C, HDL-C, eGFR, ALT, and AST. Nearest-neighbor matching used MatchIt at a 1:2 ratio without replacement (caliper 0.1).

Continuous variables were mostly summarized as medians with interquartile ranges (IQRs) and compared using the Wilcoxon rank-sum test. Categorical variables were presented as counts and percentages, with between-group comparisons performed using the χ^2 test or Fisher's exact test. Cumulative incidences of dyslipidemia, hyperglycemia, elevated liver enzymes (ALT or AST), and renal dysfunction were estimated using the Kaplan–Meier method, and between-group differences were evaluated with the log-rank test. Multivariable Cox proportional hazards regression models were employed to identify independent predictors of metabolic and renal adverse outcomes.

All statistical tests were two-sided, and a $p < 0.05$ was considered statistically significant.

2.6. Ethics statement

The study protocol was conducted in accordance with the ethical principles of the Declaration of Helsinki (1975) and was approved by the Institutional Review Board of Shenzhen Third People's Hospital (Approval No. 2025-097-02). All participants provided written informed consent prior to enrollment.

3. Results

3.1. Baseline characteristics

Prior to PSM, several clinically relevant baseline imbalances were observed between the two treatment groups (Table 1). Specifically, participants initiating BIC/FTC/TAF were significantly younger (median age: 35 years [interquartile range, IQR: 29–45] *vs.* 43 years [IQR:32–60] in the DTG+3TC group), had a higher proportion of male participants (90.8% [950/1,046] *vs.* 84.8% [552/651]), demonstrated higher $CD8^+$ T-cell counts (857 [560–1,258] *vs.* 754 [468–1,131] cells/μL), higher eGFR (110.61 [98.13–120.17] *vs*. 103.19 [87.22–116.45] mL/min/1.73 m^2), and lower fasting plasma glucose levels (5.11 [4.78-5.53] *vs*. 5.20 [4.83-5.84] mmol/L) compared with those initiating DTG+3TC (all $p < 0.001$).

After 1:2 PSM (BIC/FTC/TAF, $n = 901$; DTG+3TC, $n = 544$), baseline covariates were well balanced (all $p > 0.05$; Table 1).

3.2. Virologic and immunologic outcomes

At the 6-month follow-up after ART initiation, virologic suppression (HIV RNA < 50 copies/mL) was achieved in 867 out of 901 participants (96.2%) in the BIC/FTC/TAF group, compared with 513 of 544 participants (94.3%) in the DTG+3TC group ($p = 0.328$). By month 12, viral suppression rates increased to 96.7% and 96.0% in the two groups, respectively ($p = 0.432$). At month 18, both groups achieved 99.3%, and by month 24, the rates were 99.7% (BIC/FTC/TAF) and 100.0% (DTG+3TC). No statistically significant intergroup differences in virologic suppression rates were observed at any of the four time points (Figure 1).

Both groups demonstrated significant increases in $CD4^+$ T-cell counts over time compared to baseline, without any statistically significant between-group differences in absolute $CD4^+$ T-cell counts at any time point (all $p > 0.05$). $CD8^+$ T-cell counts remained largely stable throughout the 24-months follow-up period between the two groups (all $p > 0.05$; Figure 2).

3.3. Weight outcome

Throughout the 24-months follow-up period, mean body weight increased modestly in both groups, from 64.35 to 67.55 kg with BIC/FTC/TAF and from 64.05 to 66.51 kg with DTG+3TC.

Between-group differences in absolute body weight at months 3, 6, 9, 12, 15, 18, 21, and 24 were not statistically significant (all $p > 0.05$; Figure 3A). Consistent with these observations, mean weight changes from baseline increased progressively over time and were numerically higher in the BIC/FTC/TAF group than in the DTG+3TC group: 1.46, 2.13, 2.43, 2.72, 2.74, 2.91, 3.02, and 3.2 kg versus 1.03, 1.38, 1.84, 2.05, 2.18, 2.17, 2.43, and 2.46 kg at months 3, 6, 9, 12, 15, 18, 21, and 24, respectively. However, between-group differences in weight change did not achieve statistical significance at any time point (all $p > 0.05$; Figure 3B).

3.4. Serum lipid profile

Both treatment groups exhibited increased lipid parameters compared with baseline. At 24 months, cumulative incidences of dyslipidemia were comparable between the BIC/FTC/TAF and DTG+3TC groups.

Table 1. Baseline Characteristics of HIV-1 Patients Before and After Propensity Score Matching (PSM)

Variables	Before PSM			After PSM		
	BIC/FTC/TAF	DTG+3TC	*p*	BIC/FTC/TAF	DTG+3TC	*p*
Total	1046	651		901	544	
Male	950 (90.8)	552 (84.8)	< 0.001	809 (89.8)	468 (86.0)	0.098
Age, yr	35 (29, 45)	43 (32, 60)	< 0.001	36 (30, 47)	38 (30, 53)	0.102
BMI,kg/m²	21.88 (19.85, 24.34)	21.60 (19.49, 24.22)	0.046	21.98 (19.84, 24.34)	21.75 (19.63, 24.45)	0.904
Route of transmission						
Heterosexual contact	418 (40.0)	357 (54.8)	< 0.001	387 (43.0)	267 (49.1)	0.097
Male-to-male sex contact	608 (58.1)	269 (41.3)		494 (54.8)	261 (48.0)	
Other	20 (1.9)	25 (3.8)		20 (2.2)	16 (2.9)	
Time from diagnosis to treatment initiation, months	14.00 (8.00, 29.75)	16.00 (9.00, 32.00)	0.032	15.00 (8.00, 31.00)	15.50 (8.00, 32.00)	0.325
HIV RNA, log copies/ml	5.19 (4.55, 5.75)	5.17 (4.58, 5.74)	0.523	5.16 (4.53, 5.71)	5.19 (4.60, 5.74)	0.432
CD4, cells/μL	230.50 (91.25, 355)	203 (53.5, 335)	0.004	225 (84, 360)	210 (67, 343)	0.384
CD8, cells/μL	857 (560, 1258)	754 (468, 1131)	< 0.001	827 (526, 1210)	780 (494.75, 1158.50)	0.15
Glucose, mmol/L	5.11 (4.78, 5.53)	5.20 (4.83, 5.84)	< 0.001	5.12 (4.79, 5.56)	5.16 (4.81, 5.64)	0.159
TC, mmol/L	4.11 (3.52, 4.74)	4.02 (3.34, 4.71)	0.015	4.12 (3.52, 4.78)	4.04 (3.40, 4.71)	0.092
TG, mmol/L	1.28 (0.95, 1.84)	1.38 (0.97, 1.99)	0.029	1.31 (0.97, 1.88)	1.35 (0.95, 2.00)	0.349
HDL, mmol/L	1.00 (0.84, 1.22)	0.99 (0.80, 1.18)	0.016	1.00 (0.84, 1.20)	1.00 (0.83, 1.19)	0.420
LDL, mmol/L	2.59 (2.10, 3.11)	2.46 (1.98, 3.01)	0.002	2.56 (2.10, 3.07)	2.46 (1.99, 3.04)	0.072
eGFR, mL/min/1.73m²	110.61 (98.13, 120.17)	103.19 (87.22, 116.45)	< 0.001	108.88 (96.53, 118.70)	106.73 (92.59, 118.48)	0.291
ALT, U/L	22.20 (15, 35)	21 (14, 34)	0.072	23 (15, 35)	21 (14, 34)	0.135
AST, U/L	23 (18, 32)	24 (18.85, 31)	0.800	23 (18.5, 32)	24 (18.45, 31)	0.779

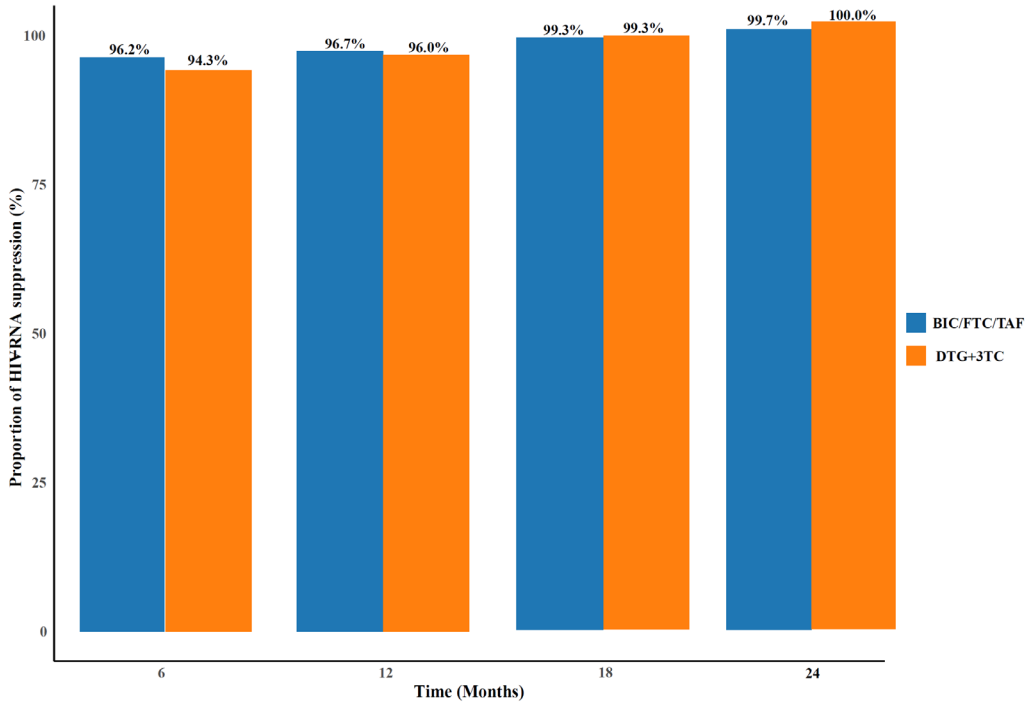

Figure 1. HIV-1 RNA suppression at 6, 12, 18 and 24 months. *Abbreviations*: BIC, bictegravir; FTC, emtricitabine; TAF, tenofovir alafenamide; DTG, dolutegravir; 3TC, lamivudine.

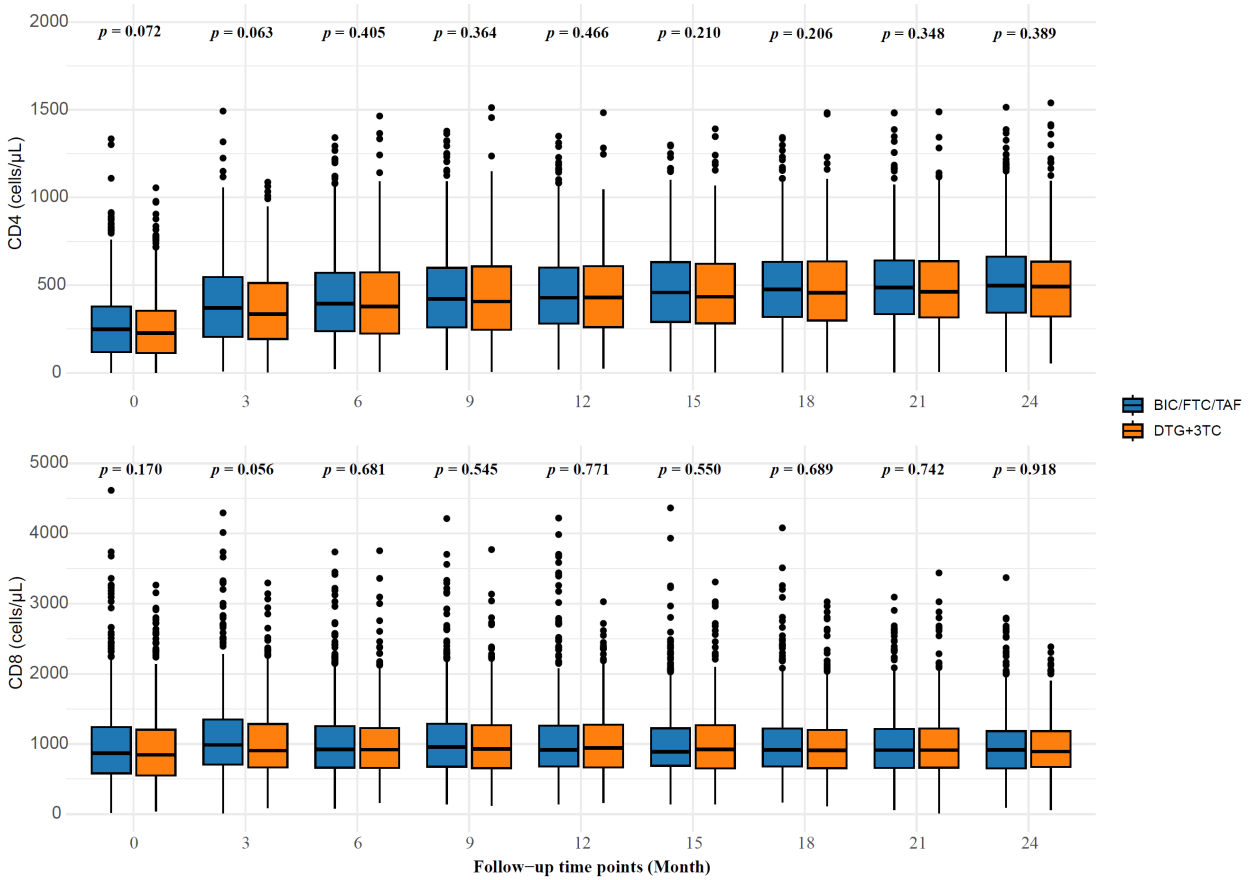

Figure 2. Longitudinal CD4⁺ and CD8⁺ T-cell counts at baseline and months 3, 6, 9, 12, 15, 18, 21, and 24. Panel A: CD4⁺ T-cell counts; panel B: CD8⁺ T-cell counts. Box and whisker plots depict the median (horizontal line), interquartile range (box), and 1.5 × IQR whiskers; individual dots represent outliers. Blue boxes correspond to participants receiving BIC/FTC/TAF, and orange boxes to those receiving DTG + 3TC. P values above each pair of boxes indicate between group comparisons at the respective time point (Wilcoxon test), none of which reached statistical significance.

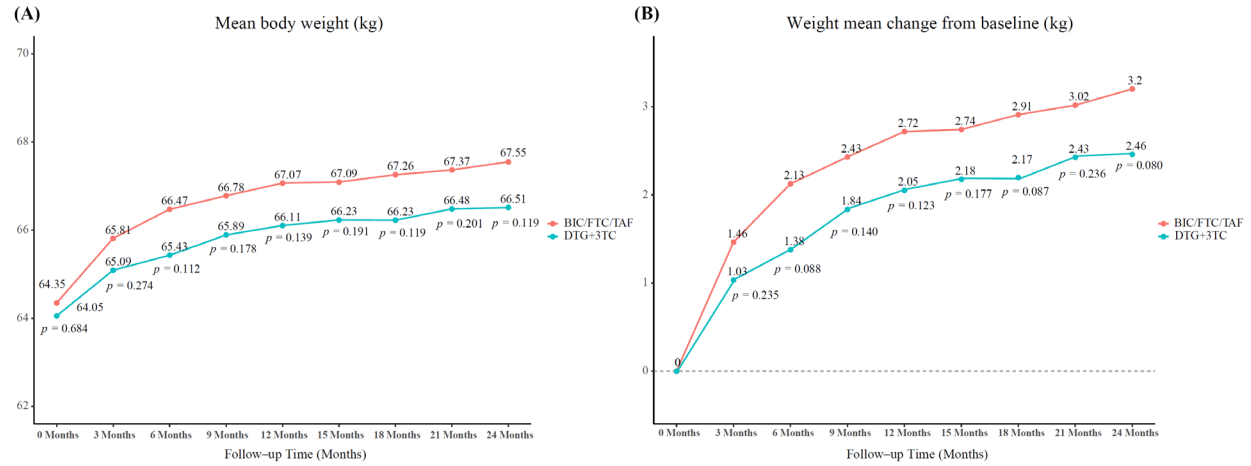

Figure 3. Longitudinal body weight measurements at baseline and at months 3, 6, 9, 12, 15, 18, 21, and 24. (A): mean body weight (kg); **(B)**: mean change from baseline (kg). Line-and-point plots represent group means at each scheduled visit; numeric labels denote the mean value (**A**) or mean change (**B**). Orange lines indicate participants receiving BIC/FTC/TAF, and blue lines represent those receiving DTG+3TC. *p*-values displayed adjacent to each time point correspond to between-group comparisons at the respective visit (pairwise derived from linear mixed-effects models); none achieved statistical significance.

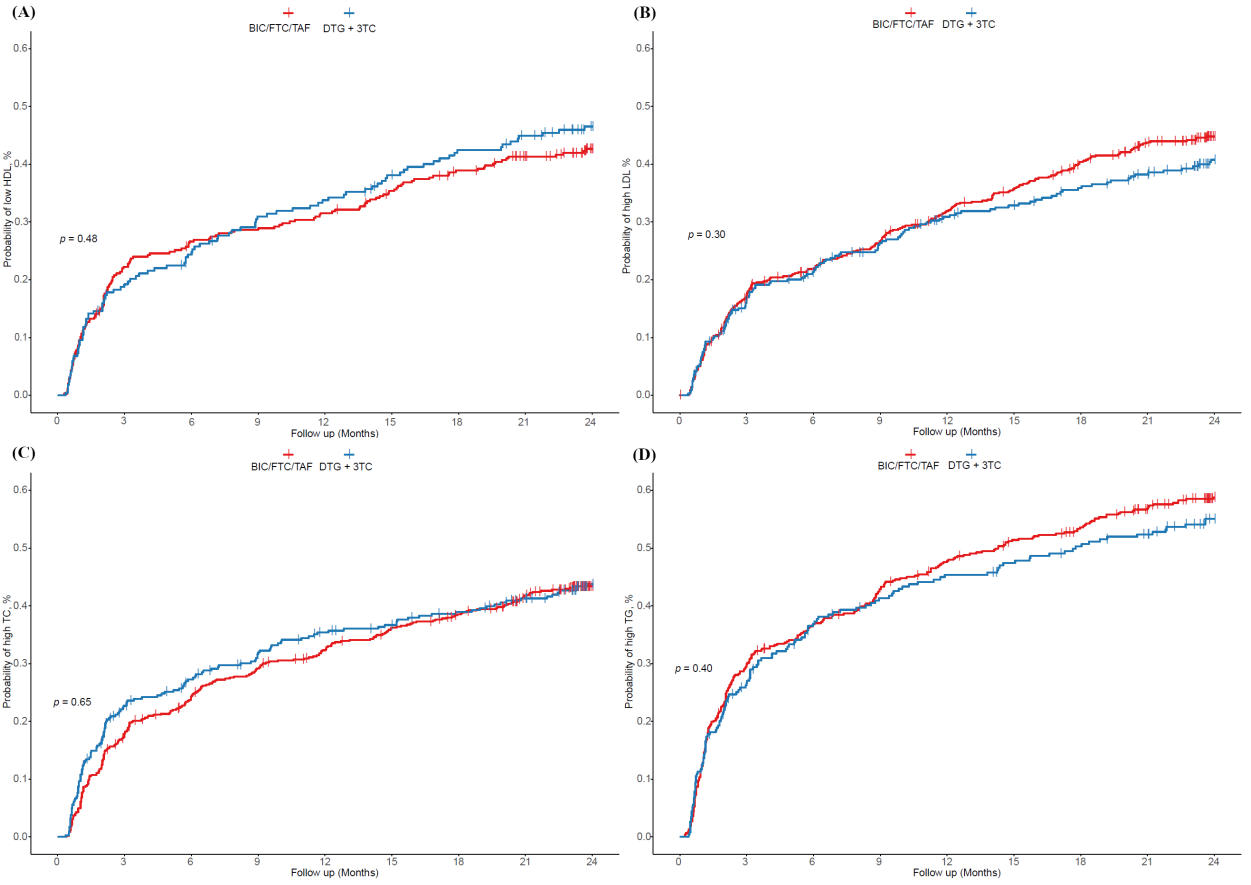

Figure 4. Kaplan-Meier survival curves illustrating the cumulative incidence of incident dyslipidemia over 24 months. Panels A – D depict the cumulative incidence of specific lipid elevations: **(A)** high density lipoprotein cholesterol (HDL-C), **(B)** low density lipoprotein cholesterol (LDL-C), **(C)** total cholesterol (TC), and **(D)** triglycerides (TG). Red curves correspond to participants receiving BIC/FTC/TAF; Blue curves represent those receiving DTG + 3TC. Shaded areas indicate 95 % confidence intervals. Intergroup differences were evaluated using the log-rank test; no statistically significant differences were observed for any lipid parameter.

Table 2. Analysis of Associated Factors for Dyslipidemia in People Living With HIV

Variables	TC		TG		LDL		HDL	
	HR (95% CI)	*p*	HR (95% CI)	*p*	HR (95% CI)	*p*	HR (95% CI)	*p*
Age, yr	1.01 (1.00 to 1.02)	0.235	1.01 (0.99 to 1.02)	0.223	1.01 (1.00 to 1.03)	0.041	1.01 (1.00 to 1.03)	0.039
BMI, kg/m²	1.02 (0.99 to 1.06)	0.528	1.03 (1.00 to 1.05)	0.203	1.01 (0.97 to 1.04)	0.732	1.03 (0.99 to 1.06)	0.179
HIV RNA, log copies/ml	1.11 (0.98 to 1.24)	0.096	1.04 (0.94 to 1.14)	0.637	1.05 (0.94 to 1.18)	0.413	1.14 (1.02 to 1.28)	0.021
Time interval between diagnosis to initiation of treatment,mo	1.00 (1.00 to 1.00)	0.273	1.00 (1.00 to 1.00)	0.950	1.00 (1.00 to 1.00)	0.423	1.00 (1.00 to 1.00)	0.323
Sex								
Male	1		1		1		1	
Female	1.50 (1.01 to 2.25)	0.135	1.18 (0.82 to 1.70)	0.436	0.81 (0.50 to 1.32)	0.326	1.14 (0.73 to 1.78)	0.634
Route of transmission								
Male-to-male sex contact	1		1		1		1	
Heterosexual contact	1.14 (0.87 to 1.49)	0.356	1.12 (0.90 to 1.39)	0.423	0.99 (0.76 to 1.28)	0.834	0.90 (0.69 to 1.18)	0.456
Other	1.13 (0.57 to 2.24)	0.736	1.27 (0.74 to 2.17)	0.383	1.28 (0.68 to 2.39)	0.567	0.96 (0.48 to 1.91)	0.904
Glucose, mmol/L	1.11 (0.96 to 1.28)	0.255	1.05 (0.94 to 1.17)	0.366	1.09 (0.96 to 1.23)	0.377	0.99 (0.85 to 1.15)	0.875
eGFR, mL/min/1.73m²	0.99 (0.99 to 1.00)	0.107	1.00 (0.99 to 1.00)	0.095	1.00 (0.99 to 1.00)	0.421	0.99 (0.99 to 1.00)	0.123
ALT, U/L	1.00 (1.00 to 1.01)	0.085	1.01 (1.00 to 1.01)	0.012	1.00 (1.00 to 1.01)	0.373	1.01 (1.00 to 1.01)	0.038
AST, U/L	0.99 (0.98 to 1.00)	0.143	0.99 (0.98 to 1.00)	0.096	1.00 (0.99 to 1.01)	0.831	1.00 (0.98 to 1.01)	0.476
CD4, cells/μL	1.00 (1.00 to 1.00)	0.352	1.00 (1.00 to 1.00)	0.378	1.00 (1.00 to 1.00)	0.825	1.00 (1.00 to 1.00)	0.063
CD8, cells/μL	1.00 (1.00 to 1.00)	0.643	1.00 (1.00 to 1.00)	0.428	1.00 (1.00 to 1.00)	0.512	1.00 (1.00 to 1.00)	0.437
Regimen								
BIC/FTC/TAF	1		1		1		1	
DTG+3TC	1.03 (0.81 to 1.37)	0.637	1.07 (0.81 to 1.21)	0.647	1.07 (0.82 to 1.34)	0.432	0.96 (0.79 to 1.21)	0.931

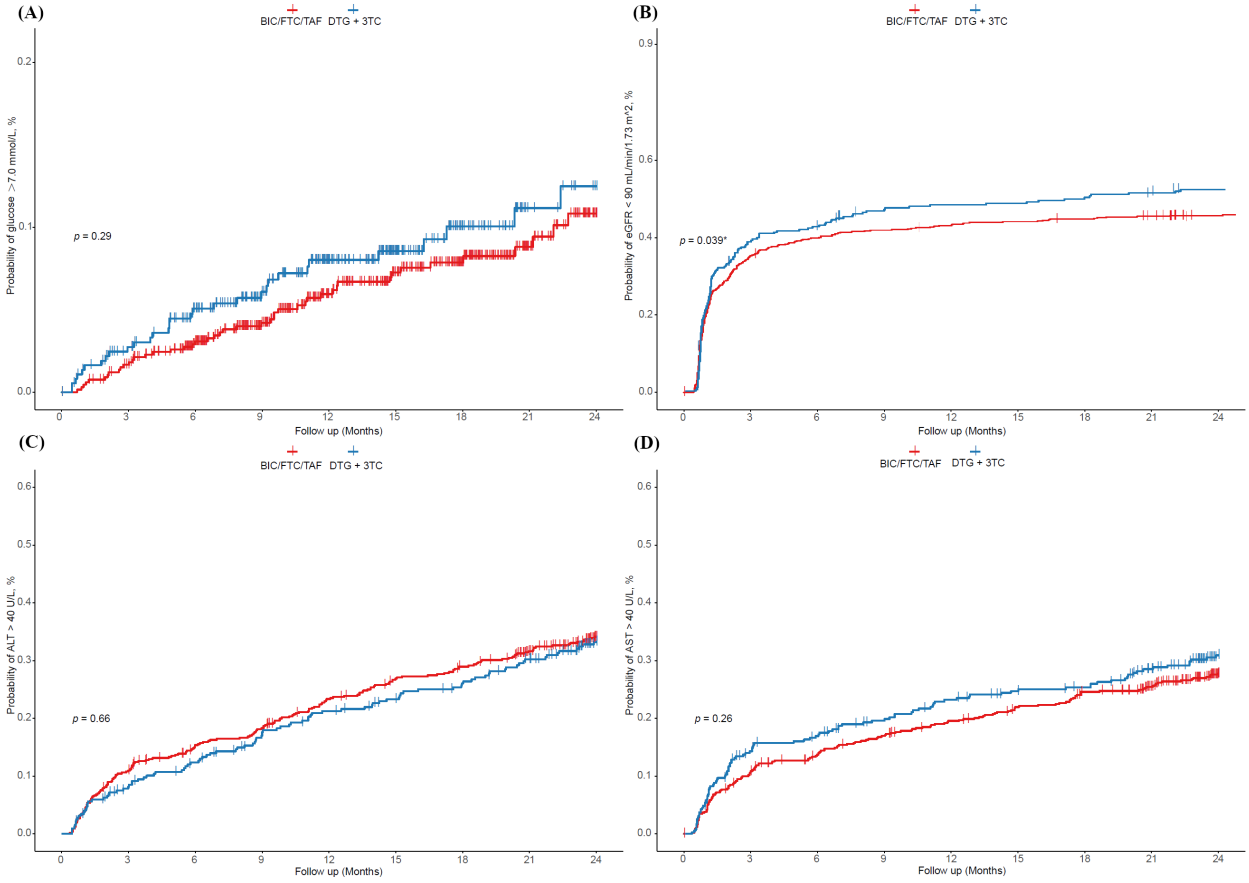

Figure 5. Kaplan-Meier survival curves depicting the cumulative incidence of incident hyperglycemia, renal dysfunction, and hepatic dysfunction over a 24-month period. (A): cumulative incidence of hyperglycemia. **(B)**: cumulative incidence of renal dysfunction (eGFR < 90 mL/min/1.73m²). **(C,D)**: cumulative incidence of hepatic dysfunction – **(C)** cumulative incidence of ALT > 40 U/L, **(D)** cumulative incidence of AST > 40 U/L.

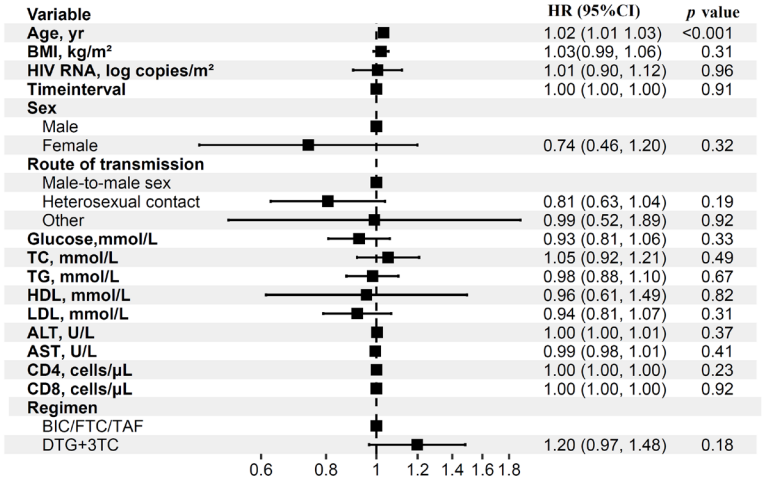

Figure 6. Multivariable predictors of eGFR < 90 mL/min/1.73 m² at 24 months. Forest plot illustrating adjusted hazard ratios (HRs) with 95 % confidence intervals derived from a Cox proportional hazards model. Each square is centered on the HR estimate and sized inversely to its variance; horizontal bars represent 95 % CIs. Variables assessed encompassed demographic factors (age, sex, transmission route), baseline clinical parameters (BMI, HIV-1 RNA, CD4 and CD8 counts), metabolic indicators (glucose, total cholesterol [TC], triglycerides [TG], high density lipoprotein cholesterol [HDL-C], low density lipoprotein cholesterol [LDL-C]), hepatic enzymes (ALT, AST), and antiretroviral regimen (reference = BIC/FTC/TAF). Age emerged as the sole independent predictor of eGFR decline (HR 1.02 per year, 95 % CI 1.01 – 1.03; $p < 0.001$). No significant associations were detected for sex, baseline metabolic markers, or treatment regimen (DTG + 3TC *vs* BIC/FTC/TAF: HR 1.20, 95 % CI 0.97 – 1.48; $p = 0.18$). A vertical dashed line indicates the null value (HR = 1); values to the right signify elevated risk.

Specifically, incidence rates of high TC were 44.3% (95% CI 39.2–49.8%) versus 44.8% (95% CI 39.3–49.2%), high TG 59.1% (95% CI 52.3–63.4%) versus 53.2% (95% CI 48.6–59.1%), high LDL-C 46.7% (95% CI 40.2–51.2%) versus 41.3% (95% CI 36.2–47.2%), and low HDL-C 43.6% (95% CI 37.4–49.3%) versus 49.2% (95% CI 44.3–55.3%), respectively. No statistically significant between-group differences were observed (all $p > 0.05$; Figure 4A–D).

In multivariable Cox models, regimen was not associated with lipid elevations; higher baseline ALT predicted TG elevation (HR 1.01; 95% CI 1.00–1.01; $p = 0.012$), and older age predicted high LDL-C and low HDL-C (both HR 1.01; $p < 0.05$; Table 2).

3.5. Glycemic and hepatic outcomes

The cumulative incidence of hyperglycemia during follow-up was similar between the groups. By 24 months, incidence rates were 12.2% (95% CI 9.3–17.1%) in the BIC/FTC/TAF group and 14.9% (95% CI 10.2–15.8%) in the DTG+3TC group, with no statistically significant difference ($p = 0.29$; Figure 5A–B). Similarly, cumulative incidences of elevated ALT and AST were also comparable (ALT: $p = 0.66$; AST: $p = 0.26$; Figure 5C–D).

3.6. Renal outcomes

The cumulative incidence of eGFR < 90 mL/min/1.73 m² differed significantly between the treatment groups (log-rank $p = 0.039$). By 24 months, the incidence was higher in the DTG+3TC group than in the BIC/FTC/TAF group (54.8% [95% CI 49.3–59.4%] vs 40.7% [95% CI 35.9–46.3%]; Figure 5B). However, multivariable Cox regression analysis revealed that the ART regimen was not independently associated with eGFR decline. Older age was the only significant predictor (HR 1.02 per year; 95% CI 1.01–1.03; $p < 0.001$), whereas sex, body mass index, $CD4^+$ and $CD8^+$ T-cell counts, and alanine aminotransferase levels showed no significant association with risk (Figure 6).

4. Discussion

In this real-world PSM cohort study conducted at two major HIV treatment centers in China, we compared 24-month effectiveness and safety of two widely used INSTI-based first-line regimens in treatment-naive PWH. Both regimens achieved high and durable virologic suppression with parallel immunologic recovery throughout follow-up. Weight trajectories and cumulative incidence of metabolic abnormalities, including dyslipidemia, hyperglycemia, and transaminase elevations, did not differ significantly between groups. Renal outcomes were also similar after adjustment for baseline characteristics. Collectively, these findings support both regimens as viable first-line options and provide region-specific real-world evidence to guide individualized treatment selection.

We observed sustained viral suppression > 99% at 24 months in both groups, with continuous $CD4^+$ T-cell recovery and stable $CD8^+$ T-cell levels, consistent with clinical trials and real-world studies (*9,18-22*). Favorable immunologic responses may reflect participants' young age, good baseline immune status, and short interval from diagnosis to ART initiation. Our study reinforces the evidence supporting both dual-drug and triple-drug INSTI strategies as effective first-line ART strategies in Chinese PWH.

Weight gain related to ART continues to be a significant concern in PWH. In our study, weight gain occurred predominantly during the first year of therapy in both groups, followed by a deceleration phase, resulting in modest mean 24-month gains of 3.2 kg and 2.46 kg, in the BIC/FTC/TAF and DTG+3TC groups respectively (representing < 5% of baseline body weight), aligning with trials and real-world studies (*21-24*). While ADVANCE reported greater weight gain with TAF versus TDF, we only found a tendency towards greater weight gain with BIC/FTC/TAF as compared to DTG+3TC, without reaching statistical significance (*25,26*). These findings imply that weight gain during INSTI-based therapy is a multifactorial process involving return-to-health effects and lifestyle factors, rather than a regimen-specific phenomenon in the short to medium term, underscoring the importance of considering patient-level risk factors (*e.g.* sex, baseline BMI) and providing counseling and follow-up (*27,28*).

Lipid changes were modest and comparable between regimens over 24 months. These findings align with pivotal trials (TANGO, GS-US-380-4030, SALSA) and real-world data from southern China reporting mild lipid changes across INSTI strategies (*7,8,22,29*), and a retrospective comparison of continued TAF versus switching to DTG+3TC found no significant difference in LDL-C at 12 months (*30*).

Our findings highlight that TAF is unlikely to be a primary driver of dyslipidemia. Instead, lipid changes may reflect complex host-metabolic adaptations following ART initiation. In our multivariable analysis, baseline ALT, rather than regimen type, emerged as an independent predictor of lipid abnormalities. Current international guidelines do not recommend discontinuing TAF solely for lipid management. In light of the REPRIEVE trial, moderate-intensity statin therapy is advised for individuals aged 40–75 years with elevated cardiovascular risk (*4*). Although our cohort was relatively young, the substantial prevalence of lipid abnormalities highlights the necessity of routine lipid monitoring and individualized cardiovascular risk assessment. Previous research from our group further suggests that early identification of metabolic risk markers may be crucial for preventing long-term

cardiovascular events (*31-33*).

Regarding glycemic and hepatic parameters, we observed broadly comparable rates of hyperglycemia and transaminase elevations between the two regimens. These findings are consistent with international evidence indicating that INSTI-associated glycemic alterations are generally modest and often secondary to weight gain or insulin resistance rather than direct hepatotoxicity (*34-35*). Nevertheless, ongoing monitoring of glucose and liver enzymes remains warranted, particularly in individuals with metabolic syndrome, obesity, or chronic viral hepatitis, for whom even minor biochemical changes may possess greater clinical relevance.

In unadjusted analyses, the DTG+3TC group demonstrated a higher cumulative incidence of eGFR < 90 mL/min/1.73 m². However, this association was not sustained following multivariable adjustment, with age identified as the sole independent predictor of renal deterioration. This outcome suggests that patient-specific characteristics, rather than regimen-specific nephrotoxicity, likely explain the observed unadjusted disparity. Mechanistically, dolutegravir is known to inhibit tubular creatinine secretion (*36*). Therefore, modest eGFR reductions may reflect DTG alterations in creatinine handling rather than clinically significant renal impairment. Notably, employing an eGFR threshold of < 90 mL/min/1.73 m² may overestimate early renal dysfunction in relatively young and predominantly male cohorts, who typically demonstrate higher baseline eGFR values. Furthermore, this threshold may fail to capture clinically relevant deterioration. Subsequent studies incorporating more robust renal endpoints—such as eGFR < 60 mL/min/1.73 m², a ≥ 30% decline from baseline, or progression to chronic kidney disease—would provide a more clinically meaningful assessment of renal safety (*37,38*).

Several limitations warrant consideration. First, although the study utilized a multicenter design in two Chinese hospitals, its retrospective nature may limit generalizability, and residual confounding due to unmeasured variables cannot be excluded. Second, significant lifestyle and behavioral factors, including diet, physical activity, alcohol consumption, socioeconomic status, drug–drug interactions, and objective adherence metrics, were not documented and could have influenced metabolic or renal outcomes. Third, despite follow-up extending to 24 months, longer observation periods are necessary to comprehensively delineate long-term metabolic and renal trajectories. Fourth, regimen switches were handled through censoring, which might have introduced informative censoring bias if changes were driven by adverse events. Finally, the predominance of male participants may constrain applicability to women. Future prospective studies incorporating standardized lifestyle assessments and extended follow-up will be essential to further elucidate the independent metabolic and renal impacts of these regimens.

In this PSM real-world cohort study, BIC/FTC/TAF and DTG+3TC exhibited comparable virologic efficacy and overall metabolic and renal safety profiles over 24 months in more than 1400 treatment-naive PWH. These results support either regimen as an appropriate first-line option in routine clinical practice. Continued long-term studies incorporating more detailed metabolic and renal endpoints will be crucial to further clarify their long-term safety profiles in diverse populations.

Acknowledgements

We are deeply grateful to all the participants enrolled and the clinical staff involved at the Shenzhen Third People's Hospital for their crucial contributions to this study.

Funding: This work was supported by the National Natural Science Foundation of China (No.82574171), the project of the Guangdong Basic and Applied Basic Research Foundation (No. 2024A1515012118), the Guangdong Provincial Medical Science and Technology Research Fund Project (No.A2025250), National Key Research and Development Program of China (No. 2024YFC2311105), National Science and Technology Major Project for Prevention and Control of Emerging, Re-emerging and Major Infectious Diseases(No. SQ2025AAA170352), Shenzhen Clinical Research Center for Emerging Infectious Diseases (No. LCYSSQ20220823091203007), Shenzhen High level Hospital Construction Fund (No. G2022153), the Special Funds for Strategic Emerging Industry of Shenzhen (No. F2022Z99502266), and Sanming Project of Medicine in Shenzhen (SZSM202311033).

Conflict of Interest: The authors have no conflicts of interest to disclose.

References

1. UNAIDS. Global HIV & AIDS statistics—Fact sheet *https://www.unaids.org/en/resources/fact-sheet* (accessed April 1, 2026).
2. Gandhi RT, Landovitz RJ, Sax PE, *et al*. Antiretroviral Drugs for Treatment and Prevention of HIV in Adults: 2024 Recommendations of the International Antiviral Society-USA Panel. JAMA. 2025; 333:609-628.
3. World Health Organization. Consolidated guidelines on HIV prevention, testing, treatment, service delivery and monitoring: recommendations for a public health approach.*https://www.who.int/publications/i/item/9789240031593* (accessed April 1, 2026).
4. Panel on Antiretroviral Guidelines for Adults and Adolescents, Department of Health and Human Services. Guidelines for the Use of Antiretroviral Agents in Adults and Adolescents With HIV. *https://clinicalinfo.hiv.gov/en/guidelines/hiv-clinical-guidelines-adult-and-adolescent-arv/whats-new.* (accessed April 1, 2026).
5. EACS Guidelines version 13.0, October 2025. *https://www.eatg.org/hiv-news/eacs-guidelines-2025-*

version-13-0/ (accessed October 18, 2025).
6. Cahn P, Madero JS, Arribas JR, *et al*. Dolutegravir plus lamivudine versus dolutegravir plus tenofovir disoproxil fumarate/emtricitabine in antiretroviral-naive adults with HIV-1 infection (GEMINI-1 and GEMINI-2): week 48 results from two multicentre, double-blind, randomised, non-inferiority, phase 3 trials. Lancet. 2019; 393:143-155.
7. Gallant J, Lazzarin A, Mills A, *et al*. Bictegravir, emtricitabine, and tenofovir alafenamide versus dolutegravir, abacavir, and lamivudine for initial treatment of HIV-1 infection (GS-US-380-1489): a double-blind, multicentre, phase 3, randomised controlled non-inferiority trial. Lancet. 2017; 390:2063-2072.
8. Osiyemi O, De Wit S, Ajana F, *et al*. Efficacy and Safety of Switching to Dolutegravir/Lamivudine Versus Continuing a Tenofovir Alafenamide-Based 3- or 4-Drug Regimen for Maintenance of Virologic Suppression in Adults Living With Human Immunodeficiency Virus Type 1: Results Through Week 144 From the Phase 3, Noninferiority TANGO Randomized Trial. Clin Infect Dis.2022; 75:975-986.
9. Zhao F, Lu H. Renal safety of tenofovir alafenamide-based antiretroviral therapy in people with HIV: a mini-review. BioSci Trends. 2024; 18:141-152.
10. Sax PE, Erlandson KM, Lake JE, *et al*. Weight Gain Following Initiation of Antiretroviral Therapy: Risk Factors in Randomized Comparative Clinical Trials. Clin Infect Dis. 2020; 71:1379-1389.
11. Hill A, Hughes SL, Gotham D, Pozniak AL. Tenofovir alafenamide versus tenofovir disoproxil fumarate: is there a true difference in efficacy and safety? J Virus Erad. 2018; 4:72-79.
12. Lake JE, Currier JS. Metabolic disease in HIV infection. Lancet Infect Dis. 2013; 13:964-975.
13. Acquired Immunodeficiency Syndrome Professional Group, Society of Infectious Diseases, Chinese Medical Association; Chinese Center for Disease Control and Prevention. Chinese guidelines for the diagnosis and treatment of human immunodeficiency virus infection/acquired immunodeficiency syndrome (2024 edition). Chin Med J (Engl). 2024; 137:2654-2680.
14. Joint Committee for the Revision of Chinese Guidelines for the Management of Dyslipidemia. Chinese guidelines for the management of dyslipidemia in adults (2023 edition). Beijing: People's Medical Publishing House; 2023.
15. Chalasani N, Younossi Z, Lavine JE, *et al*. The diagnosis and management of nonalcoholic fatty liver disease: Practice guidance from the American Association for the Study of Liver Diseases. Hepatology. 2018; 67:328-357.
16. Chinese Diabetes Society. Guidelines for the prevention and treatment of type 2 diabetes in China (2024 edition). Chin J Diabetes Mellitus. 2024; 16:1-58.
17. National Kidney Foundation. K/DOQI clinical practice guidelines for chronic kidney disease: evaluation, classification, and stratification. Am J Kidney Dis. 2002; 39: S1-266.
18. Wohl DA, Yazdanpanah Y, Baumgarten A, *et al*. Bictegravir combined with emtricitabine and tenofovir alafenamide versus dolutegravir, abacavir, and lamivudine for initial treatment of HIV-1 infection: week 96 results from a randomised, double-blind, multicentre, phase 3, non-inferiority trial. Lancet HIV. 2019; 6:e355-e363.
19. Pérez-Valero I, Corona Mata D, Camacho Espejo A, *et al*. Cohorte de la Red Española de Investigación en SIDA (CoRIS) Cohort. Real-world Effectiveness and Safety of Bictegravir/Emtricitabine/Tenofovir Alafenamide in Comparison With Other Regimens in People With HIV Starting Therapy With AIDS-Defining Conditions: Results From the CoRIS Cohort-The ACTUAS II Study. Clin Infect Dis. 2025;81: e93-e101.
20. Fraysse J, Priest J, Turner M, Hill S, Jones B, Verdier G, Letang E. Real-World Effectiveness and Tolerability of Dolutegravir and Lamivudine 2-Drug Regimen in People Living with HIV: Systematic Literature Review and Meta-Analysis. Infect Dis Ther. 2025; 14:357-383.
21. Tao M, Xia M, Yu T, Li B, Peng J, Cai S, Xu X. Longitudinal analysis of metabolic changes in people with HIV on integrase inhibitor-based versus efavirenz-based therapy: a prospective real-world cohort study in China. BMC Infect Dis. 2026; 26:302.
22. Llibre JM, Brites C, Cheng CY, *et al*. Efficacy and Safety of Switching to the 2-Drug Regimen Dolutegravir/Lamivudine Versus Continuing a 3- or 4-Drug Regimen for Maintaining Virologic Suppression in Adults Living With Human Immunodeficiency Virus 1 (HIV-1): Week 48 Results From the Phase 3, Noninferiority SALSA Randomized Trial. Clin Infect Dis. 2023; 76:720-729.
23. Gan L, Xie X, Fu Y, Yang X, Ma S, Kong L, Song C, Song Y, Ren T, Long H. Bictegravir/Emtricitabine/Tenofovir Alafenamide Versus Dolutegravir Plus Lamivudine for Switch Therapy in Patients with HIV-1 Infection: A Real-World Cohort Study. Infect Dis Ther. 2023; 12:2581-2593.
24. Shi J, Zhang W, Han J, Zhang Z, Yan D, Zheng R, Li F, Wang Y. Metabolic Health Consequences of Switching to the Bictegravir/Emtricitabine/Tenofovir Alafenamide and Dolutegravir Plus Lamivudine Regimens in Virologically Suppressed People Living with HIV Aged > 40 Years: A Retrospective Real-World Study. Infect Drug Resist. 2025; 18:2703-2716.
25. Sokhela S, Venter WDF, Bosch B, *et al*. Final 192-Week Efficacy and Safety Results of the ADVANCE Trial, Comparing 3 First-line Antiretroviral Regimens. Open Forum Infect Dis. 2024;11: ofae007.
26. Mallon PW, Brunet L, Hsu RK, Fusco JS, Mounzer KC, Prajapati G, Beyer AP, Wohlfeiler MB, Fusco GP. Weight gain before and after switch from TDF to TAF in a U.S. cohort study. J Int AIDS Soc. 2021; 24:e25702.
27. Wohl DA, Koethe JR, Sax PE, McComsey GA, Kuritzkes DR, Moyle G, Kaplan L, van Wyk J, Campo RE, Cohen C. Antiretrovirals and Weight Change: Weighing the Evidence. Clin Infect Dis. 2024; 79:999-1005.
28. Palella FJ, Hou Q, Li J, Mahnken J, Carlson KJ, Durham M, Ward D, Fuhrer J, Tedaldi E, Novak R, Buchacz K. Weight Gain and Metabolic Effects in Persons With HIV Who Switch to ART Regimens Containing Integrase Inhibitors or Tenofovir Alafenamide. J Acquir Immune Defic Syndr. 2023; 92:67-75.
29. Yang J, Wang L, Zhang X, *et al*. Safety and efficacy of lamivudine/dolutegravir *vs.* bictegravir/emtricitabine/tenofovir alafenamide in antiretroviral-naive adults with HIV-1 infection in Shanghai, China: a single-centre retrospective study. J Med Microbiol. 2025; 74:001949.
30. Damas J, Munting A, Fellay J, *et al*. Swiss HIV Cohort Study (SHCS): Weight, Anthropometric and Metabolic Changes After Discontinuing Antiretroviral Therapy Containing Tenofovir Alafenamide in People With HIV. Clin Infect Dis. 2024; 79:990-998.
31. Li X, Sun L, He Y, Zhao F, Luo Y, Liu C, Hu Y, Jiang Y, Lu H, Liu J. HDL-C as a novel predictor of immune

reconstitution in people living with HIV: insights from a baseline-to-dynamic change cohort study in China, 2005-2022. Front Immunol. 2025; 16:1520615.
32. Luo Y, Sun L, He Y, Zhao F, Shan D, Bu F, Ge L, Li X, Hu Y, Xiao X, Lu H, Liu J. The triglyceride-glucose index trajectories are associated with cardiovascular diseases in people living with HIV: evidence from a prospective cohort study in China, 2005-2022. BMC Public Health. 2025; 25:465.
33. Sun L, Luo Y, Jia X, Wang H, Zhao F, Zhang L, Ju B, Wang H, Shan D, He Y, Lu H, Liu J. Association between the triglyceride to high-density lipoprotein cholesterol ratio and cardiovascular diseases in people living with human immunodeficiency virus: Evidence from a retrospectively cohort study 2005-2022. Chin Med J (Engl). 2024; 137:2712-2719.
34. Eckard AR, McComsey GA. Weight gain and integrase inhibitors. Curr Opin Infect Dis. 2020; 33:10-19.
35. Kerchberger AM, Sheth AN, Angert CD, *et al*. Weight Gain Associated With Integrase Stand Transfer Inhibitor Use in Women. Clin Infect Dis. 2020; 71:593-600.
36. Cahn P, Pozniak AL, Mingrone H, *et al*. Dolutegravir versus raltegravir in antiretroviral-experienced, integrase-inhibitor-naive adults with HIV: week 48 results from the randomised, double-blind, non-inferiority SAILING study. Lancet. 2013; 382:700-708.
37. Milburn J, Jones R, Levy JB. Renal effects of novel antiretroviral drugs. Nephrol Dial Transplant. 2017; 32:434-439.
38. Lee DH, Malat GE, Bias TE, Harhay MN, Ranganna K, Doyle AM. Serum creatinine elevation after switch to dolutegravir in a human immunodeficiency virus-positive kidney transplant recipient. Transpl Infect Dis. 2016; 18:625-627.

Received November 11, 2025; Revised April 18, 2026; Accepted April 21, 2026.

[§]These authors contributed equally to this work.
**Address correspondence to:*
Hongzhou Lu and Yun He, Department of Infectious Diseases, National Clinical Research Center for Infectious Diseases, Shenzhen Third People's Hospital, Shenzhen, Guangdong, China.
E-mail: lluhongzhou@fudan.edu.cn (HL), yuer-he@163.com (YH)

Ping Cen, Laboratory of Infectious Diseases, HIV/AIDS Clinical Treatment Center of Guangxi (Nanning), The Fourth People's Hospital of Nanning, Nanning, Guangxi, China.
E-mail: cenping877@163.com

Jiaye Liu, School of Public Health, Shenzhen University Medical School, Shenzhen, Guangdong, China.
E-mail: liujiaye1984@163.com

Jean-Pierre Routy, Division of Hematology, Chronic Viral Illness Service, and Research Institute of the McGill University Health Centre, Montreal, QC, Canada.
E-mail: jean-pierre.routy@mcgill.ca

Released online in J-STAGE as advance publication April 24, 2026.

Original Article

DOI: 10.5582/bst.2026.01058

Allele-specific effects of distinct *SLC26A4* variants on cochlear function and transcriptomic programs in compound heterozygous models

Yue Li[1,2,3], Yiding Yu[1,2,3], Yan Zhao[1,2,3], Lin Deng[1,2,3], Jinge Xie[1,2,3], Shan Gao[1,2,3], Ying Li[1,2,3], Qingjia Cui[1,2,3], Shuo Wang[1,2,3,*], Lihui Huang[1,2,3,*]

[1] Department of Otolaryngology-Head and Neck Surgery, Beijing Tongren Hospital, Capital Medical University, Beijing, China;
[2] Beijing Institute of Otolaryngology, Beijing, China;
[3] Key Laboratory of Otolaryngology Head and Neck Surgery (Capital Medical University), Ministry of Education, Beijing, China.

SUMMARY: *SLC26A4* is a major causative gene for hereditary hearing loss, its mutation spectrum shows pronounced population specificity. In Chinese populations, patients predominantly carry biallelic mutations, and compound heterozygous genotypes are prevalent, which results in a wide spectrum of auditory phenotypes. However, how different alleles interact within these contexts to shape phenotypic variability remains poorly understood. We employed cellular and mouse models to explore the allele-specific mechanisms associated with two novel mutations, a frameshift mutation and a missense mutation, in compound heterozygous that share the same splice-site pathogenic allele. *In vitro*, wild-type (WT) and mutant (c.574delC, c.1211C>A) *SLC26A4* constructs were expressed in HeLa cells to assess pendrin localization. Both mutations reduced membrane enrichment and increased intracellular retention. *In vivo*, compound heterozygous knock-in mouse models (*Slc26a4*$^{c.574delC/c.919-2A>G}$ and *Slc26a4*$^{c.1211C>A/c.919-2A>G}$) were generated using CRISPR/Cas9. The auditory function and cochlear pathology were investigated. Both compound mutants exhibited elevated ABR thresholds, with more severe hearing loss in *Slc26a4*$^{c.574delC/c.919-2A>G}$ mice. Correspondingly, these mice showed marked hair cell disruption, stereociliary loss, and cochlear structural abnormalities, whereas the *Slc26a4*$^{c.1211C>A/c.919-2A>G}$ mice displayed milder changes. Transcriptomic profiling examined by bulk RNA-sequencing revealed broader differential expression in *Slc26a4*$^{c.574delC/c.919-2A>G}$ mice, enriched in structural and developmental pathways, while the missense model showed predominantly immune-related signatures. Our findings demonstrate that allele-specific functional divergence in compound heterozygous *SLC26A4* mutations leads to distinct auditory dysfunction, cochlear pathology, and transcriptional programs. These findings provide mechanistic insight into the phenotypic heterogeneity of hearing loss and may indicate future allele-specific interventions or therapeutic strategies.

Keywords: pendrin, CRISPR/Cas9, hearing loss, cochlear malformations, RNA-seq

1. Introduction

Hearing loss is among the most prevalent sensory disorders worldwide, and a substantial proportion is attributable to genetic causes (*1*). *SLC26A4* gene mutations are among the major causes of autosomal recessive hearing loss and include DFNB4 and Pendred syndrome (*2,3*). Affected individuals display a broad spectrum of auditory phenotypes that range from congenital to fluctuating or progressive hearing loss of different severities, and these phenotypes are often accompanied by inner ear malformations such as enlarged vestibular aqueducts (EVAs) (*4-7*).

SLC26A4 encodes pendrin, a member of the solute carrier 26 (SLC26) family of anion exchangers, which is expressed in epithelial cells of the inner ear, thyroid, and kidneys (*2,4*). Pendrin plays a critical role in ion transport (I^-, Cl^-, and HCO_3^-) and endolymph homeostasis (*8,9*). Previous studies have reported that pendrin deficiency or loss of function leads to abnormal cochlear development, altered ionic balance, and sensory hair cell degeneration (*9-11*).

Clinically, a wide spectrum of *SLC26A4* mutations, such as frameshift, missense, and splice-site mutations, have been associated with various disease severities and clinical phenotypes (*12-14*). Among these mutations, the splice-site mutation c.919−2A>G is the most common mutation in Chinese populations, and associated hearing loss most commonly arises from biallelic compound heterozygous mutations. Affected individuals exhibit a

broad spectrum of auditory phenotypes (*3,13*), which suggests that disease expression may be influenced by the specific allelic composition.

In prior clinical investigations, we identified two previously uncharacterized *SLC26A4* mutations, c.574delC and c.1211C>A, in two unrelated probands. In both cases, these mutations were present in compound heterozygosity with the shared splice-site mutation c.919−2A>G (*15,16*). Despite sharing an identical splice-site allele, the two probands were diagnosed as producing different degrees of hearing impairment—one proband produced profound hearing loss and the other proband produced severe hearing loss. Computed tomography (CT) imaging revealed bilateral EVAs in both individuals. These observations suggest that *SLC26A4*-associated hearing loss is not solely determined by the presence of a pathogenic splice-site mutation but may be modulated by the nature of the second allele within compound heterozygous configurations. Importantly, how distinct classes of mutations—such as frameshift versus missense mutations—differentially affect pendrin function and contribute to phenotypic variability when paired with the same splice site mutation remains unknown.

To date, multiple *Slc26a4* knock-in (KI) mouse models carrying missense mutations (including p.L236P, p.C565Y, p.H723R, and p.T721M) and splice-site mutations (such as c.919−2A>G) have been generated in either homozygous or compound heterozygous states (*17-20*). Different *Slc26a4* mutations give rise to highly variable phenotypes in mouse models. For example, homozygous p.L236P mice exhibit hearing loss that ranges from mild to profound, whereas other reported mutations appear nonpathogenic and therefore make it more difficult to recapitulate human disease. While these models highlight the phenotypic diversity associated with *Slc26a4* mutations, they do not allow for direct, controlled comparisons of how distinct classes of mutations—such as frameshift versus missense mutations—differentially affect pendrin expression, cochlear development, or auditory function within a clinically relevant compound heterozygous context. To address this gap, we generated mutation-specific cellular models and corresponding compound heterozygous KI mouse models with the same severe and profound hearing loss phenotypes observed in human patients. Through this integrated approach, we aimed to evaluate the functional consequences of distinct *SLC26A4* alleles and identify mutation-dependent mechanisms underlying phenotypic variability in *SLC26A4*-related hearing loss.

2. Materials and Methods

2.1. Plasmid construction

Three types of plasmids were generated: a wild-type *SLC26A4* construct and two mutant constructs (c.574delC and c.1211C>A). The full-length human *SLC26A4* cDNA (NM_000441.2) and its mutant sequences were subcloned and inserted into the pcDNA3.1(+)-3×Flag vector using the *BamHI* and *NheI* restriction sites, respectively. Each construct was verified by double digestion and confirmed with Sanger sequencing to ensure sequence integrity and the presence of the intended mutations.

2.2. Cell culture and transfection

HeLa cells were cultured in Dulbecco's modified Eagle's medium (DMEM) (Gibco) supplemented with 10% fetal bovine serum (FBS) (Gibco) under 5% CO_2 at 37°C. Cells were transfected with 0.5 μg plasmid DNA per flask using JetPRIME® (Polyplus). After 4 h, the transfection mixture was replaced with complete DMEM supplemented with 10% FBS, and cells were further incubated for 48 h prior to analysis.

2.3. Immunofluorescence analysis in transfected cells

Transfected HeLa cells were fixed with 4% paraformaldehyde (PFA) for 15 min at room temperature, permeabilized with 0.1% Triton X-100 for 10 min, and blocked for 1 h with 5% bovine serum albumin (BSA) in PBS. Pendrin was detected using a rabbit anti-Flag primary antibody (1:100; Abcam; Cat# ab205606) and an Alexa Fluor 488-conjugated goat anti-rabbit IgG secondary antibody (1:200; ZSGB-Bio; Cat# ZF-0511). F-actin was labeled with Alexa Fluor 594–conjugated phalloidin (1:500; Beyotime, Cat# C2205S), and the nuclei were counterstained with DAPI (Beyotime, Cat# C1002). Fluorescence images were obtained using a Nikon Ti2 inverted microscope (Nikon Instruments).

2.4. Generation of *Slc26a4* -mutant KI mice

Ethical approval for all animal experimental procedures was provided by the Animal Experiments and Experimental Animal Welfare Committee of Capital Medical University (No. AEEI-2020-053). The mice were generated in a C57BL/6J background (MGI:3028467). The *Slc26a4* mouse gene sequence was obtained from the Ensembl database, ID (Mouse): ENSMUSG00000020651. *Slc26a4* c.574delC, c.1211C>A, and c.919-2A>G KI mice were generated using CRISPR/Cas9 nickase-mediated homology-directed repair. KI mouse models carried a c.574delC frameshift mutation (ACACTCACT → ACATCACT), a c.1211C>A missense mutation (ACC → AAC), and a splice-site mutation c.919-2A>G (TTATTTCAG → TTATTTCGG). For each mutation, single guide RNAs (sgRNAs) flanking the target site were designed and evaluated for cleavage efficiency, and the most efficient sgRNAs were selected. Cas9 nickase, sgRNAs, and the corresponding single-stranded oligodeoxynucleotide

donor were microinjected into fertilized zygotes, which were subsequently transferred into pseudopregnant females. Founder (F0) mice were identified, and KI was confirmed by PCR and Sanger sequencing following embryo transfer. Sequence-validated F0 mice were crossed with wild-type mice to obtain F1 offspring, and germline transmission was verified.

To generate compound heterozygous mouse models, mice carrying individual *Slc26a4* mutations (c.574delC, c.1211C>A, or c.919-2A>G) were bred according to the experimental design. Homozygous mutant mice for each mutation were obtained by intercrossing heterozygous F1 mice and verified by PCR and Sanger sequencing. Then, c.574delC homozygous mice were crossed with c.919-2A>G homozygous mice, and c.1211C>A homozygous mice were crossed with c.919-2A>G homozygous mice to generate c.574delC/c.919-2A>G and c.1211C>A/c.919-2A>G compound heterozygous mice, respectively. Genotypes were confirmed by PCR amplification and Sanger sequencing of both mutant loci, and verified compound heterozygous mice were used for subsequent experiments.

2.5. Auditory brainstem response (ABR)

ABR tests were performed in WT (n = 10), heterozygous c.574delC/c.919-2A>G (n = 10), and c.1211C>A/c.919-2A>G (n = 10) mice every week between the ages of 3 and 12 weeks using an RZ6 acoustic system (Tucker-Davis Technologies). ABR testing was initiated at 3 weeks of age after the postnatal maturation of auditory sensitivity in C57BL/6J mice (*21,22*). Weekly measurements from 3–12 weeks were performed to longitudinally capture early-onset and progressive hearing changes before the emergence of strain-related age-dependent hearing loss (*23,24*). The mice were anesthetized *via* intraperitoneal injection of ketamine (100 mg/kg) and xylazine (10 mg/kg). The anesthetized mice were moved into a soundproof chamber, an active electrode was connected subdermally to the forehead, a reference electrode was connected below the pinna of one ear, and a ground electrode was connected below the contralateral ear. The ABR thresholds for click and tone-burst stimuli at frequencies of 8, 16, 24, and 32 kHz were measured, with stimulus intensities starting at 90 dB SPL and decreasing in 10 dB increments. Thresholds were determined by the lowest stimulus intensity at which a repeatable wave II should be recorded.

2.6. Cochlear immunofluorescence

Cochleae from 8-week-old mice were harvested for cryosection immunofluorescence analysis of *SLC26A4* localization, fixed in 4% paraformaldehyde for 24 h at 4°C, and then decalcified in 10% EDTA for 48 h. After being rinsed, the cochleae were cryoprotected in 15% and 30% sucrose solutions for 1.5 h each, embedded in optimal cutting temperature compound (Sakura) at 4°C overnight, preserved at -20°C, and subsequently cryosectioned at a thickness of 10 μm. The sections were blocked in 10% FBS with 1% Triton X-100 for 3 h and incubated with primary antibodies (anti-*SLC26A4*, PA5-115911) overnight at 4°C. After washing with PBS, the sections were incubated with an Alexa Fluor 594-conjugated secondary antibody for 1 h, followed by staining with DAPI for 20 min at room temperature.

For whole-mount cochlear preparations, cochleae from 4-week-old mice, a stage at which cochlear hair cell morphology is fully established, were fixed in 4% paraformaldehyde for 24 h at 4°C, after which the sensory epithelium (organ of Corti) was dissected. The samples were blocked in QuickBlock™ buffer containing Triton X-100 (Beyotime) for 1 h, followed by incubation with a rabbit anti-myosin VIIa antibody (1:200, Proteus Biosciences, Cat# 25-6790) at 4°C overnight. After washing with PBS, tissues were incubated with Alexa Fluor 568-conjugated goat anti-rabbit IgG secondary antibody (1:1000; Abcam, Cat#ab175471) for 1 h in the dark and counterstained with DAPI. Fluorescence images were obtained using an Olympus FV1000 confocal microscope.

2.7. Scanning electron microscopy (SEM)

Cochleae from 4-week-old mice were harvested and fixed in 2.5% glutaraldehyde (Servicebio) for 4 h at 4°C. Following decalcification in 10% EDTA solution, the cochlear epithelium was exposed using microdissection. Samples were subsequently rinsed three times in 0.1 M phosphate buffer (PB, pH 7.4) for 15 min each. Samples were postfixed in 1% osmium tetroxide prepared in 0.1 M PB for 1.5 h at room temperature, protected from light, and then washed three times in 0.1 M PB for 15 min each. Cochlear tissues were dehydrated through an ethanol gradient, transitioned through isoamyl acetate for 15 min, dried using a critical point dryer (Quorum), and sputter-coated under vacuum. Images were obtained using a Hitachi SU8100 scanning electron microscope.

2.8. Hematoxylin and Eosin (HE) staining

Cochlear tissues were harvested from 12-week-old mice (a fully mature adult stage), fixed and decalcified as described for immunofluorescence, and processed through graded ethanol dehydration. Tissues were embedded in paraffin, and 5 μm thick sections were cut. Sections were deparaffinized with xylene and rehydrated with ethanol. Sections were stained with hematoxylin solution for 1–2 minutes, followed by washing, and then stained with eosin for 2–5 minutes.

2.9. RNA sequencing

Total RNA from the cochleae of 1-month-old (P28) mice

(WT, *Slc26a4*$^{c.574delC/c.919-2A>G}$, *Slc26a4*$^{c.1211C>A/c.919-2A>G}$, *n* = 6 per group) was extracted using TRIzol (*Invitrogen*) according to the manufacturer's protocol. RNA quality was assessed using an Agilent 2100 Bioanalyzer (Agilent Technologies). Samples that met the quality requirements for transcriptome sequencing were used for library preparation. Sequencing libraries were prepared from total RNA using standard protocols for poly(A)-enriched mRNA sequencing. Briefly, poly(A)+ RNA was isolated using oligo(dT) magnetic beads, fragmented, and reverse transcribed to generate first-strand cDNA, followed by second-strand synthesis to produce double-stranded cDNA. After end repair, A-tailing, and adaptor ligation, the libraries were amplified using PCR and subsequently purified. Library quality and fragment size distribution were assessed prior to sequencing. Pooled libraries were subjected to paired-end sequencing using an Illumina NovaSeq 6000 platform (Illumina, Inc.).

2.10. Bioinformatic analysis

2.10.1. RNA-seq data processing and differential expression analysis

A quality assessment of raw sequencing reads was performed to ensure overall data reliability. Exploratory analyses using principal component analysis (PCA) and Pearson correlation–based distance heatmaps were performed to assess sample dispersion and detect potential outliers. Samples exhibiting discordant global expression patterns and reduced within-group correlation were considered outliers. One biological replicate per group met these criteria and was excluded prior to downstream analysis. Five biological replicates per group were retained for differential expression analysis. Differential gene expression analysis was conducted in R 4.5.1. Pairwise comparisons were performed between the WT and each mutant group (*Slc26a4*$^{c.574delC/c.919-2A>G}$ *vs.* WT; *Slc26a4*$^{c.1211C>A/c.919-2A>G}$ *vs.* WT), as well as between the two mutant groups. Genes with an adjusted *P* value (P_{adj}) < 0.05 and an absolute $\log_2$-fold change > 0.2 were defined as differentially expressed genes (DEGs).

2.10.2. Data visualization

To visualize global expression patterns, PCA results were displayed as biplots, and Pearson correlation-based sample-to-sample distance heatmaps were generated to examine relationships and clustering (*25*). The numbers of upregulated and downregulated DEGs identified in each pairwise comparison were summarized and visualized as bar plots using GraphPad Prism 10.6.1. The differential expression results were further visualized using volcano plots. To identify shared and unique transcriptional changes between the compound heterozygous mice mutants, Venn diagram analyses were performed to determine overlapping upregulated and downregulated DEGs.

2.10.3. Functional enrichment analysis

A functional enrichment analysis was conducted to characterize the biological relevance of the DEGs. Gene Ontology (GO) enrichment analysis for the biological process (BP), cellular component (CC), and molecular function (MF) categories was performed using the "clusterProfiler" package. For each comparison, we summarized the top enriched GO terms. Commonly upregulated or downregulated genes in both mutant groups were further subjected to functional enrichment analysis using DAVID (Database for Annotation, Visualization and Integrated Discovery). Enrichment results for the GO categories (BP, CC, and MF) and Kyoto Encyclopedia of Genes and Genomes (KEGG) pathways were summarized to identify biological processes and pathways associated with shared transcriptional alterations in *Slc26a4* gene mutations.

2.11. *In silico* cell-type mapping using public cochlear single-cell datasets

To provide cellular context for representative DEGs identified in bulk RNA-seq analysis, we performed *in silico* cell-type mapping using publicly available mouse cochlear single-cell and single-nucleus RNA sequencing datasets hosted on the gEAR portal (umgear.org) (*26*). The following datasets were examined: Single cell RNA-seq analysis of P20 mouse cochlear cells (*27*) and Adult mouse single-nucleus RNA-seq (methanol-fixed; Hoa) (*28*). Expression patterns of selected DEGs were visualized across annotated cochlear cell populations, including hair cells, supporting cells, stria vascularis (SV) cell types, and macrophages. This analysis was used solely for contextual interpretation and did not involve reprocessing of raw sequencing data.

2.12. Co-immunoprecipitation and LC–MS/MS analysis

To investigate whether mutation class alters pendrin-associated molecular complexes, co-immunoprecipitation coupled with Liquid Chromatography–Tandem Mass Spectrometry (LC–MS/MS) was performed in HEK293T cells transfected with Flag-tagged WT or mutant *SLC26A4* constructs (c.574delC and c.1211C>A). Immunocomplexes were captured using anti-Flag magnetic beads and subjected to in-gel digestion followed by LC–MS/MS analysis. Proteins were identified using a target–decoy database with a false discovery rate < 1%. Selected candidate genes identified from proteomic analysis were further validated by quantitative PCR (qPCR). Detailed experimental procedures are provided in Supplementary Methods.

2.13. Statistical Analysis

Statistical analyses were performed using SPSS (IBM) and GraphPad Prism (GraphPad Software). Confocal images with intensity profiles plotting were generated in Fiji (ImageJ) along manually drawn lines across the plasma membrane to assess spatial correlation between pendrin and F-actin signals. Intensity values were normalized to the maximum signal within each channel. ABR thresholds are presented as the mean ± the standard deviation (SD). Group differences at each frequency and time point were assessed using an unpaired two-tailed Student's *t* test. When no ABR response was detected at the maximum stimulus level (90 dB SPL), the threshold was assigned as 90 dB SPL for statistical purposes. For hair cell quantification, data are presented as mean values. Differences among groups and cochlear regions (apex, middle, and base) were analyzed using two-way analysis of variance (ANOVA), followed by Sidak's multiple comparisons test. A p value < 0.05 was considered to indicate statistical significance.

3. Results

3.1. Mutations alter pendrin intracellular distribution in transfected cells

To investigate the potential pathogenic effects of the identified *SLC26A4* mutations, the location of *SLC26A4* mutations at the gene and protein levels was examined (Figure 1A and 1B). WT and two mutant plasmids were generated and verified. We investigated the subcellular distribution of WT and mutant pendrin in transfected cells using immunofluorescence staining

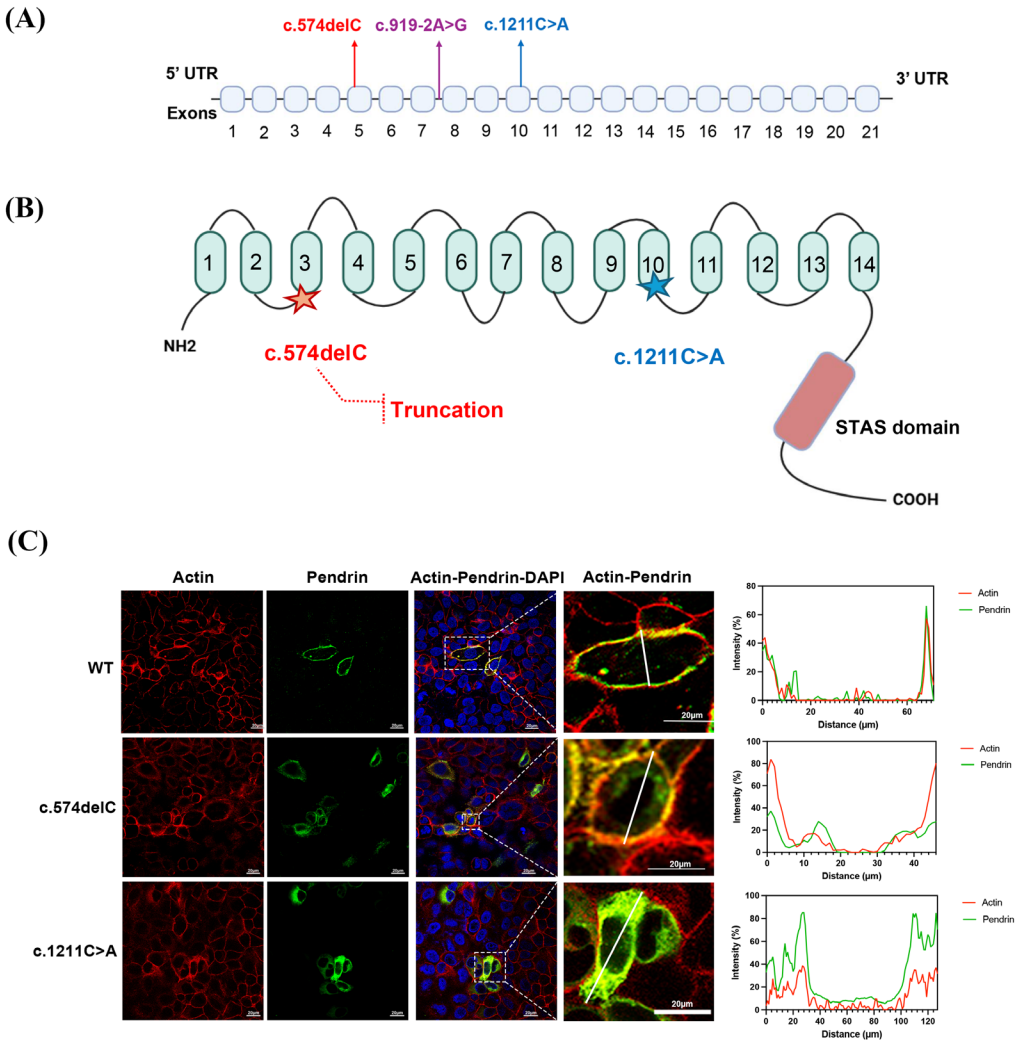

Figure 1. *SLC26A4* mutations and their effects on pendrin subcellular localization. (A) Schematic representation of the *SLC26A4* gene structure showing exon organization and the positions of the mutations c.574delC, c.919-2A>G, and c.1211C>A. **(B)** Predicted domain architecture of the pendrin protein, including multiple transmembrane segments and the C-terminal anti-sigma factor antagonist (STAS) domain. The splice-site mutation c.919-2A>G is intronic and does not directly alter the encoded amino acid sequence, previous studies have shown that it disrupts normal splicing, resulting in exon 8 skipping and truncated protein. **(C)** Representative confocal immunofluorescence images show the subcellular localization of Flag-tagged WT and mutant *SLC26A4* in HeLa cells. Pendrin was detected using an anti-Flag antibody followed by a fluorescein-conjugated secondary antibody (green). Actin filaments were stained with phalloidin (red), and nuclei were counterstained with DAPI (blue). Merged images and magnified insets (dashed boxes) are shown to illustrate membrane localization patterns. Line-scan intensity profiles were generated using Fiji (ImageJ) along the indicated white lines of individual cells to quantitatively assess spatial correlation between pendrin and actin signals. Scale bar, 20 μm.

to assess whether the mutations altered its intracellular distribution. Distinct localization patterns were detected in HeLa cells transfected with WT and mutant *SLC26A4* constructs (Figure 1C). WT pendrin was enriched predominantly at the plasma membrane in transfected HeLa cells. In contrast, compared with WT cells, cells with both the c.574delC mutation and the c.1211C>A mutation presented reduced membrane enrichment and increased intracellular distribution. Although partial membrane-associated signals were still observed, a substantial proportion of mutant pendrin was distributed within intracellular compartments.

3.2. Generation and validation of *Slc26a4* compound heterozygous KI mouse models

For subsequent analyses of auditory function, we generated clinically relevant *Slc26a4* KI mouse models carrying the c.574delC, c.1211C>A, and c.919-2A>G mutations, which targeted exon 5, exon 10, and the splice acceptor site of intron 7 (Figure 2A). Precise introduction of each mutation was confirmed by PCR genotyping and Sanger sequencing in single-mutant lines. Single KI mice carrying c.574delC, c.1211C>A, or c.919-2A>G mutations were first crossed with wild-type mice to obtain heterozygous offspring. Homozygous mutant mice were subsequently generated by intercrossing heterozygous animals. Homozygous mutant lines were intercrossed to generate *Slc26a4*$^{c.574delC/c.919-2A>G}$ and *Slc26a4*$^{c.1211C>A/c.919-2A>G}$ compound heterozygous mice (Figure 2B and C). Sanger sequencing of compound heterozygous mice further confirmed the presence of two distinct *Slc26a4* mutant alleles within individual animals (Figure 2D).

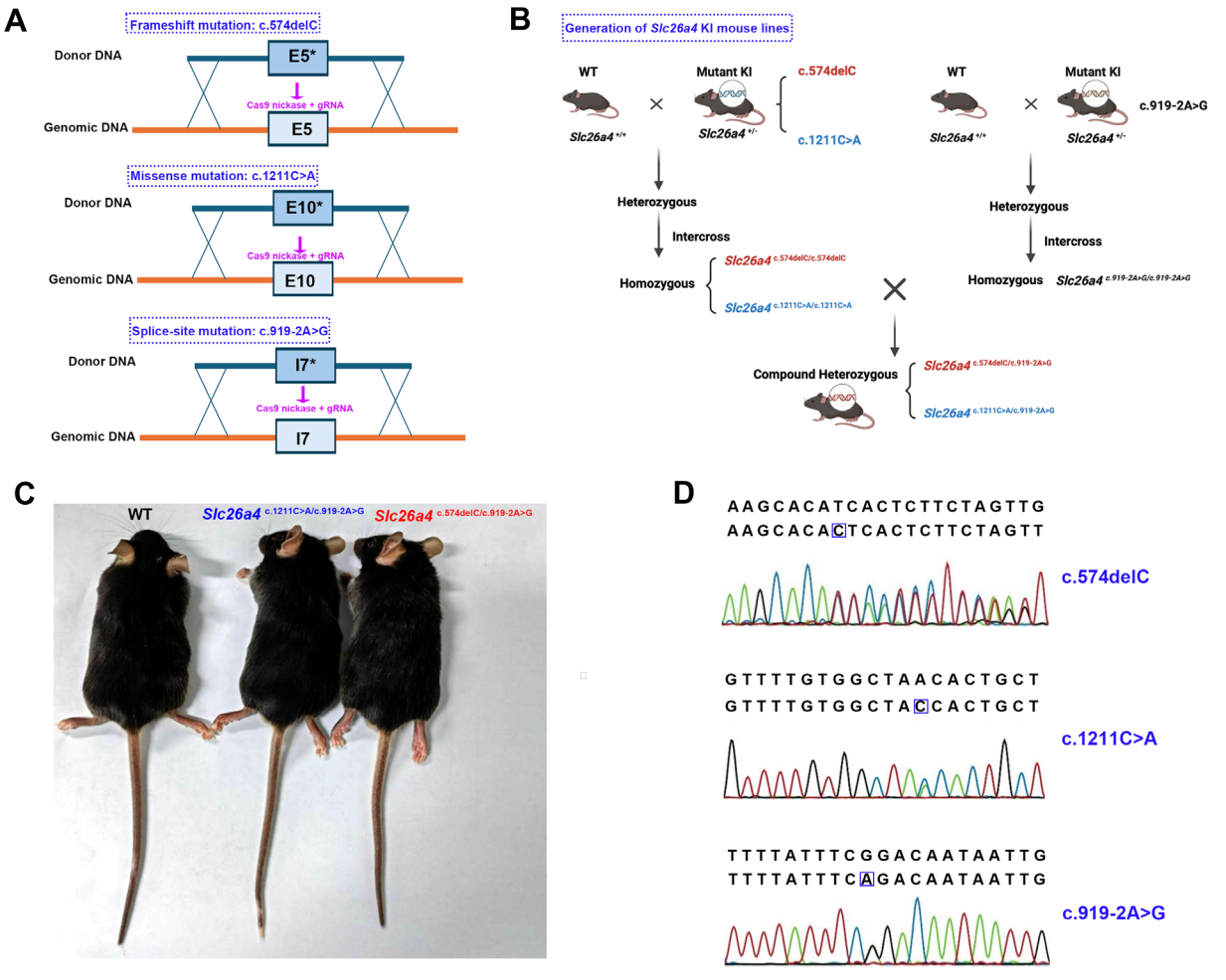

Figure 2. Generation and validation of *Slc26a4* compound heterozygous knock-in (KI) mouse models. (A) Schematic diagrams of the CRISPR/Cas9-mediated KI strategy used to introduce three pathogenic *Slc26a4* mutations into the mouse genome. Donor single-stranded oligodeoxynucleotides carrying the desired mutation were coinjected with Cas9 nickase and sgRNAs targeting exon 5 (c.574delC), exon 10 (c.1211C>A), or intron 7 (c.919-2A>G), followed by homology-directed repair. **(B)** Generation scheme for compound heterozygous mice. Wild-type (WT) mice were crossed with founder KI mice to generate F1 heterozygotes. Intercrossing heterozygous F1 mice yielded homozygous mutants, which were crossed between different alleles to produce compound heterozygous mice (c.574delC/c.919-2A>G and c.1211C>A/c.919-2A>G). **(C)** Representative images of WT and two compound heterozygous mutant mice. **(D)** Sanger sequencing confirmed KI mutations at each genomic locus in compound heterozygous mice. The introduced mutant nucleotides are marked.

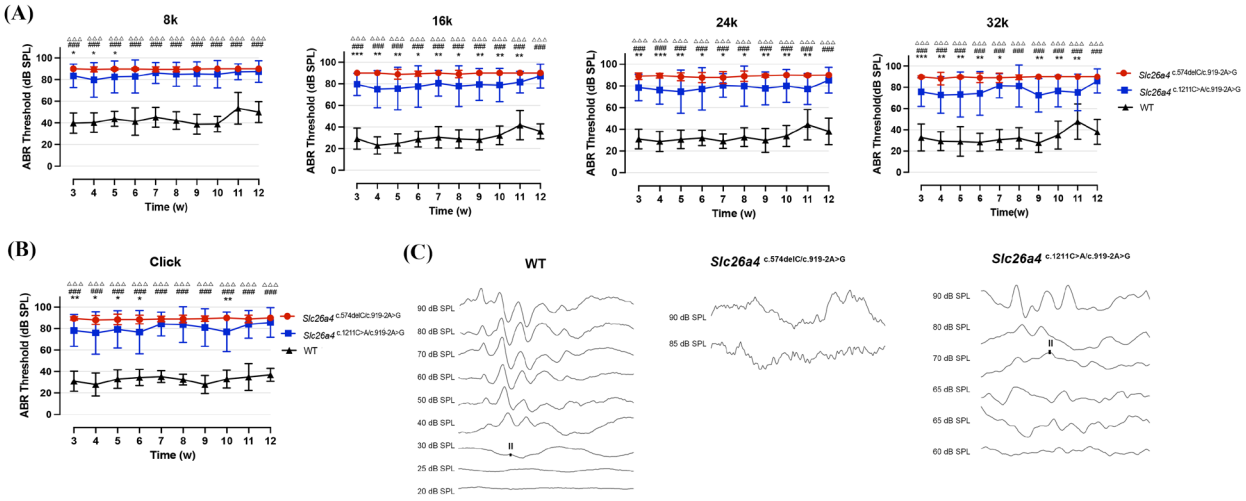

Figure 3. Compound heterozygous *Slc26a4* KI mice exhibit elevated ABR thresholds. (A–B) Longitudinal auditory brainstem response (ABR) thresholds of wild-type (WT) and compound *Slc26a4* KI mice from 3–12 weeks of age in response to tone burst stimuli at 8, 16, 24, and 32 kHz **(A)** and click stimuli **(B)**. Compared with the WT controls, the compound mutant strains displayed significantly elevated ABR thresholds at all ages and frequencies. ABR data are shown as the mean ± SD. One-way ANOVA was used for statistical comparisons. An * indicates $P < 0.05$, ** indicates $P < 0.01$, and *** indicates $P < 0.001$ for *Slc26a4*$^{c.574delC/c.919-2A>G}$ compared with *Slc26a4*$^{c.1211C>A/c.919-2A>G}$; a # indicates $P < 0.05$, ## indicates $P < 0.01$, and ### indicates $P < 0.001$ for *Slc26a4*$^{c.1211C>A/c.919-2A>G}$ compared with WT; a Δ indicates $P < 0.05$, ΔΔ indicates $P < 0.01$, and ΔΔΔ indicates $P < 0.001$ for *Slc26a4*$^{c.574delC/c.919-2A>G}$ compared with WT. **(C)** Representative click ABR waveforms were recorded from WT and mutant mice at 3 weeks of age.

3.3. *Slc26a4* compound heterozygous mice show elevated ABR thresholds

To assess whether the two compound heterozygous *Slc26a4* mutations recapitulated the auditory phenotype observed in human patients, we performed ABR tests using click and tone-burst stimuli at 8, 16, 24, and 32 kHz beginning at postnatal week 3. As shown in Figure 3AB, compared with age-matched wild-type controls, both compound heterozygous lines exhibited significantly elevated ABR thresholds across all tested frequencies ($P < 0.001$). Thresholds in *Slc26a4*$^{c.574delC/c.919-2A>G}$ mice were consistently higher than those in *Slc26a4*$^{c.1211C>A/c.919-2A>G}$ mice. Notably, profound hearing loss was evident at 3 weeks of age; ABR thresholds approached the maximum stimulus level (90 dB SPL), and there were no identifiable waveforms in most *Slc26a4*$^{c.574delC/c.919-2A>G}$ mice (Figure 3C).

3.4. Impaired hair cell integrity and altered cochlear morphology in compound heterozygous mice

To characterize cochlear structural alterations associated with both compound heterozygous *Slc26a4* mutations, hair cell morphology, ultrastructural features, cochlear histopathology, and pendrin expression were systematically examined (Figure 4).

Whole-mount immunofluorescence staining of 4-week-old mice for Myosin7a revealed well-organized and continuous rows of inner hair cells (IHCs) and outer hair cells (OHCs) across the apical, middle, and basal turns in WT mice (Figure 4A and Supplementary Figure S1, *https://www.biosciencetrends.com/action/getSupplementalData.php?ID=291*). In contrast, *Slc26a4*$^{c.574delC/c.919-2A>G}$ mice exhibited pronounced disruption of OHC organization and discontinuity of hair cell rows in all cochlear turns, which were characterized by reduced Myosin VIIa and DAPI signal intensity. In *Slc26a4*$^{c.1211C>A/c.919-2A>G}$ mice, the overall hair cells survived, with only sporadic loss of individual OHCs observed, and the general organization of hair cell rows remained comparable to that of WT mice (Figure 4C).

SEM of 4-week-old mice demonstrated further differences in stereociliary architecture between the two compound genotypes (Figure 4B). In *Slc26a4*$^{c.574delC/c.919-2A>G}$ mice, more severe ultrastructural abnormalities included extensive loss of OHC stereocilia, fusion, disorganized arrangement, and IHC stereocilia bundle collapse. In comparison, *Slc26a4*$^{c.1211C>A/c.919-2A>G}$ mice retained mostly intact hair bundles; however, OHC stereocilia exhibited loose organization and localized structural deformities. Relative to WT mice, IHC stereocilia of *Slc26a4*$^{c.1211C>A/c.919-2A>G}$ mice displayed locally disrupted orientation but retained their overall bundle structure. Similar stereociliary abnormalities were also observed in the apex, middle, and basal turns of the cochlea, although representative SEM images from the middle and basal turns were limited by incomplete fields of view for *Slc26a4*$^{c.1211C>A/c.919-2A>G}$ mice (Supplementary Figure S2, *https://www.biosciencetrends.com/action/getSupplementalData.php?ID=291*).

HE staining of cochlear sections from 12-week-old mice revealed the cochlear architecture and structure of the organ of Corti (Figure 4D). In *Slc26a4*$^{c.574delC/c.919-2A>G}$

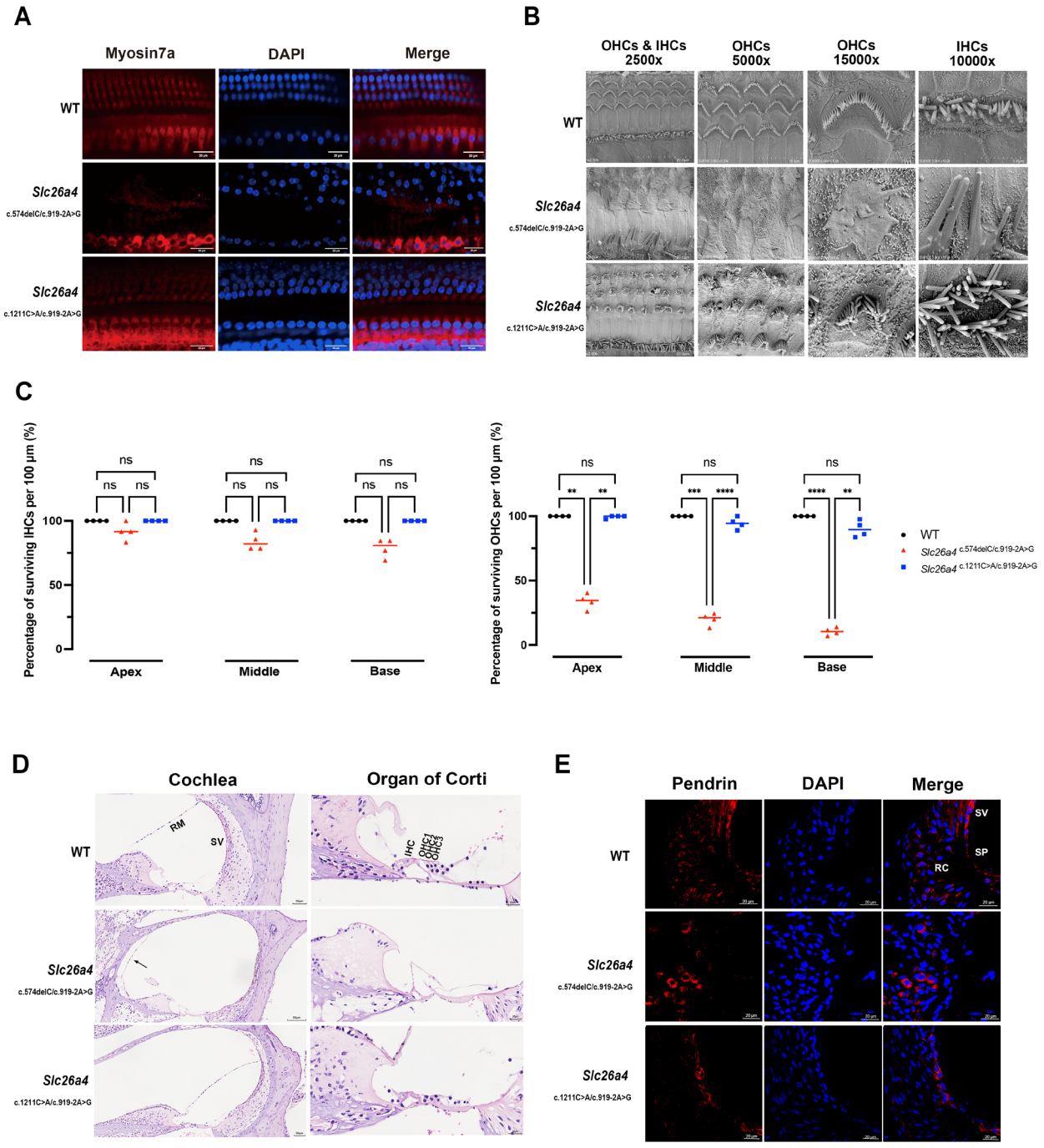

Figure 4. Impaired hair cell integrity, altered cochlear morphology and pendrin expression in two different compound heterozygous mice. **(A)** Whole-mount immunofluorescence images of the cochlear sensory epithelium stained for myosin VIIa and DAPI show differences in the extent of loss of outer hair cells (OHCs) and inner hair cells (IHCs) between two different compound heterozygous mice and WT mice at the middle turns. Scale bar, 20 µm. **(B)** Scanning electron microscopy (SEM) images of mouse cochlear epithelial apical turns show that *Slc26a4*$^{c.574delC/c.919-2A>G}$ mice have severe ultrastructural abnormalities, including extensive loss and fusion of OHC stereocilia, a disorganized arrangement, and collapse of IHCs stereociliary bundles. *Slc26a4*$^{c.1211C>A/c.919-2A>G}$ mice preserve the overall bundle structure and loose organization of the OHC stereocilia and disrupted orientation of the IHCs stereocilia. **(C)** Quantification of surviving IHCs and OHCs in WT and mutant mice. Individual values are shown. Data are shown as the mean of the biological replicates. Statistical analysis was performed using two-way ANOVA followed by Sidak's multiple comparisons test. ns, not significant; *$P < 0.05$, **$P < 0.01$, ***$P < 0.001$, ****$P < 0.0001$. **(D)** Hematoxylin and eosin (HE) staining of cochlear sections of mouse cochlear middle turns. WT cochleae show an intact cochlear architecture with an intact Reissner's membrane (RM), normal scala media, a stria vascularis (SV), and an organ of Corti with clear IHCs and three OHC rows. *Slc26a4*$^{c.574delC/c.919-2A>G}$ mice exhibit pronounced morphological abnormalities, including dilation of the scala media (as indicated by the black arrow pointing to Reissner's membrane) and disorganization of the organ of Corti. In *Slc26a4*$^{c.1211C>A/c.919-2A>G}$ mice, overall cochlear morphology was preserved. **(E)** Immunofluorescence staining of cochlear sections showing pendrin expression in the SV and adjacent regions. Representative images are shown from the middle turn of the cochlea. In WT mice, pendrin expression is detected in the spiral prominence (SP) and root cells (RC). A similar pendrin localization pattern was observed in the two mutant mice.

mice, marked histopathological abnormalities included dilation of the scala media, atrophy of the SV, and disorganization of the organ of Corti, with indistinct hair cell morphology. In contrast, *Slc26a4*$^{c.1211C>A/c.919-2A>G}$ mice maintained overall cochlear structure and had identifiable hair cell layers in the organ of Corti.

Immunolocalization further demonstrated that pendrin was expressed in the SV adjacent regions of the cochleae, including the spiral prominence (SP) and root cells (RCs), in WT mice (Figure 4E). Similar pendrin expression was detected in the *Slc26a4*$^{c.574delC/c.919-2A>G}$ and *Slc26a4*$^{c.1211C>A/c.919-2A>G}$ mice. No overt alteration in pendrin localization was evident among WT and compound heterozygous *Slc26a4* mice.

3.5. Transcriptomic profiling reveals distinct and shared gene expression changes in response to compound *Slc26a4* mutations

3.5.1. Global transcriptomic variation

A PCA revealed clear separation among WT cochleae and cochleae from the two *Slc26a4* mutants (Figure 5A, Supplementary Figure S3, *https://www.biosciencetrends.com/action/getSupplementalData.php?ID=291*). Samples from *Slc26a4*$^{c.574delC/c.919-2A>G}$ and *Slc26a4*$^{c.1211C>A/c.919-2A>G}$ mice formed distinct clusters that were spatially separated from those of WT mice, which indicated pronounced transcriptomic differences between mutant and WT cochleae. In addition, the two mutant groups were partially separated from each other along principal component axes, which suggested the presence of genotype-specific transcriptional signatures. Consistent with the PCA results, sample-to-sample distance heatmaps based on Pearson correlations demonstrated high within-group similarity and clear clustering according to genotype (Figure 5B, Supplementary Figure S3, *https://www.biosciencetrends.com/action/getSupplementalData.php?ID=291*).

3.5.2. Differential patterns of transcriptomic changes in *Slc26a4* mutant cochleae

Differential expression analysis revealed substantial transcriptional changes in both *Slc26a4* mutants compared with the WT group. The numbers of upregulated and downregulated DEGs with different fold changes varied across comparisons, as summarized in Figure 5C. Notably, compared with WT cochleae, cochleae from the *Slc26a4*$^{c.574delC/c.919-2A>G}$ mice exhibited a greater number of DEGs than cochleae from the *Slc26a4*$^{c.1211C>A/c.919-2A>G}$ mice did, which indicated that more transcriptional alteration occurred in the former.

Volcano plot visualization highlighted distinct DEG distributions for each pairwise comparison and illustrated the magnitude and statistical significance of gene expression changes (Figure 5D–F). In addition to differences relative to WT mice, a direct comparison between the two mutant models revealed further transcriptional differences (Figure 5F) that indicated genotype-specific gene expression changes. Together, these results demonstrated that each *Slc26a4* mutant model exhibited a characteristic and distinguishable transcriptional signature.

3.5.3. Distinct functional enrichment programs differentiate the two *Slc26a4* mutant models

GO enrichment analysis revealed markedly distinct functional signatures between cochleae from the two *Slc26a4* mutants. Analyses were performed separately for upregulated and downregulated DEGs; representative top terms for upregulated DEGs are shown in Figure 5G-I, and downregulated terms are shown in Supplementary Figure S4 (*https://www.biosciencetrends.com/action/getSupplementalData.php?ID=291*). In *Slc26a4*$^{c.574delC/c.919-2A>G}$ cochleae, upregulated DEGs were predominantly enriched in biological processes related to cell–substrate adhesion, Wnt signaling, and organ development (Figure 5G). Correspondingly, enriched cellular components included the plasma membrane and junctional complexes, whereas molecular functions were dominated by extracellular matrix structural constituents and integrin- and collagen-binding activities. In contrast, a different enrichment profile occurred in *Slc26a4*$^{c.1211C>A/c.919-2A>G}$ cochleae, and upregulated DEGs included functional categories that were associated primarily with immune-related and regulatory processes such as leukocyte migration, chemotaxis, and cytokine activity, as well as membrane microdomain-related cellular components (Figure 5H).

A direct comparison of DEGs between the two mutant models further revealed that the upregulated genes were predominantly enriched in biological processes associated with extracellular matrix organization, external encapsulating structure organization, Wnt signaling, and ear and sensory organ development. Additional enrichment was observed for developmental processes related to inner ear morphogenesis and connective tissue development (Figure 5I). Consistent with these findings, cellular component analysis highlighted enrichment in the basement membrane, apical and basolateral plasma membranes, and junctional complexes. Molecular function categories were enriched mainly for extracellular matrix structural constituents, integrin and collagen binding, glycosaminoglycan binding, and ion transport-related activities.

3.5.4. Shared transcriptional alterations between the two *Slc26a4* mutant models

To identify common gene expression changes associated with *Slc26a4* mutations, Venn diagram analysis was

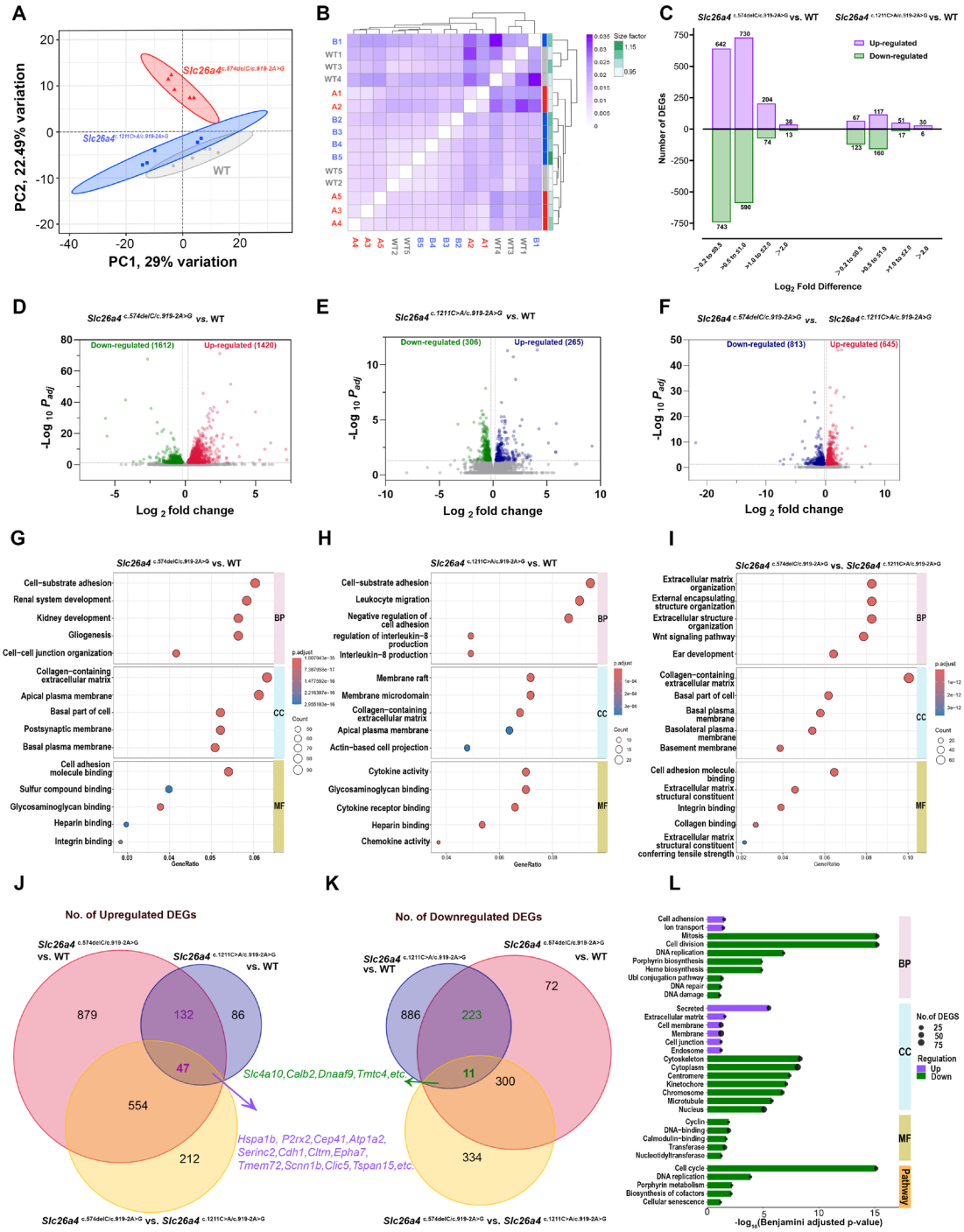

Figure 5. Transcriptomic changes and functional enrichment in *Slc26a4* mutant mouse cochleae. (A) Principal component analysis (PCA) of normalized gene expression profiles from wild-type (WT) and mutant cochleae. The samples clustered according to genotype, which indicated distinct global transcriptomic profiles for three groups. **(B)** Sample-to-sample distance heatmap based on Pearson correlations showing hierarchical clustering of samples. Samples from the same genotype cluster together and demonstrate high within-group similarity and clear separation between the WT and mutant groups. WT1–5 represent five different samples from the WT group, A1–5 represent samples from the *Slc26a4*$^{c.574delC/c.919-2A>G}$ group, and B1–5 represent samples from the *Slc26a4*$^{c.1211C>A/c.919-2A>G}$ group. **(C)** Bar plots summarizing the numbers of upregulated and downregulated differentially expressed genes (DEGs) identified in each pairwise comparison between *Slc26a4* mutants and WT, stratified by $\log_2$-fold change ranges. (D–F) Volcano plots illustrating DEGs in pairwise comparisons. **(D)** *Slc26a4*$^{c.574delC/c.919-2A>G}$ versus (*vs.*) WT, (E) *Slc26a4*$^{c.1211C>A/c.919-2A>G}$ *vs.* WT, **(F)** *Slc26a4*$^{c.574delC/c.919-2A>G}$ *vs. Slc26a4*$^{c.1211C>A/c.919-2A>G}$. Each dot represents one gene, with the $\log_2$ fold change plotted against the $-\log_{10}$ adjusted p value. Significantly upregulated and downregulated genes are highlighted in different colors. **(G–I)** Gene Ontology (GO) enrichment analysis of upregulated DEGs from each pairwise group comparison, showing the top five enriched terms in the biological process (BP), cellular component (CC), and molecular function (MF) categories. Dot size represents the number of genes associated with each term, and color indicates the adjusted *P* value. **(J, K)** Venn diagrams showing overlap for upregulated **(J)** and downregulated **(K)** DEGs between the two mutant groups and the WT group, which highlight shared and genotype-specific transcriptional changes. **(L)** Functional enrichment analysis of DEGs that were commonly upregulated (179 genes) or downregulated (234 genes) in both mutant models. Enriched GO terms (BP, CC, and MF) and KEGG pathways are shown. Bar length represents the –log10 of the Benjamini-adjusted P value and color indicates up or down regulation.

performed. A subset of DEGs, including commonly upregulated and downregulated genes, was shared between the two mutant groups and the WT group (Figure 5J and Figure 5K, Supplementary Table S1, *https://www.biosciencetrends.com/action/getSupplementalData.php?ID=291*).

A total of 47 genes were consistently upregulated in cochleae from mutant mice compared with those from WT mice, and higher expression levels occurred in the *Slc26a4*$^{c.574delC/c.919-2A>G}$ mutant than in the *Slc26a4*$^{c.1211C>A/c.919-2A>G}$ mutant (Supplementary Table S1, *https://www.biosciencetrends.com/action/getSupplementalData.php?ID=291*). These commonly upregulated genes included extracellular matrix components (*e.g.*, *Lama1*, *Sparc*, and *Cdh1*), antioxidant enzymes (*e.g.*, *Gpx3 and Hspa1b*), and stress-responsive molecules (*e.g.*, *Timp2*, *Ndrg2*, *and S100a10*), as well as ion transport related genes (*e.g.*, *P2rx2*, *Scnn1b*, *and Atp1a2*). Many of these genes are known to contribute to epithelial integrity, oxidative stress responses, and ion homeostasis maintenance in the cochleae. Functional enrichment analysis of these 47 shared upregulated DEGs was performed using DAVID and revealed significant enrichment in GO terms. These upregulated genes were significantly enriched in biological processes related to extracellular matrix organization, cell adhesion, calcium ion binding, and stress responses (Supplementary Table S2, *https://www.biosciencetrends.com/action/getSupplementalData.php?ID=291*). In addition, compared with those in the WT cochleae, the expression of 132 genes in mutant cochleae was also upregulated, but expression did not differ between the two mutant models; these genes were considered to be shared mutation-associated responses that were independent of genotype-specific effects.

To further characterize the transcriptional programs commonly affected by *Slc26a4* mutation, we performed DAVID analyses on consistently upregulated DEGs (179 genes) or downregulated DEGs (234 genes) in cochleae from both mutants relative to WT mice (Fig. 5L). Commonly upregulated genes were enriched primarily in pathways and biological processes related to extracellular matrix organization, cell adhesion, ion transport, and secretory or membrane-associated components. Commonly downregulated DEGs were enriched consistently in pathways associated with fundamental cellular processes, including cell cycle regulation, mitosis, DNA replication, DNA repair, and chromosome organization, and enriched cellular components included the nucleus, chromosome, centromere, kinetochore, and microtubule-associated structures.

3.5.5. Cell-type contextualization of mutation-associated DEGs

To provide cell-type context for bulk RNA-seq findings, we performed *in silico* mapping of mutation-associated DEGs using public cochlear single-cell atlases (gEAR; Figure 6). Ion transport– and epithelial-related genes, such as *P2rx2*, *Atp1a2*, *Epyc, Clic5* were enriched in SV, hair cells and supporting cells in the organ of Corti, whereas immune-related genes such as *Trem2* and *Lbp* were predominantly detected in macrophages and SV associated compartments.

3.6. Mutation-dependent alteration of pendrin-associated interactions

Given the mutation-severity–dependent transcriptional remodeling observed *in vivo*, we further examined whether pendrin-associated protein complexes were differentially altered according to mutation class. WT specific enriched gel regions were selectively excised and subjected to LC–MS/MS analysis (Supplementary Figure S5, *https://www.biosciencetrends.com/action/getSupplementalData.php?ID=291*). This band-guided strategy identified 462 candidate pendrin-associated proteins. Functional annotation (GO/KEGG) suggested their predominant involvement in (1) protein folding and endoplasmic reticulum processing, (2) membrane and junctional organization, and (3) metabolic regulation. The related representative genes are presented in Supplementary Table S3 (*https://www.biosciencetrends.com/action/getSupplementalData.php?ID=291*). qPCR validation of selected representative genes (*HSPA5*, *HSPA1B*, *LTF*, *and JUP*) demonstrated expression trends associated with mutation-dependent molecular remodeling (Supplementary Figure S6, *https://www.biosciencetrends.com/action/getSupplementalData.php?ID=291*).

4. Discussion

In this study, we investigated two novel *SLC26A4* mutations, the frameshift mutation c.574delC and the missense mutation c.1211C>A, which were identified in prior clinical observations. These mutations were associated with different severities of hearing loss in compound heterozygous mouse carriers due to the presence of a common shared splice-site mutation (c.919-2A>G). By generating mutation-specific cellular models and compound heterozygous KI mouse models, we identified how a distinct *SLC26A4* mutation class of alleles shaped cochlear pathology when paired with the same splice-site mutation, and we explored the molecular mechanisms underlying *SLC26A4*-related hearing loss.

Pendrin is characterized by multiple transmembrane domains at the N-terminus and a highly conserved C-terminal sulfate transporter and anti-sigma factor antagonist (STAS) domain. Recent cryo-EM structural analyses of pendrin have provided a mechanistic framework for interpreting mutation-specific differences in pendrin (*8*). Disease-associated mutations are highly enriched within the anion-binding pocket, gating

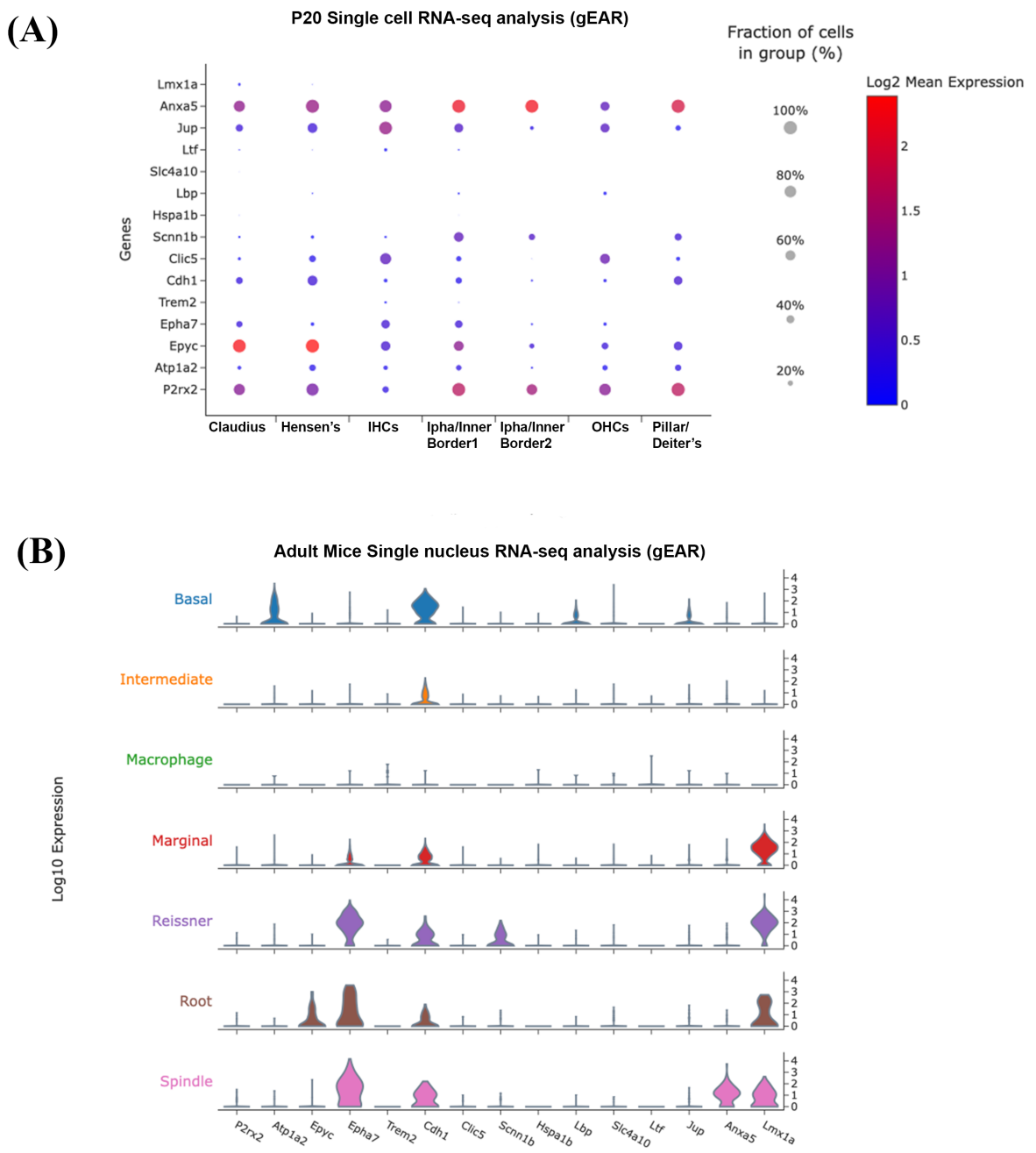

Figure 6. *In silico* cell-type mapping of representative DEGs using gEAR single-cell datasets. (A) Expression patterns of selected DEGs across annotated single cell RNA-seq analysis of P20 mouse cochlear cells. Dot size represents fraction of expressing cells: Claudius cells (Claudius); Hensen's cells (Hensen's); inner hair cells (IHCs); outer hair cells (OHCs); inner phalangeal/inner border cells (Ipha/Inner Border) Type 1 and Type 2; Pillar and Deiters' cells (Pillar/Deiter's), color intensity indicates $\log_2$ mean expression. **(B)** Expression distribution of representative genes across annotated adult mouse single-nucleus RNA-seq (methanol-fixed; Hoa) dataset. Violin plots depict $\log_{10}$ expression levels across basal, intermediate, marginal, macrophage, Reissner's membrane, root, and spindle cell populations.

regions, and STAS-mediated dimerization interfaces, which are essential for anion recognition, transport cycling, and protein stability (*11,29-31*). Disruption of these core architectural elements is expected to result in ion transport-related functional loss. The two *SLC26A4* mutations investigated in this study affected distinct structural and functional regions of pendrin. The c.574delC mutation introduces a frameshift and premature termination codon that results in a severely truncated protein that lacks the entire C-terminal STAS domain, whereas the c.1211C>A mutation is a missense mutation located within the transmembrane core domain. Although the c.1211C>A mutation produced a full-length pendrin protein, perturbation of the core domain is likely to impair regulatory functions in anion transport or exchange activities (*8*).

Consistent with these structural differences, *in vitro* overexpression experiments revealed intracellular

distribution patterns in two identified mutations. Both mutations resulted in reduced membrane-associated signals in transfected cells. These observations reflect distribution patterns in heterologous overexpression systems and do not necessarily represent the physiological localization of pendrin in native cochlear cells. Notably, immunolocalization analyses in cochlear sections did not reveal an overt redistribution of pendrin in the SP or RCs among WT and compound heterozygous mice. This suggests that gross pendrin localization may be preserved *in vivo* despite functional impairment. Such preservation may reflect limitations in detecting subtle changes in membrane residency *via* immunostaining, differences between overexpression systems and endogenous regulation, or compensatory mechanisms that maintain apparent localization without fully restoring transporter activity. These findings are aligned with those of previous studies in which truncating *SLC26A4* mutations often lead to complete loss of function, whereas missense mutations may retain partial activity but exhibit impaired trafficking or stability (*10,32*). Thus, these findings indicate that pendrin function relies upon different mechanisms, such as structural truncation and functional dysregulation, loss of protein integrity for c.574delC, and impaired trafficking or processing for c.1211C>A, which may diminish effective membrane-localized transporter activity.

In the inner ear, pendrin is essential for maintaining endolymphatic pH and ionic composition, thereby supporting normal cochlear development and hair cell survival (*9,33*). Disruption of the structure or trafficking of pendrin might differentially affect cochlear homeostasis. In this context, truncating mutations and mutations that abolish pendrin integrity are likely to induce more severe perturbations than missense mutations are, which was consistent with the severity gradient observed between both compound heterozygous KI mouse models. In mice, auditory thresholds mature by postnatal day 14–21, and both KI models demonstrated markedly elevated ABR thresholds by postnatal week 3, which indicated an early-onset pattern of hearing loss. Importantly, the thresholds were higher in *Slc26a4*$^{c.574delC/c.919-2A>G}$ mice, which was in agreement with more severe hearing loss observed clinically in this proband genotype. Morphological analyses further supported a severity gradient: *Slc26a4*$^{c.574delC/c.919-2A>G}$ mice exhibited pronounced disruption of hair cell organization and stereociliary architecture, including extensive stereocilia loss or fusion in OHCs and IHC bundle collapse, along with dilation of the scala media, SV atrophy, and disorganization of the organ of Corti. In contrast, *Slc26a4*$^{c.1211C>A/c.919-2A>G}$ mice retained hair-bundle structures with loose organization and a relatively intact cochlear architecture.

These findings are in accordance with clinical observations of Pendred syndrome and DFNB4, in which frameshift or splice-site *SLC26A4* mutations are frequently associated with severe-to-profound, early-onset hearing loss that is accompanied by inner ear malformations (*13,34,35*). Notably, previous experimental studies have also shown that the c.919-2A>G mutation, particularly in homozygous or functionally severe compound heterozygous states, is associated with more pronounced auditory phenotypes (*18,19*). Our findings encompass clinical phenotypes, auditory physiology, and cochlear histopathology in mouse models and extend previous observations by demonstrating that disease severity can be further modulated by the functional nature of a second *SLC26A4* allele when a shared splice-site mutation (c.919-2A>G) is present. Specifically, the combination of c.919-2A>G with a truncating mutation (c.574delC) resulted in more severe functional and structural cochlear abnormalities than did pairing it with a missense mutation (c.1211C>A), which indicates that residual pendrin function contributed by the second allele may influence the phenotypic outcome. These features closely resemble the phenotypes reported in *Slc26a4*-null or severely hylomorphic mouse models, thus supporting the notion that pendrin deficiency primarily disrupts epithelial integrity and endolymphatic homeostasis (*17,33,36*).

In this study, transcriptomic profiling revealed shared and mutation-specific alterations in gene expression in both compound heterozygous *Slc26a4* mouse models. Compared with *Slc26a4*$^{c.1211C>A/c.919-2A>G}$ mice, *Slc26a4*$^{c.574delC/c.919-2A>G}$ mice exhibited a markedly greater number of DEGs and broader disruption of gene expression profiles. This parallel between molecular and phenotypic severity suggests that the extent of transcriptomic dysregulation reflects the degree of cochlear pathology induced by different *Slc26a4* mutations. Compared with WT mice, upregulated genes in the cochleae of *Slc26a4*$^{c.574delC/c.919-2A>G}$ mice were predominantly enriched in pathways related to extracellular matrix organization, cell–substrate adhesion, and epithelial membrane compartments. Cochlear development and hair cell maturation depend on precise regulation of extracellular matrix composition and cell–matrix adhesion, which provide both structural support and signaling cues (*37-39*). Given the established roles of extracellular matrix composition, basement membrane integrity, and apical–basal polarity in cochlear morphogenesis, these transcriptional changes likely reflect a disturbance of epithelial structural programs during inner ear development (*40-43*). In contrast, upregulated DEGs associated with the *Slc26a4*$^{c.1211C>A/c.919-2A>G}$ mutation were enriched mainly in immune-related and regulatory processes, including leukocyte migration and cytokine signaling, as well as membrane raft-associated cellular components and cytokine/chemokine activity, which indicates a predominant regulatory transcriptional response in tissue damage or cochlear repair (*44-47*). Interestingly, enrichment of kidney and renal system development were also observed in DEGs

of both two mutant types compared to WT. Given the well-established expression profile of pendrin and its ion transport function in the kidneys, related genes and enrichment might reflect shared epithelial transport and polarity gene networks that are utilized in the cochleae and kidneys (*48-50*).

In addition, a direct comparison between the two mutant models revealed a distinct set of DEGs that demonstrated mutation severity-dependent transcriptional remodeling. Genes upregulated in *Slc26a4*$^{c.574delC/c.919-2A>G}$ mice were strongly enriched in pathways related to extracellular structure organization, cell–substrate adhesion, Wnt signaling, and ear development, which indicates disruption of epithelial architecture and developmental programs. Given that pendrin is a membrane-localized anion exchanger essential for epithelial polarity and ion homeostasis in the inner ear, the activation of extracellular matrix- and Wnt-associated pathways likely reflects maladaptive structural remodeling and failed developmental compensation (*51-53*) and is consistent with the more severe congenital hearing loss observed in patients with truncating or splice-disrupting *SLC26A4* mutations.

Despite genotype-specific differences, both mutant models shared substantial transcriptional alterations relative to WT mice. Commonly upregulated genes were enriched in cell adhesion and ion transport pathways, which suggested pendrin dysfunction and an impact on the cochlear epithelium system. Conversely, commonly downregulated genes were robustly and consistently enriched in pathways related to cell cycle regulation, mitosis, DNA replication, and chromosome organization. While mature cochlear sensory cells are mostly postmitotic, suppression of these pathways may reflect altered supporting-cell states, impaired structural repair susceptibility, or shifts in cellular composition secondary to developmental injury(*54*). Notably, 47 shared upregulated DEGs and 11 shared downregulated DEGs exhibited greater expression bias in *Slc26a4*$^{c.574delC/c.919-2A>G}$ cochleae, which suggests a potential association with disease severity.

Notably, several of the disease severity–associated genes identified in this study have previously been implicated in cochlear epithelial ion regulation and electrochemical homeostasis, such as upregulated *P2rx2* (a known deafness gene), *Atp1a2* (Na^+/K^+ ion transport), *Scnn1b* (facilitating Na^+ absorption) and downregulated *Slc4a10* (acid extrusion), suggesting disruption of coordinated ion transport networks (*55-57*). Public single-cell atlases indicate that these genes are enriched mostly in SV, Reissner membrane and hair cells, supporting cells in organ of Corti, supporting the notion that pendrin deficiency perturbs epithelial ion homeostasis at the tissue level. Second, structural and adhesion-related genes, including hair cell–enriched *Clic5*, supporting cell-enriched *Epyc*, epithelial adhesion gene *Cdh1*, and SV cell-enriched *Lmx1a*, *Epha7*, were more strongly upregulated in the c.574delC genotype (*28,58-62*). This gradient mirrors the morphological severity observed in *Slc26a4*$^{c.574delC/c.919-2A>G}$ mice, characterized by greater structure disruption, hair cell loss and stereociliary fusion, suggesting different epithelial remodeling responses scale. Third, immune and stress responsive genes including *Trem2*, *Lbp*, and *Hspa1b*, were consistently elevated, with stronger induction in the c.574delC genotype (*63-65*). They localize predominantly to SV and in macrophage cell populations, suggesting that the immune signature observed in bulk RNA-seq likely reflects activation of resident immune compartments in SV-related structures. Together, these findings support a model in which truncating mutations impose a greater effect in the cochlea, leading to amplified epithelial ion imbalance, related structural stress responses, and enhanced immune activation in different important regions of cochlea. The graded magnitude of these transcriptional changes parallels the observed severity of auditory dysfunction, providing a coherent molecular framework for allele-class–dependent phenotypic variability.

The distinct transcriptional signatures between mutation classes may reflect intrinsic differences in their molecular consequences. The truncating mutation c.574delC introduces a premature termination codon and may therefore be subject to nonsense-mediated mRNA decay (NMD), potentially reducing transcript stability and pendrin abundance. This could limit sustained protein-folding stress while triggering compensatory transcriptional responses associated with epithelial remodeling and stress adaptation. In contrast, the missense mutation c.1211C>A preserves transcript length but may destabilize at the protein level, leading to conformational perturbation and engagement of endoplasmic reticulum (ER) quality-control pathways.

Consistent with this distinction, IP–LC–MS/MS analysis revealed pendrin associated protein enrichment of ER chaperones and proteostasis-related components, including *HSPA5, HSP90B1*, *LTF*, *etc*. *In vitro* qPCR revealed mutation-dependent modulation of proteostasis pathways. *HSPA5* upregulation under the missense condition is consistent with ER folding stress and adaptive unfolded protein response activation, whereas its reduction in the truncating construct, together with decreased *HSPA1B*, suggests limited sustained cytosolic stress engagement. Concurrent downregulation of *LTF* further indicates adjustment of ER-associated secretory load. Collectively, these patterns support a model in which the missense mutation induces conformational stress–driven folding engagement, while the truncating mutation may be rapidly cleared with reduced proteostatic activation. Although derived from a heterologous system, these findings provide a plausible mechanistic link between mutation class and divergent transcriptional remodeling observed *in vivo*. Together, these data raise the possibility that mutation severity

influences not only ion transport capacity but also the stability and organization of pendrin-associated protein networks.

Although the transcriptomic, proteomic, and cellular analyses provide converging evidence for mutation-dependent molecular remodeling, the present study primarily establishes associations rather than direct causal relationships. In particular, the mechanisms of hearing impairment require further validation through spatial localization and functional perturbation experiments. In addition, the cell-type mapping analysis was performed using publicly available single-cell datasets and therefore provides an inferred cellular context rather than direct spatial validation in the knock-in mouse models. Future studies incorporating ion transport function measurement in cells, earlier postnatal time points measurement in mice models, spatial transcriptomic or in situ validation, as well as quantitative assessment of immune-related factors or anti-inflammatory interventions, will be important to further refine the mechanistic framework (*65*).

Multiple basic proof-of-concept studies have demonstrated that restoring pendrin expression or function can rescue inner ear phenotypes (*30,66,67*). In recent years, approaches such as gene supplementation, viral-mediated gene delivery, and genomic strategies including DNAJC14 modulation, CRISPR/Cas9-mediated exon skipping, and antisense oligonucleotide approaches have demonstrated the therapeutic potential of restoring pendrin function in *Slc26a4*-mutant mice (*68-70*). Recent studies have reported that postnatal AAV-mediated *Slc26a4* gene supplementation can restore pendrin expression and significantly improve hearing and inner ear morphology in missense mutation knock-in mouse models (*71*). Building on these advances and our findings, future studies will integrate the evaluation of mutation-specific severity and allele-dependent pathogenic mechanisms to guide the exploration of precision therapies for *SLC26A4*-related hearing loss.

5. Conclusion

In summary, our study demonstrated that distinct *SLC26A4* mutations conferred differential cochlear pathology and transcriptional remodeling when paired with a common splice-site mutation, which resulted in a graded severity of hearing loss. These findings establish a mutation-specific mechanistic framework for *SLC26A4*-associated deafness and provide a foundation for the development of future therapeutic strategies.

Acknowledgements

We thank all team members who contributed to the experiments and data acquisition. We acknowledge the animals used in this study for their scientific contribution.

Funding: This research was funded by Beijing Nova Program (20230484450), the High-Level Public Health Technical Talent Training Plan (Discipline backbone-02-42) and National Natural Science Foundation of China (82071064).

Conflict of Interest: The authors have no conflicts of interest to disclose.

Availability of data and materials: The RNA-seq datasets generated in this study can be accessed from the corresponding author upon reasonable request.

References

1. GBD 2019 Hearing Loss Collaborators. Hearing loss prevalence and years lived with disability, 1990-2019: findings from the Global Burden of Disease Study 2019. Lancet. 2021; 397:996-1009.
2. Honda K, Griffith AJ. Genetic architecture and phenotypic landscape of SLC26A4-related hearing loss. Hum Genet. 2022; 141:455-464.
3. Dai P, Huang LH, Wang GJ, *et al*. Concurrent Hearing and Genetic Screening of 180,469 Neonates with Follow-up in Beijing, China. Am J Hum Genet. 2019; 105:803-812.
4. Smith RJH, Azaiez H, Odell AM. SLC26A4-Related Sensorineural Hearing Loss. In: GeneReviews® (Adam MP, Ardinger HH, Pagon RA, *et al*., eds.). University of Washington, Seattle, WA, USA, 1993.
5. Ito T, Choi BY, King KA, Zalewski CK, Muskett J, Chattaraj P, Shawker T, Reynolds JC, Butman JA, Brewer CC, Wangemann P, Alper SL, Griffith AJ. SLC26A4 genotypes and phenotypes associated with enlargement of the vestibular aqueduct. Cell Physiol Biochem. 2011; 28:545-552.
6. Deng L, Yang X, Cheng X, Wen C, Yu Y, Li Y, Gao S, Liu H, Liu D, Ruan Y, Xie J, En H, Xian J, Huang L. Hearing loss trajectory and prediction model for children with enlarged vestibular aqueduct. American Journal of Otolaryngology. 2025; 46:104573.
7. Wang QJ, Zhao YL, Rao SQ, Guo YF, Yuan H, Zong L, Guan J, Xu BC, Wang DY, Han MK, Lan L, Zhai SQ, Shen Y. A distinct spectrum of SLC26A4 mutations in patients with enlarged vestibular aqueduct in China. Clin Genet. 2007; 72:245-254.
8. Liu Q, Zhang X, Huang H, *et al*. Asymmetric pendrin homodimer reveals its molecular mechanism as anion exchanger. Nature Communications. 2023; 14:3012.
9. Wangemann P, Nakaya K, Wu T, Maganti RJ, Itza EM, Sanneman JD, Harbidge DG, Billings S, Marcus DC. Loss of cochlear HCO3− secretion causes deafness *via* endolymphatic acidification and inhibition of Ca^{2+} reabsorption in a Pendred syndrome mouse model. American Journal of Physiology-Renal Physiology. 2007; 292:F1345-F1353.
10. Dossena S, Rodighiero S, Vezzoli V, Nofziger C, Salvioni E, Boccazzi M, Grabmayer E, Bottà G, Meyer G, Fugazzola L, Beck-Peccoz P, Paulmichl M. Functional characterization of wild-type and mutated pendrin (SLC26A4), the anion transporter involved in Pendred syndrome. J Mol Endocrinol. 2009; 43:93-103.
11. Dossena S, Nofziger C, Tamma G, Bernardinelli E, Vanoni S, Nowak C, Grabmayer E, Kössler S, Stephan S, Patsch W,

Paulmichl M. Molecular and functional characterization of human pendrin and its allelic variants. Cell Physiol Biochem. 2011; 28:451-466.
12. Wen C, Yang X, Cheng X, *et al*. Optimized concurrent hearing and genetic screening in Beijing, China: A cross-sectional study. Biosci Trends. 2023; 17:148-159.
13. Huang S, Gao X, Jiang Y, *et al*. Reevaluation of Enlarged Vestibular Aqueduct. JAMA Otolaryngol Head Neck Surg. 2025; 151:1046-1056.
14. Ali A, Tabouni M, Kizhakkedath P, Baydoun I, Allam M, John A, Busafared F, Alnuaimi A, Al-Jasmi F, Alblooshi H. Spectrum of genetic variants in bilateral sensorineural hearing loss. Front Genet. 2024; 15:1314535.
15. Zhao X, Cheng X, Huang L, Wang X, Wen C, Wang X. Novel compound heterozygous mutations in SLC26A4 gene in a Chinese family with enlarged vestibular aqueduct. Biosci Trends. 2018; 12:502-506.
16. Wen C, Wang S, Zhao X, Wang X, Wang X, Cheng X, Huang L. Mutation analysis of the SLC26A4 gene in three Chinese families. Biosci Trends. 2019; 13:441-447.
17. Lu YC, Wu CC, Shen WS, Yang TH, Yeh TH, Chen PJ, Yu IS, Lin SW, Wong JM, Chang Q, Lin X, Hsu CJ. Establishment of a knock-in mouse model with the SLC26A4 c.919-2A>G mutation and characterization of its pathology. PLoS One. 2011; 6:e22150.
18. Hu CJ, Lu YC, Tsai CY, Chan YH, Lin PH, Lee YS, Yu IS, Lin S-W, Liu TC, Hsu CJ, Yang TH, Cheng YF, Wu CC. Insights into phenotypic differences between humans and mice with p.T721M and other C-terminal variants of the SLC26A4 gene. Scientific Reports. 2021; 11:20983.
19. Hu C-J, Lu Y-C, Yang T-H, Chan Y-H, Tsai C-Y, Yu I-S, Lin S-W, Liu T-C, Cheng Y-F, Wu C-C, Hsu C-J. Toward the Pathogenicity of the SLC26A4 p.C565Y Variant Using a Genetically Driven Mouse Model. International Journal of Molecular Sciences. 2021; 22:2789.
20. Wen Z, Zhu H, Li Z, Zhang S, Zhang A, Zhang T, Fu X, Sun D, Zhang J, Gao J. A knock-in mouse model of Pendred syndrome with Slc26a4 L236P mutation. Biochemical and Biophysical Research Communications. 2019; 515:359-365.
21. Panganiban CH, Barth JL, Tan J, Noble KV, McClaskey CM, Howard BA, Jafri SH, Dias JW, Harris KC, Lang H. Two distinct types of nodes of Ranvier support auditory nerve function in the mouse cochlea. Glia. 2022; 70:768-791.
22. Saunders JC, Dolgin KG, Lowry LD. The maturation of frequency selectivity in C57BL/6J mice studied with auditory evoked response tuning curves. Brain Res. 1980; 187:69-79.
23. Walton JP, Barsz K, Wilson WW. Sensorineural hearing loss and neural correlates of temporal acuity in the inferior colliculus of the C57BL/6 mouse. J Assoc Res Otolaryngol. 2008; 9:90-101.
24. Kane KL, Longo-Guess CM, Gagnon LH, Ding D, Salvi RJ, Johnson KR. Genetic background effects on age-related hearing loss associated with Cdh23 variants in mice. Hear Res. 2012; 283:80-88.
25. Tang D, Chen M, Huang X, Zhang G, Zeng L, Zhang G, Wu S, Wang Y. SRplot: A free online platform for data visualization and graphing. PLOS ONE. 2023; 18:e0294236.
26. Orvis J, Gottfried B, Kancherla J, *et al*. gEAR: Gene Expression Analysis Resource portal for community-driven, multi-omic data exploration. Nat Methods. 2021; 18:843-844.
27. Xue N, Song L, Song Q, Santos-Sacchi J, Wu H, Navaratnam D. Genes related to SNPs identified by Genome-wide association studies of age-related hearing loss show restriction to specific cell types in the adult mouse cochlea. Hear Res. 2021; 410:108347.
28. Gu S, Olszewski R, Taukulis I, Wei Z, Martin D, Morell RJ, Hoa M. Characterization of rare spindle and root cell transcriptional profiles in the stria vascularis of the adult mouse cochlea. Sci Rep. 2020; 10:18100.
29. Rapp C, Bai X, Reithmeier RAF. Molecular analysis of human solute carrier SLC26 anion transporter disease-causing mutations using 3-dimensional homology modeling. Biochim Biophys Acta Biomembr. 2017; 1859:2420-2434.
30. Yoon JS, Park H-J, Yoo S-Y, Namkung W, Jo MJ, Koo SK, Park H-Y, Lee W-S, Kim KH, Lee MG. Heterogeneity in the processing defect of SLC26A4 mutants. J Med Genet. 2008; 45:411-419.
31. de Moraes VCS, Bernardinelli E, Zocal N, Fernandez JA, Nofziger C, Castilho AM, Sartorato EL, Paulmichl M, Dossena S. Reduction of Cellular Expression Levels Is a Common Feature of Functionally Affected Pendrin (SLC26A4) Protein Variants. Mol Med. 2016; 22:41-53.
32. Taylor JP, Metcalfe RA, Watson PF, Weetman AP, Trembath RC. Mutations of the PDS Gene, Encoding Pendrin, Are Associated with Protein Mislocalization and Loss of Iodide Efflux: Implications for Thyroid Dysfunction in Pendred Syndrome. J Clin Endocrinol Metab. 2002; 87:1778-1784.
33. Everett LA, Belyantseva IA, Noben-Trauth K, Cantos R, Chen A, Thakkar SI, Hoogstraten-Miller SL, Kachar B, Wu DK, Green ED. Targeted disruption of mouse Pds provides insight about the inner-ear defects encountered in Pendred syndrome. Hum Mol Genet. 2001; 10:153--161.
34. Pryor SP, Madeo AC, Reynolds JC, Sarlis NJ, Arnos KS, Nance WE, Yang Y, Zalewski CK, Brewer CC, Butman JA, Griffith AJ. SLC26A4/PDS genotype-phenotype correlation in hearing loss with enlargement of the vestibular aqueduct (EVA): evidence that Pendred syndrome and non-syndromic EVA are distinct clinical and genetic entities. J Med Genet. 2005; 42:159-165.
35. Madden C, Halsted M, Meinzen-Derr J, Bardo D, Boston M, Arjmand E, Nishimura C, Yang T, Benton C, Das V, Smith R, Choo D, Greinwald J. The Influence of Mutations in the SLC26A4 Gene on the Temporal Bone in a Population With Enlarged Vestibular Aqueduct. Archives of Otolaryngology–Head & Neck Surgery. 2007; 133:162-168.
36. Nishio A, Ito T, Cheng H, Fitzgerald TS, Wangemann P, Griffith AJ. Slc26a4 expression prevents fluctuation of hearing in a mouse model of large vestibular aqueduct syndrome. Neuroscience. 2016; 329:74-82.
37. Legan PK, Richardson GP. Extracellular matrix and cell adhesion molecules in the developing inner ear. Semin Cell Dev Biol. 1997; 8:217–224.
38. Cosgrove D, Gratton MA. Extracellular matrix and inner ear development and function. In: Advances in Developmental Biology (Tuan RS, Lo CW, eds.). Elsevier Academic Press, San Diego, CA, USA, 2005; pp. 169-201.
39. Kim DK, Kim JA, Park J, Niazi A, Almishaal A, Park S. The release of surface-anchored α-tectorin, an apical extracellular matrix protein, mediates tectorial membrane organization. Sci Adv. 2019; 5:eaay6300.
40. Jayadev R, Morais MRPT, Ellingford JM, *et al*. A

basement membrane discovery pipeline uncovers network complexity, regulators, and human disease associations. Sci Adv. 2022; 8:eabn2265.
41. Chiarugi P, Giannoni E. Anoikis: A necessary death program for anchorage-dependent cells. Biochem Pharmacol. 2008; 76:1352-1364.
42. Montcouquiol M, Kelley MW. Development and Patterning of the Cochlea: From Convergent Extension to Planar Polarity. Cold Spring Harb Perspect Med. 2020; 10:a033266.
43. Driver EC, Kelley MW. Development of the cochlea. Development. 2020; 147: dev162263.
44. Mastrogiovanni M, Juzans M, Alcover A, Di Bartolo V. Coordinating Cytoskeleton and Molecular Traffic in T Cell Migration, Activation, and Effector Functions. Front Cell Dev Biol. 2020; 8:591348.
45. Sarris M, Masson J-B, Maurin D, Van der Aa LM, Boudinot P, Lortat-Jacob H, Herbomel P. Inflammatory chemokines direct and restrict leukocyte migration within live tissues as glycan-bound gradients. Curr Biol. 2012; 22:2375-2382.
46. Hu T, Liu C-H, Lei M, Zeng Q, Li L, Tang H, Zhang N. Metabolic regulation of the immune system in health and diseases: mechanisms and interventions. Signal Transduct Target Ther. 2024; 9:268.
47. Ye M, Zhang C, Ding D, Chen GD, Adler HJ, Sharaf R, Hu BH. Organ of Corti macrophages: a distinct group of cochlear macrophages with potential roles in supporting cell degeneration and survival. Front Immunol. 2025; 16:1617146.
48. Royaux IE, Wall SM, Karniski LP, Everett LA, Suzuki K, Knepper MA, Green ED. Pendrin, encoded by the Pendred syndrome gene, resides in the apical region of renal intercalated cells and mediates bicarbonate secretion. Proc Natl Acad Sci U S A. 2001; 98:4221-4226.
49. Chambrey R, Eladari D. Novel insight on physiological regulation of the Cl^-/HCO_3^- exchanger pendrin. Am J Physiol Renal Physiol. 2023; 324:F431-F432.
50. Wagner CA, Finberg KE, Stehberger PA, Lifton RP, Giebisch GH, Aronson PS, Geibel JP. Regulation of the expression of the Cl^-/anion exchanger pendrin in mouse kidney by acid-base status. Kidney International. 2002; 62:2109-2117.
51. Chai R, Kuo B, Wang T, Liaw EJ, Xia A, Jan TA, Liu Z, Taketo MM, Oghalai JS, Nusse R, Zuo J, Cheng AG. Wnt signaling induces proliferation of sensory precursors in the postnatal mouse cochlea. Proc Natl Acad Sci U S A. 2012; 109:8167-8172.
52. Shi F, Hu L, Jacques BE, Mulvaney JF, Dabdoub A, Edge AS. β-Catenin is required for hair-cell differentiation in the cochlea. J Neurosci. 2014; 34:6470-6479.
53. Santi PA, Aldaya R, Brown A, Johnson S, Stromback T, Cureoglu S, Rask-Andersen H. Scanning Electron Microscopic Examination of the Extracellular Matrix in the Decellularized Mouse and Human Cochlea. J Assoc Res Otolaryngol. 2016; 17:159-171.
54. Ding D, Chen GD, Zhang C, Ye M, Adler HJ, Sharaf R, Naldrett K, Mittal T, Hu BH. Supporting cell involvement in cochlear damage and repair: Novel insights from a quantitative analysis of cyclodextrin-induced ototoxicity in mice. Hear Res. 2025; 459:109201.
55. Bouzid A, Smeti I, Dhouib L, Roche M, Achour I, Khalfallah A, Gibriel AA, Charfeddine I, Ayadi H, Lachuer J, Ghorbel A, Petit C, Masmoudi S. Down-expression of P2RX2, KCNQ5, ERBB3 and SOCS3 through DNA hypermethylation in elderly women with presbycusis. Biomarkers. 2018; 23:347-356.
56. Faletra F, Girotto G, D'Adamo AP, Vozzi D, Morgan A, Gasparini P. A novel P2RX2 mutation in an Italian family affected by autosomal dominant nonsyndromic hearing loss. Gene. 2014; 534:236-239.
57. Hosoya M, Ueno M, Shimanuki MN, Nishiyama T, Oishi N, Ozawa H. Cell-specific α and β subunit expression patterns of Na(+)/K(+)-ATPases in the common marmoset cochlea. Sci Rep. 2025; 15:26814.
58. Hanada Y, Nakamura Y, Ishida Y, Takimoto Y, Taniguchi M, Ozono Y, Koyama Y, Morihana T, Imai T, Ota Y, Sato T, Inohara H, Shimada S. Epiphycan is specifically expressed in cochlear supporting cells and is necessary for normal hearing. Biochem Biophys Res Commun. 2017; 492:379-385.
59. Korrapati S, Taukulis I, Olszewski R, Pyle M, Gu S, Singh R, Griffiths C, Martin D, Boger E, Morell RJ, Hoa M. Single Cell and Single Nucleus RNA-Seq Reveal Cellular Heterogeneity and Homeostatic Regulatory Networks in Adult Mouse Stria Vascularis. Front Mol Neurosci. 2019; 12:316.
60. Ryals M, Morell RJ, Martin D, Boger ET, Wu P, Raible DW, Cunningham LL. The Inner Ear Heat Shock Transcriptional Signature Identifies Compounds That Protect Against Aminoglycoside Ototoxicity. Front Cell Neurosci. 2018; 12:445.
61. Liu H, Chen L, Giffen KP, Stringham ST, Li Y, Judge PD, Beisel KW, He DZZ. Cell-Specific Transcriptome Analysis Shows That Adult Pillar and Deiters' Cells Express Genes Encoding Machinery for Specializations of Cochlear Hair Cells. Front Mol Neurosci. 2018; 11:356.
62. Kim YJ, Ibrahim LA, Wang SZ, Yuan W, Evgrafov OV, Knowles JA, Wang K, Tao HW, Zhang LI. EphA7 regulates spiral ganglion innervation of cochlear hair cells. Dev Neurobiol. 2016; 76:452-469.
63. Lei S, Huang L, Liu Y, Xu L, Wang D, Yang L. Association between polymorphisms of heat-shock protein 70 genes and noise-induced hearing loss: A meta-analysis. PLoS One. 2017; 12:e0188539.
64. Mukherjee U, Reddy PH. Gut-brain relationship in dementia and Alzheimer's disease: Impact on stress and immunity. Ageing Res Rev. 2025; 111:102843.
65. Wang X, Wang Y, Yang L, Zhang Y, Yang L. $TREM2^+$ macrophages: a key role in disease development. Front Immunol. 2025; 16:1550893.
66. Ishihara K, Okuyama S, Kumano S, Iida K, Hamana H, Murakoshi M, Kobayashi T, Usami S, Ikeda K, Haga Y, Tsumoto K, Nakamura H, Hirasawa N, Wada H. Salicylate restores transport function and anion exchanger activity of missense pendrin mutations. Hear Res. 2010; 270:110-118.
67. Backliwal G, Hildinger M, Kuettel I, Delegrange F, Hacker DL, Wurm FM. Valproic acid: a viable alternative to sodium butyrate for enhancing protein expression in mammalian cell cultures. Biotechnol Bioeng. 2008; 101:182-189.
68. Kim MA, Kim SH, Ryu N, Ma JH, Kim YR, Jung J, Hsu CJ, Choi JY, Lee KY, Wangemann P, Bok J, Kim UK. Gene therapy for hereditary hearing loss by SLC26A4 mutations in mice reveals distinct functional roles of pendrin in normal hearing. Theranostics. 2019; 9:7184-7199.
69. Takeda H, Miwa T, Kim MY, Choi BY, Orita Y, Minoda R. Prenatal electroporation-mediated gene transfer restores

Slc26a4 knock-out mouse hearing and vestibular function. Scientific Reports. 2019; 9:17979.
70. Feng P, Xu Z, Chen J, *et al*. Rescue of mis-splicing of a common SLC26A4 mutant associated with sensorineural hearing loss by antisense oligonucleotides. Mol Ther Nucleic Acids. 2022; 28:280-292.
71. Tsai YH, Wu PY, Chuang YC, *et al*. Postnatal Slc26a4 gene therapy improves hearing and structural integrity in a hereditary hearing loss model. J Clin Invest. 2026. doi:10.1172/JCI193812.

Received February 25, 2026; Revised March 17, 2026; Accepted March 19, 2026.

**Address correspondence to:*
Lihui Huang and Shuo Wang, Department of Otolaryngology-Head and Neck Surgery, Beijing Tongren Hospital, Capital Medical University, Beijing 100730, P.R. China; Beijing Institute of Otolaryngology, Beijing, 100005, P. R. China; Key Laboratory of Otolaryngology Head and Neck Surgery (Capital Medical University), Ministry of Education, Beijing, 100005, P. R. China.
E-mail: huanglihui@ccmu.edu.cn (LH); shannonwsh@aliyun.com (SW)

Released online in J-STAGE as advance publication March 21, 2026.

Original Article

DOI: 10.5582/bst.2026.01043

Modeling of the hepatitis B virus life cycle and the efficacy of antivirals in human iPSC-derived hepatic organoids

Tanbin Liu[1,§], Junming Xu[2,§], Xiaoni Chen[3], Jingyi Li[1], Jie Ke[3], Jiasen Xu[1], Hongzhou Lu[1,*], Fenfang Wu[1,3,*]

[1] The Third People's Hospital of Shenzhen and the Second Affiliated Hospital, Southern University of Science and Technology, Shenzhen, Guangdong, China.
[2] Department of Hepatobiliary and Pancreatic Surgery, the Eighth Affiliated Hospital of Sun Yat-sen University, Shenzhen, Guangdong, China.
[3] Central Laboratory, Shenzhen Hospital, Beijing University of Chinese Medicine, Shenzhen, Guangdong, China.

SUMMARY: Hepatitis B virus (HBV) infection remains a major global health burden, affecting approximately 296 million people worldwide, and yet progress in mechanistic studies and development of antivirals has been limited by the lack of physiologically relevant and sustainable *in vitro* models. This study established a human induced pluripotent stem cell (hiPSC)-derived multilineage hepatic organoid system that robustly supports the complete HBV life cycle, including viral entry, replication, covalently closed circular DNA (cccDNA) formation, antigen secretion, and production of infectious progeny virus. These organoids exhibit stable expression of sodium taurocholate cotransporting polypeptide (NTCP), a key receptor for HBV entry, and remain viable long term under infection conditions for at least 20 days, with sustained secretion of HBsAg and HBeAg. Importantly, the model recreates key pathological features of chronic HBV infection, including downregulation of hepatocyte functional genes (*e.g.*, ALB and CYP3A4) and induction of fibrosis-associated markers such as COL1A1, reflecting early extracellular matrix remodeling. Moreover, results indicated the utility of this platform in the evaluation of antivirals. Treatment with tenofovir effectively reduced viral DNA and antigen production without affecting cccDNA levels, whereas bulevirtide resulted in stage-specific inhibition of viral entry, highlighting the model's capacity to resolve mechanism-of-action differences. At the same time, drug-induced hepatotoxicity was assessed within the same system. Collectively, this hiPSC-derived hepatic organoid model provides a scalable and physiologically relevant platform that bridges the gap between conventional cell culture and *in vivo* systems, offering a powerful tool for studying HBV pathogenesis, host–virus interactions, and preclinical antiviral discovery.

Keywords: human iPSC-derived hepatic organoids, hepatitis B virus (HBV), cccDNA persistence, liver fibrosis, antiviral screening

1. Introduction

Hepatitis B virus (HBV) infection is a major pathological factor leading to liver fibrosis, cirrhosis, and hepatocellular carcinoma and it remains a substantial global health burden, with HBV infection affecting approximately 296 million people (*1*). HBV is a hepatotropic DNA virus with a natural infection that is highly restricted to humans and non-human primates, while common rodent animals are non-permissive hosts (*2*). Consequently, the development of pathophysiologically relevant experimental systems for HBV has been particularly challenging. Currently available models for studying HBV-related liver diseases—including various animal models, immortalized cell lines, and primary hepatocytes (*3,4*) — fail to faithfully recreate the process of long-term HBV infection in the liver. These models exhibit notable limitations: they neither support sustained long-term infection nor replicate the human liver microenvironment. Moreover, factors such as the high cost, prolonged modeling time, and ethical concerns associated with animal models significantly hinder progress in HBV research.

Hepatic organoids (HOs) derived from hiPSCs possess a three-dimensional physiological architecture and exhibit the cellular composition and functional characteristics of human liver tissues (*5*). These organoids have been widely used in disease modeling, mechanistic studies, and drug testing (*6,7*). In recent years, significant progress has been made using HOs in research on HBV infection, replication, and tumorigenesis (*8,9*). For

instance, De Crignis *et al*. established an HBV infection model using primary hepatocyte-derived HOs and they evaluated the anti-HBV activity and drug-induced toxicity of two compounds (*10*). Nie *et al*. established an HBV infection model using HOs co-cultured from hiPSC-derived hepatocytes, umbilical vein endothelial cells, and mesenchymal cells, and they demonstrated that the level and duration of HBV replication in these organoids surpassed those in conventional cell culture models (*11*). While these studies represent preliminary explorations of hiPSC-derived HOs to model HBV infection, the existing models still fail to recreate the pathological processes following HBV infection, and particularly the liver fibrosis that develops during long-term HBV infection. Thus, there is a pressing need for a human-relevant HBV organoid model that not only sustains persistent infection but that also displays captures the progressive fibrotic remodeling of the liver.

Building on our previously established *in vitro* organoid platform, we have generated functionally mature hepatobiliary organoids (*12*). Using a directed co-differentiation strategy from hiPSC-derived mesoderm and endoderm, we successfully established multicellular hepato-biliary organoids in which hepatic parenchymal and non-parenchymal lineages coexist (*13,14*). Incorporation of our proprietary MIX cocktail further enabled long-term maintenance and stability of these organoids (*12*). Together, these features recreate the complete HBV life cycle, including viral attachment, entry, uncoating, replication, assembly, and production of infectious virions. Importantly, the non-parenchymal cell compartment within the organoids was configured to permit the emergence of fibrosis-like pathological changes that arise during chronic HBV infection, thereby enabling parallel analysis of viral and fibrogenic responses.

Thus, reported here are multi-lineage hiPSC-derived HOs that recreate persistent HBV infection and concomitant fibrosis *in vitro*. This model was further used to assess the efficacy and hepatotoxicity of antiviral compounds. This approach overcomes the inability of traditional animal models to emulate the human HBV infection microenvironment, thereby providing a potential platform for drug screening and mechanistic studies on hepatitis B fibrosis.

2. Materials and Methods

2.1. Cell lines and culture

Cell culture was performed with the hiPSC line UC (passages 30 to 37), purchased from Beijing Saibei Biotechnology Company Ltd., Beijing, China. Undifferentiated hiPSCs were cultured on qualified Matrigel Basement Membrane Matrix Growth Factor Reduced (Corning, NY, USA)-coated 6-well plates (Thermo Fisher Scientific, MA, USA) and maintained in mTeSR medium (STEMCELL Technologies, BC, Canada) at 37°C with 5% CO_2 and 95% air. The medium was replaced every 24 h.

The HepAD38 cells and HepG-Puro-NTCP cells were maintained on 10 cm dishes with DMEM and 20% fetal bovine serum (Life Technologies, Gaithersburg, USA). All cells were maintained at 37°C in an incubator with 5% CO_2.

2.2. Differentiation and generation of HOs

HOs were generated from hiPSCs following previously described protocols (*12*) in which a small fraction of mesodermal cells is intentionally retained during definitive endoderm specification. Upon subsequent directed differentiation, definitive endoderm cells give rise to hepatic parenchymal cells, while the residual mesodermal cells differentiate into non-parenchymal lineages, including endothelial cells. HOs were used for HBV infection experiments as well as other analyses.

2.3. HBV preparation and infection

HBV stocks were derived from supernatants of HepAD38 cells (*15*), which were stably transfected with a complete HBV genome (genotype D). HiPSCs-HOs and HepG-puro-NTCP cells (*16*) were infected with HBV [100 genome equivalents (GEq)/cell or 3,000 GEq/cell] in the presence of 4% polyethylene glycol 8000 in 24-well plates. After the indicated days post-infection, cultured cells were then harvested. Pre-genomic RNA (pgRNA) was quantified using SYBR Green (Vazyme Bio, Nanjing, China) with specific primers (Thermo Fisher Scientific). The expression of pgRNA was normalized against expression of GAPDH.

2.4. RNA isolation and quantification

RT-qPCR was used to determine pgRNA levels. Total RNA was extracted with TRIzol reagent (Thermo Fisher Scientific) according to the manufacturer's instructions. RNA was reverse-transcribed with Superscript III reverse transcriptase (Thermo Fisher Scientific). Real-time PCR was performed using the CFX96 Touch System (Bio-Rad, CA, USA). The primers used are available upon request.

2.5. DNA isolation and quantification

Infected HOs were collected after infection. Total DNA in the cells was purified using the DNeasy Blood & Tissue Kit (QIAGEN, Hilden, Germany). The concentration of total DNA was determined using a NanoDrop spectrophotometer (Thermo Fischer Scientific), and the DNA concentration was adjusted to 20 ng/μL for further experiments. Two μL of adjusted DNA sample was used to quantify vDNA with SYBR Green using a standard curve plotted using plasmid pUC-HBV over

a range of 10^7-10^2 copies. To quantify HBV covalently closed circular DNA (cccDNA) copies, adjusted DNA samples of 25 μL [20 ng/μL] of HBV DNA were treated with plasmid-safe DNase. After digestion, two μL of the sample was used to quantify cccDNA copies with SYBR Green using a standard curve plotted using plasmid pUC-HBV over a range of 10^7-10^2 copies. The primers used for HBV DNA and cccDNA quantification are available upon request.

2.6. Detection of HBsAg and HBeAg

A total of 450 μL of the HOs or cell supernatant was collected after infection and used for the detection of HBsAg and HBeAg. The HBsAg and HBeAg ELISA Kit (Wantai Bio, Beijing, China) were used to detect of HBsAg and HBeAg, respectively, from the supernatant of the infected organoids according to the manufacturer's instructions.

2.7. Immunofluorescence analysis

HOs were washed with PBS at the indicated time points post-infection, fixed with 4% paraformaldehyde for 30 min at room temperature, and permeabilized with 0.15% Triton X-100 for 30 min. After blocking with 10% normal donkey serum in PBS for 60 min at RT, the organoids were incubated with rabbit Hepatitis B Virus Core Antigen antibody (1:200) and mouse Hepatitis B Virus Surface Antigen antibody (1:200) (Thermo Fischer Scientific) for 12 h at 4 ℃, and they were then washed with PBS three times. The organoids were then incubated with secondary antibodies - Alexa Fluor™ 488 Donkey anti-Mouse IgG (H+L) Highly Cross-Adsorbed Secondary Antibody and Alexa Fluor™ 647 Donkey anti-Rabbit IgG (H+L) Highly Cross-Adsorbed Secondary Antibody (1:400) - for 1 h at RT. After they were washed three times with PBS, the organoids were examined by using the ZEISS LSM 980 Confocal Laser Scanning Microscope and Airyscan.

2.8. Statistical analysis

Statistical significance was analyzed using the two-tailed unpaired Student's *t*-test and the software GraphPad Prism 8.0 (GraphPad, San Diego, CA, USA). A *p*-value of < 0.05 was considered significant.

3. Results

3.1. Generation of functional HOs from hiPSCs

Building on our previous work on HO models (*12,17*), we differentiated hiPSCs into HOs using the established protocol (Figure 1A). Morphological analysis indicated that, relative to day 0, hepatocytes on day 25 exhibited pronounced aggregation and a more mature hepatic morphology, characterized by polygonal cell shapes and frequent multinucleation (Figure 1B). Before differentiation, flow cytometry indicated that more than 90% of hiPSCs on day 0 co-expressed the pluripotency markers SSEA4 and TRA1-81. By day 4, over 70% of the cells co-expressed the definitive endoderm markers SOX17 and FOXA2, as confirmed by flow cytometry (Figure 1C). Immunofluorescence analysis on day 15 indicated that a substantial proportion of cells expressed SOX9 and HNF4α, a hallmark feature of bipotent hepatoblasts. During liver development, signals from the endothelial lineage not only promote liver bud formation but also guide biliary morphogenesis (*18,19*).

To investigate this in our system, we tracked the mesoderm-derived endothelial lineage and observed a significant upregulation of the mature vascular endothelial marker CD31 by day 15. The cultures were subsequently treated with HBM medium for an additional 10 days to further support maturation. By the end of this stage, mature hepatocyte markers including CYP3A4 and HNF4α were detectable (Figure 1D). Moreover, quantitative polymerase chain reaction (qPCR) analysis of mature HOs indicated robust expression of key liver-specific genes (*20-23*), including *ALB* (albumin), *G6PC* (glucose-6-phosphatase catalytic subunit), and *RBP4* (retinol-binding protein 4), as well as cytochrome P450 enzymes (*CYP3A4, CYP3A7* and *CYP2C9*) (Figure 1E). Collectively, these findings demonstrate that our defined *in vitro* culture system reliably generates well-differentiated, functionally competent HOs with appropriate lineage-specific marker expression from a single hiPSC line.

3.2. Modeling HBV infection in hiPSC HOs

HOs derived from hiPSCs were cultivated in HCM for 25 days before being infected with recombinant HBV produced from HepAD38 cells, a subclone of the HepG2 cell line that stably expresses HBV (Figure 2A). Sodium taurocholate co-transporting polypeptide (NTCP) is a crucial transporter located on the basement membrane of hepatocytes and is vital for HBV infection (*16*). To determine whether HOs can serve as a source of HBV infection, RT-PCR was used to detect NTCP expression in HepG-puro-NTCP, hiPSCs, and HOs. Results indicated that NTCP was highly expressed in HOs as of 20 days after post-differentiation and the level of expression was significantly higher than that in HepG-puro-NTCP cells (Figure 2B). Immunofluorescence was used to detect NTCP, and results indicated that the HOs exhibited high levels of NTCP on days 20 and 25 post-differentiation (Figure 2C). Next, the sensitivity of HBV generated by HepAD38 in HOs was examined in order to model the HBV life cycle in HOs. After the HOs were infected with varying viral doses (ranging from 0 to 3,000 GEq/cell), the alterations in HBV cccDNA, pgRNA, and supernatant vDNA were examined 7 days post-

infection (dpi). As the results indicated, elevated levels of HBV cccDNA, pgRNA, and supernatant vDNA were associated with infection in a dose-dependent manner (Figure 3D-F). HBeAg and HBsAg were also detected and quantified in supernatants of infected organoids as an additional indicator of active HBV replication (Figure 2G-H). The presence of foci of HBV replication in HBV-infected organoids, was confirmed by immunostaining with antibodies that recognize the HBcAg, resulting in distinct nuclear and cytoplasmic staining in infected HOs 10 dpi (Figure 2I). Therefore, differentiated HOs offer a viable *ex vivo* HBV infection platform that enables for the analysis of the roles played by distinct host and virus factors.

3.3. HOs remain viable long term in an infected state and produce infectious HBV

Next, the capacity of differentiated HOs to serve as a model of chronic infection was assessed. Following

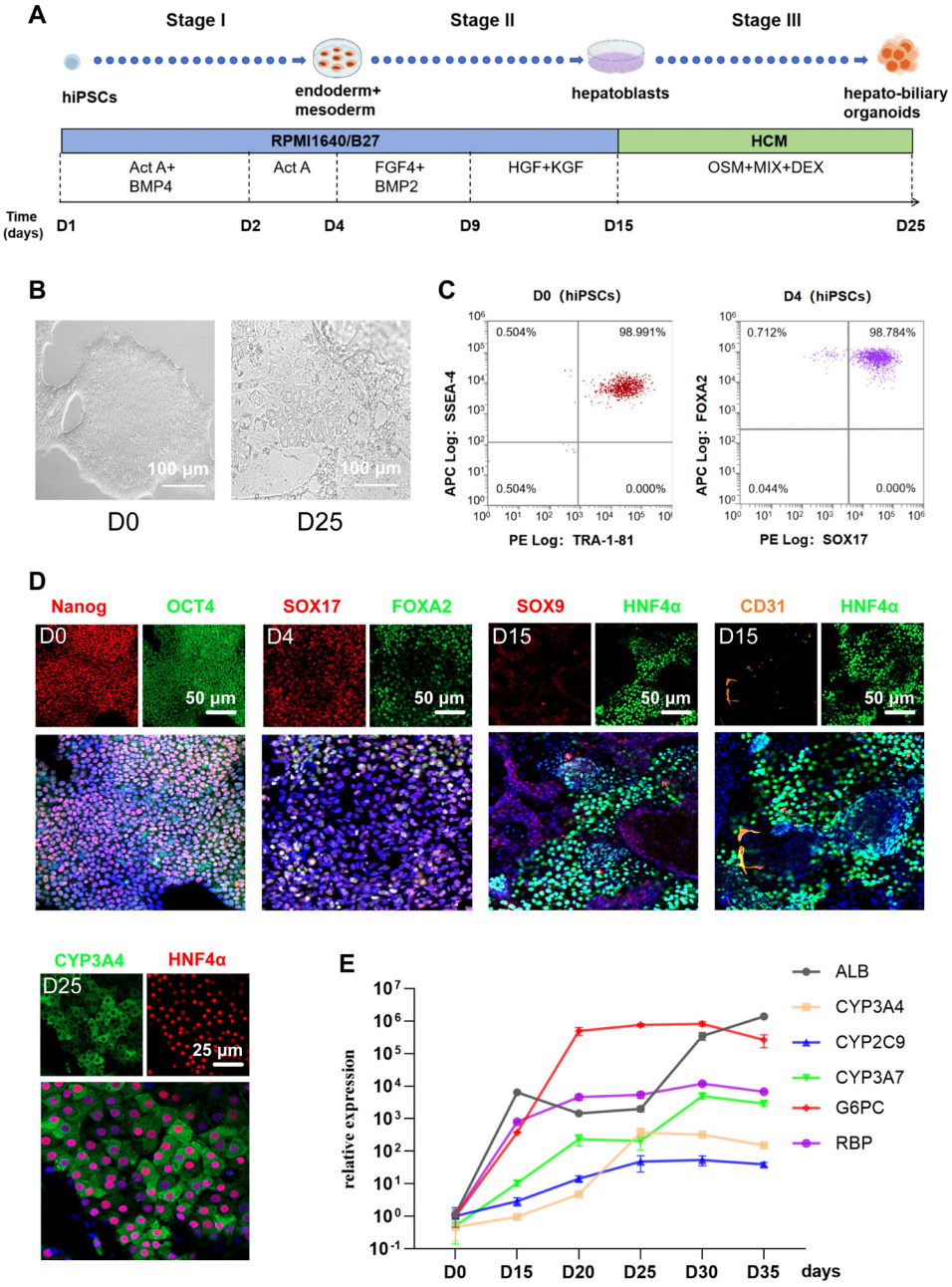

Figure 1. Generation of functional hepatic organoids from hiPSCs. (A) Schematic representation of the differentiation procedure. **(B)** Sequential morphological changes (day 0 and 25) as hiPSC differentiated into hepatic organoids. Scale bars = 100 μm. hiPSCs, human induced pluripotent stem cells. **(C)** Flow cytometry confirmed that most day-0 hiPSCs were positive for SSEA4 and TRA1-81, and most day-4 cells were positive for FOXA2 and SOX17. **(D)** Immunofluorescence analysis of stage-specific markers and differentiation efficiency at the end of each key stage. Scale bars, 50 μm. (E) qPCR analysis of hepatic genes (*ALB, G6PC, RBP4, CYP3A4, CYP3A7* and *CYP2C9*) in day-25 hepatic organoids ($n = 3$).

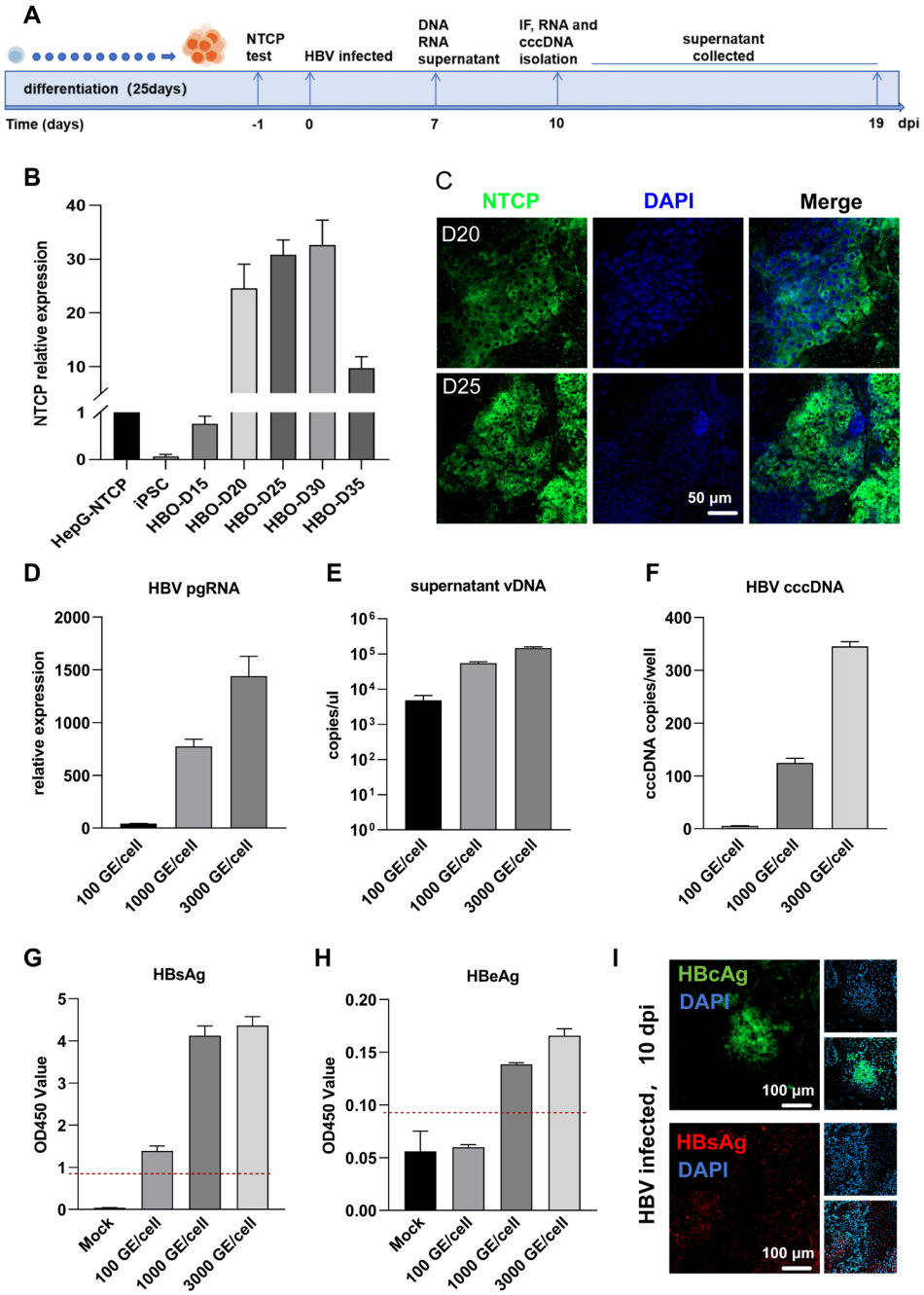

Figure 2. Modeling HBV infection in hiPSC hepatic organoids. (A) Experimental design of infection experiments. Arrows indicate the time points for HBV detection. **(B)** Q-PCR analysis of NTCP expression in HepG-puro-NTCP cells, iPSCs, and differentiated HOs (n = 3). **(C)** Immunofluorescence analysis of NTCP in differentiated HOs. Scale bars = 50 μm. **(D-F)** Q-PCR quantification of HBV pgRNA **(D)**, supernatant vDNA **(E)** and cccDNA **(F)** in HOs (n = 3) infected with a range of doses of 100-3,000 GE/cell 7 days post-infection (dpi). **(G-H)** HBeAg and HBsAg from the supernatant of infected HOs were quantified with an enzyme-linked immunosorbent assay (ELISA). Negative bars correspond to positive and negative controls provided by the kit manufacturer. **(I)** Immunofluorescence analysis of HBcAg and HBsAg in HO sinfected at a dose of 1,000 GEq/cell 10 dpi, Scale bars = 100 μm.

infection of HOs with low doses of HBV, HOs were found to remain viable for at least 20 days (Figure 3A). Dynamic monitoring indicated that HBsAg are constantly secreted in HOs for a minimum of 19 days (Figure 3B). Immunofluorescence also revealed HBcAg and HBsAg 20 dpi (Figure 3C). Chronic HBV infection poses a serious risk to human health because it quickly leads to liver fibrosis, which can then develop into cirrhosis, liver failure, and hepatocellular cancer. The development of HBV-induced liver fibrosis, however, is difficult for current HBV research models to faithfully reproduce. Remarkably, immunofluorescence revealed considerably higher levels of COL1A1 expression 2 weeks after HOs were infected with HBV compared to the control group (Figure 3D-E). HBV-infected HOs develop liver dysfunction during the infection

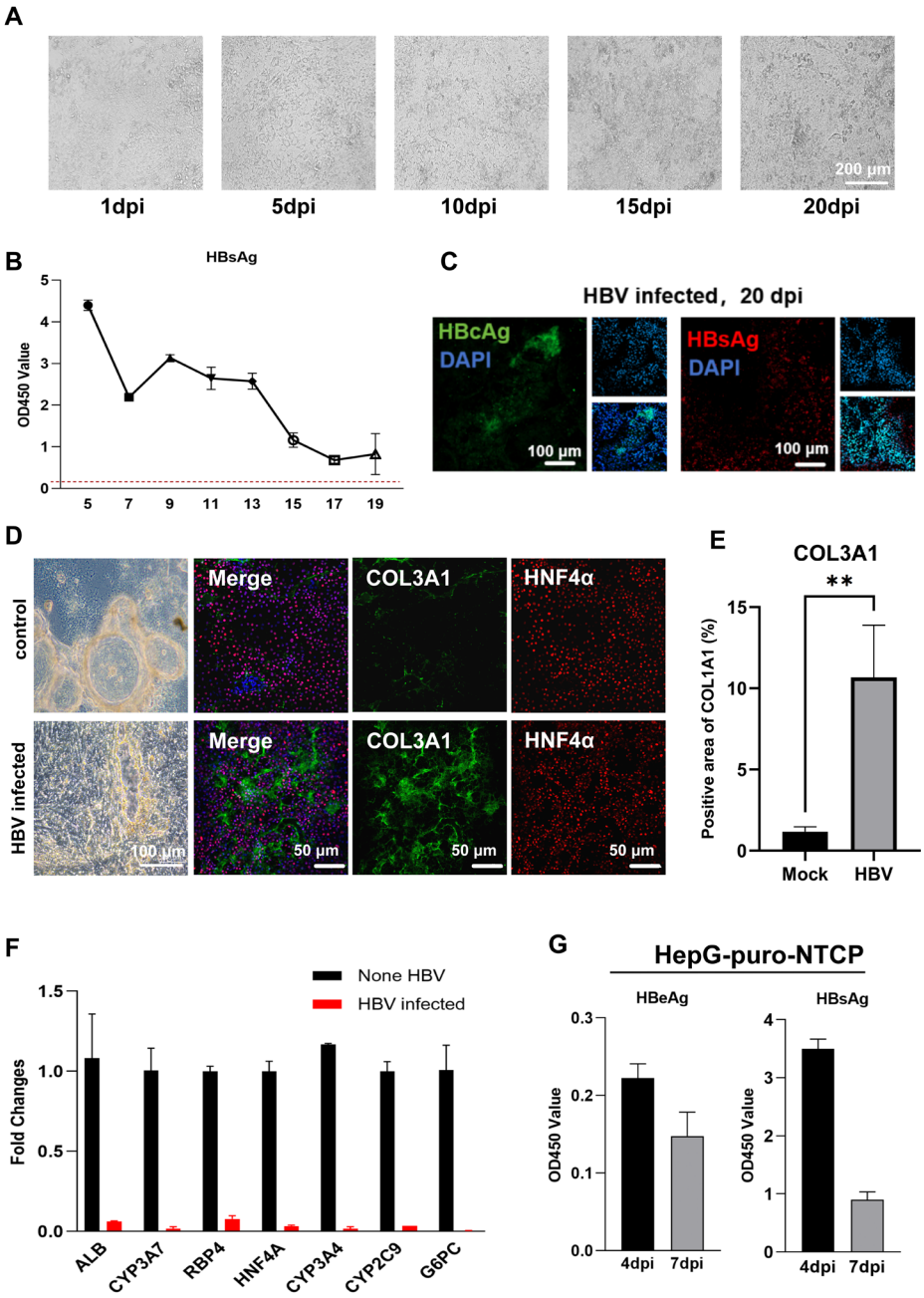

Figure 3. Hepatic organoids remain viable long term in an infected state and produce infectious HBV (A) Representative bright-field images of HOs infected with HBV for 1 to 20 days as indicated. **(B)** HBeAg from the supernatant of infected organoids for 1 to 20 days was quantified with ELISA. **(C)** Immunofluorescence analysis of HBcAg and HBsAg in HOs infected at a dose of 1,000 GEq/cell 20 dpi, Scale bars = 100 μm. **(D-E)** Immunofluorescence analysis of COL3A1 in HOs 20 dpi, Scale bars = 100 μm. **(F)** Q-PCR quantification of the hepatic genes *ALB, G6PC, RBP, CYP3A4, CYP3A7*, and *CYP2C9* in HOs 20 dpi, $n = 3$. **(G)** ELISA analysis of HBeAg and HBsAg in HepG-puro-NTCP cells infected with the supernatant of infected hepatic organoids (10-20 dpi).

process, as evinced by the significantly lower mRNA levels of ALB, CYP3A7, RBP4, HNF4α, CYP3A4, CYP2C9 and G6PC in the infected group compared to the normal group, according to RT-PCR measurement of mRNA levels of substances relevant to liver function (Figure 3F). To further investigate whether infectious progeny viruses could be produced by infected HOs, the supernatant was collected from infected hiPSC-HOs at 20 dpi (20 dpi-Sup, from day 10 to day 20), and its infectivity was examined in HepG-puro-NTCP cells. Notably, the progeny virus displayed infectivity, confirmed by detection of HBeAg and HBsAg in HepG-puro-NTCP cells (Figure 3G). These findings suggest that this organoid system can serve as a model of chronic *ex vivo* infection.

3.4. HBV-infected HOs are a viable platform for evaluation of antivirals

Over the past few years, organoids have been widely used as drug screening instruments and have been crucial to the creation of novel drugs. Next, using the setup shown in Figure 4A, we investigated whether the *ex vivo* infected HO platform would be suitable for anti-HBV drug evaluation to track the antiviral activity and drug-induced toxicity of two distinct medications, tenofovir and bulevirtide. Tenofovir is a nucleoside reverse transcriptase inhibitor that prevents HBV pre-genomic RNA from being reverse-transcribed to DNA (*24*). Bulevirtide, an NTCP inhibitor, can inhibit HBV entry into liver cells and block HBV infection in hepatocytes (*25*). Due to the well-established detrimental effects of tenofovir and bulevirtide on the viability of primary human hepatocytes, we sought to evaluate their drug-induced toxicity on HOs. The decreased cell viability was apparent in the phenotype of the 10 μM of tenofovir-treated and 4 μM of bulevirtide-treated organoids compared to controls according to microscopy (Figure 4B). Treatment with 5 μM of tenofovir after HBV infection of HOs indicated that production of HBeAg (Figure 4C) and HBV viral DNA (Figure 4F) in the culture supernatant was inhibited by tenofovir, whereas, as expected, HBV cccDNA (Figure 4D) and pgRNA (Figure 4E) levels remained the same. After HOs were infected with HBV and treated with bulevirtide either 1 day before infection or 1 day after infection, results indicated that the pre-treatment group significantly suppressed HBeAg, cccDNA, pgRNA, and vDNA, while the post-treatment group did not (Figure 4C-F). Thus the organoid *ex vivo* infection platform not only allows the quantification of the antiviral efficacy of drugs but it also provides information on how they work by enabling the identification of specific stages of the HBV life cycle that are blocked and targeted.

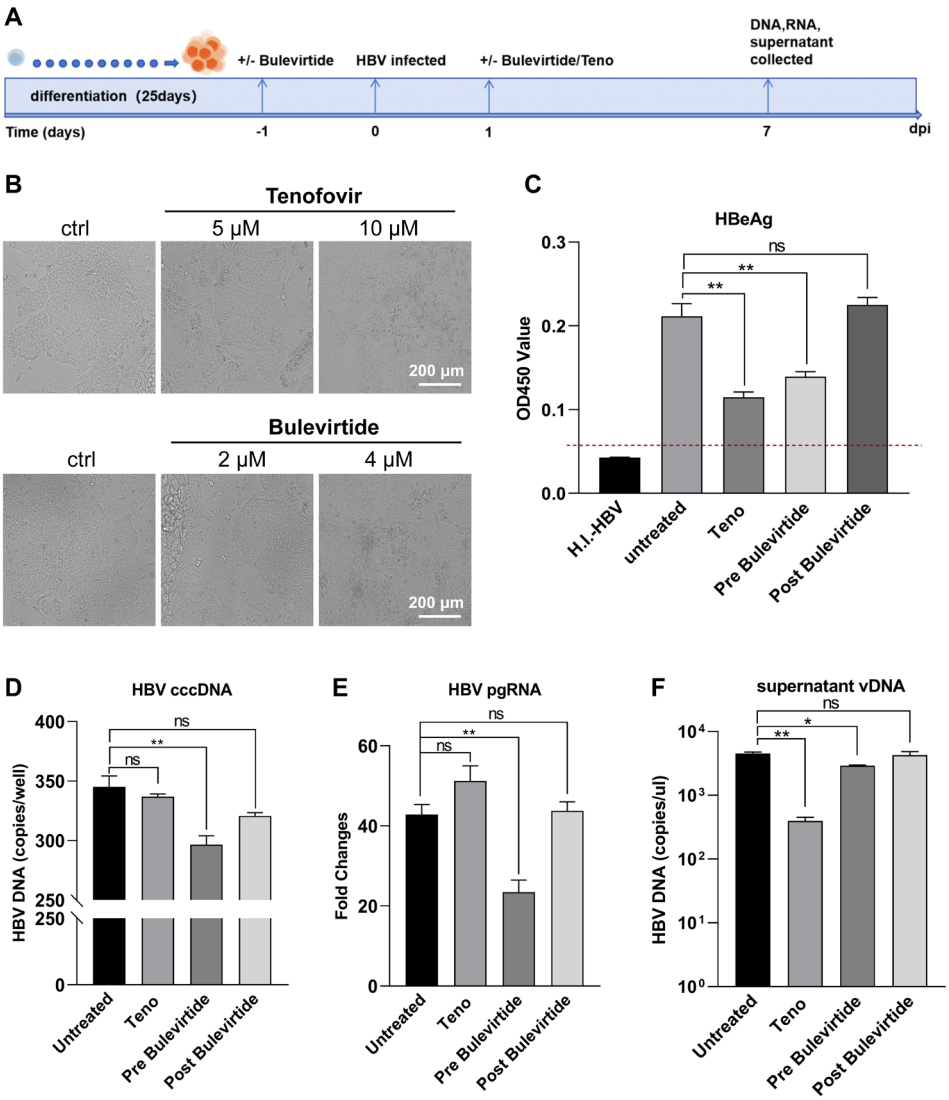

Figure 4. HBV-infected hepatic organoids are a viable platform for evaluation of antivirals. (A) Experimental design of the drug treatment of HBV-infected hepatic organoids followed by assessment of antiviral activity. **(B)** Representative bright-field images of hepatic organoids treated for 4 days with the control or increasing concentrations of the antivirals tenofovir or bulevirtide as indicated. **(C)** ELISA analysis of HBeAg in hepatic organoids (pre- or post-drug treatment) 7 dpi. **(D-F)** Q-PCR quantification of cccDNA **(D)**, HBV pgRNA **(E)**, and supernatant vDNA **(F)** in hepatic organoids ($n = 3$) at 7 dpi with drug treatment. *$p < 0.05$, **$p < 0.01$, ns, not significant.

4. Discussion

This study, differentiated functionally mature HOs from human-derived iPSCs. This single-cell-derived differentiation system successfully generated multilineage HOs that not only exhibited efficient liver differentiation but that also displayed a high level of susceptibility to HBV. The HOs can simulate the complete cycle of HBV infection, remain viable long term under infectious conditions, and secrete infectious viruses. This organoid system also mimics virus-induced liver dysfunction and fibrosis, suggesting that viral infection in HOs may authentically reproduce the *in vivo* virus-host interaction mechanism. Moreover, this organoid system serves as a platform with which to screen the antiviral activity of HBV drugs.

HBV infection affects over 250 million people worldwide (*26*), posing a major health challenge. Conventional cell lines and primary human hepatocyte (PHH) cultures struggle to replicate the liver's complexity, limiting research on host-pathogen interactions (*27,28*). Animal models exhibit a high level of species specificity, limiting their broad applicability (*29*). Hepatocellular carcinoma cell lines have undergone tumorigenic changes, failing to mimic the progression from normal hepatocytes to cancer (*30*). Primary hepatocytes are difficult to obtain and have limited expansion capacity, making them unsuitable for large-scale analysis. Compared to PHHs, HepaRG cells, and iPSC-derived HOs as were previously reported, the current system offers several advantages, including single-cell-derived multilineage differentiation, stable NTCP expression, long-term viral persistence, and the emergence of fibrosis-like features. These characteristics collectively position this model as a complementary and scalable tool for research on HBV pathogenesis and development of antivirals.

Although the current organoid system does not incorporate immune components such as Kupffer cells or lymphocytes, this feature provides a unique advantage for distinguishing hepatocyte-intrinsic responses to HBV infection. The absence of immune-mediated cytotoxicity enables the model to depict early hepatocellular alterations, including metabolic dysfunction and ECM remodeling, which are often masked in immune-competent systems. Future integration of immune cells or microfluidic co-culture platforms may further extend the utility of this model to the study of immune-driven liver injury and chronic inflammation.

Notably, NTCP was found to be expressed at high levels in HOs. Since NTCP is the specific receptor for HBV entry into hepatocytes, only cells or organoids stably expressing high levels of it can facilitate the complete viral infection cycle, making them suitable for disease modeling and antiviral screening. Numerous drugs enter hepatocytes *via* NTCP transport and interact with bile acid metabolism, potentially causing drug-induced liver injury (*31*). Models with sustained, high levels of NTCP expression are crucial to evaluating such chronic or cumulative toxicity. Levels of NTCP expression serve as one of the gold standards for hepatocyte maturation and functionalization (*32*). Its long-term stable expression indicates that organoid models possess stable, primary-like hepatic metabolic functions. This characteristic makes these organoids an ideal platform for studying HBV infection, bile acid metabolism, and the long-term hepatotoxicity of related drugs, providing a powerful tool for liver disease modeling and drug screening.

Chronic hepatitis B virus infection is a major global cause of chronic cirrhosis and hepatocellular carcinoma (HCC). The fibrosis-like phenotype observed in HBV-infected organoids, characterized by COL1A1 upregulation, likely represents an early-stage ECM remodeling response. While this does not fully recreate advanced fibrosis, it provides a valuable window into the initial fibrogenic events triggered by persistent viral infection. Incorporating hepatic stellate cells or modulating TGF-β signaling in future studies may enable reconstruction of a more complex fibrotic architecture.

The evaluation of antivirals as was performed in this study focused on tenofovir and bulevirtide as representative inhibitors targeting distinct stages of the HBV life cycle. This proof-of-concept design demonstrates that the organoid platform is capable of recreating stage-specific antiviral mechanisms. Future expansion to capsid assembly modulators, siRNA-based therapies, and cccDNA-targeting agents will further validate the platform's potential for preclinical drug screening.

In summary, functional HOs have been successfully established. This organoid system can mimic the whole life cycle of HBV and exhibit HBV-induced liver failure and fibrosis. These findings imply that the model serves as a viable and feasible model for study of HBV infection.

Funding: This work was supported by grants from the National Key R&D Program of China (2025YFC3408900, 2025ZD01904500), the Shenzhen Science and Technology Program (JCYJ20220818103407016), the Shenzhen Medical Research Fund (SMRF.D2301015), the Guangdong Basic and Applied Basic Research Foundation (2024A1515011222), the National Natural Science Foundation of China (82172107), the Special Funds for Strategic Emerging Industry of Shenzhen (Grant No. F-2022-Z99-502266), the Shenzhen Longgang District Science and Technology Innovation Special Fund (LGKCYLWS2022007), the Shenzhen Clinical Research Center for Emerging Infectious Diseases (No. LCYSSQ20220823091203007), the Guangdong Key Lab for Diagnosis & Treatment of Emerging Infectious Diseases, and the Shenzhen Key Laboratory for Infectious Diseases.

Conflict of Interest: The authors have no conflicts of interest to disclose.

References

1. World Health O. Hepatitis B vaccines: WHO position paper, July 2017 - Recommendations. Vaccine. 2019; 37:223-225.
2. Dandri M, Lutgehetmann M, Petersen J. Experimental models and therapeutic approaches for HBV. Semin Immunopathol. 2013; 35:7-21.
3. Burwitz BJ, Zhou Z, Li W. Animal models for the study of human hepatitis B and D virus infection: New insights and progress. Antiviral Res. 2020; 182:104898.
4. Yuan L, Jiang J, Liu X, *et al*. HBV infection-induced liver cirrhosis development in dual-humanised mice with human bone mesenchymal stem cell transplantation. Gut. 2019; 68:2044-2056.
5. Andrews MG, Kriegstein AR. Challenges of Organoid Research. Annu Rev Neurosci. 2022; 45:23-39.
6. Hendriks D, Brouwers JF, Hamer K, Geurts MH, Luciana L, Massalini S, Lopez-Iglesias C, Peters PJ, Rodriguez-Colman MJ, Chuva de Sousa Lopes S, Artegiani B, Clevers H. Engineered human hepatocyte organoids enable CRISPR-based target discovery and drug screening for steatosis. Nat Biotechnol. 2023; 41:1567-1581.
7. Rumsey JW, Lorance C, Jackson M, *et al*. Classical Complement Pathway Inhibition in a "Human-On-A-Chip" Model of Autoimmune Demyelinating Neuropathies. Adv Ther (Weinh). 2022; 5.
8. Sharma S, Rawal P, Kaur S, Puria R. Liver organoids as a primary human model to study HBV-mediated Hepatocellular carcinoma. A review. Exp Cell Res. 2023; 428:113618.
9. Rao S, Hossain T, Mahmoudi T. 3D human liver organoids: An *in vitro* platform to investigate HBV infection, replication and liver tumorigenesis. Cancer Lett. 2021; 506:35-44.
10. De Crignis E, Hossain T, Romal S, *et al*. Application of human liver organoids as a patient-derived primary model for HBV infection and related hepatocellular carcinoma. Elife. 2021; 10.
11. Nie YZ, Zheng YW, Miyakawa K, Murata S, Zhang RR, Sekine K, Ueno Y, Takebe T, Wakita T, Ryo A, Taniguchi H. Recapitulation of hepatitis B virus-host interactions in liver organoids from human induced pluripotent stem cells. EBioMedicine. 2018; 35:114-123.
12. Wu F, Wu D, Ren Y, Huang Y, Feng B, Zhao N, Zhang T, Chen X, Chen S, Xu A. Generation of hepatobiliary organoids from human induced pluripotent stem cells. J Hepatol. 2019; 70:1145-1158.
13. Shi Y, Deng J, Sang X, Wang Y, He F, Chen X, Xu A, Wu F. Generation of Hepatocytes and Nonparenchymal Cell Codifferentiation System from Human-Induced Pluripotent Stem Cells. Stem Cells Int. 2022; 2022:3222427.
14. Xu J, Sang X, He Y, Ke J, Xu J, Liu T, Wang J, Zhai H, Chen X, Shi X, Wu F. Lycii radicis cortex alleviates fibrosis in hiPSC-derived multilineage hepatic organoids *via* the cAMP-PKA pathway. Front Pharmacol. 2025; 16:1730255.
15. Ladner SK, Otto MJ, Barker CS, Zaifert K, Wang GH, Guo JT, Seeger C, King RW. Inducible expression of human hepatitis B virus (HBV) in stably transfected hepatoblastoma cells: A novel system for screening potential inhibitors of HBV replication. Antimicrob Agents Chemother. 1997; 41:1715-1720.
16. Yan H, Zhong G, Xu G, *et al*. Sodium taurocholate cotransporting polypeptide is a functional receptor for human hepatitis B and D virus. Elife. 2012; 1:e00049.
17. Wu D, Chen X, Sheng Q, Chen W, Zhang Y, Wu F. Production of Functional Hepatobiliary Organoids from Human Pluripotent Stem Cells. Int J Stem Cells. 2021; 14:119-126.
18. Matsumoto K, Yoshitomi H, Rossant J, Zaret KS. Liver organogenesis promoted by endothelial cells prior to vascular function. Science. 2001; 294:559-563.
19. Zong Y, Panikkar A, Xu J, Antoniou A, Raynaud P, Lemaigre F, Stanger BZ. Notch signaling controls liver development by regulating biliary differentiation. Development. 2009; 136:1727-1739.
20. Godoy P, Hewitt NJ, Albrecht U, *et al*. Recent advances in 2D and 3D *in vitro* systems using primary hepatocytes, alternative hepatocyte sources and non-parenchymal liver cells and their use in investigating mechanisms of hepatotoxicity, cell signaling and ADME. Arch Toxicol. 2013; 87:1315-1530.
21. Prior N, Inacio P, Huch M. Liver organoids: from basic research to therapeutic applications. Gut. 2019; 68:2228-2237.
22. Youn DY, Xiaoli AM, Zong H, Okada J, Liu L, Pessin J, Pessin JE, Yang F. The Mediator complex kinase module is necessary for fructose regulation of liver glycogen levels through induction of glucose-6-phosphatase catalytic subunit (G6pc). Mol Metab. 2021; 48:101227.
23. Bell CC, Lauschke VM, Vorrink SU, Palmgren H, Duffin R, Andersson TB, Ingelman-Sundberg M. Transcriptional, Functional, and Mechanistic Comparisons of Stem Cell-Derived Hepatocytes, HepaRG Cells, and Three-Dimensional Human Hepatocyte Spheroids as Predictive *In Vitro* Systems for Drug-Induced Liver Injury. Drug Metab Dispos. 2017; 45:419-429.
24. Tong S, Revill P. Overview of hepatitis B viral replication and genetic variability. J Hepatol. 2016; 64:S4-S16.
25. Bogomolov P, Alexandrov A, Voronkova N, Macievich M, Kokina K, Petrachenkova M, Lehr T, Lempp FA, Wedemeyer H, Haag M, Schwab M, Haefeli WE, Blank A, Urban S. Treatment of chronic hepatitis D with the entry inhibitor myrcludex B: First results of a phase Ib/IIa study. J Hepatol. 2016; 65:490-498.
26. Schweitzer A, Horn J, Mikolajczyk RT, Krause G, Ott JJ. Estimations of worldwide prevalence of chronic hepatitis B virus infection: a systematic review of data published between 1965 and 2013. Lancet. 2015; 386:1546-1555.
27. Verrier ER, Colpitts CC, Schuster C, Zeisel MB, Baumert TF. Cell Culture Models for the Investigation of Hepatitis B and D Virus Infection. Viruses. 2016; 8.
28. Ortega-Prieto AM, Dorner M. Immune Evasion Strategies during Chronic Hepatitis B and C Virus Infection. Vaccines (Basel). 2017; 5.
29. Liu Y, Maya S, Ploss A. Animal Models of Hepatitis B Virus Infection-Success, Challenges, and Future Directions. Viruses. 2021; 13.
30. Torresi J, Tran BM, Christiansen D, Earnest-Silveira L, Schwab RHM, Vincan E. HBV-related hepatocarcinogenesis: The role of signalling pathways and innovative *ex vivo* research models. BMC Cancer. 2019; 19:707.
31. Watashi K, Sluder A, Daito T, *et al*. Cyclosporin A and its analogs inhibit hepatitis B virus entry into cultured

hepatocytes through targeting a membrane transporter, sodium taurocholate cotransporting polypeptide (NTCP). Hepatology. 2014; 59:1726-1737.
32. Park JH, Iwamoto M, Yun JH, *et al*. Structural insights into the HBV receptor and bile acid transporter NTCP. Nature. 2022; 606:1027-1031.

Received February 10, 2026; Revised March 19, 2026; Accepted March 22, 2026.

[§]These authors contributed equally to this work.
*****Address correspondence to:*
Fenfang Wu, Biotherapy Clinical Research Center, The Third People's Hospital of Shenzhen and the Second Affiliated Hospital of Southern University of Science and Technology, Shenzhen, Guangdong, China.
E-mail: wufenfang19@126.com

Hongzhou Lu, The National Clinical Research Center for Infectious Diseases, the Third People's Hospital of Shenzhen and the Second Affiliated Hospital of Southern University of Science and Technology, Shenzhen, Guangdong, China.
E-mail: luhongzhou@szsy.sustech.edu.cn

Released online in J-STAGE as advance publication March 26, 2026.

Brief Report

DOI: 10.5582/bst.2026.01046

Biallelic inactivation of *EXT1* in patient-derived iPSCs confirms the "Two-hit" hypothesis in hereditary multiple osteochondromas

Yali Yang[1,2,3], Zhenzhong Han[1,2,3], Guowei Li[1,2,3], Zihan Li[1,2,3], Chonghao Shao[1,2,3], Wentao Li[1,2,3], Jing Wang[1,2,3], Jing Luan[1,2,3,*], Yazhou Cui[1,2,3,4,*], Jinxiang Han[1,2,3,*]

[1] Biomedical Sciences College, Shandong Medicinal Biotechnology Centre, Shandong First Medical University & Shandong Academy of Medical Sciences, Ji'nan, Shandong, China;
[2] Department of Orthopedic Surgery, The First Affiliated Hospital of Shandong First Medical University, Ji'nan, Shandong, China;
[3] Key Lab for Biotech-Drugs of National Health Commission, Ji'nan, Shandong, China;
[4] Qingdao Academy of Chinese Medical Science, Shandong University of Traditional Chinese Medicine, Ji'nan, Shandong, China.

SUMMARY: Hereditary Multiple Osteochondromas (HMO) is a rare autosomal dominant skeletal disorder caused by heterozygous loss-of-function mutations in *EXT1* or *EXT2*, which encode glycosyltransferases essential for heparan sulfate (HS) biosynthesis. Whether haploinsufficiency alone suffices or biallelic inactivation is required for osteochondroma formation remains a central unresolved question. In this study, we employed CRISPR/Cas9 combined with PiggyBac transposon technology to introduce a second pathogenic mutation (c.1883+1G>T) into patient-derived induced pluripotent stem cells (iPSCs) carrying a heterozygous EXT1 c.1126C>T mutation. This approach enabled the generation of isogenic iPSC lines: wild-type (WT), single-mutant (SM), and double-mutant (DM). These iPSCs were differentiated through induced mesenchymal stem cells (iMSCs) into chondrocytes. Biallelic *EXT1* mutation in DM cells led to significant upregulation of *SOX9*, *COL2A1*, and *ACAN*, elevated glycosaminoglycan (GAG) levels, and markedly reduced HS, whereas SM cells remained indistinguishable from WT. Three-dimensional (3D) chondrogenic organoid cultures revealed that DM organoids were enlarged and structurally disorganized, partially recapitulating key histopathological features of osteochondromas. Transcriptomic analysis identified the Wnt signaling pathway as the most significantly enriched pathway among differentially expressed genes following *EXT1* loss. Collectively, these findings provide direct human cellular evidence that complete EXT1 inactivation—not haploinsufficiency—drives aberrant chondrogenesis, likely through impaired sequestration of morphogen ligands, thereby supporting the Two-hit pathogenic model.

Keywords: hereditary multiple osteochondromas, heparan sulfate, chondrogenesis, Two-hit hypothesis, Wnt signaling pathway, ligand sequestration

1. Introduction

Hereditary Multiple Osteochondromas (HMO) is a rare autosomal dominant skeletal disorder caused by loss-of-function mutations in *exostosin glycosyltransferase 1* (*EXT1*) or *exostosin glycosyltransferase 2* (*EXT2*) (*1*). *EXT1* mutations account for 60–70% of all HMO cases, and the global prevalence of HMO is approximately 1/50000 (*2*). Up to 5% of affected patients undergo malignant transformation to secondary peripheral chondrosarcoma (*3*). EXT1 and EXT2 assemble into a heteromeric complex within the endoplasmic reticulum (ER) before translocating to the Golgi apparatus, where the complex catalyzes heparan sulfate (HS) chain polymerization through the alternating addition of N-acetylglucosamine (GlcNAc) and glucuronic acid residues (GlcA) (*4*) (Figure 4A). As a critical component of heparan sulfate proteoglycans (HSPGs), HS fine-tunes the spatial distribution and signaling activity of multiple morphogens—including Indian Hedgehog (IHH), fibroblast growth factors (FGFs), bone morphogenetic proteins (BMPs), and Wnt family ligands—thereby maintaining chondrocyte proliferation, differentiation, and columnar organization within the growth plate (*5,6*). Studies in *Ext1*-deficient mice have demonstrated aberrant IHH signaling gradients and consequent skeletal patterning defects (*7*), and zebrafish *dackel* (*ext2*) mutants display severe chondrocyte stacking disorganization (*8*).

Knudson originally proposed the Two-hit hypothesis in the context of retinoblastoma, positing that tumor suppressor gene inactivation requires loss of both

functional alleles (*9*). This model has since been extended to HMO, where accumulating evidence suggests that osteochondroma formation requires biallelic *EXT* inactivation through loss of heterozygosity (LOH) at the somatic level (*10,11*). Heterozygous *Ext* mice develop no osteochondromas, whereas conditional biallelic knockout in chondrocytes or perichondrial progenitor cells recapitulates the full spectrum of HMO skeletal pathology (*10,11*). De Andrea *et al.* demonstrated that heterozygous *EXT* mutations do not compromise chondrogenic differentiation capacity in human bone marrow-derived mesenchymal stem cells, and further detected LOH in 63% of surgically resected osteochondromas (*12*). Nevertheless, inherent species differences between murine models and human disease, together with the limited availability of patient-derived osteochondroma specimens for molecular analysis, have constrained the ability to establish direct genotype–phenotype relationships in a controlled human cellular context.

To address these limitations, we employed patient-derived induced pluripotent stem cells (iPSCs) combined with footprint-free CRISPR/Cas9–PiggyBac genome editing to reconstitute the Two-hit event *in vitro* within a fully isogenic human system. HSPGs are known to regulate Wnt ligand distribution and signal transduction *(13)*. We therefore examined how graded EXT1 loss, from monoallelic to biallelic, affects Wnt pathway activity, aiming to provide mechanistic support for the Two-hit model.

2. Materials and Methods

2.1. sgRNA design and HDR donor construction

sgRNAs targeting the splice donor site of *EXT1* intron 9 (c.1883+1G) were designed using CRISPOR (*http://crispor.tefor.net*) and cloned into lentiCRISPRv2 (Addgene, USA; #52961). An HDR donor was constructed with ~650 bp homology arms flanking a PiggyBac ITR-bracketed PuroΔTK dual-selection cassette, with the left arm harboring the desired c.1883+1G>T mutation.

2.2. iPSCs culture and genome editing

Patient-derived iPSCs (male; heterozygous *EXT1 c.1126C>T*; informed consent under ethics approval) were maintained on Matrigel® (Corning, Corning, NY, USA)-coated plates in mTeSR™ Plus (STEMCELL Technologies, Vancouver, BC, Canada) at 37°C/5% CO_2. At ~80% confluency, iPSCs were co-transfected with Cas9–sgRNA and HDR donor using Lipofectamine™ 3000 (Thermo Fisher Scientific, USA) with 10 μM Y-27632. After 14-day puromycin selection, the PiggyBac cassette was excised *via* hyPBase transposase and acyclovir negative selection. Site-specific integration was verified by junction PCR (P1/P2). Following PiggyBac excision, PCR using primers P3/P4 designed within the transposon cassette sequence confirmed complete cassette removal by the absence of amplification products. Footprint-free excision was further confirmed by Sanger sequencing. The biallelic mutant (c.1126C>T + c.1883+1G>T) was designated double-mutant (DM); parental heterozygous iPSCs as single-mutant (SM); and an isogenic wild-type clone as WT control.

2.3. iMSC induction and chondrogenic differentiation

iPSCs were differentiated into iMSCs using the StemMACS™ MSC Differentiation Kit (STEMCELL Technologies). For 2D chondrogenesis, iMSCs (passage 4–6) were cultured on gelatin-coated plates in high-glucose DMEM (Gibco, USA) with 10 ng/mL TGF-β1 (PeproTech, USA), 100 nM dexamethasone, 50 μg/mL ascorbate-2-phosphate (Sigma-Aldrich), 1% ITS, and 1% penicillin–streptomycin (Gibco) for 21 days. For 3D culture, 2.5×10^5 iMSCs were pelleted (300 × g, 5 min) in 15 mL conical tubes and maintained in suspension culture with identical medium for 21 days. The resulting iPSC-derived chondrocyte organoids (iChOs) were fixed in 4% PFA, cryosectioned, and stained with H&E, Safranin O, Alcian Blue, and immunofluorescence.

2.4. RT-qPCR

Total RNA was extracted with TRIzol® (*Invitrogen*, USA), quantified by NanoDrop™ 2000 (Thermo Fisher Scientific), and reverse-transcribed using SPARKscript II RT Plus Kit (SparkJade, Qingdao, China). RT-qPCR was performed on QuantStudio™ 5 (Applied Biosystems, USA) with 2× SYBR® Green Premix (Accurate Biology, Changsha, China). GAPDH served as internal reference; relative expression was calculated by the $2^{-}\Delta\Delta Ct$ method. Primers are listed in Table 1.

2.5. Biochemical quantification, transcriptomic analysis, and experimental validation

Total sulfated GAG was quantified by DMMB assay (Haling Biotech, China); HS levels were measured using a human-specific ELISA kit (Cusabio, China). For transcriptomic profiling, total RNA was extracted from chondrocytes at day 21 of differentiation (three biological replicates per genotype) and sequenced on the Illumina NovaSeq 6000 platform (Novogene, China). Key differentially expressed genes identified by RNA-seq were validated at the mRNA level by RT-qPCR and at the protein level by Western blot analysis.

2.6. Statistical analysis

Data are mean ± SD from ≥ 3 biological replicates. Three-group comparisons used Kruskal–Wallis test

Table 1. Sequences of primers used in this study

Primers Target	Forward/Reverse primer (5′-3′)
OCT4	CCTCACTTCACTGCACTGTA/ CAGGTTTTCTTTCCCTAGCT
SOX2	CCCAGCAGACTTCACATGT/ CCTCCCATTTCCCTCGTTTT
NANOG	AAGGTCCCGGTCAAGAAACAG/ CTTCTGCGTCACACCATTGC
GAPDH	GTGGACCTGACCTGCCGTCT/ GGAGGAGTGGGTGTCGCTGT
P1/P2	GTGTCTCTTAAACTGTGCATC/ CTGAGTAGGTGTCATTCTAT
P3/P4	GCATACATTATACGAAGTTA/ ACAAATGTGGTATGGCTGAT
MIX-L1	GGATCCAGCTTTTATTTTCTCCCCT/ AGGAGCACAGTGGTTGAGGA
Brachyury	TATGAGCCTCGAATCCACATAGT/ CCTCGTTCTGATAAGCAGTCAC
Sox9	AAGATGACCGACGAGCAG/ CACGGGGAACTTGTCCT
ACAN	TGCAGAACAGTGCCATCA/ CTCCATAGCAGCCTTCCC
Col2a1	TCCCACCCTCTCACAGTTC/ TGCCCAGTTCAGGTCTCTT

with Dunn's post hoc correction; pairwise comparisons used Mann–Whitney *U* test (two-tailed). Analyses were performed in GraphPad Prism 9.0 (San Diego, CA, USA); $p < 0.05$ was significant.

3. Results and Discussion

3.1. Generation of an isogenic EXT1 biallelic mutant iPSC model

To investigate the phenotypic consequences of graded *EXT1* loss in a genetically controlled human system, we established an integrated CRISPR/Cas9–PiggyBac editing platform to introduce a second pathogenic mutation (c.1883+1G>T) into patient-derived iPSCs already carrying the heterozygous *EXT1* c.1126C>T mutation (Supplementary Figure S1, *https://www.biosciencetrends.com/action/getSupplementalData.php?ID=292*). Junction PCR with P1/P2 primers confirmed successful homologous recombination at the intended EXT1 locus in approximately 80% of screened clones. After hyPBase-mediated transposon excision, P3/P4 PCR showed no amplification, confirming complete removal of the selection marker. Sanger sequencing further verified the engineered c.1883+1G>T mutation (Figure 1A–D). The resulting iPSCs-DM retained expression of pluripotency markers (OCT4, NANOG, SSEA-4), normal karyotype, and tri-lineage differentiation potential (Supplementary Figure S2, *https://www.biosciencetrends.com/action/getSupplementalData.php?ID=292*), and differentiated efficiently into iMSCs and subsequently into chondrocytes (Supplementary Figure S3, *https://www.biosciencetrends.com/action/getSupplementalData.php?ID=292*).

Because WT, SM, and DM lines share an identical genetic background—differing exclusively at the engineered *EXT1* locus—all phenotypic differences are attributable solely to the introduced second hit. This isogenic single-variable design, achieved through footprint-free PiggyBac excision preserving endogenous genomic architecture, partially compensates for single-patient derivation and fundamentally distinguishes our approach from unmatched inter-individual specimen comparisons (*14–16*).

3.2. Biallelic EXT1 mutation disrupts HS biosynthesis and alters extracellular matrix content

To determine whether graded *EXT1* loss differentially affects HS biosynthesis and extracellular matrix (ECM) composition, we quantified HS and total GAG levels in day 21 chondrocyte cultures across all three genotypes. HS was markedly reduced in DM cell lysates and conditioned supernatants compared with WT ($p < 0.001$), with no significant difference between SM and WT (Figure 2A). This marked HS reduction in DM is consistent with the near-complete absence of HS immunostaining reported in human osteochondroma cartilage caps (*17*). Notably, total sulfated GAG as measured by the DMMB assay was markedly elevated in DM relative to WT and SM ($p < 0.0001$). Total sulfated GAG in cartilage comprises several species, predominantly chondroitin sulfate (CS) and keratan sulfate (KS), alongside the functionally critical heparan sulfate (HS). Because CS is the dominant GAG species on the major cartilage proteoglycan aggrecan, and HS was severely depleted in DM cells, the observed net increase in total sulfated GAG is most parsimoniously explained by a compensatory elevation of CS. Bachvarova *et al.* have clearly demonstrated this compensatory mechanism in *Ext1*-deficient mouse chondrocytes: $Ext1^{gt/gt}$ cells, which produce only approximately 20% of normal HS levels, exhibited a 70% increase in CS content and a 65% elevation in total GAG, accompanied by significant upregulation of aggrecan (*ACAN*) expression—aggrecan being the principal core protein carrying additional CS chains (*18*). Furthermore, Huegel *et al.* demonstrated that perturbation of HS function triggers cellular responses similar to *Ext* gene ablation, including enhanced chondrogenic differentiation and upregulation of cartilage-specific genes such as *ACAN* (*19*), consistent with the concurrent *ACAN* mRNA upregulation observed in our DM group.

3.3. EXT1 biallelic inactivation drives aberrant chondrogenesis in 2D and 3D culture systems

To investigate the functional consequences of *EXT1* loss on chondrocyte differentiation, we evaluated cartilage formation in both 2D monolayer and 3D organoid culture systems.

In 2D monolayer chondrogenic culture, WT and SM

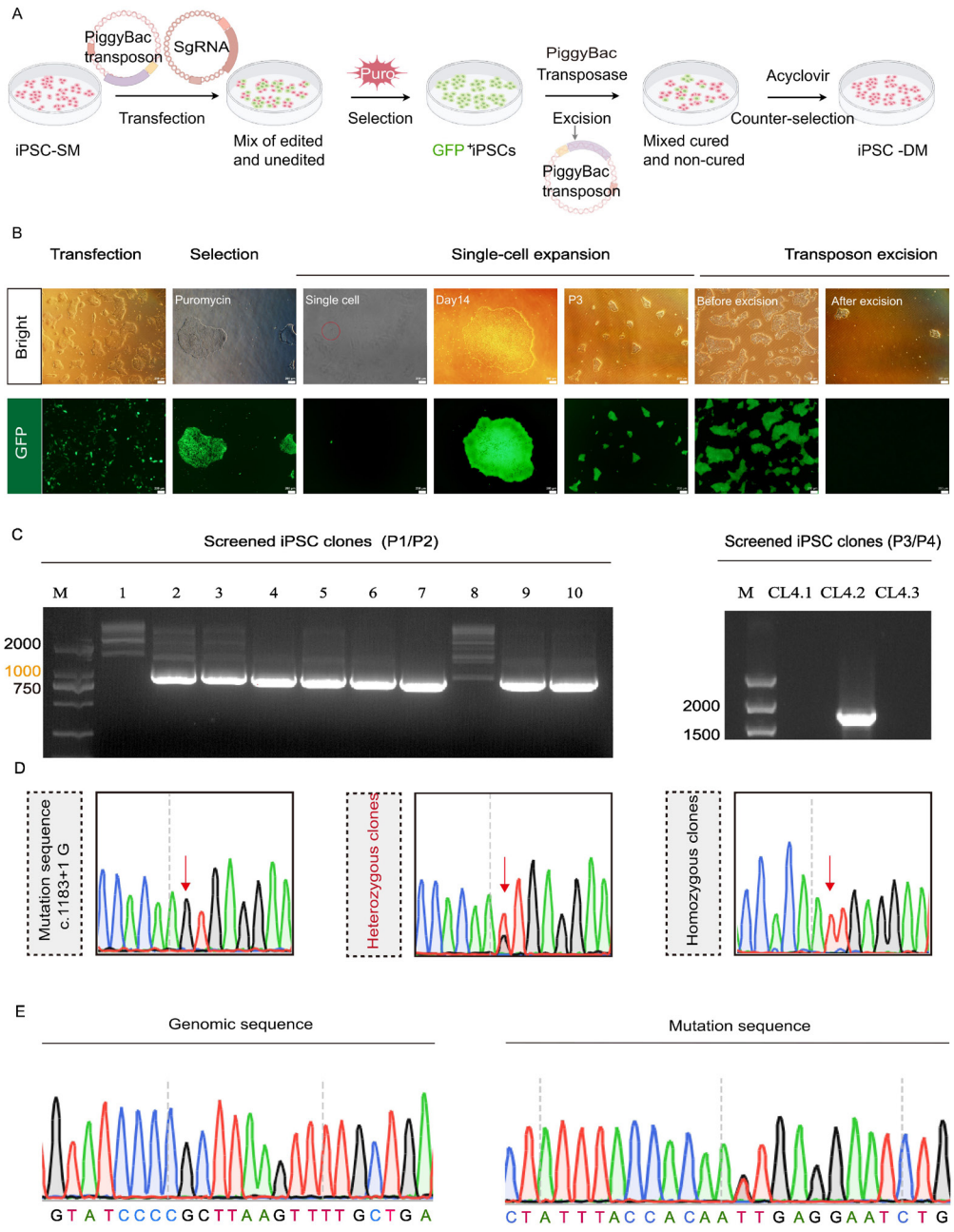

Figure 1. Genotypic validation of footprint-free EXT1 biallelic mutant iPSCs. (A) Schematic overview of the CRISPR/Cas9 and PiggyBac-mediated editing workflow. **(B)** Representative bright-field and fluorescence micrographs documenting GFP-positive integration and subsequent transposon excision. **(C)** PCR analysis confirming site-specific integration (P1/P2) and complete PiggyBac cassette excision (P3/P4). **(D)** Sanger sequencing chromatograms verifying the engineered c.1883+1G>T mutation in isolated clones. **(E)** Sanger sequencing confirming the footprint-free restoration of the native genomic sequence at the transposon integration site.

iMSCs underwent normal chondrogenic differentiation, whereas DM iMSCs exhibited markedly enhanced chondrogenic marker expression. Immunofluorescence analysis revealed significantly intensified ACAN signal and complete absence of EXT1 protein in iChOs-DM (Figure 2B). RT-qPCR demonstrated that *ACAN*, *SOX9*, and *COL2A1* mRNA levels were all significantly elevated in DM, most pronounced at day 21. *ACAN* and *SOX9* showed time-dependent progressive increases, while *COL2A1* was initially low at days 4 and 7 before sharp upregulation at day 21 (Figure 2C), suggesting that biallelic *EXT1* loss disrupts the normal temporal coordination of chondrogenic differentiation. Previous studies have reported consistent findings: *Ext1*-deficient periosteal progenitor cells displayed enhanced chondrogenic capacity (*16*), and simultaneous silencing of *EXT1* and *FGFR3* in ATDC5 cells similarly promoted chondrogenesis (*20*).

In 3D organoid culture, DM chondrogenic organoids (iChOs-DM) were visibly larger and exhibited irregular, asymmetric morphology compared with WT and SM organoids. H&E staining revealed marked internal structural disorganization in iChOs-DM. Safranin O and Alcian Blue staining demonstrated intense but spatially

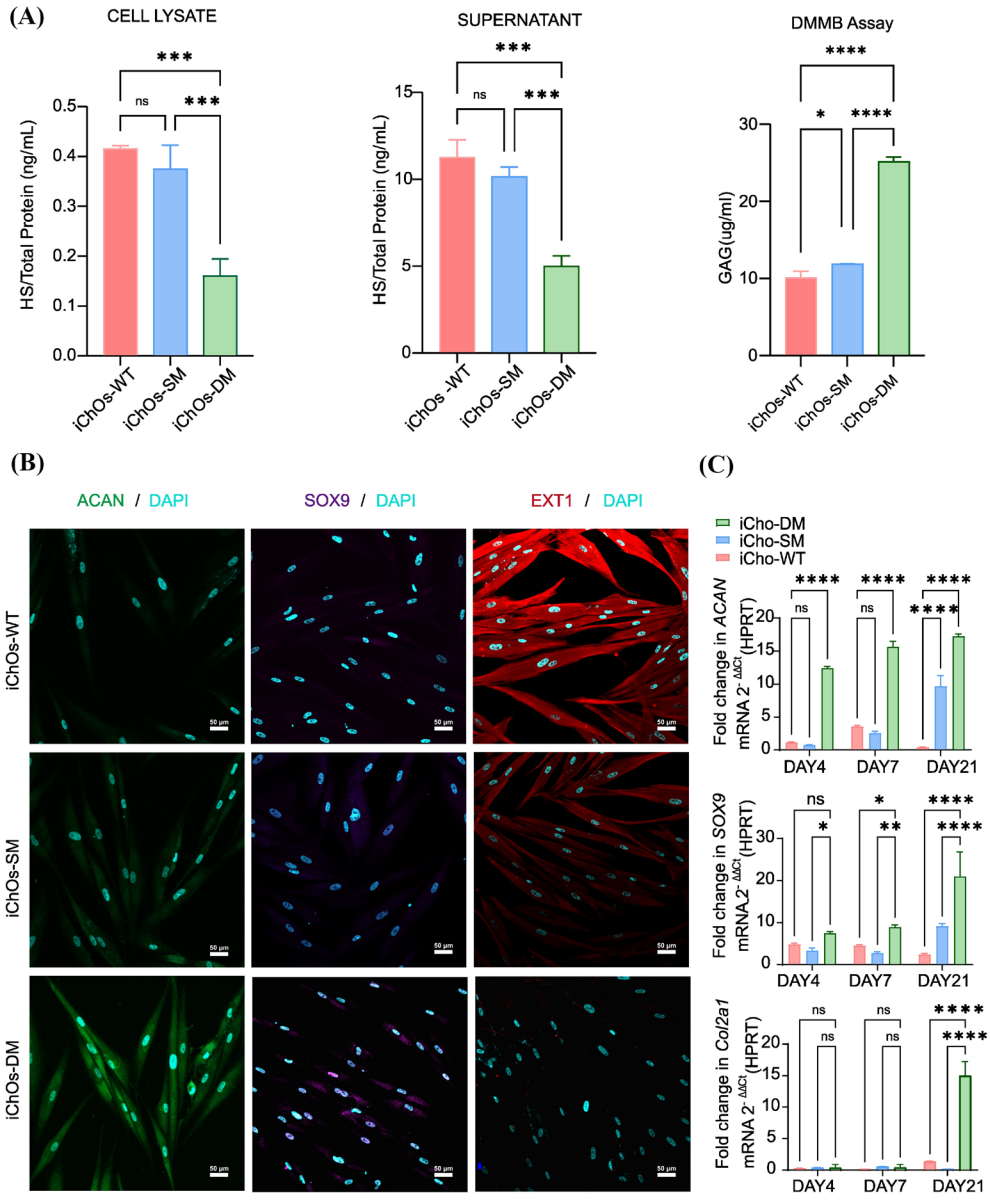

Figure 2. Biallelic *EXT1* inactivation disrupts ECM homeostasis and accelerates 2D chondrogenesis. (A) Quantification of HS by ELISA and total GAG by DMMB assay at day 21. **(B)** Immunofluorescence for ACAN (green), SOX9 (purple), and EXT1 (red) in 2D chondrocyte cultures. Scale bar: 50 µm. **(C)** RT-qPCR of *ACAN*, *SOX9*, and *COL2A1* at days 4, 7, 21. Data: mean ± SD; Kruskal–Wallis test with Dunn's post hoc correction.

heterogeneous proteoglycan deposition (Figure 3A), consistent with the approximately 50% GAG elevation reported in *Ext1*-hypomorphic mouse cartilage (*21*). Immunofluorescence confirmed markedly enhanced ACAN and complete EXT1 absence in iChOs-DM (Figure 3B). These phenotypic features partially recapitulate osteochondroma histopathology observed in *Ext1*-knockout mouse models (*14,22*).

Critically, SM iMSCs and organoids were indistinguishable from WT in both culture systems, and only DM exhibited accelerated chondrogenesis and tissue disorganization. This finding agrees with de Andrea *et al.* (*12*), who demonstrated that heterozygous *EXT* mutation does not impair chondrogenic differentiation and that osteochondroma formation is contingent upon LOH. Collectively, biallelic *EXT1* inactivation drives excessive chondrogenic gene expression, aberrant proteoglycan accumulation, and tissue architectural disruption, successfully recapitulating key pathological features of HMO *in vitro*.

3.4. Wnt signaling is the most significantly enriched pathway following EXT1 loss

To identify downstream signaling networks disrupted by *EXT1* loss, we performed transcriptomic profiling of day 21 chondrocytes. Comparative analysis identified substantial uniquely and overlappingly differentially expressed genes across genotypic transitions (Figure 4B), and principal component analysis (PCA) further

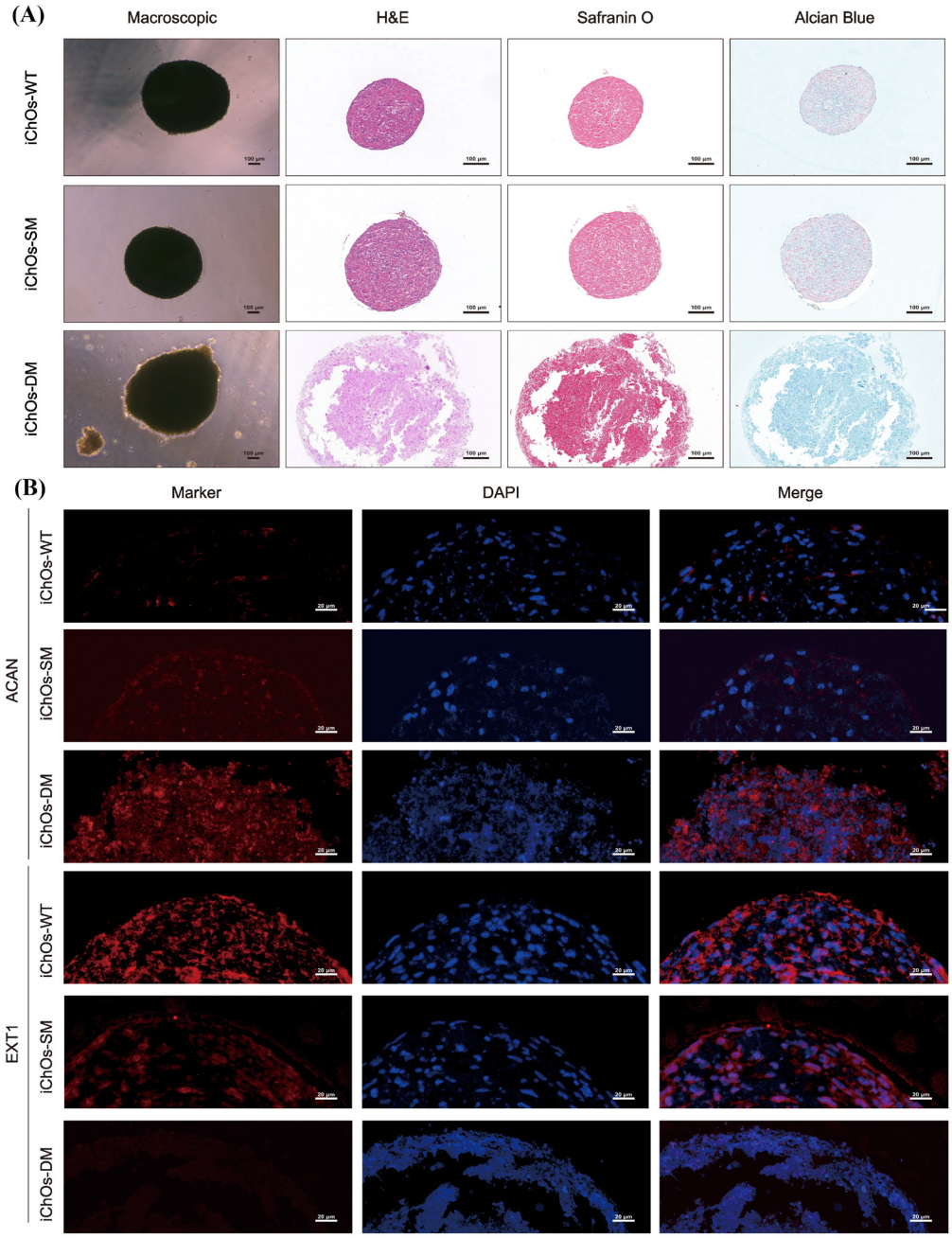

Figure 3. Complete *EXT1* loss promotes aberrant cartilage matrix deposition in 3D chondrogenic organoid culture. (A) Representative microscopic appearance of chondrogenic organoids at day 21 (top), H&E (second row), Safranin O (third row), and Alcian Blue (bottom row). Scale bar: 100 μm. **(B)** Immunofluorescence for ACAN (green) and EXT1 (red) with DAPI. Scale bar: 20 μm.

revealed distinct global expression signatures among the WT, SM, and DM groups (Figure 4C). We subsequently mapped the hierarchical clustering of core Wnt-related genes (Figure 4D), guided by KEGG pathway enrichment analysis which placed Wnt signaling as the most significantly enriched pathway (Figure 4E). Because HSPGs regulate Wnt ligand spatial distribution through differentially sulfated HS domains (*13,23*), these transcriptomic findings prompted targeted validation by RT-qPCR (Figure 4G).

Canonical Wnt ligands *WNT10B* and *WNT2B* were exclusively and significantly upregulated in DM ($p <$ 0.0001), mirroring the DM-specific cartilage marker pattern (*24,25*). Secreted frizzled-related protein (*SFRP1* and *SFRP4*) mRNA levels were already markedly elevated in SM—higher than in DM—suggesting that partial HS reduction triggers compensatory Wnt antagonist upregulation. Despite elevated *SFRP4* mRNA in SM, SFRP4 protein was paradoxically lowest in SM (Figure 4F), likely reflecting active extracellular secretion for Wnt buffering (*26*). The β-catenin target *CCND2* (cyclin D2) was elevated at both mRNA and protein levels in DM (Figure 4F, G), confirming canonical Wnt/β-catenin activation (*27*). WNT10B protein did not

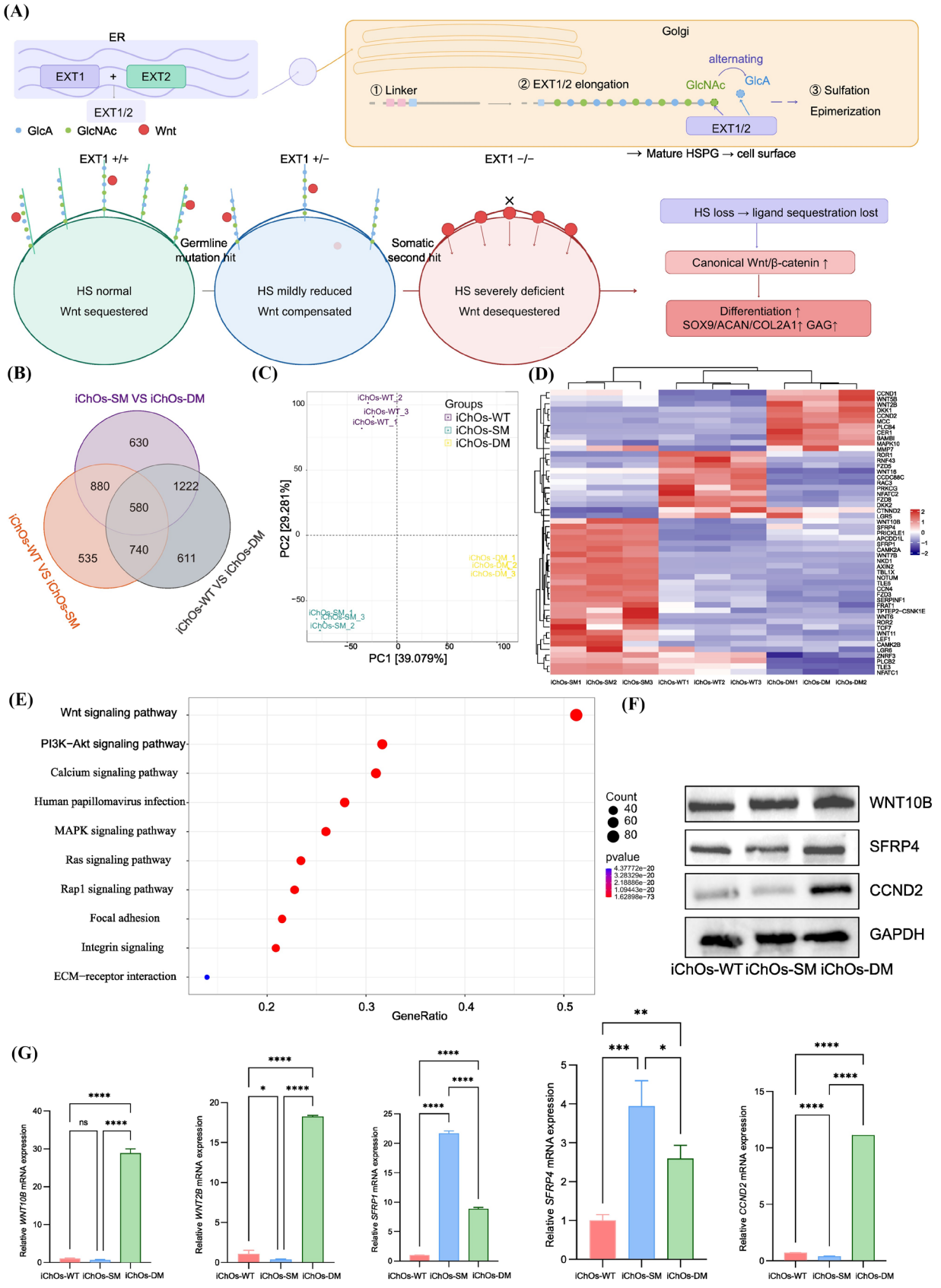

Figure 4. Transcriptomic analysis reveals Wnt signaling remodeling. (A) Schematic of the proposed EXT1/HSPG-dependent morphogen ligand sequestration model illustrating the consequences of graded EXT1 loss on canonical Wnt/β-catenin signaling (WT: intact gatekeeper; SM: compensated; DM: gatekeeper collapse). **(B)** Venn diagram. **(C)** PCA. **(D)** Heatmap. **(E)** KEGG enrichment. **(F)** Western blot: WNT10B, SFRP4, CCND2, GAPDH. **(G)** RT-qPCR: *WNT10B*, *WNT2B*, *SFRP1*, *SFRP4*, *CCND2*. Data: mean ± SD; Kruskal–Wallis with Dunn's correction.

proportionally mirror its mRNA, possibly due to loss of HSPG-mediated surface retention and accelerated extracellular release (*13,28*).

These data collectively support a "molecular gatekeeper" model in which HS sequesters morphogens—IHH, BMPs, FGFs, and Wnts—at the cell surface and within the pericellular matrix, maintaining signaling homeostasis (*7,13,28*). Approximately 50% of normal *EXT1* activity (SM) suffices to maintain this threshold; complete loss (DM) triggers a "signal eruption"—uncontrolled morphogen release overstimulating chondrogenesis (Figure 4A).

We propose a two-stage pathogenic framework. In the first stage ("priming"), germline heterozygous EXT1 mutation depletes the HS biosynthetic reserve without altering steady-state levels, thereby triggering compensatory SFRP1/4 upregulation—as evidenced by peak transcription in SM—sufficient to maintain normal differentiation. In the second stage ("triggering"), somatic second hit causes complete EXT1 inactivation and HS biosynthetic collapse. Compensatory SFRP buffering is overwhelmed: canonical Wnt ligands WNT10B and WNT2B are released in excess, and unrestrained canonical Wnt/β-catenin activation drives pathological chondrogenesis, concordant with LOH detection in 63% of clinical osteochondromas (*12*).

Mechanistically, HS loss simultaneously liberates canonical Wnt ligands and destabilizes SFRP antagonists whose stability depends on HSPG scaffolding (28). Gerstner *et al*. proposed an *EXT1*–Wnt regulatory feedback loop whose disruption may explain the explosive DM upregulation as overshoot compensation. The mRNA–protein discordance for WNT10B and SFRP4 can be explained by a unified mechanism: HS loss alters the extracellular fate of secreted canonical Wnt components—ligands lose surface tethering and undergo accelerated release, while antagonists exhibit reduced intracellular accumulation due to enhanced secretory flux. These findings further establish HS deficiency as a critical driver of canonical Wnt pathway dysregulation.

Notably, our use of iMSCs recapitulates periosteal mesenchymal progenitor differentiation, modeling the periosteal origin of osteochondromas (*14,16*)—a mechanism the traditional growth plate hypothesis cannot explain. Complete *EXT1* inactivation thus emerges as the decisive switch redirecting mesenchymal progenitor fate from osteogenic maintenance toward aberrant chondrogenesis.

In conclusion, by combining patient-derived iPSCs with footprint-free CRISPR/Cas9–PiggyBac editing, we demonstrate that complete EXT1 inactivation—not haploinsufficiency—is required to collapse HS-dependent morphogen gating, unleash canonical Wnt signaling, and drive pathological chondrogenesis. These findings provide direct human cellular evidence supporting the Two-hit model of HMO pathogenesis. However, as all iPSC lines derive from a single patient, validation across additional EXT1 or EXT2 genotypes is warranted. Furthermore, the *in vitro* system does not fully recapitulate the *in vivo* growth plate microenvironment; future studies employing *in vivo* transplantation and Wnt pathway modulation will be essential to evaluate therapeutic potential and model malignant progression toward secondary chondrosarcoma.

Acknowledgements

We sincerely thank Lingqun Ye, Ph.D., from Soochow University for kindly providing the original plasmids required for our gene editing research using the CRISPR-Cas9 and PiggyBac systems.

Funding: This work was supported by a grant from Shandong First Medical University (LJ001).

Conflict of Interest: The authors have no conflicts of interest to disclose.

References

1. Bovée JVMG. Multiple osteochondromas. Orphanet J Rare Dis. 2008; 3:3.
2. Schmale GA, Conrad EU, Raskind WH. The natural history of hereditary multiple exostoses. J Bone Joint Surg Am. 1994; 76:986-992.
3. Ahmed AR, Tan TS, Unni KK, Collins MS, Wenger DE, Sim FH. Secondary chondrosarcoma in osteochondroma: Report of 107 patients. Clin Orthop Relat Res. 2003; 411:193-206.
4. McCormick C, Duncan G, Goutsos KT, Bhatt L. The putative tumour suppressor EXT1 alters the expression of cell-surface heparan sulfate. Nat Genet. 1998; 19:158-161.
5. Lin X. Functions of heparan sulfate proteoglycans in cell signaling during development. Development. 2004; 131:6009-6021.
6. Bernfield M, Götte M, Park PW, Reizes O, Fitzgerald ML, Lincecum J, Zako M. Functions of cell surface heparan sulfate proteoglycans. Annu Rev Biochem. 1999; 68:729-777.
7. Koziel L, Kunath M, Kelly OG, Vortkamp A. Ext1-dependent heparan sulfate regulates the range of Ihh signaling during endochondral ossification. Dev Cell. 2004; 6:801-813.
8. Clement A, Wiweger M, von der Hardt S, Ruber MA, Crome A, Schulte-Merker S, Knust E. Regulation of zebrafish skeletogenesis by ext2/dackel and papst1/pinscher. PLoS Genet. 2008; 4:e1000136.
9. Knudson AG. Mutation and cancer: Statistical study of retinoblastoma. Proc Natl Acad Sci U S A. 1971; 68:820-823.
10. Zak BM, Schuksz M, Koyama E, Munoz C, De Jong DS, Koober DG, Pacifici M, Esko JD. Compound heterozygous loss of Ext1 and Ext2 is sufficient for formation of multiple exostoses in mouse ribs and long bones. Bone. 2011; 48:979-987.
11. Stickens D, Zak BM, Rougier N, Esko JD, Bhatt SR. Mice deficient in Ext2 lack heparan sulfate and develop exostoses. Development. 2005; 132:5055-5068.
12. de Andrea CE, Reijnders CMA, Kroon HM, de Jong

D, Hogéndoorn PCW, Szuhai K, Bovée JVMG. Secondary peripheral chondrosarcoma evolving from osteochondroma as a result of outgrowth of cells with functional EXT. Oncogene. 2012; 31:1095-1104.
13. Mii Y, Takada S. Heparan sulfate proteoglycans as Wnt co-receptors and their role in Wnt signaling. Front Cell Dev Biol. 2020; 8:631.
14. Jones KB, Piombo V, Searby C, Kurriger G, Yang B, Grabellus F, Roughley PJ, Morcuende JA, Buckwalter JA, Capecchi MR, Vortkamp A, Sheffield VC. A mouse model of osteochondromagenesis from clonal inactivation of Ext1 in chondrocytes. Proc Natl Acad Sci U S A. 2010; 107:2054-2059.
15. Matsumoto K, Irie F, Mackem S, Yamaguchi Y. A mouse model of chondrocyte-specific somatic mutation reveals a role for Ext1 loss of heterozygosity in multiple hereditary exostoses. Proc Natl Acad Sci U S A. 2010; 107:10932-10937.
16. Inubushi T, Nozawa S, Matsumoto K, Irie F, Yamaguchi Y. Aberrant perichondrial BMP signaling mediates multiple osteochondromagenesis in mice. JCI Insight. 2017; 2:e90049.
17. Huegel J, Sgariglia F, Enomoto-Iwamoto M, Koyama E, Dormans JP, Pacifici M. Heparan sulfate in skeletal development, growth, and pathology: the case of hereditary multiple exostoses. Dev Dyn. 2013; 242:1021-1032.
18. Bachvarova V, Dierker T, Esko JD, Hoffmann D, Kjellén L, Vortkamp A. Chondrocytes respond to an altered heparan sulfate composition with distinct changes of heparan sulfate structure and increased levels of chondroitin sulfate. Matrix Biol. 2020; 93:43-59.
19. Huegel J, Enomoto-Iwamoto M, Sgariglia F, Koyama E, Pacifici M. Heparanase stimulates chondrogenesis and is up-regulated in human ectopic cartilage: A mechanism possibly involved in hereditary multiple exostoses. Am J Pathol. 2015; 185:1676-1685.
20. Zhang F, Wang Y, Li T, Liu H, Chen W, Guo J. EXT1 and FGFR3 co-silencing promotes chondrogenesis in ATDC5 cells. Mol Med Rep. 2024; 29:7.
21. Gerstner M, Jouanno Y, Gericke M, Wienhold T, Dierker T, Osterhaus K, Gorsi HS. A cartilage-specific EXT1 mouse model recapitulates features of hereditary multiple osteochondromas. Bone. 2021; 143:115794.
22. Jones KB, Pacifici M, Hilton MJ. Multiple hereditary exostoses (MHE): Elucidating the pathogenesis of a rare skeletal disorder through interdisciplinary research. J Biomed Biotechnol. 2012; 2012:462049.
23. Mii Y, Nakazato K, Pack CG, Ikeda T, Makino Y, Ito A, Shimono C, Takada S. Asymmetric Wnt ligand distribution on the cell surface by heparan sulfate proteoglycans. eLife. 2022; 11:e73818.
24. Bennett CN, Ouyang H, Ma YL, Zeng Q, Gerin I, Sousa KM, Lane TF, Krishnan V, Hankenson KD, MacDougald OA. Wnt10b increases postnatal bone formation by enhancing osteoblast differentiation. J Bone Miner Res. 2007; 22:1924-1932.
25. Riedl M, Witzmann C, Koch M, Lang S, Kerschbaum M, Grifka J, Grässel S. WNT2B mediates chondrogenic commitment of human bone marrow-derived mesenchymal stromal cells. Sci Rep. 2020; 10:7113.
26. Nakanishi R, Shimizu M, Mori M, Akiyama H, Okudaira S, Otsuki B, Hashimoto M, Higuchi K, Watanabe M, Nishi H, Kondoh T, Sano S, Nakamura T. Secreted frizzled-related protein 4 is a negative regulator of peak BMD in SAMP6 mice. Sci Rep. 2016; 6:25198.
27. Day TF, Guo X, Garrett-Beal L, Yang Y. Wnt/beta-catenin signaling in mesenchymal progenitors controls osteoblast and chondrocyte differentiation during vertebrate skeletogenesis. Dev Cell. 2005; 8:739-750.
28. Üen A, Reichsman F, Anest V, Taylor WG, Muraiso K, Bottaro DP, Cumberledge S, Rubin JS. Secreted frizzled-related protein-1 binds directly to Wingless and is a biphasic modulator of Wnt signaling. J Biol Chem. 2000; 275:4374-4382.

Received February 10, 2026; Revised March 20, 2026; Accepted March 24, 2026.

Address correspondence to:
Jing Luan and Jinxiang Han, Biomedical Sciences College, Shandong First Medical University, Ji'nan, Shandong 250117, China.
E-mail: luanjing@sdfmu.edu.cn (JL); jxhan9888@aliyun.com (JH)

Yazhou Cui, Qingdao Academy of Chinese Medical Science, Shandong University of Traditional Chinese Medicine, Ji'nan, Shandong 250355, China; Biomedical Sciences College, Shandong First Medical University, Ji'nan, Shandong 250117, China.
E-mail: cuiyazhou@sdutcm.edu.cn

Released online in J-STAGE as advance publication March 26, 2026.

BST
BioScience Trends

Guide for Authors

1. Scope of Articles

BioScience Trends (Print ISSN 1881-7815, Online ISSN 1881-7823) is an international peer-reviewed journal. *BioScience Trends* devotes to publishing the latest and most exciting advances in scientific research. Articles cover fields of life science such as biochemistry, molecular biology, clinical research, public health, medical care system, and social science in order to encourage cooperation and exchange among scientists and clinical researchers.

2. Submission Types

Original Articles should be well-documented, novel, and significant to the field as a whole. An Original Article should be arranged into the following sections: Title page, Abstract, Introduction, Materials and Methods, Results, Discussion, Acknowledgments, and References. Original articles should not exceed 5,000 words in length (excluding references) and should be limited to a maximum of 50 references. Articles may contain a maximum of 10 figures and/or tables. Supplementary Data are permitted but should be limited to information that is not essential to the general understanding of the research presented in the main text, such as unaltered blots and source data as well as other file types.

Brief Reports definitively documenting either experimental results or informative clinical observations will be considered for publication in this category. Brief Reports are not intended for publication of incomplete or preliminary findings. Brief Reports should not exceed 3,000 words in length (excluding references) and should be limited to a maximum of 4 figures and/or tables and 30 references. A Brief Report contains the same sections as an Original Article, but the Results and Discussion sections should be combined.

Reviews should present a full and up-to-date account of recent developments within an area of research. Normally, reviews should not exceed 8,000 words in length (excluding references) and should be limited to a maximum of 10 figures and/or tables and 100 references. Mini reviews are also accepted, which should not exceed 4,000 words in length (excluding references) and should be limited to a maximum of 5 figures and/or tables and 50 references.

Policy Forum articles discuss research and policy issues in areas related to life science such as public health, the medical care system, and social science and may address governmental issues at district, national, and international levels of discourse. Policy Forum articles should not exceed 3,000 words in length (excluding references) and should be limited to a maximum of 5 figures and/or tables and 30 references.

Communications are short, timely pieces that spotlight new research findings or policy issues of interest to the field of global health and medical practice that are of immediate importance. Depending on their content, Communications will be published as "Comments" or "Correspondence". Communications should not exceed 1,500 words in length (excluding references) and should be limited to a maximum of 2 figures and/or tables and 20 references.

Editorials are short, invited opinion pieces that discuss an issue of immediate importance to the fields of global health, medical practice, and basic science oriented for clinical application. Editorials should not exceed 1,000 words in length (excluding references) and should be limited to a maximum of 10 references. Editorials may contain one figure or table.

News articles should report the latest events in health sciences and medical research from around the world. News should not exceed 500 words in length.

Letters should present considered opinions in response to articles published in *BioScience Trends* in the last 6 months or issues of general interest. Letters should not exceed 800 words in length and may contain a maximum of 10 references. Letters may contain one figure or table.

3. Editorial Policies

For publishing and ethical standards, *BioScience Trends* follows the Recommendations for the Conduct, Reporting, Editing, and Publication of Scholarly Work in Medical Journals issued by the International Committee of Medical Journal Editors (ICMJE, *https://icmje.org/recommendations*), and the Principles of Transparency and Best Practice in Scholarly Publishing jointly issued by the Committee on Publication Ethics (COPE, *https://publicationethics.org/resources/guidelines-new/principles-transparency-and-best-practice-scholarly-publishing*), the Directory of Open Access Journals (DOAJ, *https://doaj.org/apply/transparency*), the Open Access Scholarly Publishers Association (OASPA, *https://oaspa.org/principles-of-transparency-and-best-practice-in-scholarly-publishing-4*), and the World Association of Medical Editors (WAME, *https://wame.org/principles-of-transparency-and-best-practice-in-scholarly-publishing*).

BioScience Trends will perform an especially prompt review to encourage innovative work. All original research will be subjected to a rigorous standard of peer review and will be edited by experienced copy editors to the highest standards.

Ethical Approval of Studies and Informed Consent: For all manuscripts reporting data from studies involving human participants or animals, formal review and approval, or formal review and waiver, by an appropriate institutional review board or ethics committee is required and should be described in the Methods section. When your manuscript contains any case details, personal information and/or images of patients or other individuals, authors must obtain appropriate written consent, permission and release in order to comply with all applicable laws and regulations concerning privacy and/or security of personal information. The consent form needs to comply with the relevant legal requirements of your particular jurisdiction, and please do not send signed consent form to *BioScience Trends* to respect your patient's and any other individual's privacy. Please instead describe the information clearly in the Methods (patient consent) section of your manuscript while retaining copies of the signed forms in the event they should be needed. Authors should also state that the study conformed to the provisions of the Declaration of Helsinki (as revised in 2013, *https://wma.net/what-we-do/medical-ethics/declaration-of-helsinki*). When reporting experiments on animals, authors should indicate whether the institutional and national guide for the care and use of laboratory animals was followed.

Reporting Clinical Trials: The ICMJE (*https:// icmje.org/recommendations/browse/publishing-and-editorial-issues/clinical-trial-registration.html*) defines a clinical trial as any research project that prospectively assigns people or a group of people to an intervention, with or without concurrent comparison or control groups, to study the relationship between a health-related intervention and a health outcome. Registration of clinical trials in a public trial registry at or before the time of first patient enrollment is a condition of consideration for publication in *BioScience Trends*, and the trial registration number will be published at the end of the Abstract. The registry must be independent of for-profit interest and publicly accessible. Reports of trials must conform to CONSORT 2010 guidelines (*https://consort-statement.org/consort-2010*). Articles reporting the results of randomized trials must include the CONSORT flow diagram showing the progress of patients throughout the trial.

Conflict of Interest: All authors are required to disclose any actual or potential conflict of interest including financial interests or relationships with other people or organizations that might raise questions of bias

in the work reported. If no conflict of interest exists for each author, please state "There is no conflict of interest to disclose".

Submission Declaration: When a manuscript is considered for submission to *BioScience Trends*, the authors should confirm that 1) no part of this manuscript is currently under consideration for publication elsewhere; 2) this manuscript does not contain the same information in whole or in part as manuscripts that have been published, accepted, or are under review elsewhere, except in the form of an abstract, a letter to the editor, or part of a published lecture or academic thesis; 3) authorization for publication has been obtained from the authors' employer or institution; and 4) all contributing authors have agreed to submit this manuscript.

Initial Editorial Check: Immediately after submission, the journal's managing editor will perform an initial check of the manuscript. A suitable academic editor will be notified of the submission and invited to check the manuscript and recommend reviewers. Academic editors will check for plagiarism and duplicate publication at this stage. The journal has a formal recusal process in place to help manage potential conflicts of interest of editors. In the event that an editor has a conflict of interest with a submitted manuscript or with the authors, the manuscript, review, and editorial decisions are managed by another designated editor without a conflict of interest related to the manuscript.

Peer Review: *BioScience Trends* operates a single-anonymized review process, which means that reviewers know the names of the authors, but the authors do not know who reviewed their manuscript. All articles are evaluated objectively based on academic content. External peer review of research articles is performed by at least two reviewers, and sometimes the opinions of more reviewers are sought. Peer reviewers are selected based on their expertise and ability to provide quality, constructive, and fair reviews. For research manuscripts, the editors may, in addition, seek the opinion of a statistical reviewer. Every reviewer is expected to evaluate the manuscript in a timely, transparent, and ethical manner, following the COPE guidelines (*https://publicationethics.org/files/cope-ethical-guidelines-peer-reviewers-v2_0.pdf*). We ask authors for sufficient revisions (with a second round of peer review, when necessary) before a final decision is made. Consideration for publication is based on the article's originality, novelty, and scientific soundness, and the appropriateness of its analysis.

Suggested Reviewers: A list of up to 3 reviewers who are qualified to assess the scientific merit of the study is welcomed. Reviewer information including names, affiliations, addresses, and e-mail should be provided at the same time the manuscript is submitted online. Please do not suggest reviewers with known conflicts of interest, including participants or anyone with a stake in the proposed research; anyone from the same institution; former students, advisors, or research collaborators (within the last three years); or close personal contacts. Please note that the Editor-in-Chief may accept one or more of the proposed reviewers or may request a review by other qualified persons.

Language Editing: Manuscripts prepared by authors whose native language is not English should have their work proofread by a native English speaker before submission. If not, this might delay the publication of your manuscript in *BioScience Trends*.

The Editing Support Organization can provide English proofreading, Japanese-English translation, and Chinese-English translation services to authors who want to publish in *BioScience Trends* and need assistance before submitting a manuscript. Authors can visit this organization directly at *https://www.iacmhr.com/iac-eso/support.php?lang=en*. IAC-ESO was established to facilitate manuscript preparation by researchers whose native language is not English and to help edit works intended for international academic journals.

Copyright and Reuse: Before a manuscript is accepted for publication in *BioScience Trends*, authors will be asked to sign a transfer of copyright agreement, which recognizes the common interest that both the journal and author(s) have in the protection of copyright. We accept that some authors (*e.g.*, government employees in some countries) are unable to transfer copyright. A JOURNAL PUBLISHING AGREEMENT (JPA) form will be e-mailed to the authors by the Editorial Office and must be returned by the authors by mail, fax, or as a scan. Only forms with a hand-written signature from the corresponding author are accepted. This copyright will ensure the widest possible dissemination of information. Please note that the manuscript will not proceed to the next step in publication until the JPA Form is received. In addition, if excerpts from other copyrighted works are included, the author(s) must obtain written permission from the copyright owners and credit the source(s) in the article.

4. Cover Letter

The manuscript must be accompanied by a cover letter prepared by the corresponding author on behalf of all authors. The letter should indicate the basic findings of the work and their significance. The letter should also include a statement affirming that all authors concur with the submission and that the material submitted for publication has not been published previously or is not under consideration for publication elsewhere. The cover letter should be submitted in PDF format. For an example of Cover Letter, please visit: *https://www.biosciencetrends.com/downcentre* (Download Centre).

5. Submission Checklist

The Submission Checklist should be submitted when submitting a manuscript through the Online Submission System. Please visit Download Centre (*https://www.biosciencetrends.com/downcentre*) and download the Submission Checklist file. We recommend that authors use this checklist when preparing your manuscript to check that all the necessary information is included in your article (if applicable), especially with regard to Ethics Statements.

6. Manuscript Preparation

Manuscripts are suggested to be prepared in accordance with the "Recommendations for the Conduct, Reporting, Editing, and Publication of Scholarly Work in Medical Journals", as presented at *https://www.ICMJE.org*.

Manuscripts should be written in clear, grammatically correct English and submitted as a Microsoft Word file in a single-column format. Manuscripts must be paginated and typed in 12-point Times New Roman font with 24-point line spacing. Please do not embed figures in the text. Abbreviations should be used as little as possible and should be explained at first mention unless the term is a well-known abbreviation (*e.g.* DNA). Single words should not be abbreviated.

Title page: The title page must include 1) the title of the paper (Please note the title should be short, informative, and contain the major key words); 2) full name(s) and affiliation(s) of the author(s), 3) abbreviated names of the author(s), 4) full name, mailing address, telephone/fax numbers, and e-mail address of the corresponding author; 5) author contribution statements to specify the individual contributions of all authors to this manuscript, and 6) conflicts of interest (if you have an actual or potential conflict of interest to disclose, it must be included as a footnote on the title page of the manuscript; if no conflict of interest exists for each author, please state "There is no conflict of interest to disclose").

Abstract: The abstract should briefly state the purpose of the study, methods, main findings, and conclusions. For articles that are Original Articles, Brief Reports, Reviews, or Policy Forum articles, a one-paragraph abstract consisting of no more than 250 words must be included in the manuscript. For Communications, Editorials, News, or Letters, a brief summary of main content in 150 words or fewer should be included in the manuscript. For articles reporting clinical trials, the trial registration number should be stated at the end of the Abstract. Abbreviations must be kept to a minimum and non-standard

abbreviations explained in brackets at first mention. References should be avoided in the abstract. Three to six key words or phrases that do not occur in the title should be included in the Abstract page.

Introduction: The introduction should provide sufficient background information to make the article intelligible to readers in other disciplines and sufficient context clarifying the significance of the experimental findings

Materials/Patients and Methods: The description should be brief but with sufficient detail to enable others to reproduce the experiments. Procedures that have been published previously should not be described in detail but appropriate references should simply be cited. Only new and significant modifications of previously published procedures require complete description. Names of products and manufacturers with their locations (city and state/country) should be given and sources of animals and cell lines should always be indicated. All clinical investigations must have been conducted in accordance Materials/ Patients and Methods.

Results: The description of the experimental results should be succinct but in sufficient detail to allow the experiments to be analyzed and interpreted by an independent reader. If necessary, subheadings may be used for an orderly presentation. All Figures and Tables should be referred to in the text in order, including those in the Supplementary Data.

Discussion: The data should be interpreted concisely without repeating material already presented in the Results section. Speculation is permissible, but it must be well-founded, and discussion of the wider implications of the findings is encouraged. Conclusions derived from the study should be included in this section.

Acknowledgments: All funding sources (including grant identification) should be credited in the Acknowledgments section. Authors should also describe the role of the study sponsor(s), if any, in study design; in the collection, analysis, and interpretation of data; in the writing of the report; and in the decision to submit the paper for publication. If the funding source had no such involvement, the authors should so state.

In addition, people who contributed to the work but who do not meet the criteria for authors should be listed along with their contributions.

References: References should be numbered in the order in which they appear in the text. Citing of unpublished results, personal communications, conference abstracts, and theses in the reference list is not recommended but these sources may be mentioned in the text. In the reference list, cite the names of all authors when there are fifteen or fewer authors; if there are sixteen or more authors, list the first three followed by *et al*. Names of journals should be abbreviated in the style used in PubMed. Authors are responsible for the accuracy of the references. The EndNote Style of *BioScience Trends* could be downloaded at **EndNote** (*https://ircabssagroup.com/examples/BioScience_Trends.ens*).

Examples are given below:

Example 1 (Sample journal reference):

Inagaki Y, Tang W, Zhang L, Du GH, Xu WF, Kokudo N. Novel aminopeptidase N (APN/CD13) inhibitor 24F can suppress invasion of hepatocellular carcinoma cells as well as angiogenesis. Biosci Trends. 2010; 4:56-60.

Example 2 (Sample journal reference with more than 15 authors):

Darby S, Hill D, Auvinen A, *et al*. Radon in homes and risk of lung cancer: Collaborative analysis of individual data from 13 European case-control studies. BMJ. 2005; 330:223.

Example 3 (Sample book reference):

Shalev AY. Post-traumatic stress disorder: Diagnosis, history and life course. In: Post-traumatic Stress Disorder, Diagnosis, Management and Treatment (Nutt DJ, Davidson JR, Zohar J, eds.). Martin Dunitz, London, UK, 2000; pp. 1-15.

Example 4 (Sample web page reference):

World Health Organization. The World Health Report 2008 – primary health care: Now more than ever. *http://www.who.int/whr/2008/whr08_en.pdf* (accessed September 23, 2022).

Tables: All tables should be prepared in Microsoft Word or Excel and should be arranged at the end of the manuscript after the References section. Please note that tables should not in image format. All tables should have a concise title and should be numbered consecutively with Arabic numerals. If necessary, additional information should be given below the table.

Figure Legend: The figure legend should be typed on a separate page of the main manuscript and should include a short title and explanation. The legend should be concise but comprehensive and should be understood without referring to the text. Symbols used in figures must be explained. Any individually labeled figure parts or panels (A, B, *etc*.) should be specifically described by part name within the legend.

Figure Preparation: All figures should be clear and cited in numerical order in the text. Figures must fit a one- or two-column format on the journal page: 8.3 cm (3.3 in.) wide for a single column, 17.3 cm (6.8 in.) wide for a double column; maximum height: 24.0 cm (9.5 in.). Please make sure that the symbols and numbers appeared in the figures should be clear. Please make sure that artwork files are in an acceptable format (TIFF or JPEG) at minimum resolution (600 dpi for illustrations, graphs, and annotated artwork, and 300 dpi for micrographs and photographs). Please provide all figures as separate files. Please note that low-resolution images are one of the leading causes of article resubmission and schedule delays.

Units and Symbols: Units and symbols conforming to the International System of Units (SI) should be used for physicochemical quantities. Solidus notation (*e.g.* mg/kg, mg/mL, mol/mm^2/min) should be used. Please refer to the SI Guide *www.bipm.org/en/si/* for standard units.

Supplemental data: Supplemental data might be useful for supporting and enhancing your scientific research and *BioScience Trends* accepts the submission of these materials which will be only published online alongside the electronic version of your article. Supplemental files (figures, tables, and other text materials) should be prepared according to the above guidelines, numbered in Arabic numerals (*e.g.*, Figure S1, Figure S2, and Table S1, Table S2) and referred to in the text. All figures and tables should have titles and legends. All figure legends, tables and supplemental text materials should be placed at the end of the paper. Please note all of these supplemental data should be provided at the time of initial submission and note that the editors reserve the right to limit the size and length of Supplemental Data.

5. Submission Checklist

The Submission Checklist will be useful during the final checking of a manuscript prior to sending it to *BioScience Trends* for review. Please visit Download Centre and download the Submission Checklist file.

6. Online Submission

Manuscripts should be submitted to *BioScience Trends* online at *https://www.biosciencetrends.com/login*. Receipt of your manuscripts submitted online will be acknowledged by an e-mail from Editorial Office containing a reference number, which should be used in all future communications. If for any reason you are unable to submit a file online, please contact the Editorial Office by e-mail at *office@biosciencetrends.com*

8. Accepted Manuscripts

Page Charge: Page charges will be levied on all manuscripts accepted for publication in *BioScience Trends* (Original Articles / Brief Reports / Reviews / Policy Forum / Communications: $140 per page for black white pages, $340 per page for color pages; News / Letters: a total cost of $600). Under exceptional circumstances, the author(s) may apply to the editorial office for a waiver of the publication charges by stating the reason in the Cover Letter when the manuscript online.

Misconduct: *BioScience Trends* takes seriously all allegations of potential misconduct and adhere to the ICMJE Guideline (*https://icmje.org/recommendations*) and COPE Guideline (*https://publicationethics.org/files/Code_of_conduct_for_journal_editors.pdf*). In cases of suspected research or publication misconduct, it may be necessary for the Editor or Publisher to contact and share submission details with third parties including authors' institutions and ethics committees. The corrections, retractions, or editorial expressions of concern will be performed in line with above guidelines.

(As of December 2022)

BioScience Trends
Editorial and Head Office
Pearl City Koishikawa 603,
2-4-5 Kasuga, Bunkyo-ku,
Tokyo 112-0003, Japan.
E-mail: office@biosciencetrends.com